2022

Biosensing with Back-gated Graphene Field Effect Transistors

O'Driscoll, Benjamin

http://hdl.handle.net/10026.1/20053

http://dx.doi.org/10.24382/799
University of Plymouth

Copyright Statement

UNIVERSITY OF
PLYMOUTH

Biosensing with Back-gated Graphene Field Effect Transistors

by

Benjamin O'Driscoll

A thesis submitted to the Doctoral College of the University of Plymouth, in partial fulfilment of the degree of

DOCTOR OF PHILOSOPHY

School of Engineering, Computing and Mathematics

May 2022

Acknowledgements

A sincere thank you goes out to all of those who assisted me throughout this PhD. More specifically;

I would like to firstly extend my warmest thanks to my loving wife Kerri O'Driscoll for her unwavering support, from applying in the first instance all the way through to thesis submission. She has been a pillar of strength which I have been fortunate enough to rely on during the most difficult times.

Thank you Dr Vikram Srinivasa Raghavan, post-doctoral researcher, based at the Optics and Microfluidics Instrumentation Lab, Department of Instrumentation and Applied Physics, Indian Institute of Science, Bangalore. I have had the immense pleasure of collaborating with Vikram on several projects throughout my PhD. From this I have elevated my scientific knowledge and expertise and gained a fantastic insight into the world of academic collaboration.

Thank you to Dr Carrie Haslam, for her open and honest support during a critical time for her own studies, teaching me the fundamentals of cleanroom fabrication, characterisation and biofunctionalisation.

Thank you to Associate Professor David Jenkins for the continued assistance and support throughout this PhD. I have appreciated the additional opportunities you have made available to me throughout this process to develop me further as a researcher. In addition, your support with all things cleanroom has been greatly appreciated.

Thank you to all of the Davy building floor four technicians. Namely; Mr Andy Atfield, Biochemistry & Toxicology Senior Technician, Dr Joceline Triner, Histology & Microscopy Senior Technician, Dr William Vevers, Molecular Biology and Cell Culture Senior Technician and Miss Shannon-Marie Murtagh, Technician. Along with providing me with the critical biological handling techniques that I needed for this project this group were all incredibly positive and open to assisting me with any issues I had. As an outsider to their school I was really humbled by how supportive they were with their knowledge, equipment and resources and I applaud their 'let's give it a go mentality' to project work.

Thank you to all Plymouth Electron Microscopy Centre staff for being so open to collaborating with me on this project and being a set of friendly faces I could rely on. In particular, thank you to Mr Glenn Harper, Electron Microscopy Senior Technician, Dr Alex Strachan, Electron Microscopy Technical Specialist and Dr Tom O’Hanlon, Engineering and Material Sciences Technical Specialist, for providing insightful discussions and practical techniques to improve this contribution.

Thank you to Mr Nick Fry, Wolfson Nanomaterials and Devices Laboratory technician and Dr Ahmed Suhail for their patience and support in all aspects of cleanroom fabrication and maintenance. Thank you Mr John Welsh, Electronics Senior Technician, and Dr Stuart MacVeigh, Electronics Senior Technician, for always being so helpful with electronics related queries and requests; their open-door outlook to students is one that the school should be immensely proud of.

Thank you to Mr Terry Richards, Materials and Structures Senior Technician, Dr Jeremy Clark, Materials and Structures Senior Technician and Mrs Katie Shore, Materials and Structures Senior Technician for assisting me with the use of their equipment.

Thank you to Dr Toby Whitley, my Director of Studies for guiding me through the process of writing this thesis. Thank you to Dr Shakil Awan and Dr Paul Davey who were my second and third supervisors. Thank you Theodore Bungon, PhD candidate, for your useful discussions throughout.

Thank you to MolView and its developers for providing an online open-source tool for drawing molecular structures.

Finally, I would like to extend thanks to all of the nameless host creatures large and small that were used to manufacture the antibodies that this work benefited from. Without their silent contribution so much of science would be without progress.

Author's Declaration

At no time during the registration for the degree of Doctor of Philosophy has the author been registered for any other University award without prior agreement of the Doctoral College Quality Sub-Committee.

Work submitted for this research degree at the University of Plymouth has not formed part of any other degree either at the University of Plymouth or at another establishment.

This study was financed with the aid of a studentship from the University of Plymouth, project code: GD110025-104. Additional funding relating to specific aptamers used in this work is also acknowledged and attributed to the Global Challenges Research Fund (GCRF), Project code: SP/GCRF-19/003. The x-ray photoelectron (XPS) data collection was performed at the EPSRC National Facility for XPS ("HarwellXPS"), operated by Cardiff University and UCL, under Contract No. PR16195.

Word count of main body of thesis: ……61,626…………..

Signed: ……….. …………..

Date: …………05/05/2022………….

Abstract

Aptamer Functionalisation of Back-gated Graphene Field Effect Transistors for Pb2+ Sensing

Benjamin O'Driscoll

The widespread existence of the heavy metal lead in the environment is a severe threat to the health of humans. Lead is a neurotoxin that accumulates over time in the body restricting the cognitive, behavioural and psychological development of children. Since water is one exposure route for chemical hazards like Pb^{2+} it is envisioned that monitoring drinking water sources with low-cost, sensitive and field-suitable devices is one way that human exposure can be limited. Herein presents graphene field effect transistors (GFETs) functionalised with aptamers as bioreceptors, for the specific detection of Pb^{2+} ions in water.

Functionalising GFETs with bioreceptors facilitates the specific detection of target analytes. Traditionally antibodies have been used to do this but owing to their poor stability, high expense and batch to batch variability the recent trend in biosensing technologies has focussed on the functionalisation of short-base single stranded DNA chains called aptamers. Herein, their immobilisation on sensor surfaces is demonstrated in two ways; indirectly, using the intermediary bi-directional molecule 1-pyrenebutyric acid N-hydroxysuccinimide ester (PBASE) and directly, exploiting aptamers modified with pyrene groups able to stack directly on the graphene surface. This work provides an evaluation of these two immobilisation strategies for the detection of Pb^{2+}.

Alongside the development of these sensors, this contribution presents robust characterisation and testing strategies for the GFET devices in order to improve the confidence in the conclusions made about metrics describing their essential features. Open-source, customisable and innovative data analysis packages are also introduced in this work which facilitate the rapid, facile and detailed manipulation of large data sets arising from characterisation techniques. These tools dramatically decrease the time between data acquisition and analysis allowing new insights into how the GFETs are working to be uncovered.

Publications and Posters

Publications

- **SCRAMBLE: Sweep Comparison Research Application for Multiple Back-gated fieLd Effect measurements of graphene field effect transistors,** Benjamin O’Driscoll, SoftwareX, 2021. **15**:
  DOI: doi.org/10.1016/j.softx.2021.100757

- **Emerging graphene-based sensors for the detection of food adulterants and toxicants – A review,** Vikram Srinivasa Raghavan, Benjamin O'Driscoll, J.M. Bloor, Bing Li, Prateek Katare, Jagriti Sethi, Sai Siva Gorthi, David Jenkins, Food Chemistry, Volume 355, 2021, 129547
  DOI: 10.1016/j.foodchem.2021.129547.

- **Graphene FET Sensors for Alzheimer’s Disease Protein Biomarker Clusterin Detection,** Theodore Bungon, Carrie Haslam, Samar Damiati, Benjamin O’Driscoll, Toby Whitley, Paul Davey and Shakil Awan (2021) Front. Mol. Biosci. 8:651232.
  DOI: 10.3389/fmolb.2021.651232

Conference Proceedings

- **Aptamer functionalisation of back-gated field effect transistors for Pb^{2+} sensing,** Benjamin O’Driscoll, Vikram Srinivasa Raghavan, Theodore Bungon, Paul Davey, Toby Whitley, Shakil A. Awan and Sai Siva Gorthi. Proceedings of the 2nd International Electronic Conference on Biosensors, 14–18 February 2022, MDPI: Basel, Switzerland,
  DOI: 10.3390/IECB2022-12344

- **Graphene FET Sensors for Alzheimer’s Disease Protein Biomarker Clusterin Detection,** Theodore Bungon, Carrie Haslam, Samar Damiati, Benjamin O’Driscoll, Toby Whitley, Paul Davey and Shakil Awan, *Proceedings* **2020**, 60, 14.
  DOI: 10.3390/IECB2020-07229

Poster Presentations

- **Raman Spectroscopy of Graphene Biosensors**
  Benjamin O'Driscoll, Theodore Bungon, Paul Davey, Toby Whitley and Shakil Awan, Bath University C3Bio Conference - September 2019.
- **Raman Spectroscopy of Graphene Biosensors**
  Benjamin O'Driscoll, Theodore Bungon, Paul Davey, Toby Whitley and Shakil Awan, Plymouth University School of Engineering Computing and Mathematics Launch Event - December 2019.
- **Raman Spectroscopy of Graphene Biosensors**
  Benjamin O'Driscoll, Theodore Bungon, Paul Davey, Toby Whitley and Shakil Awan, Plymouth University Research Showcase - December 2019.

Table of Contents

List of Abbreviations

Ab – Antibodies

AFM – Atomic force microscopy

BLG – Bi-layer graphene

BSA - Bovine serum albumin

CNT – Carbon nanotube

CVD – Chemical vapour deposition

DC – Direct current

DIW – Deionised water

DNA – Deoxyribose nucleic acid

DUT – Device under test

ELISA – Enzyme linked immunosorbent assays

Fab – Antigen-binding fragments

FET – Field effect transistor

FTA – Fluorescently tagged antibodies

FWHM – Full width at half maximum

GFET – Graphene field effect transistor

hCG – Human chorionic gonadotropin

HOPG – Highly ordered pyrolytic graphite

Ig – Immunoglobulins

IPA – Isopropyl alcohol

LOD – Limit of detection

LOR – Lift of resist

MLG – Multi-layer graphene

PBASE/ PYR-NHS – 1-pyrenebutyric acid N-hydroxysuccinimide ester

PBS – Phosphate buffered saline

PMMA – Poly(methyl methacrylate)

POC – Point of care

PR – Photoresist

PTDA (PTBA) – Pyrene tagged DNA (TBA)

PVD – Physical vapour deposition

SDA – Semiconductor device analyser

SELEX – Systematic evolution of ligands by exponential enrichment

SLG – Single-layer graphene

SMU – Signal measurement units

SWCNT – Single walled carbon nanotubes

TBA – Thrombin binding aptamer

UV – Ultraviolet (light)

XPS – X-ray photoelectron spectroscopy

Chapter 1 – Introduction

Research groups the world over have been fascinated with graphene based research ever since its discovery in 2004 [1]. In particular it offers a plethora of advantageous electronic properties over silicon (Si) based devices for biosensing technologies including its ease for chemical functionalisation [2], sensitivity and biocompatibility [3]. Graphene is a two-dimensional allotrope of sp^2 hybridised carbon [4] and therefore offers a large surface area to volume ratio making it particularly sensitive to its surroundings, a characteristic that has engaged research groups keen to exploit this for sensing technologies [5]. One common application of this material as a biosensor is in graphene field effect transistors (GFETs) [4, 6]. GFETs are realized by connecting a conducting graphene channel between metal source and drain electrodes, achieved in either the top- [7] or back-gated [8] configuration. These biosensors replace the doped Si channel in traditional FETs with graphene which is subsequently functionalised with bioreceptors to target specific analytes.

Graphene is either deposited directly onto pre-patterned devices [3, 9] or plasma etched from a bulk graphene-insulator-substrate stack [4, 8]. For both configurations, a current is passed through the conducting graphene channel when a voltage drop is created across the source and drain electrodes. Sweeping the gate voltage modulates the charge carrier contributions in the graphene channel producing distinctive transfer curve characteristics [10]. Recombination events between the target analytes and the immobilised bioreceptors on the graphene surface can be transduced as measurable signals via changes in the graphene's electronic properties. Graphene's compatibility with existing planar complementary metal-oxide semiconductor (CMOS) manufacturing processes [10] combined with its ease of functionality [2] and high sensitivity will facilitate these low-cost and integrable devices as truly disruptive biosensing technologies in the future.

This contribution demonstrates the use of GFET devices for an environmental biosensing application. Techniques associated with the characterisation procedures are optimised alongside software technologies used to automate the data analysis. The functionalisation processes, essential to any specific biosensor, are then demonstrated. It is the ambition of this work to progress this technology one step further into being realised as real-word biosensors.

1.1 Motivation

The recent Coronavirus disease 2019 (COVID-19) outbreak has acted to raise awareness and boost demand for accurate, cost-effective and rapid biosensors as governments across the globe have scrambled to roll out effective testing systems in quantities never seen before. In a highly sensitive approach, Seo’s group were early to publish work demonstrating a proof-of-concept Field Effect Transistor (FET) based biosensor deploying graphene sheets for highly sensitive label-free diagnostic clinical testing of patients with the SARS-COV-2 virus [11]. In an alternative strategy, the group led by Papamatthaiou demonstrated a Lab-on-PCB nucleic acid amplification test (NAAT) which was capable of rapid (30 min) SARS-COV-2 identification with the added benefit of simplified detection using the sample-in-answer-out model [12]. Amongst the rush to produce vast quantities of COVID-19 testing, rapid lateral flow tests were selected as the diagnostic tool of choice to facilitate self-testing for the population by the UK government. This self-testing strategy aligns with a modern trend of “point-of-care” (POC) testing whereby measurements and results are acquired and realised at the site of care [13].

POC technologies can be extended out of the clinical setting to the environmental monitoring field whereby information gathered can be acted on rapidly at the information source. This paradigm shift moves away from previous techniques which are based on expensive, complex and difficult to use equipment located in centralised laboratories and favours technologies that are simple to use, inexpensive and can be deployed at distributed locations where they are needed the most [13]. The monitoring of environmental toxicants such as lead sets to benefit from a focussed shift to POC sensing.

The widespread existence of the heavy metal lead in the environment is a severe threat to the health of humans [14]. Lead is a neurotoxin that accumulates over time in the body restricting the cognitive, behavioural and psychological development of children [15]. Since water is one exposure route for chemical hazards like Pb^{2+} it is envisioned that monitoring drinking water sources using POC sensors which are low-cost, sensitive and field-suitable is one way that human exposure can be limited. GFET devices, customised with specific bioreceptors towards Pb^{2+} ions are one exciting candidate for this sensing scheme in the future and are demonstrated in this work as being sensitive with a highly scalable fabrication process. Another way that this work contributes amongst a modern research trend is with regards to the surface functionalisation of the devices. This work exploits single stranded DNA oligonucleotides to enhance the specificity of the GFET devices towards Pb^{2+} ions.

It was shown that only seven months after the roll out of the COVID-19 lateral flow tests were announced by the UK government, the US Food and Drug Agency (FDA) raised concerns about the Innova SARS-COV-2 antigen rapid qualitative test recommending their destruction or return to the manufacturers. This Class 1 recall, which represents the highest risk to serious injury and death, was advised after “significant concerns that the performance of the test has not been adequately established presenting a risk to health” [16]. This recall highlights the need for rigorous testing of any biosensing platform before roll out and forms a key part of this contribution. Concurrently with the development of the physical GFET device, the work in this thesis evidences robust testing strategies and device handling protocols so that measurement led conclusions are reliable.

Different approaches to biosensing all offer contrasting trade-offs between sensitivity, cost, accuracy and scalability to name a few. It is clear that the COVID pandemic has increased the awareness of the need for these technologies to help resolve some of the world’s biggest challenges relating to environmental and medical testing. It is therefore envisaged that research into the field of biosensors will flourish for many years to come.

1.2 Objectives

The primary objectives of this work are written below:

- Fabricate scalable GFET devices suitable for biosensing strategies.
- Develop rigorous standard operating procedures (SOPs) for the reliable and accurate characterisation of the GFET devices.
- Develop a suite of software which automates the data analysis of the raw files captured throughout the characterisation processes.
- Develop effective strategies for the functionalisation of bioreceptors onto the graphene channel alongside characterisation methods to confirm immobilisation.
- Apply the above techniques to demonstrate the sensitive detection of Pb^{2+} ions.

The development of all of these objectives will pave the way for this technology to take the complicated step out of the laboratory and realise its potential in the real world as part of future POC devices. Such devices will be appropriate for the distributed sensing of water infrastructure to monitor Pb^{2+} levels in order that human exposure to this metal can be reduced.

1.3 Outline

The contribution presented in this thesis is truly interdisciplinary, spanning multiple subjects across science and technology. This is one of the reasons that this is such an active and exciting field of research. Engineering principles related to high vacuum systems are involved in the fabrication of the devices. Knowledge of physics is used to describe the conductive and material properties of graphene. Surface chemistry is exploited alongside biological conjugation methods to improve the immobilisation schemes between graphene and attaching molecules. Techniques related to data science are developed to enhance the understanding of the information captured through the variety of characterisation methods. Biotechnologists are highly skilled in these areas and are therefore able to apply a range of concepts and knowledge to different scenarios.

Chapters in this thesis can be can be divided into four main parts. The first part consisting of chapters 1-5 form a comprehensive review of the current landscape for GFET biosensing platforms. Secondly, chapter 6 describes the equipment and techniques necessary to investigate, improve and optimise these platforms. Chapter 7, which is split into 8 sections, describes the contribution of this work to the field. Finally, chapter 8 provides a summary and conclusive remarks. A description of the chapters used to structure the work presented in this thesis is given below:

- ***Chapter 1:*** Introduction of the work completed along with a description of the objectives and thesis structure.
- ***Chapter 2:*** Description of the structure and resulting properties of graphene. This chapter then explores the various methods of growing and then transferring this material.
- ***Chapter 3:*** A review of the broad biosensing landscape is given in this chapter. The key figures of merit used to compare these devices are described. Various bioreceptors which are used to functionalise sensor surfaces are explored before some transduction methods are introduced.
- ***Chapter 4:*** The topic of FETs is reviewed here. Biosensors which deploy these structures as their sensing mechanism are then presented. The operating principles of GFETs are then introduced which is followed by a detailed description into graphene functionalisation methods.
- ***Chapter 5:*** This chapter reviews the Pb^{2+} sensing landscape. It describes the toxicity of the material before looking into the requirement for testing. Gold standard

technologies are introduced initially before the focus shifts towards developmental techniques which aim to disrupt this sector.

- ***Chapter 6:*** A description of the techniques and equipment used throughout this contribution is detailed here. Details related to the fabrication process for the GFET devices is given. Material and electrical characterisation methods for graphene and GFETs are described along with methods of preparing reagents.
- ***Chapter 7:*** This chapter presents the results obtained throughout this contribution.
    - *Section 7.1:* A description of the SCRAMBLE data analysis software developed to process electrical characterisation data
    - *Section 7.2:* A description of the RAMAN_VIEWER data analysis software developed to process Raman characterisation data
    - *Section 7.3:* This describes the derivation of the optimum parameters used during the electrical and Raman characterisation to ensure accurate and reliable results throughout this contribution.
    - *Section 7.4:* Typical GFET fabrication results are presented in this section showing the impact the process has on graphene. The effect of an alternative fabrication process is also presented.
    - *Section 7.5:* A study into the effect of atmospheric adsorbents on GFETs is provided in this section.
    - *Section 7.6:* This describes the development of a reliable technique to conjugate 1-pyrenebutyric acid N-hydroxysuccinimide ester (PBASE) molecules onto the graphene surface.
    - *Section 7.7:* Two techniques are demonstrated to immobilise DNA aptamers onto the graphene channel.
    - *Section 7.8:* Aptamer functionalised GFET devices are used for the sensitive detection of Pb^{2+} ions.
- ***Chapter 8:*** Summarises and concludes the work detailed in the proceeding chapters. Then, new avenues for further investigation are proposed.

Chapter 2 – Graphene

2.1 Carbon

2.1.1 Carbon Structure

Carbon (C) has six electrons in total and fills up its orbitals following the aufbau principle by placing the electrons into low energy orbitals first before filling up higher energy orbitals. The first and second orbitals, known as 1s and 2s respectively, are spherical in electron distribution and are at increasing energy levels. The next three states that are available for the electrons in carbon are the $2p_x$, $2p_y$ and $2p_z$ (dependent on axis) orbitals, dumbbell in electron distribution shape, they are degenerate and so they all have equal energy. Following Pauli's exclusion principle, each orbital can hold only two electrons of opposite spin. When electrons fill degenerate orbitals, they follow Hund's rule which means they fill up separate orbitals first before pairing off within an orbital with an electron of opposite spin. Consequently, an isolated carbon atom has an electronic structure of $1s^2 2s^2 2p_x^1 2p_y^1$. The shell number is signified by the number preceding the letter. Note that the $2p_z$ orbital is empty [17].

2.1.2 Carbon Hybridisation

When carbon atoms form molecules, the orbitals of the second shell can mix in three different ways; sp^3, sp^2 and sp hybridisation refer to the mixing of the 2s orbital with three, two or one of the 2p orbitals respectively. During hybridisation the total number of hybrid states is equal to the number of original orbitals that combined together. Each hybrid state is degenerate but different in energy level to the original orbitals, having a higher (lower) energy level than the constituent 2s (2p) orbitals. The electron distribution of these hybrid states looks like a dumbbell with one minor and major lobe, reflecting the larger contribution of the 2p orbitals over the 2s orbital during hybridisation. Hybridised orbitals occupy distributions that are farthest away from one another. This deformed electron distribution explains why hybridisation occurs, as the larger orbitals allow for better overlap between atoms [17].

Graphene is formed from carbon that is sp^2 hybridised, which has three hybrid sp^2 orbitals and an original $2p_z$ orbital that are all half-filled with one electron (Figure 2.1A). Contrary to what is written above, it is energetically favourable for the sixth electron to fill the $2p_z$

orbital rather than continue to fill up the orbitals of equal energy, because the difference in energy level between the sp^2 hybrid and $2p_z$ orbitals is small. The $2p_z$ orbital energy level remains unchanged during hybridisation and therefore sits at a higher level to the three hybrid sp^2 states. As with all hybridisation states the orbitals naturally occupy spaces that are farthest away from one another. As the $2p_z$ orbital is unchanged it sits above and below the x-y plane which leaves the three sp^2 orbitals to position themselves in the x-y plane located at 120 º from each other as depicted in Figure 2.1B [17].

Figure 2.1 has been removed due to Copyright restrictions

Figure 2.1. A) Energy levels of carbon before and after sp^2 hybridisation [17] B) Geometry of electron distribution for sp^2 hybridisation (adapted) [17]

During sp^2 hybridisation a half-filled sp^2 orbital from one carbon atom bonds with another half-filled sp^2 orbital from another carbon atom to form strong covalent bonds called sigma (σ) bonds. These bonds are strong and are formed due to the overlapping orbitals. These σ bonds explain the trigonal shaped nature of carbon atoms in graphene.

It is the interactions between the half-filled $2p_z$ orbitals perpendicular to the x-y plane that give rise graphene’s planar nature. The $2p_z$ orbitals from adjacent carbon atoms overlap side-on to produce pi (π) bonds which restrict the rotation of the lattice to a more energetically favourable orientation. The adjacent $2p_z$ orbitals overlap, bind covalently and merge to form a ring-like lobe of electron distribution. The weakly bound π electrons are said to be delocalised in this region and therefore no longer restricted locally between two carbon atoms, it is these electrons that contribute to the conductivity within graphene [17-19].

2.2 Graphene

2.2.1 Structure of Graphene

Carbon is arranged into a hexagonal lattice in graphene, with a distance of approximately 1.42 Å (a in equation 2-1 below) separating the lattice points. The unit cell for graphene is comprised of two nearest neighbour carbon atoms as the basis that are attached to every lattice point [18, 20, 21]. The sub-lattices are show in Figure 2.2A and B. The primitive unit cell can be visualised as a parallelogram that when repeated through the lattice vectors in two-dimensional space makes up the entire hexagonal structure. This can also be visualised by considering two interpenetrating triangular lattices created by the basis atoms as in Figure 2.2B [21]. Elementary trigonometry deduces the lattice vectors as:

$$\boldsymbol{a_1} = \frac{a}{2}(3, \sqrt{3}), \ \ \boldsymbol{a_2} = \frac{a}{2}(3, -\sqrt{3}) \qquad 2\text{-}1$$

By considering reciprocal space, the Brillouin zone, which represents the smallest cell closest to a reciprocal lattice point, can be constructed and is given in Figure 2.2C. The lattice vectors in reciprocal space are given in equation 2-2 and shown in Figure 2.2C.

$$\boldsymbol{b_1} = \frac{2\pi}{3\mathrm{a}}(1, \sqrt{3}), \qquad \boldsymbol{b_2} = \frac{2\pi}{3\mathrm{a}}(1, -\sqrt{3}) \qquad 2\text{-}2$$

The Dirac points are located at the corners of graphene's Brillouin zone and are also known as the K and K' points, which are shown in Figure 2.2C. Most of graphene's novel properties occur due to charge carriers in the vicinity of these sites [21, 22].

Figure 2.2 has been removed due to Copyright restrictions

Figure 2.2. A) Graphene lattice structure in real space with unit cell visualised as a parallelogram [18], B) Visualisation of real-space lattice vectors [21], C) Construction of Brillouin zone in reciprocal space from reciprocal space lattice vectors [21].

Graphene is a 2D crystal allotrope of carbon formed of sp^2 hybridised atoms in a hexagonally shaped lattice. It is the basic building block of other carbon allotropes (Figure

2.3); 0D fullerenes are formed by wrapping graphene into a spherical shape, with a minimum of 60 carbon atoms and the introduction of pentagons into the lattice, 1D nanotubes are cylinders of rolled graphene and 3D graphite can be visualised as stacked graphene layers bound together by weak van der Waals forces [21]. Graphene was first discovered by Geim and Novoselov in 2004, by comparing the contrast in optical microscope images when it was located on top of a SiO_2 substrate after the micromechanical cleaving of individual layers from a graphite block [1].

Figure 2.3 has been removed due to Copyright restrictions

Figure 2.3. Graphene-2D (top left) as a building block for graphite-3D (top right), nanotubes-2D (bottom left) and fullerenes-0D (bottom right) [21]

2.2.2 Properties of Graphene

The structure of graphene gives rise to several appealing properties. Firstly, the electron mobility of up to 250,000 $cm^2 V^{-1}s^{-1}$ is the highest of any known material and even approaches the theoretical limit [2]. The 2D nature of graphene allows the ballistic π-electrons to travel sub-micrometre distances without scattering contributing to this property [23].

A direct result of the valence and conduction bands of graphene touching at the q=0 momentum point is that graphene is a zero band-gap semiconductor [22]. As these energy levels touch, the Fermi level will always exists within either of these bands which allows graphene to always exhibit a conducting metallic nature with either holes or electrons as majority charge carriers. A result of this, is that conduction within graphene based transistor structures is in the “ALWAYS ON” state. In comparison, traditional semiconducting materials such as doped Si have an electronic structure where the conduction and valence bands are separated by a finite energy, with an external potential difference necessary to overcome this band-gap and move the Fermi level into the conduction band allowing conduction [22]. A feature of being a gapless semiconductor is that the transport regime via the charge carriers can be tuned on application of an electric field making graphene an ambipolar conductor [24].

The mechanical strength (Young’s modulus of 1 TPA), low sheet resistance (as low as 30 $\Omega\square^{-1}$) and high light transmittance (97.7% per layer) properties that graphene offer are essential characteristics for future wearable and flexible electronics. Graphene has also shown a fracture strain limit ten times greater than indium tin oxide (ITO) which is the favoured material used for conductive coatings. Although ITO currently shows favourable electrical and optical properties for these applications, graphene’s higher fracture limit shows that it would be capable of folding in future devices [2].

From a biosensing point of view, graphene has lots of properties that explain the recent interest in incorporating it into sensing architectures. As graphene is a two-dimensional material, it has a near infinite surface area to volume ratio and its specific surface area of 2630 m^2/g ranks it with the highest of materials making it’s conductance very sensitive to its environment [25]. The material has also shown that it can be easily chemically functionalised allowing specific biosensors to be designed that are capable of detecting target analytes within complex mixtures [2].

2.2.3 Graphene’s Surface Roughness

In reality the graphene lattice is not a perfect 2D crystal as both theory and experimental results have predicted and observed that this is not thermodynamically possible [23]. Such experiments stress the importance of a supporting substrate with similar lattice parameters which offer a third dimension, to prevent the 2D lattice from segregating into islands. Suspended graphene sheets were investigated by Meyer et al to further determine the intrinsic structure of graphene [23]. Using suspended graphene differentiated this investigation as previous studies had only considered probing the material’s structure when it was part of a larger 3D bulk substrate assembly such as graphene on SiO_2. Meyer showed that graphene sheets have a more corrugated topology with normal deformations reaching up to 1 nm, which could help to explain why this 2D allotrope of carbon is thermodynamically stable. Scrolling at the edges of the prepared sheets was observed for monolayer (bilayer) graphene by single (double) dark lines in transmission electron microscopy (TEM) images where the incident electron beam was parallel to the local folding. Next, this group analysed the effect of tilting the electron beam on the homogeneous graphene patches on their electron diffraction patterns. Crystal lattices with three dimensions exhibit dimming of the Bragg peaks when the incident angle of the electron beam changes. The diffraction pattern for monolayer graphene on the other hand consists only of the Laue zone. The group observed no significant dimming of the dominant Bragg reflections with tilt angle which has become a useful technique for graphene identification in TEM studies. However, the group observed not only the broadening of Bragg peaks when the tilt angle was increased, but a positive correlation between the amount of broadening and the distance of the Bragg peak from the tilt angle. These observations combined to suggest that the suspended graphene has random deformations across all axes. This effect is explained by imagining that a perfect 2D lattice of graphene would form a perfectly periodic diffraction pattern. Any topological variations in the graphene sheet would cause a superposition of Bragg peaks from smaller 2D lattices positioned at different normal angles relative to the perfectly flat 2D crystal, hence combining the Bragg peaks in a way that maintains the same intensity but varies the width of the peaks. It was noticed that this effect was weaker in bilayer and multilayer graphene structures. It was determined that analysing the broadening of these Bragg peaks is an effective technique for estimating the surface roughness of a graphene sample [23].

2.3 Graphene Growth

One of the primary challenges facing the widespread uptake of graphene as a disruptive technology has been the limitations associated with mass growth of the material to possess the same attractive properties as the highest quality achieved in small scale laboratory settings [2]. Three of the most popular ways single layer graphene can be synthesised are by epitaxial growth on silicon carbide (SiC), mechanical exfoliation and chemical vapour deposition (CVD) each offering their own advantages and disadvantages.

2.3.1 Epitaxial Growth on SiC

Growing single graphene layers by epitaxy starts with heating SiC to temperatures exceeding 1200 ºC under ultra-high vacuum conditions. During this process silicon (Si) atoms are sublimated away from the SiC surface leaving C atoms to reconstruct into graphene sheets, this is only possible due to the small mismatch in lattice parameters between SiC and the graphene honeycomb structure [26]. The characteristics of the graphene grown in this way depend on the SiC surface (Si or C), the temperature and the vacuum conditions. If growth is conducted on the C terminating face, multi-layer graphene (MLG) is most commonly formed with decreasing electron doping levels through the graphene layers, this results in charge mobility and carrier densities of 10^4-10^5 cm^{2}V^{-1}s^{-1} and 10^{13} cm^{-2} respectively [26]. If growth is conducted on the Si terminating face, the yield for number of layers is lower but the charge mobility is reduced to 10^2-10^3 cm^{2}V^{-1}s^{-1} with similar charge carrier densities as mentioned above [26]. One of the advantages of this technique is that growing graphene directly onto the insulating SiC surface removes the need to subsequently transfer the graphene onto another substrate [26]. However, the high cost of the substrate material SiC along with conducting such processes in high temperatures and vacuum conditions, coupled with the small yield in atomically flat graphene, as terraced growth is favoured on the SiC surface, currently limits this technique into niche low output experiments [26].

2.3.2 Chemical Vapour Deposition

The method of CVD relies on decomposing small chain hydrocarbon gases such as methane and ethylene onto transition metal surfaces such as Nickel (Ni) and Copper (Cu) and is illustrated in Figure 2.4. This process begins by heating the catalytic transition metal substrate to between 800-1000 ºC under vacuum conditions. Next, hydrocarbon gases are added to the chamber where they absorb and then decompose onto the surface resulting in carbon atoms that reconstruct into graphene. The exact processes for this growth are debated in literature although recently it has been shown that CVD growth relies heavily on the carbon solubility of the substrate material [26]. For example, the growth process for metal substrates like Ni with a high carbon solubility, begins when carbon is absorbed within the substrate forming a solid solution of carbon. Once cooled, the carbon solubility of the substrate decreases and therefore the carbon atoms separate from the solid solution, diffuse through the substrate and deposit on the catalytic surface forming graphene crystals. The growth process is different for metal substrates like Cu which have a low carbon solubility. For Cu, the absorption stage is seldom observed which means that the growth of graphene occurs directly on the catalytic surface. The characteristics of the graphene grown in this way depend on the initial heating time and temperature, the precursor gas concentration and flow rate, the metal substrate and the cooling rate. More layers of graphene can be grown using metals with a higher carbon solubility due to the increased rate of carbon separation and deposition on the substrate. Whereas, cooling the mixture quickly has the effect of producing more instances of single layer graphene (SLG) and few layer graphene (FLG). In order to completely cover the metal substrate with graphene it is necessary to use metals with a low carbon solubility and increase the time of the initial heating stage. It is important to note that the CVD process is believed to be self-limiting, i.e. graphene growth will eventually stop when surface of the metal has been covered. This is because once the graphene layer(s) have been deposited, the carbon atoms can no longer rely on the catalytic effect of exposed metal atoms to form more graphene crystals [26].

Figure 2.4 has been removed due to Copyright restrictions

Figure 2.4 Schematic of CVD growth mechanism on different carbon soluble materials. A) Multi-layer growth on Ni substrate. B) Single-layer growth on Cu substrate [27]

This technique has been effective at producing large areas of SLG which is suitable for larger-scale applications and manufacturing processes. Graphene films of predominantly SLG were successfully manufactured onto 30-inch films by Bae's group [28]. CVD growth on Cu has shown to give surface coverage of 95%, a charge carrier mobility of 10^4 $cm^2V^{-1}s^{-1}$ and ~2 mm crystallinity. The requirement to transfer the graphene layer off the metal substrate is one major drawback of this growth process. In addition, terraced growth is also observed for CVD on Cu, where the graphene grown matches the surface morphology of the non-flat Cu substrate. Once the graphene is transferred onto an insulating substrate terraces and wrinkles are located in complimentary locations to the growing sites and boundaries of the substrate metal [26].

2.3.3 Mechanical Exfoliation

The techniques of mechanical exfoliation rely on being able to peel off graphene layers from a graphite substrate [29]. This layer by layer peeling can be achieved by applying forces in one of two directions, normal and lateral to the graphite substrate surface, with the purpose of breaking the weak van der Waals forces which couple graphene layers together [29, 30]. The “Scotch tape method”, which was used to isolate single layer graphene sheets for the first time in Novoselov and Geim’s breakthrough paper in 2004, relies on the mechanical cleavage of Highly Ordered Pyrolytic Graphite (HOPG) [1, 29]. This cleaving process relies on the process of applying Scotch tape to the surface of HOPG and then peeling off the tape, exerting a normal force, consequently separating layers off the main bulk material. This results in thin amounts of graphite on the adhesive side of the tape. By repetitively applying and removing the tape to this graphite patch, patches of SLG will eventually form. Although this method is currently difficult to scale up, it can be used to produce large areas of high quality SLG patches, suitable for small-scale niche laboratory experiments.

Larger-scale production of single-layer graphene can be achieved by using sonication assisted liquid phase exfoliation (LPE) of graphite which is depicted in Figure 2.5. This process relies on the cavitation of the dispersion medium, which is the process of vapour bubbles forming due to pressure variations in the medium caused by incident high energy ultrasonic sound waves. When these bubbles collapse in close proximity to the graphite, shock waves are formed which introduce compressive stress through the material. At the graphite boundary with the medium, these stress waves are reflected back as tensile stress. The repetitive action of being stressed in these directions acts to exert normal forces on the graphene layers consequently cleaving them into smaller single-layer fragments [29]. Another consequence of sonicating the graphite is that the shockwaves exert a force directly between the graphene layers analogous with a wedge being driven between the layers. Also, a shear force is applied during sonication when the unbalanced movement of the stacked layers caused by the compressive and tensile waves result in lateral movements of the graphene sheets. The temperature, sonication time, graphite concentration, level of surfactants, polymers and solvents are just some of the parameters that are optimised to produce graphene in this way. The efficiency of sonication is limited by the static cavitation field that a fixed ultrasonic source provides. This results in areas of high and low cavitation whereby material that is cleaved off once and moves to a different part of the vessel may not have repetitive exposure to a large field [29].

Figure 2.5 has been removed due to Copyright restrictions

Figure 2.5 Schematic visualisation of forces acting on graphitic stack during LPE process [29]

The primary advantage of this technique is its ease to implement. The high level of defects in the resulting graphene caused by the harsh effects of sonication is one of the main drawbacks of using this method, contrary to belief that this technique produces defect and disorder free graphene layers [29]. The high local temperatures (~several thousand K), pressures (~several thousand atm) and temperature changes (~several billion Ks^{-1}) caused by cavitation actually damages the graphene and has been shown to introduce oxygen and oxygen functionalised groups into the basal plane of the graphene lattice [29].

2.3.4 Alternative Growth Mechanisms

Graphene inks, which are based on graphene flakes but include additional reagents such as dispersants and solvents, which function to maintain the ink in the liquid phase, have been used in inkjet printers for large-scale production of graphene based electronics and are manufactured in much the same way as the process for graphene flakes [31, 32]. Torrisi et al started with graphite flakes which were ultrasonicated, centrifuged and filtered to remove the flakes > 1 μm which could clog the printing nozzle. Next, this ink was characterised to confirm that it consisted of a mixture of SLG, bi-layer graphene (BLG) and FLG before being used to print thin film transistors based on treated and pristine Si/SiO_2 substrates. The group reported mobility values of up to 95 $cm^2V^{-1}s^{-1}$ for their transistors, demonstrating their suitability for transparent electronics [31].

A significant study into graphene flake production via LPE was conducted by Kauling et al and highlighted large statistical differences in the graphene content of labelled graphene flakes provided by industry [33]. By analysing the graphene content from 60 companies across the globe, Kauling showed that most companies are actually producing fine graphite stacks over graphene flakes, with none of the providers supplying graphene with more than 60% sp^2 bonds, indicating high levels of contamination for all samples. They recommend more rigorous standards are introduced in order that suppliers improve their products and developers have a deeper understanding of what they are purchasing. This forms an attempt to improve the current situation, which they correlate with the limited development in graphene based technologies using this source [33].

2.3.5 Graphene Transfer

One of the main drawbacks of the popular CVD method for graphene synthesis is the requirement to transfer the graphene sheet from the metal catalytic surface (Cu or Ni) onto the target substrate such as a Si/SiO_2 stack. During this transfer process it is essential that no damage is done to the material to ensure that the intrinsic properties of graphene are maintained for the desired device [34]. One method of achieving graphene transfer relies on the use of an additional polymer based supportive layer. Currently poly(methyl methacrylate) (PMMA) is a commonly used medium for this particular technique [8, 34, 35].

By spin coating a uniform layer of PMMA onto the graphene/metal surface and then chemically etching the metal substrate away, the remaining PMMA/graphene stack can then be scooped onto a substrate. Next the PMMA is removed by annealing or dissolution in acetone before the graphene/substrate stack is shaped further [34].

The regular transfer method detailed above has been shown to produce large areas of PMMA residue on the graphene surface which can cause additional p-doping and charge scattering changing graphene’s intrinsic structure and altering charge carrier mobility in GFETs [34, 36]. Even after 2 h in acetone and followed by an additional annealing step, Barin et al showed that PMMA residue is still present on the graphene surface [34]. Only after two separate layers of PMMA (with decreasing concentrations) were added, could large scale areas free of PMMA residue and cracking be observed [34]. Li’s group showed a reduction in cracking on the graphene layer by also introducing a secondary PMMA layer during their transfer process. This secondary layer acted to dissolve the pre-cured primary

PMMA layer which allowed the graphene layer to become more flexible subsequently relaxing, forming better contact with the underlying substrate [35].

Suk's group transferred graphene from Cu foils onto a SiO_2 substrate using three concentrations (10, 40 and 80 mg/mL of chlorobenzene) of PMMA films as the sacrificial transfer layer, which produced roughly 80 nm, 200 nm and 700 nm thick films respectively after spin coating. For back-gated sweep measurements in vacuum and in air, the GFETs fabricated using a lower concentration of PMMA showed less p-doping (a Dirac voltage closer to 0 V) and higher conductivity values. They suggested that the higher overlapping of polymer chains in more concentrated PMMA solutions corresponds to stronger interactions between them which causes them to resist conventional solvents, hence leaving more residue on the graphene surface [36].

One other way to reduce the PMMA residue on graphene substrates is to apply deep UV (DUV) treatment prior to PMMA etching, where the PMMA/graphene/substrate structure is exposed to UV light at 254 nm for 20 min whilst being baked on a hotplate for 180 ºC. Suhail et al show that this treatment technique not only reduces the occurrence of PMMA residue but also the amount of defects in the lattice [8]. In this study, the sheet resistance for graphene treated with DUV was shown to be 450 ±50 Ω/□ which is in agreement with the values obtained previously for graphene transferred via the "Scotch Tape" method. DUV has shown to be effective at increasing the conductance of graphene and is particularly attractive to fabrication environments due to its rapid, simple and low cost nature [8].

2.4 Summary

This chapter provides an introduction into graphene focussing on its structure, properties and growth mechanisms. Initially, the electronic configuration of carbon atoms is described. When carbon molecules are formed, the hybridisation process between orbital states give rise to sp^2 hybridised carbon atoms. Strong covalent bonding occurs between them which produces the trigonal shape commonly associated with carbon atoms in a graphene lattice. Π-bonds are also formed between overlapping orbitals perpendicular to the basal plane, producing delocalised electrons which contribute to the conductivity of the material.

The hexagonal graphene lattice, produced from periodic translations of the parallelogram shaped unit cell is then introduced. Positions known as the K and K' points, which exist at the edges of graphene's Brillouin zone, are areas where unique phonon/electron interactions give rise to the material's exciting properties. Graphene's high mobility values are attributed to ballistic π-electrons which are facilitated by its planar 2D structure. Its 2D nature is exploited in this body of work for biosensing purposes since its extraordinary surface area to volume ratio make its conductive properties highly sensitive to its surroundings. The planar structure of the lattice also make it easy to functionalise with a wide range of bioreceptors designed to target specific analytes.

Epitaxial growth on SiC and Mechanical Exfoliation via the "Scotch-tape method" tend to produce high quality graphene which exhibits the greatest mobility values but in very small batches suitable only for very niche experiments. LPE on the other hand tends to produce large quantities of highly damaged graphene. The CVD process is one of the most popular candidates for graphene production since it balances cost-effectiveness with quality and production size. One of the drawbacks for this particular technique though is the requirement to transfer the graphene off of the metal catalyst used to support the growth; this process causes dopants to be introduced into the graphene, consequences of which are observed throughout this contribution.

The CVD process has been successfully commercialised by several international suppliers. This has produced a reliable, cost-effective source for "off-the-shelf" monolayer graphene. Since the expertise and equipment associated with growing graphene directly has not been available during this work, CVD graphene has been purchased from one supplier in order to de-risk the quality and repeatability of the base material. The supplier conducts rigorous testing to ensure repeatable quality prior to shipping. Relying on such a source has allowed this project to focus its contribution towards the application of the graphene into biosensing devices rather than the optimisation of its manufacturing procedure.

Chapter 3 - Biosensing

3.1 Definition and Overview

3.1.1 Introduction

A biosensor is a device which converts the detection of biological/chemical analytes into quantifiable signals. They are used across a variety of different fields including food adulteration testing to detect the fructose sweetening agent [37], sunset yellow and tatrazine artificial additives [38] and E. *coli* bacteria [39]. Biosensors have shown to be effective at environmental monitoring, detecting pesticides used in agriculture [40, 41], toxic mercury ions [42] and anthrax inducing B. *anthracis* [43]. Great developments have been made in the medical diagnostics sector, where biosensors have been deployed for the monitoring of heart failure [44] and cancer risk biomarkers [4]. With regard to the diagnostic sector the opportunity for highly sensitive biosensors able to detect ultra-low concentrations of disease biomarkers, present at the early stages of illnesses, allowing for earlier life-saving interventions, is one of the many reasons why this research area is so active at the moment [45].

3.1.2 Architecture

A simple biosensor has two primary responsibilities; to interact with biological material and transduce this interaction as a measurable signal as summarised in Figure 3.1. The structure of a biosensor can be broken down into two main components. Bioreceptors immobilised onto the surface of the sensing element are selected to complement the biological analyte of interest. The transducer element of a biosensor converts the biological interaction between the receptors and the analyte into a measurable signal. More advanced biosensors consist of electronics to aid signal amplification, conditioning and conversion from analogue to digital signals [46].

3.1.3 Challenges

Although currently a growing field with exciting applications, along with the lateral flow pregnancy test the electrochemical based glucose biosensor is the only other platform for medical diagnostics to experience a global commercial success. Currently there are several limitations preventing the mass uptake of biosensing technology.

Figure 3.1 has been removed due to Copyright restrictions

Figure 3.1. Simplified biosensor architecture [47]

It has proved difficult to transfer these biosensors from the academic world into industry due to their commercial viability. One key hurdle in doing this is the rigorous regulatory framework associated with the development of technologies for the clinical setting. Also, biosensor technology is truly an interdisciplinary field which requires a translational approach whereby researchers of broad backgrounds in biology, engineering, physics and chemistry must work across boundaries to resolve challenges. In addition the cost, ease of use and stability of results over extended periods of time are further risks that industry has been reluctant to face [46].

However, with the continued investment over the past decade and improvements in the way scientists have interacted across disciplines, the challenges mentioned above are being overcome. The field of Nanotechnology has shown to offer several exciting opportunities to progress biosensors forward. By reducing the size of biosensors to the micro- or nano- scale, lower sample volumes are required reducing processing steps and therefore cost. In addition, miniaturisation offers an improvement in the signal to noise ratio as the surface area to volume ratio of the sensing element becomes much larger at these scales. With ever increasing miniaturisation, a similar size sensing element to a target analyte reduces the non-selective detections and allows for the ultimate goal for highly sensitive biosensors of single molecular recognition [46].

3.2 Characteristics of Biosensors

There are several attributes that are optimised during biosensor design which ultimately balance the requirements of detection with the cost of production. A major consideration during the design stage is to decide whether the platform will act as a single-use disposable sensor (to reduce the chance of cross-contamination) or whether continued long-term monitoring of analytes is required necessitating more stable devices [48, 49]. The inexpensive cost and opportunity for mass manufacturing of screen printed electrodes has a proven popular for disposable biosensing applications [48].

3.2.1 Figures of Merit

In order to simplify comparisons between different biosensors in the literature a few key figures of merit (FOMs) provide useful descriptors of sensors’ characteristics. With infinite combinations of fabrication procedures, geometries, materials and transducer methods, these merits aim to benchmark discussions across the literature.

3.2.1.1 Specificity

The specificity of a biosensor relates its effectiveness at producing a signal to its targeted analyte along with minimising signals of interactions with any other untargeted substance [50]. To facilitate specific measurements, devices are functionalised with selective bioreceptors that bind only to the target analyte. Considering the interaction between antigens (in solution) and antibodies (immobilised on the sensor surface) is one way to visualise specificity.The sensor should only register a detection event when the antigen of a complimentary shape combines with the selected antibody at its active site. The target analyte is usually within a solution that could contain other analytes and therefore it is essential that the bioreceptors deployed also supress these substances from non-specific interactions. Blocking the sensor surface where bioreceptors are not present is another way to prevent non-specific binding, these methods aim to supress false positive detections [48].

3.2.1.2 Stability

Stability describes how resilient the biosensors are to the environment surrounding it. Biosensors should produce repeatable measurements independent of their environment however local disturbances in temperature, contaminants and humidity for example can cause finite drift in their measurement output. Bioreceptors are often sensitive to several environmental factors and degrade over time without appropriate storage and handling strategies. Supporting electronics can be used as a way of supressing the drift in measurement signal [46].

3.2.1.3 Sensitivity

The sensor's ability to convert biorecognition events into transduced signals is a measure of its sensitivity and is influenced by several factors including the surface coverage, affinity with the target analyte and the orientation of the bioreceptors on the sensor surface to name a few. The Limit of Detection (LOD) is the smallest amount of a target analyte that is detectable by a device [45].

3.2.1.4 Linearity

The trait of a biosensor to have a one to one ratio between the concentration of analyte and the output signal is defined as the linearity. This trait is essential in determining the presence of unknown concentrations of analytes against calibrated results. It relates to the resolution of the biosensor which is the smallest change in the concentration of the target analyte that is detectable [46].

3.2.1.5 Labelling

The label-free approach to biosensors involves the direct interaction between the target analyte and the transducer producing a signal. This method is favourable in sensing applications due to the reduction in expense and time associated with using tags and fluorophores [51, 52]. Labelling the target analyte with additional molecules in order to increase the binding efficiency of the interaction is one way to improve the signal performance at the cost of additional processing steps [51].

3.2.2 Bioreceptors

One of the key characteristics of any biosensor is the surface of the sensing element. It is designed so that bioreceptors can be immobilised to the surface allowing specific binding events with target analytes to be measured. It is the biorecognition events between the bioreceptor and the target analytes that induce measureable signals from the device.

3.2.2.1 Antibodies

The term immunogen is used to describe a microorganism, protein, glycoprotein or lipoprotein that stimulates a specific immune response whereby immunity is developed. This term is incorrectly used in the literature interchangeably with the term antigen, which describes any substance that is capable of binding specifically to an antibody or T-cell receptor [53, 54].

Figure 3.2 has been removed due to Copyright restrictions

Figure 3.2. A) Diagram of IgG showing three main regions [55]. B) Schematic structure of IgG polypeptide chains [53].

Biosensors which use antibodies, antibody fragments or antigens as immobilised biorecognition elements are called immunosensors [48]. Specifically shaped glycoproteins called antibodies (Ab), produced by living organisms during a specific immune response are found in blood plasma and are known collectively as Immunoglobulins (Igs). Antibodies are formed of four polypeptide chains, two identical light (25 kDa) and two identical heavy (50 kDa), joined together by disulphide bonds [55] (Figure 3.2). These chains make up three distinct regions and shape the antibody into a Y. The two units at the top of the antibody are known as the fragment antigen binding portions (or Fabs) and are responsible for recognising and binding to antigens. These binding sites are complimentary in shape to the antigen determinant (or epitope) which describes the specific portion of the immunogen which causes the formation of antibodies. Each antibody is therefore capable of binding to two antigens simultaneously. At the other end of the antibody, the carboxyl terminated heavy chains are known as the fragment crystallisable portion (or Fc) and are required to interact with phagocytes and large granular lymphocytes, both responsible for the removal of foreign bodies [53, 55]. Antibodies are specific to one epitope only but are categorised into one of the five major Ig isotypes IgG, IgM, IgA, IgE and IgD depending on their structure, usually on the amino acid sequence of their heavy chains. The IgG class of immunoglobulins is the most abundant and is often used as an example to describe the generic antibody structure [53].

Using antibodies is therefore one way of increasing the specificity of the biosensor as only the target analytes complimentary to their shape will interact with them and produce a detectable response. The response of immunosensors depends on the immobilisation techniques used as this will impact their orientation, density and surface interaction.

It is possible to cleave antibodies into their individual sub units using proteases, which are proteolytic enzymes that break down polypeptide chains into smaller fragments. Using the specific protease, papain, one can separate antibodies into two identical Fab fragments along with the Fc fragment. As an alternative to papain, pepsin is another protease that can dissect antibodies, yielding one F(ab')$_2$ fragment (which contains two antigen-binding sites joined together with additional amino acids) along with the Fc component fragmented into many smaller parts [55]. The action of using papain and pepsin on a typical IgG Ab is provided in Figure 3.3.

Figure 3.3 has been removed due to Copyright restrictions

Figure 3.3. Schematic showing the dissection of antibodies fragments using A) Papain and B) Pepsin [55].

For the same specificity as antibodies, the advantage of using Fabs over conventional antibodies is their smaller dimensions [48]. A full size antibody has a height of approximately 10-15 nm compared to that of a Fab of approximately 2-3 nm [52]. When the electrical double layer is produced during top-gated biosensing measurements (described in more detail in 4.3.1.1) interactions between target antigens and antibodies which take place beyond the Debye length will not be measured as the change in charge is screened. Using Fab fragments, which are shorter and therefore closer to the sensing element brings the binding event within the Debye length which ensures that interactions can be measured [52].

3.2.2.2 DNA and Aptamers

Deoxyribonucleic acid (DNA) is a molecule formed of two chains of deoxyribonucleotide subunits (Figure 3.4). These subunits consist of three components, the deoxyribose sugar group, the phosphate group and one of the four bases; adenine (A), thymine (T), cytosine (C) and guanine (G). The deoxyribonucleotides are covalently bonded through the periodic sugar, phosphate ester bonds between the deoxyribose and phosphate groups. The two chains are bonded together via hydrogen bonds which form specifically between the A (C) and T (G) base pairs positioned perpendicular to the sugar-phosphate backbone. It follows that the two chains are complimentary to one another. The sequence of base pairs in DNA is the code where all genetic information in cells is stored [53, 54].

Figure 3.4 has been removed due to Copyright restrictions

Figure 3.4. A) 3D DNA model. B) Schematic of DNA structure [53]

Ribonucleic acid (RNA) is a single stranded molecule used in cells to transcript genetic information stored in DNA (it is also the primary genetic store in some viruses). The base pair of thymine is replaced with uracil (U) in RNA. Also the sugar group is ribose and therefore this molecule is a polymer of ribonucleotide subunits. RNAs are used within cells to express genetic information, this can be the formation of proteins for example [53, 54].

Small chains of nucleotides called oligonucleotides in the form of single stranded RNA or DNA which have folded and have the ability to interact with target analytes are called aptamers. Aptamers are produced using the Systematic Evolution of Ligands by Exponential Enrichment (SELEX) technique. This process starts when a large pool of random RNA/DNA chains which are incubated with the desired target. The chains that bind often fold to form complexes with the target. Unbound oligonucleotides are removed from the pool before bound RNA/DNA chains are amplified by Polymerase Chain Reaction

(PCR) thus increasing the number of nucleic acids able to bind to the target. Further RNA/DNA chains are produced from the outputs of the PCR process, with a higher affinity for the target, which are subsequently re-introduced into the selection pool. These stages are then repeated, usually between 5-15 times, before the oligonucleotides are sequenced, identified and characterised. The resulting oligonucleotide is highly specific for the target analyte [56, 57]. An overview of the SELEX technique is given in Figure 3.5.

Figure 3.5 has been removed due to Copyright restrictions

Figure 3.5 The SELEX process [57]

A longer shelf-life, easier immobilisation on sensing elements and an improved option for re-use after detection events are all advantages that aptamers offer biosensors [48]. Aptamers offer several benefits to their use as bioreceptors over antibodies. Firstly, they are more stable than antibodies as preventing proteins from irreversible denaturing and losing their specific tertiary structure is difficult specifically at elevated temperatures. Aptamers on the other hand, can retain their original conformation after repeated denaturing/renaturation cycles. Since the SELEX process for manufacturing aptamers is reproducible, aptamers do not suffer from variations in performance between batches that is often observed from antibodies due to their production in mammalian cell cultures. Moreover, the requirement for the target analyte to produce an immune response can limit the possible targets that are available for antibodies. Aptamers however are able to bind effectively to analytes that cannot be recognised by antibodies which broadens their possible use in the field of biosensing [58].

3.2.2.3 Enzymes

Proteins that act to catalyse substrates into products are called enzymes. Redox-enzymes catalyse chemical reactions which involve the reduction or oxidation of target analytes and therefore observing the change of electron concentration or current density through the biosensor can be used to measure the concentration of the target analyte. The stability of enzymes during operation and storage is one of the major challenges of using these as bioreceptors [48]. Hydrogels encapsulated with different enzymes were patterned onto GFET channels by Bay's group as they showed the simultaneous monitoring of penicillinase- and acetylcholinesterase- functionalized hydrogels paving the way for future multiplexed GFET devices. These devices displayed additional benefits from using hydrogel environments as they prolonged the enzyme activity from a few days to one week and also showed a reduction in the nonspecific binding response when tested with Bovine Serum Albumim (BSA) [59].

3.2.3 Transducer Methods

Choosing the appropriate transducer method for a biosensor is a decision made based on a variety of factors. Where testing is prioritised for rapid results, such as in a POC settings, the biosensor needs to be portable and without complex supporting equipment. On the other hand, larger, more expensive and equipment which require highly skilled personnel may be better suited when sensitivity and low LOD are prioritised. An introduction into a handful of popular Optical, Thermal and Electrical transducer methods is provided below to represent a broad spectrum of transducer types which sets the scene for the reader into the vast biosensing landscape. It is noted here that each method presented can have varying degrees of cost, complexity and FOMs attached to them.

3.2.3.1 Optical – Lateral Flow Immunoassay (LFIA)

Immunochromatographic tests otherwise known as Lateral Flow Immunoassays (LFIA) are easy-to-use, reliable, portable biosensors which have become particularly widespread amongst developing nations due to their low-cost [13]. A schematic which shows a typical LFIA device is provided in Figure 3.6.

This sensing scheme relies on a substrate base with overlapping porous membranes, usually nitrocellulose, deposited on the surface. These porous membranes consist of recognition molecules and are designed to have appropriate pore sizes to ensure a uniform capillary flow throughout the device. When a test solution is dropped onto the sample pad, it is first filtered and then evenly distributed across the sensor. Capillary action drives the sample along the LFIA towards the section which contains the labelled bioreceptors (often antibodies). If binding between the target analyte and recognition molecule is successful, these compounds will move towards the recognition zone where an additional reaction occurs resulting in a visual line appearing at this position (the test line). The control line is there to confirm the correct flow of the analyte within the LFIA [13].

Figure 3.6 has been removed due to Copyright restrictions

Figure 3.6 Schematic showing a typical LFIA. Test solution is applied to the sample pad, which migrates through porous membrane to the detection zone [13].

A direct result of the lack of supporting equipment required to use these tests is that they have been able to proliferate in areas where medical infrastructure is decentralised. LFIA devices have thus facilitated the trend of patient-lead sensing from their invention over 60 years ago and are now continuing to progress POC sensing further into the 21st century. Popular in society for their use at determining pregnancy, LFIA became ubiquitous during the COVID-19 pandemic, as they enabled mass testing of populations worldwide in a bid to prevent future infections [13].

3.2.3.2 Optical - Surface Plasmon Resonance

Surface Plasmon Resonance (SPR) is a phenomenon that is commonly exploited in optical based biosensors. Surface plasmons are created on the surface of a conducting material between two media when it is exposed to polarized light at a specific angle (resonance angle). This resonance angle is dependent on the mass of the sensing surface. By immobilising bioreceptors onto the sensor surface, binding events which change the mass will transduce a signal via a shift in angle [51] (Figure 3.7). This technique offers highly sensitive measurements. This biosensing strategy was deployed by Piliarik's group to achieve a limit of detection for the human gonadotropin (hCG) cancer biomarker as low as 100 ng/ml with the target analyte within a diluted blood plasma sample [61].

Figure 3.7 has been removed due to Copyright restrictions

Figure 3.7. A) Schematic showing typical SPR measurement. B) Idealised graph showing resonance angle against time, highlighting key points in the sensing timeline [51]

3.2.3.1 Thermal

Thermal biosensors use calorimetry to measure the heat transfer during metabolic reactions to detect analytes. Flow calorimeters are based around a reaction chamber with immobilised bioreceptors. This chamber is constantly monitored so that when heat is given off during exothermic reactions with the target analyte the change in temperature will register as metabolic events which correlate with the concentration [47]. A fructose-selective calorimetric biosensor was used by Bhand et al to show rapid measurements of fructose in syrup by immobilised hexokinase and fructose-6-phosphate kinase enzymes in a two stage reaction whereby the heat transferred during the secondary metabolic reaction is proportional to the amount of fructose that is phosphorylated [37]. A typical schematic of a calorimeter is provided in Figure 3.8.

Figure 3.8 has been removed due to Copyright restrictions

Figure 3.8 Schematic showing typical flow-injection analysis used for calorimetry measurements [47]

3.2.3.2 Electrical - Electrochemical

Electrochemical based biosensors are constructed from three electrodes; reference, counter (or auxiliary) and working (sensing or redox). The reference electrode is designed to maintain a stable and known potential (between it and the working electrode) and is usually separated from the sensing site. The counter electrode, designed to be unreactive, is connected to the electrolytic solution and completes the sensing circuit. The working electrode acts as the site for transduction of the signal [48, 62]. A potentiostat controls the potential difference between the reference and working electrode and measures the current through the working and counter electrodes [62]. Amperometry is the name given to an electrochemical sensing method where the potential difference between the working and reference electrodes is held constant and the current is monitored, whereas during voltammetry measurements the current is recorded as the potential is swept.

Figure 3.9 has been removed due to Copyright restrictions

Figure 3.9 Schematic showing generic redox reaction at the surface of an electrode [62].

Potentiometric devices on the other hand, holds the current between the working and reference electrodes constant whilst measuring the potential difference. [48]. Measuring the oxidation or reduction rates of an electrolyte is achieved by using an amperometric sensor. The simplest form is called a Clark oxygen electrode, which is used to measure the oxygen concentration dissolved in water. A schematic showing a simplified reduction reaction at the surface of a working electrode is provided in Figure 3.9. The reader is signposted to [48] for a detailed discussion on electrochemical techniques.

3.2.3.3 Electrical – Field Effect

Immobilising bioreceptors onto the surface of the conducting channel in a Field Effect Transistor (FET) based design, and monitoring the change in electronic properties during binding events is another direction of interest for biosensor research. Haslam's group have shown a LOD of 1 pg/mL for hCG using a conductometric sensing strategy implemented with immobilised antibodies onto the surface of graphene acting as a gate material between two electrodes in a FET based design [4, 48]. A more detailed discussion on FET based biosensors is given in Chapter 4.

3.3 Summary

Biosensors are devices which translate biological and/or chemical events into measurable signals that are used across a wide variety of fields and settings. The FOMs that describe them are optimised by users for their particular application and are discussed in this chapter to introduce the reader to the characteristics that devices in this work will be evaluated against. Biosensors are realised when interactions with the target analyte can be transduced as a signal. The initial interaction with the target analyte occurs at bioreceptors which have been chosen by users to be selective to their desired target.

For the bioreceptor element of sensors there has been a convention to immobilise antibodies owing to their high selectivity. However, due to their high batch variability and narrow range of sensing targets there is an exciting trend in the use of DNA aptamers for their eventual replacement. Single stranded DNA nucleotides called aptamers have shown to be exceptional bioreceptors; they are highly stable, low in cost and widely applicable to targets which has boosted their proliferation in this area. Therefore, this project focusses on aptamers as the bioreceptors of choice and evaluate their effectiveness on devices, which will add to the body of knowledge surrounding their application.

It is the task of the transducer element of a biosensor to relay the interaction between the bioreceptors and target to the user. Several sensors which harness optical, electrical and thermal techniques have been introduced which sets the scene for the reader as to the broad landscape of this exciting biosensing field. This project targets the improvement of electrical-FET based biosensors since they can be fabricated in large scales owing to their miniature size and compatibility with semiconductor manufacturing pipelines. These two factors will also facilitate the widespread use of these devices in the future once proof of concept investigations have been optimised. Further justification for this choice along with a more detailed description into their use is provided in Chapter 4.

Chapter 4 - Graphene Field Effect Transistor Biosensors

4.1 Field Effect Transistors

4.1.1 Description and Overview

A FET is designed to control current through two electrodes (source and drain) based on a potential difference applied to a gate material. Depending on the specific design of the transistor, traditionally the gate material will be either P-type (majority hole carriers) or N-type (majority electron carriers) doped silicon. FETs are described as working in depletion (enhancement) modes if a conducting channel is (not) present between the source and drain electrodes when the voltage applied to the gate is zero. It follows that depletion and enhancement mode FETs are described as “ALWAYS-ON” and “ALWAYS-OFF” respectively when a potential difference is created between the source and drain electrodes. Devices are described as unipolar (ambipolar) if one (two) charge carriers are used to conduct current from the source to the drain electrodes. FETs can be further categorised into Junction Field Effect Transistors (JFETs) and Metal Oxide Semiconductor Field Effect Transistors (MOSFETs) [63-65].

4.1.2 Junction Field Effect Transistors

A JFET consists of source and drain electrodes separated by a doped region, called a channel, situated on top of an oppositely doped substrate layer with an additional gate region set within the channel. Figure 4.1 depicts a depletion type, N-channel JFET. With a potential difference applied across the source and drain electrodes current will flow through the conducting N-type region channel. Note that the P-type regions are electrically connected. The type of device pictured is in the “ALWAYS ON” configuration (depletion type) as current flows between the source and drain electrodes when a potential difference is set up between them with zero potential at the gate. It is therefore also called a voltage controlled device (VCD) [63, 64].

Figure 4.1 has been removed due to Copyright restrictions

Figure 4.1. Depletion type, N-channel JFET [64]

When a negative potential difference (with respect to the source-drain) is applied across the gate, the P-type regions, named the depletion regions, increase (Figure 4.2). These depletion regions reduce the cross sectional area for the charge carriers to move through subsequently reducing the current through the device. Electron build up at the source end and electron loss at the drain end produces an asymmetric depletion zone. When the depletion zones meet, the current is said to be “pinched off”, this occurs at the pinch-off voltage. Realistically, these zones will never meet (as this would result in infinite resistance) as current leakage occurs. At this point any increase in the source-drain potential difference results in only a very small rise in current through the device [63, 64].

Figure 4.2 has been removed due to Copyright restrictions

Figure 4.2. Depletion type, N-channel JFET with applied voltage across gate electrode [64]

4.1.3 Metal Oxide Semiconductor Field Effect Transistor

4.1.3.1 Depletion-Enhancement Mode MOSFETs

One of the primary differences between a MOSFET and a JFET is that the gate in a MOSFET is insulated from the doped regions by a thin oxide – usually silicon dioxide (SiO_2). Similar to the JFET, current between the source and drain is controlled by the voltage applied to the gate. A depletion type, N-channel DE-MOSFET is depicted in Figure

4.3. When there is no voltage at the gate there is a conducting channel between the source and drain electrodes via the N-type channel [63, 64].

Figure 4.3 has been removed due to Copyright restrictions

Figure 4.3. Depletion type, N-channel MOSFET schematic [64]

When a negative potential difference is applied to the gate, negatively charged electrons carriers in the N-type region are repelled from the insulating layer whilst positively charged holes are attracted to the gate. This results in a depletion region void of electrons within the N-type channel being formed which subsequently limits the current flow between the source and drain electrodes (Figure 4.4). As the potential at the gate decreases further, the depletion region will eventually block the N-type channel and no current will flow. This type of device pictured is in the “ALWAYS ON” configuration (depletion type) as current will flow when the potential applied to the gate is zero [63, 64].

Figure 4.4 has been removed due to Copyright restrictions

Figure 4.4. Depletion type, N-channel DE-MOSFET with applied voltage across the gate electrode [64]

The major advantage of the MOSFET design over the JFET is the ability to enhance/deplete the current further with an opposite polarity applied to the gate electrode. Considering the depletion type, N-channel MOSFET above, if a positive potential was applied to the gate, charge carriers would be injected into the N-type channel which would enhance the current further resulting in a greater current possible than with the potential at the gate held at zero. On the other hand, in a JFET configuration this is not possible due to forward biasing between the oppositely doped regions [64].

4.1.3.2 Enhancement Only Mode

For an E-MOSFET, the two doped regions connected to the source and drain electrodes are totally isolated from one another by a doped region that extends between the channel and across the gate resulting in zero current flow between the electrodes. This is described in Figure 4.5 [64].

Figure 4.5 has been removed due to Copyright restrictions

Figure 4.5. Enhancement type, N-type inversion layer E-MOSFET schematic [64]

When a positive potential difference is applied to the gate, a negative charge on the P-type material fills the holes leaving a neutral channel to form underneath the insulated gate layer. As the potential difference applied to the gate is further increased, more electrons are injected into this region making it an N-type region and subsequently allowing current to flow (Figure 4.6). The N-type inversion layer is the name given to the region that swaps from being P-type to N-type under these conditions. This type of device pictured is in the “ALWAYS OFF” configuration (enhancement type) as current will flow only when the potential applied to the gate is positive [64].

Figure 4.6 has been removed due to Copyright restrictions

Figure 4.6. Enhancement type, N-type inversion layer E-MOSFET with applied voltage to gate [64]

4.2 Field Effect Transistor Biosensors

4.2.1 Insulated Gate Field Effect Transistors

For biosensing applications Insulated Gate Field Effect Transistors (IGFETs) is the common term used to refer to the MOSFET structure previously discussed in section 4.1.3. The detection of the mutant p53 gene was shown by Han’s group using a silicon based IGFET biosensor by immobilising strands of DNA, that their target protein selectively bound to, onto the metal gate electrode. This biosensor was capable of detecting significant increases in the drain current due to the modified surface charge at the gate electrode (which acted in a similar way to an applied voltage to the gate), when the wild p53 gene bound to the DNA [66].

4.2.2 Ion Sensitive Field Effect Transistor

An Ion Sensitive Field Effect Transistor (ISFET) biosensor operates in the same way as a MOSFET in that the current through the device is dependent on the electric field at the gate. Compared to a MOSFET, in an ISFET design, the gate metal is replaced with an electrolyte, reference electrode and an ion-selective membrane (Figure 4.7). When the charged biomolecules within the electrolyte interact with the ion-selective membrane, the modification in potential on the surface alters the electric field subsequently changing the current through the conducting channel. This device is also sensitive to changes in pH and ion concentrations [65].

Figure 4.7 has been removed due to Copyright restrictions

Figure 4.7 Schematic showing cross-sectional view of a typical ISFET (adapted from [65])

A polycrystalline silicon ISFET was demonstrated by Yan et al who used the ISFET design to create a highly sensitive pH sensor. With the gate insulator protonated, the surface hydroxyl groups in contact with the electrolyte were positively charged therefore creating a pH dependent drop in voltage across the bilayer and subsequent current conductance change in the channel [67, 68]. This group then also showed that immobilising penicillinase enzymes on the surface of the gate insulator and monitoring the pH level change caused by the catalysed reactions, showed that their device was capable of the selective sensing of penicillin concentration [68].

4.3 Graphene Field Effect Transistors

4.3.1 Description and Overview

GFETs are realised by connecting a graphene channel between metal source and drain electrodes, achieved in either the top- or back-gated configuration. These biosensors replace the doped Si channel in traditional FETs with graphene which is subsequently functionalised with bioreceptors to target specific analytes. Graphene is either deposited directly onto pre-patterned devices [3, 9] or plasma etched from a bulk graphene-insulator-substrate stack [4, 8]. For both configurations, a current is passed through the conducting graphene channel when a voltage drop is created across the electrodes.

Sweeping the back-gate voltage modulates the charge carrier contributions in the graphene channel producing distinctive transfer curve characteristics [10]. Recombination events between the target analytes and the immobilized bioreceptors on the graphene surface can be transduced to measurable signals via changes in the graphene’s electronic properties. Graphene’s compatibility with existing planar complimentary metal oxide semiconductor (CMOS) manufacturing processes [10] combined with its ease of functionality [2] and high sensitivity will facilitate these low-cost devices as truly disruptive biosensing technologies in the future.

4.3.1.1 Top-Gated Graphene Field Effect Transistors

For top-gated GFETs (Figure 4.8A), the configuration closely resembles that of the ISFET. In this design monolayer graphene sits on the surface of a Si substrate and an electrolyte is contained on the surface of the graphene by the use of some insulating material such as PDMS [69], PMMA [70] or silicone [52, 71, 72]. A reference electrode is then immersed within the electrolyte. When a voltage is applied across the reference and source electrode, ions in the buffer solution are attracted to the electrodes and counterions attracted to these surface charges consequently forming an electrical double layer (Figure 4.8B) on the graphene surface which simulates an insulating gate [72, 73].

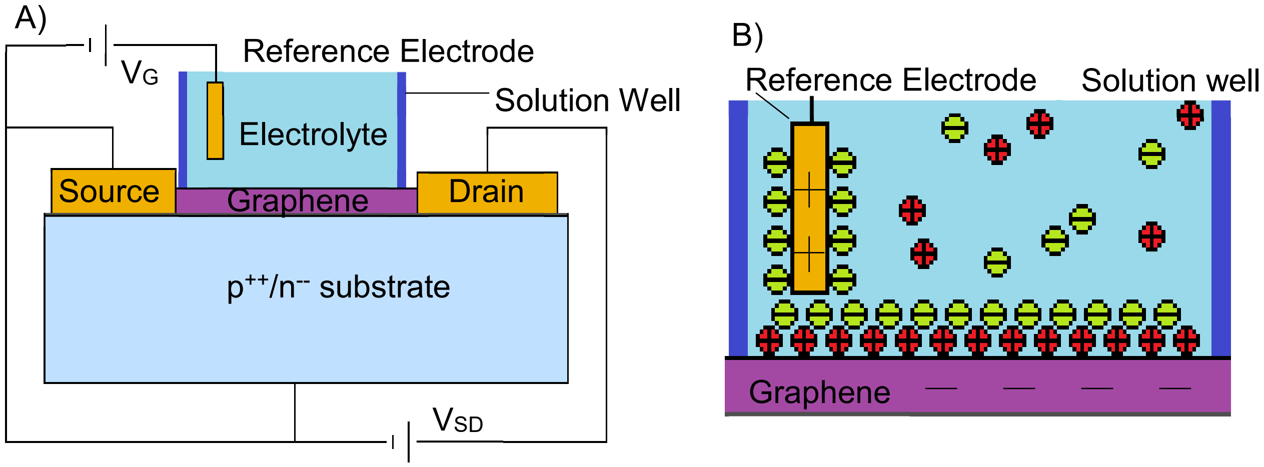

Figure 4.8. A) Schematic showing cross-sectional view of a typical top-gated GFET. B) Formation of electrical bilayer at graphene surface.

The thickness of the electrical bilayer is known as the Debye length and is dependent on the ionic strength and temperature of the electrolyte [71]. A result of this thin electrical bilayer, nominally 5 nm for a 10 mM buffer solution (against a nominally 300 nm thick SiO_2 layer for back-gated GFETs), is that smaller voltages are required to modulate the current in the graphene channel, these devices therefore offer greater transconductance values. Ohno et al calculated the transconductance ($g_m = \frac{\partial I_D}{\partial V_G}$) to be 0.14 and 36 μS for their back-gated and top-gated GFETs respectively [10, 71].

The chemically stability of graphene is exploited as an advantage over traditional semiconductor materials. This is because graphene is not easily oxidised at low voltages when it is covered in a solution as in the topology for top-gated biosensors. Graphene therefore does not require a passivation film, unlike Si or GaAs and can be used in direct contact with the solution [71]. The Debye length of the solution is of great importance to the considerations for chemical functionalisation [72].

Most GFET devices conduct their sensing activities whilst soaked in a buffer solution to maintain a relatively constant pH level as analytes are added [52]. The Debye length describes the maximum distance that charge carriers in the graphene channel are influenced by the target molecules in the detection medium [72]. Above this length, charge is effectively screened by the electrical double layer and no change in conductivity would occur in the graphene channel and therefore no detection event would be observed in the

GFET [52, 72]. One way to create a thinner Debye layer is to reduce the concentration of the buffer which has the detrimental effect of reducing the buffer effect of the solution [71].

Aptamers have been shown [42, 72, 74] to be effective bioreceptors for biosensing using GFETs. Crucially they small enough in length (~3 nm) to be within the Debye length (~5 nm at room temperature in 5-10 mM buffer solutions) allowing electrical detection. Ohno and colleagues used aptamers to enable immunoglobulin E (IgE) sensing in GFET biosensors. By studying aptamer/antibody pairings in favour of antibody/antigen pairings, they could ensure that the charge influences were detected on the graphene surface well within the Debye length [75]. They showed that their sensor was capable of not only detecting the aptamers functionalised on the surface of graphene but showing that they did not cause additional defects in the lattice, shown by an identically shaped but translated I_{SD}-V_G curve between the bare and functionalised states. In addition, this group highlighted the specificity of their GFET sensors as only the introduction of their target analyte caused a change in the channel’s conductance [72].

In another example of keeping the receptor length small, to remain within the Debye length, Okamoto and colleagues showed that using antigen-binding fragments (Fab), which are the structures at the tip of antibodies that combine with target analytes (section 3.2.2.1), allowed the group to observe specific binding events. Fabs were immobilised onto the surface of the graphene using the non-covalent linker (PYR-NHS) without introducing defects, shown by the similar transconductance values for the top gated voltage sweeps of the bare and functionalised states. By using Fabs, which have an approximate length of 3 nm, which are below the typical Debye length distances, this group were able to demonstrate high sensitivity in their GFET biosensors [52].

4.3.1.2 Back-Gated Graphene Field Effect Transistors

A common topology for back-gated GFETs is illustrated in Figure 4.9. It consists of a highly doped Si substrate, followed by a SiO_2 insulating layer with monolayer graphene on the surface. Source and drain electrodes connect the extreme ends of the graphene channel. Back-gated GFET devices offer a simplified fabrication process as it is not necessary to build the support structure to confine the electrolyte and also the requirement to insulate the electrodes does not exist [9]. In addition, the shift in Dirac voltage, one of the key metrics used to describe sensing characteristics for GFETs is often larger when compared with top-gated devices [76]. Back-gated GFETs also facilitate the detection of vapours along with offering improved sensing characteristics when detecting analytes within solutions of varying composition [76].

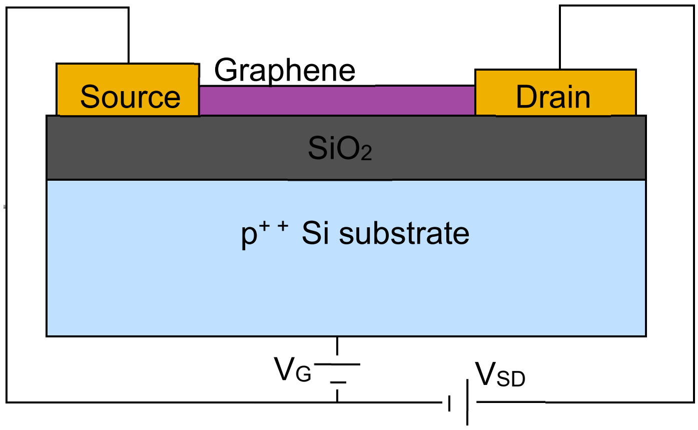

Figure 4.9. Schematic showing cross-sectional view of a typical back-gated GFET

It is common to deposit the graphene directly onto pre-patterned metallic electrodes. Ping's group used this technique to directly transfer graphene onto their chrome (Cr)/ gold (Au) pads claiming a reduction in the contamination, doping and damage to the graphene channel in their final devices. They deployed their biosensors against three increasing long DNA targets. Ping observed a linear correlation with the signal strength against oligomer length and showed detection level of 1 fM for a 60 chain DNA oligomer. This group showed that their devices had great compatibility with current CMOS technology and a fabrication technique suitable for mass production therefore assisting with the proliferation of this biosensing technology [3].

Kakatkar et al demonstrated another back-gated GFET biosensor with the source and drain electrodes previously deposited on the substrate surface with monolayer CVD graphene being transferred afterwards [9]. This "soak-and-peel" approach avoids additional contamination by reducing the amount of photolithographic steps required to fabricate the GFET. This group then tracked the Dirac voltage shifts from I_{SD}-V_G sweeps to detect binding events of picomolar concentrations for their target analytes. Poly-l-lysine and DNA were target biomolecules selected which offered contrasting net charge values to investigate their impact on the Dirac voltage shift. When poly-l-lysine, a polymer chain of the L-lysine amino acid with a net positive charge was deposited, the Dirac voltage shifted to higher values. Conversely when DNA, with a net negative charge was deposited, the Dirac voltage shifted to lower values [9]. On the other hand, Kybert et al who showed a positive shift in the Dirac voltage when DNA was immobilised onto the surface of their GFET arrays [77]. It is therefore documented that the shift in the Dirac voltage for DNA immobilisation can be in either direction depending on sensing mechanisms. Kakatkar showed that the limit of detection for their devices was calculated to be 11 pM and 8 pM for the poly-l-lysine and DNA respectively with both target analytes showing Langmuir adsorption behaviour with increasing concentrations. These devices were also shown to be recyclable without performance degradation for DNA immobilisation since they could be rinsed with water and dried to show total desorption from the graphene surface [9].

4.3.2 GFET Operating Principle

Although graphene boasts high mobility values, of up to 250,000 $cm^2V^{-1}s^{-1}$ [2], suitable for sub-10 nm transistor requirements, with the additional benefit of compatibility with traditional Si fabrication processes [78], one limiting factor in its disruptive use as a replacement for Si based logic transistors in modern electronics is its zero-band gap. Graphene is a semimetal and therefore lacks a band-gap between the valence and conduction bands. In comparison to examples of transistors discussed throughout section 4.1, this results in GFETs working in the “ALWAYS-ON” mode, with current able to flow between source and drain electrodes regardless of the voltage applied to the gate electrode [10].

This lack of band-gap is exploited in GFET sensors however, as it follows that they exhibit ambipolar characteristics. Modulating the Fermi level, which alters the charge density in the GFET channel is achieved by the application of an external voltage to the graphene [71]. The Dirac voltage (V_{DP}), is the name given to the voltage applied to the graphene whereby the minimum conductance occurs. The energy, momentum plot for graphene at the K/K’ position (Figure 2.2B) is depicted in Figure 4.10A with corresponding voltage transfer curve, plotting the gate voltage against current through the graphene channel, shown in Figure 4.10B. The region of minimum conductance corresponds to the position of the Fermi level at the intersection between the valence and conduction bands. At this point, the availability of both electron and hole carriers is at its minimum, driven by their thermal distribution in the channel; it follows that the conductance is at its lowest, but non-zero point. This region is illustrated in Figure 4.10B by the blue shading. Increasing (decreasing) the voltage above (below) the Dirac voltage, increases (decreases) the Fermi level into the conduction (valence) band, whereby electron (hole) carriers dominate the conduction and are available in large concentrations hence increasing the conductance accordingly. Hole and electron conduction are displayed in Figure 4.10B by the orange and green shading respectively [10].

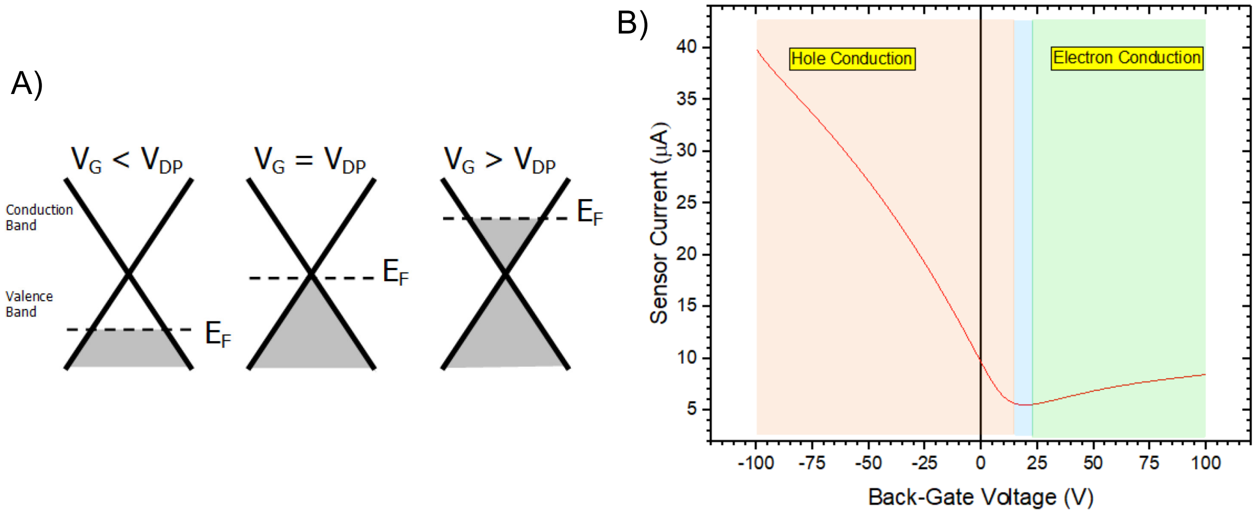

Figure 4.10. A) Idealised energy momentum diagrams for graphene at different Fermi levels. B) Typical transfer curve used for electronic characterisation of GFETs.

The theoretical transfer characteristics of GFETs should be symmetrical, mirroring the symmetric structure of the energy momentum diagram for graphene as shown in Figure 4.10A. However, in practice this is not achieved due a variety of practical limitations associated with the handling and design of such devices such as but not limited to the device geometry, the metal-graphene contact resistance, the formation of p-n junctions and contaminants adsorbing to the graphene surface. These real-world limitations cause asymmetry between the electron and hole conduction which is expressed in transfer curve measurements as left/right shifting in the position of the Dirac voltages from the $V_G = 0$ V point and variations in the gradient for both conduction schemes [10].

4.3.3 GFET Biosensors

A GFET biosensor is realised when the graphene channel is chemically functionalised by the addition of specific bioreceptors which bind selectively to target analytes. Examples of bioreceptors used to functionalise graphene channels are antibodies [69], proteins [43, 79] and aptamers [42, 72, 74]. Unlike electrochemical biosensors which rely on an electroactive species, GFET responses are based on the tendency of the target to bind with the immobilised bioreceptor directly, which induces a measurable change in the electronic characteristics of graphene.

Several different mechanisms for transducing binding events are possible and impact the graphene channel in different ways. The following processes are possible due to binding between bioreceptors and analytes and are illustrated schematically in Figure 4.11; electrostatic gating, charge transfer (doping) and charge scattering [80, 81].

For DNA sensing, Kybert proposes the electrostatic gating effect as the following. Analytes used in their work, such as isobutyric acid (which is a carboxylic acid) are subject to protonation or deprotanation are absorbed by a nanoscale water layer that is bound to the hydrophilic DNA immobilised on the graphene. When the molecules deprotonate, they become net negatively charged and bind selectively to DNA. As the net negative charge is localised near the graphene channel, a positive shift in the Dirac voltage is observed as a greater top/back-gate voltage is required in order to create the same electrostatic environment as before. For measurements with zero back-gate voltage applied (with a hole majority carrier) this is expressed in the GFET as a current increase. This group goes further to theorise the electrostatic gating effect of net neutral molecules when they examined the sensing mechanism for methyl isopropyl ketone (MIPK). They observed an opposite response in conductivity between the MIPK and the isobutyric acid. This substance differs from isobutyric acid in the replacement of a hydroxyl group with a methyl group, which is not subjected to deprotonation. They suggested that with this net neutral molecule a molecular dipole effect dominates the electrostatic gating. In this scheme, they conjectured that DNA preferentially orientates this dipole to present a positive charge to the graphene surface, left-shifting the V_{DP}, equivalent to reducing the current through the GFET at zero back-gate voltage [77].

The mechanism for graphene doping was shown to have a strong dependence on the insulating dielectric layer in measurements conducted by Levesque [82]. An example of the p-doping of graphene via charge transfer, is provided in this work and describes the combined exposure of O_2 and H_2O in the ambient environment. With a hydrophilic substrate layer of SiO_2, right shifting in the Dirac point was evident as a result of the redox reaction, but no such shift was seen when parylene (hydrophobic) was used. This was attributed to the requirement of a full layer of H_2O on the surface which hydrophilic materials offer. P-doping is caused when electrons combine with protons and dissolved oxygen at the surface of graphene to produce water, thus decreasing the concentration of electrons in the lattice [82].

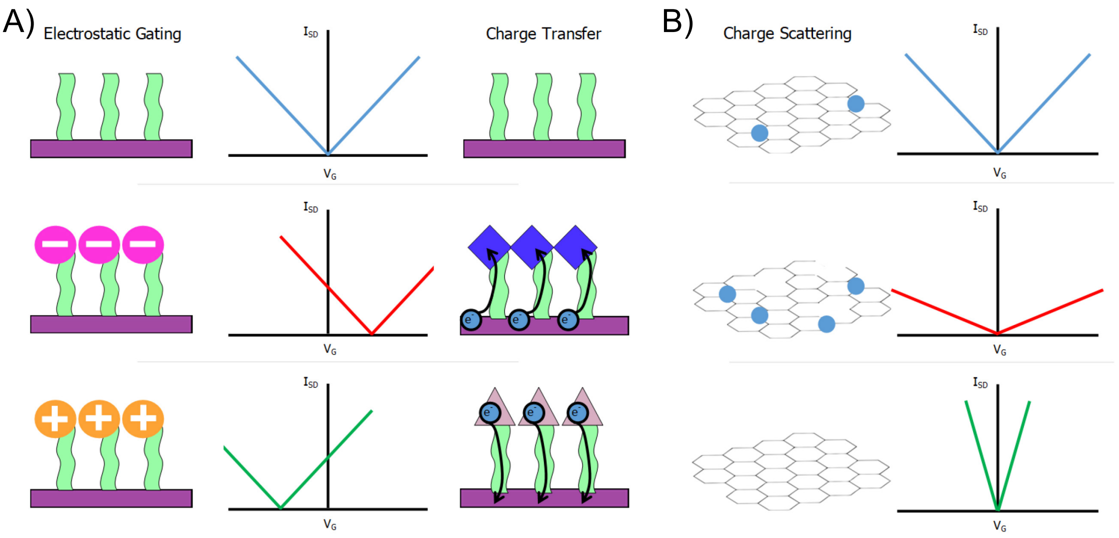

Figure 4.11 Schematics illustrating mechanisms for changing the electronic characterisation of GFETs. A) Effect of electrostatic gating and charge transfer processes showing similar changes to the electronic properties on binding with analytes. Middle panel shows increase in Dirac point caused by negatively charged species and electron acceptors. Bottom panel shows decrease in Dirac point caused by positively charged species and electron donors. B) Effect of charge scattering on transfer curve shape. Top panel shows graphene sheet with existing impurities on the surface. Middle panel shows introduction of additional impurities and defects in the lattice acting to reduce mobility. Bottom panel shows situation whereby functionalisation removes existing impurities acting to improve mobility.

Charge scattering from bio-molecular interactions alters the disorder in the graphene lattice which manifests itself as detectable changes to the mobility of the charge carriers. The mobility of the charge carriers relate the sensor's ability to determine a current response from a change in the applied voltage. The polarity of introduced scattering sites interact with the charge carriers in opposing ways which can cause differing mobility changes for the p- and n- branches. Since mobility relates to the quality of the graphene this metric can also be used to infer whether immobilisation strategies introduced defects into the lattice [81]. Yang's group were the first to show that adsorbents could improve the mobility characteristics in their devices by decreasing scattering in the graphene channel [83].

Isolating the exact mechanism from observations can be difficult since changes to the electronic characteristics can arise from a combination of them and since they are all impacted by sensor design and sample composition differently, uncertainty in this area continues [76]. However, what is clear is that binding events invoke detectable changes to the GFET characteristics which will continue to be exploited for biosensing purposes. These mechanisms can be inferred by monitoring the following primary GFET metrics; Dirac point position, mobility and conductance through the channel.

4.4 Chemical Functionalisation of Graphene

GFET biosensors designed for the specific detection of target analytes rely on the successful immobilisation of bioreceptors onto the graphene channel for them to function. Usually this is achieved using an intermediate “Linker” molecule whose moieties will be chosen based on their affinity to bind with graphene alongside their conjugation to the desired bioreceptors at alternate ends of the molecule. Two of the most common methods for immobilising such Linker molecules is covalent and non-covalent functionalisation.

4.4.1 Covalent functionalisation

Covalent functionalisation exploits existing defects in the atomic lattice or employs chemical processes to deliberately introduce functional groups onto graphene [80]. Practically this can be done by covalently bonding free radicals between the C==C bonds of graphene [84]. Although responsible for altering the electronic properties of graphene, covalent strategies tend to be extremely stable on the graphene which can facilitate measurements in areas of high flow rates [81].

4.4.1.1 Free Radical Reactions

Reactive free radicals are produced when diazonium salt is heated. These free radicals react with the sp^2 carbon atoms of the graphene to form covalent bonds. In the process of this reaction sp^2 hybridized carbon atoms are converted to sp^3 [84].

Alternatively, benzoyl peroxide can be used as a free radical to covalently bind with graphene sheets. Activating this reaction can be achieved by focussing an Ar-ion laser onto the graphene sheet submerged within a benzoyl peroxide/toluene solution. It is conjectured that hot electrons from graphene transfer into the physiabsorbed benzoyl peroxide to form radical anions that are rapidly decomposed into phenyl radicals which subsequently react with the sp^2 carbons to form covalent bonds [84].

The existence of sp^3 carbons in the graphene lattice is described as an introduction of defects since graphene is defined as a two-dimensional sp^2 hybridized carbon lattice. These defects cause the structure of graphene to change. The alteration from sp^2 to sp^3 disrupts the conjugation of π-electrons which can be evidenced as a severe decrease in the conductivity in the graphene sheet [81, 84].

Figure 4.12 has been removed due to Copyright restrictions

Figure 4.12 Schematic showing covalent functionalisation via hydroxylation. A) Bare graphene is hydroxylated via the Fenton reaction. B) APTES is used to bind to the hydroxyl groups leaving C) amine groups for further conjugation (adapted from [85]).

4.4.1.2 Hydroxylation

The graphene surface can be hydroxylated using the Fenton reaction. During the Fenton reaction an iron catalyst (Fe^{2+}) is mixed with hydrogen peroxide (H_2O_2) in acidic conditions to create radical hydroxyl groups. The Fenton reaction behaves according to the following equations [86]:

$$Fe^{2+} + H_2O_2 \rightarrow Fe^{3+} + OH^{\cdot} + OH^{-} \tag{4-1}$$

$$^{\cdot}OH + H_2O_2 \rightarrow HO^{\cdot}{}_2 + H_2O \tag{4-2}$$

$$Fe^{2+} + {}^{\cdot}OH \rightarrow Fe^{3+} + OH^{-} \tag{4-3}$$

$$Fe^{3+} + HO^{\cdot}{}_2 \rightarrow Fe^{2+} + O_2 + H^{+} \tag{4-4}$$

$$^{\cdot}OH + {}^{\cdot}OH \rightarrow H_2O_2 \tag{4-5}$$

The radical hydroxyl groups produced during this reaction covalently bind with the graphene surface. Once the surface has been activated in this way (3-Aminopropyl) triethoxysilane (APTES) can be used to form an amine decorated surface suitable for binding bioreceptors (Figure 4.12). In a study led by Teixeira, multi-layer epitaxial graphene was functionalised in this way to immobilise their antibody bioreceptors via carboxylated groups. Their amperometric immunosensors were able to detect their target hCG to concentrations 30 times lower (0.62 ng/mL) than an equivalent ELISA test [85].

4.4.2 Non-covalent functionalisation

Functionalising the graphene channel with a desired bioreceptor without introducing defects is essential to reducing the occurrence of non-specific detections (as defects behave as active sites for molecular adsorption [87]) along with maintaining the п-electrons which give graphene its highly sensitive conducting characteristic [72, 88].

4.4.2.1 1-Pyrenebutanoic acid N-hydroxysuccinimide ester (PBASE)

Non-covalent functionalisation of carbon nanotubes and graphene is commonly achieved by using the bi-functional molecule 1-Pyrenebutanoic acid N-hydroxysuccinimide ester [69, 81, 89]. Across the literature this molecule is also referred to as 1-Pyrenebutanoic acid Succinimidyl Ester, N-Hydroxysuccinimidyl Pyrenebutanoate and 1-Pyrenebutyric acid N-hydroxysuccinimide ester or under one of the shortened terms PBASE [90, 91], PBSE [92, 93] or PYR-NHS [4, 94].

Figure 4.13 has been removed due to Copyright restrictions

Figure 4.13 PBASE molecule with Pyrenyl group (blue), Succinimidyl ester group (green) and Carbonyl groups (yellow) highlighted [95]

This molecule, consists of two distinct ends, a highly aromatic pyrene group which binds to graphene and a highly reactive N-hydroxysuccinimide (NHS) ester group which binds easily to amines that are present in large numbers on surfaces of bioreceptors. The NHS group also acts to self-limit the growth of the monolayer as it blocks other PBASE molecules from binding to it [96].

The NHS ester group is a very popular crosslinking agent, used in the majority of amine-reactive conjugation techniques. These esters are water insoluble and therefore require the use of organic solvents like Methanol (CH_3OH) and Dimethylformamide (DMF) ($(CH_3)_2NCH$). Nucleophiles react with these molecules forming acyls with the NHS group being released as a by-product. When cross-linking primary or secondary amines, stable amide bonds are created during the reaction process. The formation of a stable bond using this crosslinking reaction is given in Figure 4.14, where **R** and **R’** correspond to additional moieties attached to the amine and NHS group respectively [97].

Figure 4.14 has been removed due to Copyright restrictions

Figure 4.14 Amide bond formation using NHS ester cross-linking [97]

In the presence of an inorganic solvent such as methanol, the aromatic pyrene group of this molecule binds to the Basal plane of graphene via “п-stacking” or “п-п interactions” [69, 88, 95]. These two terms describe the binding mechanisms between one or more aromatic molecule and has been criticised in the literature as to its accuracy in describing the interaction [98]. Martinex et al argue that these terms mislead those not familiar into believing that aromatic molecules favour the face-centred parallel stacking interaction (Figure 4.15). This is not favoured in most п-systems as the majority of aromatic molecules produce an electron density exhibiting a quadrupole moment; with partial negative charge above its faces and a partial positive charge around its periphery. The electrostatic attraction between two such systems would in fact favour either off-centred parallel stacking or edge-to-face interactions Figure 4.15B-D [98].

Investigations led by Hinnemo suggest that for low concentrations of PBASE, the molecules lie in a horizontal fashion with the pyrene groups stacking with the graphene in the parallel offset fashion. They argue that parallel face-centred stacking would cause the Raman 2D peak to split which is not observed across their observations. However this group goes on to argue that for higher concentrations it is energetically favourable that the pyrene groups are perpendicular to the basal plane in a t or y- shaped stack [99].

Figure 4.15 has been removed due to Copyright restrictions

Figure 4.15 Possible Interactions between aromatic systems A) Parallel face-centred, B) Parallel offset, C) Perpendicular t-shaped, D) Perpendicular y-shaped [98]

The hydrophobic nature of the pyrene group assists with the stability of this bond and prevents desorption causing the interaction to be irreversible [88]. Kodali et al show that the sp^2 hybridisation is not effected by treating graphene with PBASE, shown by the absence of the D peak in the Raman spectrum at ~1350 cm^{-1} in measurements taken on samples prepared with and without it [88]. Furthermore, Kodali was able to show that the π-band structure remained unaffected by the addition of the PBASE substance by showing that there was no change to the single Lorentzian 2D peak at ~2716 cm^{-1} [88].

As most proteins have large amounts of amine groups on their surface they can be easily conjugated with the PBASE molecule via nucleophilic substitution to form amide bonds [69, 95] exploiting the NHS ester group. Chen et al confirmed the effectiveness of PBASE molecules for functionalisation by incubating target proteins with single walled carbon nanotubes (SWCNTs) that had and had not been previously treated with PBASE. Their results show that the target proteins were only found attached onto the walls of the SWCNTs when treatment with PBASE was used as an intermediary step [95].

In order to improve the sensitivity of their Prostate-specific antigen (PSA) detecting carbon nanotube field effect transistor (CN-FET) biosensors, Kim's group deployed spacers onto the surface of their device in order to increase the distance between their bioreceptors such that their target could easily approach (Figure 4.16). They used the aromatic 1-pyrenbutanol molecules (Figure 4.16A) as their spacers and showed using SEM imaging that the distance between immobilised Au-NPs increased across the CN-FET surface with an increasing proportion of immobilised spacers.

Figure 4.16 has been removed due to Copyright restrictions

Figure 4.16 A) Structure of 1-Pyrenebutanol B) Schematic showing different ratios of Linker and Spacers Adapted from [100].

This group then studied the impact of using different ratios of PBASE to spacers on their sensors' electrical characteristics and found that introducing the spacers lowered the concentration of PSA required to produce a response in their device, thus increasing their sensitivity (Figure 4.16B) [100].

4.4.2.2 Pyrene Group Modification

In an alternative methodology, the bioreceptor can be chemically modified with a pyrene group so that it can be directly conjugated to the graphene channel. DNA Aptamers modified in this way have been shown to bind effectively to graphene for the selective sensing of E. Coli [101] and Interferon-gamma [102].

Wu’s group demonstrated a GFET that harnessed a DNA probe modified with a pyrene group to detect E.coli. They introduced spacer thymine nucleotide bases in order to separate the specific aptamer from the pyrene phosphoramidite derivative so that the probe could still undergo conformational changes in the presence of their target bacteria. Their devices were both sensitive, in showing low detection limits of 100 Colony Forming Units (CFU)/mL and stable, by demonstrating high response levels (~13%) to their target after being stored in PBS for six weeks. Such biosensing metrics display some of the advantages of DNA aptamers in practice [101]. This technique simplifies the sensing process by removing a functionalisation step however the cost and/or time to modify such bioreceptors currently limits its widespread use.

4.4.2.3 Porphyrin Linkers

Kawata’s group compared device characteristics between tetrakis(4-carboxyphenyl)porphyrin (TCPP) and PBASE against a human IgE target. Since the TCPP π-system is larger than that of PBASE they conjectured that it would bind more stably to the graphene sheet. In addition, the four carboxyl groups facilitated an increase in bioreceptor binding density. Although this technique required an additional step in order that the carboxyl groups could be activated so that the aptamers could bind to the immobilised TCPP, this group showed enhanced sensitivity, with a lower LOD of 2.2 nM compared to 13 nM for PBASE caused by these linker molecules [91].

4.5 Summary

Traditional Si-based FETs devices rely on an external voltage applied to a gate electrode to modulate current between source and drain electrodes. There are several configurations for these devices which have developed for different purposes. One such purpose is the use of FETs for biosensing. Si-based biosensors are often designed in the MOSFET configuration, whereby bioreceptors are immobilised directly onto a gate electrode (IGFETs) or onto the surface of a dielectric (ISFETs); during recombination events with target analytes, changes in the electric field have the same impact of an externally applied voltage causing charge modulation. This modification in charge modulates the current which transduces detection signals.

GFET devices are similar to Si-based FETs since they rely on the modulation of the charge carriers in the conducting graphene channel by an external voltage applied to a gate electrode. GFETs can be configured in either the top- or back-gated layout, each with their own set of benefits and drawbacks. Devices employed in this work will have a back-gated architecture since this facilitates a simplified fabrication and testing procedure. The fabrication process is further simplified in this contribution as the graphene is supplied on a stack of Si/SiO_2 which removes the requirement to transfer graphene, which is necessary when manufacturing pre-patterned devices. It follows from graphene's unique electronic structure that it exhibits ambipolar conduction, whereby the conducting channel has either majority hole or electron charge carriers depending on where the Fermi level sits with respect to the material's conduction or valence band. Since the Fermi level can be altered by an electric field induced by the application of an external voltage to a gate electrode, unique electrical transfer curve metrics are exploited herein to evaluate GFET responses.

GFET biosensors in this work are realised by immobilising bioreceptors onto the surface of the graphene channel. These devices exploit graphene's sensitivity and electronic properties to infer detection events. The exact sensing mechanism is debated in the literature and depends greatly on the design, fabrication method and functionalisation strategy for the biosensors. Binding events are therefore transduced by a mixture of field effect, doping and scattering processes between bioreceptors, analytes and the graphene lattice. By monitoring the electrical transfer curve characteristics devices fabricated throughout this work have their performance evaluated during detection events.

Graphene's ease of functionalisation is another justification for using it as a sensing material. Chemical functionalisation strategies for immobilising bioreceptors were explored in this chapter. Covalent moieties offer greater stability at the cost of interrupting the sp^2 hybridisation of carbon atoms which acts to change graphene's electronic properties. Therefore, the non-covalent functionalisation of the graphene channel is preferred in the literature and is exploited in this work. This is achieved via the intermediary bi-functional molecule PBASE, which binds to the graphene via π-stacking at the pyrene end and offers cross linking with amine groups to bioreceptors at the NHS ester end. Linker molecules like PBASE have proliferated GFET technologies into wide ranging fields since they allow a plethora of specific bioreceptors to be immobilised onto generic sensing platforms.

Chapter 5 – Lead Sensing

5.1 Introduction

The aim of this chapter is to outline the current situation with regards to the need for lead (Pb) sensing devices. Then the discussion will outline the latest bioreceptors for targeted lead ion detection before focussing on the latest applications of GFET sensing regimes. A thorough review into the latest biosensor technologies exploiting graphene derivatives for the sensitive detection of food adulterants and toxicants, which complements this chapter, has been co-written by the author and can be found in [103].

5.2 Lead Poisoning

The widespread existence of the heavy metal lead in the environment is a severe threat to the health of humans. Ever since the industrial revolution, lead's proliferation into a variety of products has caused an epidemic in exposure. Moreover, combining its continuous use in a myriad of industrial settings with its non-biodegradability has resulted in an ever-increasing accumulation of this chemical in the environment [14]. Although the removal of lead from some items including paint and gasoline has caused a reduction in lead poisoning, the contamination of lead in drinking-water is deemed to be rising. This increase has been caused by aging lead-based infrastructures (now restricted) and the alteration of water treatment and sources [104].

Although high-income nations have curtailed the exposure to lead, its use in low- and middle-income nations has continued. That said, recent case studies as demonstrated by the Flint water crisis between April 2014 and October 2015 in Flint, Michigan, USA, illustrates that this is an issue that can impact anyone. During this situation, residents of Flint had their drinking-water source changed and shortly after were complaining of skin inflammation observed in their children. Researchers uncovered lead levels in water exceeding the USA's Environmental Protection Agency's 15 µg/L action level which eventually translated into blood lead levels (BLLs) in children increasing significantly due to the residents' exposure [105].

Lead is a neurotoxin that accumulates over time in the body restricting the cognitive, behavioural and psychological development of children [15]. Specifically, two ways in which the lead ion (Pb^{2+}) has shown to impede cellular processes is its action as an effective interfering agent against calcium ions which drive ion channels in animal cells [14] and also its limiting effect on cells' ability to respond to rapid changes in the solute concentration around them due the propensity of Pb^{2+} ions to bind to sulfhydryl, phosphate and carboxyl groups of the cell membrane [106].

Lead in drinking water is an issue that particularly harms children as not only do they absorb between four to five times more per oral dose than adults do [104] but both their internal and external tissues being softer than adults make them more susceptible to damage [14]. Additionally, their under-developed blood-brain barriers allow for easier lead penetration into the brain [15].

Hou's group led a clinical study investigating the link between lead poisoning and the intellectual and behavioural abilities of children. They observed a clear negative correlation between BLL and adaptive behaviour, motor performance, language development and social behaviour, consistent with similar studies in this area [15].

In 1984, the WHO published a document with the purpose of protecting the public from constituents in water with known hazardous qualities. The guideline level for a maximum lead concentration in drinking water was recommended to be 50 µg/L [107]. By 1992, and in the second edition of this document the recommended lead concentration had dropped to 10 µg/L where it currently remains today [108, 109]. One of the reasons for such a low guideline level is that the WHO have acknowledged that there is no known safe BLL. They describe even minute concentrations of 50 µg/L of lead in blood being linked with a decrease in intelligence in children and behavioural and learning difficulties [110].

It is clear that one way of limiting the exposure of our biosphere to lead is by increasing the frequency of measurement of concentration levels from our drinking-water sources. One way to improve this testing regime is the development of low-cost, simple to use and field suitable devices that can regularly analyse lead concentrations in drinking water sources thus ensuring they remain at lower risk levels [111].

5.3 Lead Sensing Techniques

5.3.1 Gold-Standards

Most of the current techniques for accurate lead detection require highly skilled personnel using expensive, advanced and centralised lab-based equipment for their work [111]. Three of the most common techniques for detecting lead in water and blood have proved to be Atomic Absorption Spectrometry (AAS), Inductively Coupled Plasma Mass Spectrometry (ICP-MS) and Anodic Stripping Voltammetry (ASV) with field suitable ASV devices already developed. For a more detailed explanation of these techniques, the reader is invited to the review the following reference [112].

Field suitable devices are favoured over the more accurate but expensive laboratory methods when the response time is critical since sample shipping, preparation and analysis all act to delay the determination of results. This can subsequently delay any action required to prevent further exposure to lead from drinking water sources [113].

Some commercial ASV techniques are shown in Table 5.1 and demonstrate the wide variety of LODs and linear ranges alongside other features that characterise lead detection.

FIELD ANALYSER	PB CONCENTRATION RANGE	SAMPLE PREP & ANALYSIS TIME	SAMPLE VOLUME PROCESSED	CAPABILITY TO MEASURE OTHER METALS
ASV-1	10 nM – 480 nM	< 5 min	5 mL	Cu
ASV-2	1 nM – Not specified	< 5 min	15 mL	As, Hg, Cu
ASV-3	5 nM – Model dependant	< 5 min	Not detailed	As, Cd, Cr, Cu, Mn, Hg, Ni, Zn
ASV-4	2 nM – 4 µM	< 5 min	10 mL	Zn, Cd

Table 5.1 Comparison of ASV techniques for measuring Pb. Adapted from [113].

The row titled “Pb concentration range” demonstrates that all of the devices displayed in Table 5.1 currently meet the requirement to detect a Pb^{2+} concentration of 48 nM in water, the limit recommended by WHO as the maximum concentration for safe drinking water [113].

However, lower maximum permissible concentrations of Pb^{2+} are decreasing for other localised organisations. One such example is by the America Academy of Paediatrics who recommend a maximum concentration of only 4.8 nM in school drinking water [113]. This, combined with the knowledge [110] that there is no known safe BLL sets the scene for the importance of the work presented here. It is essential that new devices with improved sensitivities continue to be developed alongside the continuous decrease in the acceptable maximum levels. GFET technologies also offer the added benefit that their miniaturisation and scalability can act to reduce costs associated with measuring Pb^{2+} in water which can cost anywhere between $15-$100 in the laboratory (significantly less for portable devices). They can also simplify the process, removing the need to deal with hazardous waste disposal which is a current issue with some ASV techniques [113].

5.3.2 Graphene-based Techniques

In recent years exciting developments in the conductometric sensors have begun to take place. These sensors offer several advantages over the traditional “bulky” techniques such as simplified equipment, device miniaturisation facilitating portability and field suitable measurements which act to control drinking water quality [106]. In particular, the chemical detection of heavy metals by GFETs offers ultrasensitive, label-free and rapid detection which is made possible by the high surface area to volume ratios and charge carrier mobilities that originate from graphene’s exceptional electronic properties [114]. Surface modification is required in order to ensure specific target detection and is introduced next.

5.3.3 Functional DNA as Bioreceptors

5.3.3.1 Thrombin Binding Aptamer

One of the most popular bioreceptors for the detection of lead ions in graphene-based conductometric techniques is the Thrombin Binding Aptamer (TBA) [115, 116]. The TBA (5’ GGTTGG TGT GGTTGG 3’) is a 15 base, single stranded, DNA oligonucleotide. One possible secondary structure that TBA forms as a bioreceptor immobilized on the surface of graphene is illustrated in Figure 5.1A and is predicted using the Mfold server [117]. TBA is rich in the guanine nucleotide base and therefore is susceptible into folding into G-quartet/G-quadruplex structures (Figure 5.1B). These structures are formed when a quartet of guanine nucleotide bases are assembled into a planar structure bonded together by specialist Hoogsteen hydrogen bonds [118] as depicted by the dashed lines in Figure 5.1C. Cations stabilise these structures when they position themselves within the plane or between planes of the G-quartets (Figure 5.1B). It is conjectured that a contributing factor of lead’s toxicity and therefore damage to humans is caused by this stabilising influence it has on genetic material [119].

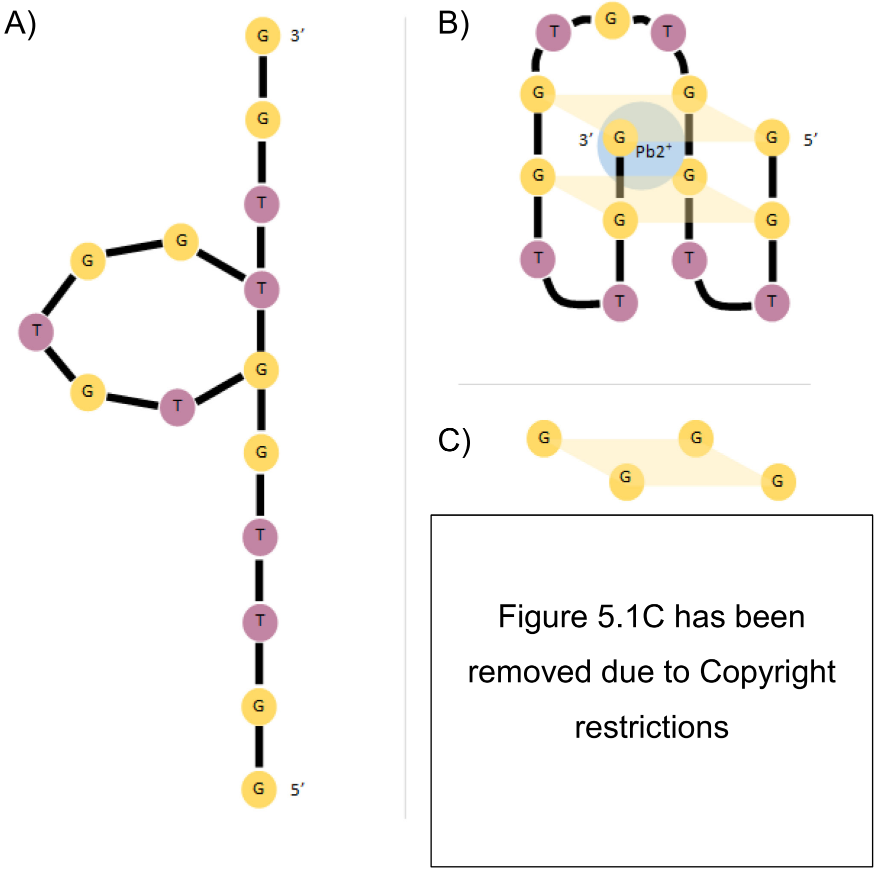

Figure 5.1C has been removed due to Copyright restrictions

Figure 5.1 A) Secondary structure prediction for TBA aptamers (predicted by Mfold server [117]). B) Schematic representation of a G-quadraplex structures formed during cation stabilisation (adapted from [119]. C) G-quartet structure from guanine bases bound together by Hoogsteen hydrogen bonds (molecule schematic from [118]).

5.3.3.2 Liu's group used this aptamer for the targeted detection of Pb^{2+} in their sensing regime, which harnessed the phenomenon of fluorescence resonance energy transfer (FRET) in order to transduce binding. In this study, TBA was modified so that there was the fluorescent group carboxyfluorescein (FAM) at the 5' end and the fluorescent quencher 4-([4-(dimethylamino)phenyl]azo)benzoic acid (DAB-CYL) at its 3' end. In solution, when the modified TBA was brought into close proximity with the Pb^{2+} ions, the TBA formed G-quartet structures which had the effect of reducing the distance between FAM and DAB-CYL thus causing the fluorescent signal to reduce. 8-17 DNAzyme

An alternative form of functional DNA are DNAzymes. These are strands of DNA that act as enzymes to catalyse molecular interactions [120]. The first demonstration of DNAzymes as bioreceptors for chemical targets was in fact the development of a highly sensitive colorimetric lead biosensor by Liu and Lu by using the 8-17 DNAzyme [120, 121]. This complex consists of two stands, the 17E enzyme strand and the 17DS substrate strand. The 17DS substrate strand consists of a scissile ribonucleic acid adenosine group (rA). This strand hybridized freely with other 12-mer DNA chains which were conjugated with Au-NPs attached to the 5’ ends. These DNA chains strongly encouraged the aggregation of the Au-NPs which resulted in a blue colour for their sample solution. In the presence of their target Pb^{2+} ions their chosen 17E strand, which has shown both high selectivity and activity towards Pb^{2+}, cleaved off the 17DS substrate at the position of the rA. This cleaving action prevented the Au-NPs from aggregating together, which resulted in a red colour for their solution [121].

Figure 5.2 has been removed due to Copyright restrictions

Figure 5.2 A) Secondary structure of 8-17 DNAzyme with black arrow showing site of cleaving. B) Pb^{2+} induced cleavage of 17DS substrate strand. C) Au Nanoparticles / DNAzyme assemblies showing different colours produced when aggregated/separated due to the absence/presence of the Pb^{2+} ion [121].

5.3.4 GFET Devices

A summary of different types of Pb^{2+} sensors is provided in Table 5.2 with a more verbose description on each provided throughout section 5.3.

TECHNIQUE	LOD	RANGE	SPECIFICITY	REFERENCE
Fluorescence Resonance Energy Transfer using TBA as bioreceptor	300 pM (water)	0.5-30 nM	100 µM: Li+ and Na+, 10 µM K+, Mg2+, and Ca2+, 100 nM Cu2+, Co2+, Ni2+, Zn2+, Cd2+, Cr3+, Al3+, Fe3+, and Au3+ Masking agent NaCN and additional DNA probes used to improve selectivity against disruptors in 100 nM category	[115]
Liquid gated GFET using TBA as bioreceptor	790 pM (water)	Non-linear: 0-2.4 µM	Mixed disruptors: Ag+, Al3+, As5+, Cu2+, Hg2+ and K+ do not significantly deviate the responses. Tests with tap/drinking water showed reliable results.	[122]
Back gated GFET using TBA as bioreceptor	2 µM	Non-linear: 10 µM – 10mM	Not detailed	[116]
Back gated GFET using TBA-AuNPs as bioreceptors	20 nM (water)	Not detailed	Not detailed	[123]
Liquid gated GFET using 8-17 DNAzyme	181 pM (blood)	~50 pM – 50 nM	Selectivity shown against 0.1 M/L for Na+, K+ and Ca2+ ions	[124]

Table 5.2 Comparison of Pb^{2+} detection techniques

Electrical sensing using a guanine rich DNA bioreceptor (similar to TBA) and graphene channels in a liquid gated FET structure was demonstrated by Li's group. With an isoelectric point close to pH 5, the charge of DNA within solutions of greater pH is regarded as negative. When these aptamers were deposited on the surface of graphene the distribution of this negative charge along the DNA backbone impacts the doping of the channel. The Pb^{2+} ions in solution bind with a high affinity to the guanine bases of the TBA strands forming G-quadruplex structures. In doing so, the DNA strands undergo conformational changes, resulting in the folding of these strands that subsequently act to bring the DNA receptors closer to the graphene surface and within the Debye length, hence increasing the hole density via electrostatic interactions, subsequently acting to pdope the channel (Figure 5.3). It is noted here that as the conformational change of the TBA brings the aptamers closer, so too are Pb^{2+} cations which would act to neutralise this effect [122]. However, the effect of DNA on the surface can show the opposite effect, as demonstrated by Manoharan et al who observed N-type doping of the graphene channel after aptamer immobilisation, which they attributed to the electron transfer to the graphene [125]. A more detailed discussion into the sensing mechanisms of GFETs is provided in 4.3.3.

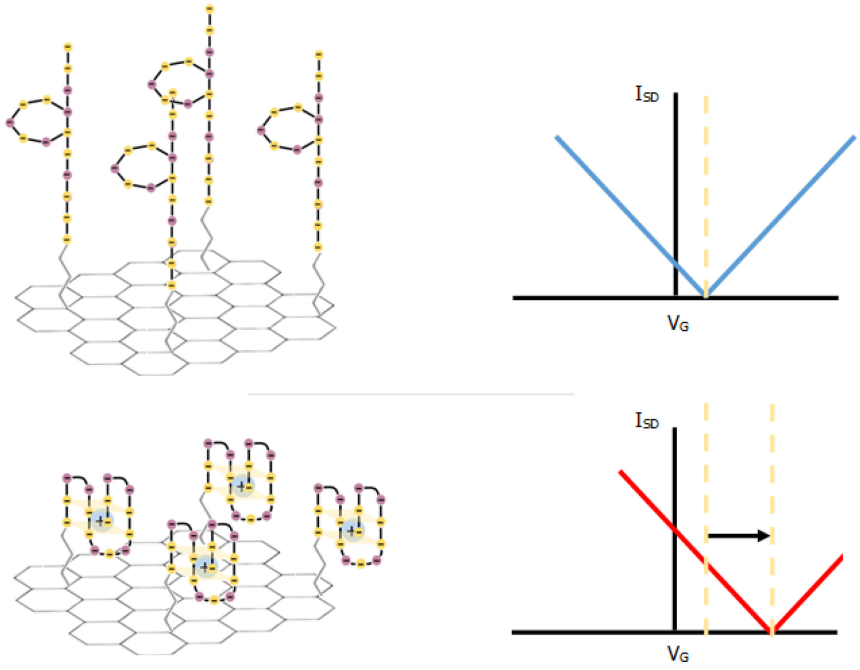

Figure 5.3 Schematic representation of impact of Pb^{2+}. Top-panel: Negatively charged DNA aptamers vertically immobilised to the graphene sheet which introduce p-type doping to the channel. Bottom-panel: After binding with Pb^{2+}, G-quadraplex structures are formed which increases density of negative charge closer to the graphene surface, hence increasing the effect of p-doping in the channel.

In a study led by Xu, back-gated GFET biosensors functionalised with TBA were used for the selective detection of lead ions down to 2 µM. The aptamers deployed as bioreceptors in this work had two modifications at opposing ends. At the 5’ end, a pyrene group was added so that the aptamer could be easily bound to the graphene surface (see section 4.4.2.2). At the 3’ end, the electron donor molecule methylene blue was added. Xu took advantage of TBA’s characteristic of forming stable G-quadraplex structures during binding with the target Pb^{2+} ions. After conformational change, the electron tunnelling distance is low enough to allow the methylene blue molecule to transfer electrons to the graphene surface. With their devices working in the p-type conduction, with majority hole carriers, additional electron transfer from this process reduces the carrier concentration thus reducing the current in the sensor. This alteration in the behaviour of the graphene device indicated successful target detection. During target binding this group also observed a left shifting in the Dirac point. They conjectured that this was caused by electron accumulation as a result of the high resistance between the contact-graphene interface which acted to n-dope the graphene channel [116].

Chee et al, harnessed guanine-rich DNA attached to graphene via Au-NPs to functionalise GFET biosensors for the detection of Pb^{2+} [123]. They observed n-doping caused by the DNA immobilisation, inferred by the left shifting of the Dirac point. After binding events between their aptamers and the Pb^{2+} ions caused G-quadraplex structures to form, they noticed a right shifting in the Dirac point caused by a p-doping effect. This group also confirmed the action of the immobilised bioreceptors by comparing the measurements of Pb^{2+} when DNA was present and absent on their devices. Their GFET biosensors had a Pb^{2+} LOD of 20 nM, which is below the ~50 nM allowable lead limit for drinking water specified by WHO [123].

A label-free, portable GFET biosensor was demonstrated by Wang et al for the detection of Pb^{2+} in blood. In this work, the group modified the structure of the 17DS substrate strand of the 8-17 DNAzyme complex. They swapped out the rA compound for an uncleavable deoxyribonucleic base adenine. In doing so, the 17E enzyme remained intact and selective towards the Pb^{2+} ions with the potential advantage of increasing the response times in their devices. A pyrene group was added to the 17E strand in order to functionalise their devices in a non-covalent manner. The GFETs were then tested against real blood samples from children, with Pb^{2+} concentration levels of 82.4 (0.40 nM), 191.1 (0.92 nM) and 491.6 ng/L (2.37 nM). Although some pre-treatment was required, the measurements observed good agreement with those taken from the ICP-MS equipment which suggested that this approach is a strong candidate for accurate BLL measurements in the future [124].

5.4 Summary

Lead is a heavy metal that is very damaging to humans, with even small BLLs associated with developmental issues. One of the many exposure routes for this metal is via polluted drinking water, and since the WHO have acknowledged that there is no known safe BLL, they advise stringent controls on the level of this toxicant from these sources. It is the ambition of this contribution to build further knowledge in detecting this toxicant since Lead poisoning has been shown to impact countries of all economic stages. This work is therefore widely applicable and urgently needed in order that this phenomenon can be addressed.

Most of the current gold-stand methods for detecting this toxicant require expensive equipment, located in centralised laboratories with highly trained personnel conducting measurements. This project focusses on the development of GFET devices which are an outstanding candidate for the next generation of sensitive, low-cost and portable, POC lead sensors. It is the ambition that this work will expedite the development of this technology, in turn facilitating the distributed mass monitoring of drinking water sources and infrastructure which will limit exposure routes for the entire biosphere.

This project exploits the Thrombin Binding Aptamer as a suitable bioreceptor to immobilise to the graphene surface since it has been shown to be highly selective to the Pb^{2+} ion amongst other interfering agents. The mechanism for detection between this bioreceptor and Pb^{2+} ions is also appropriate for GFET devices which are explored throughout this contribution. Due to its high number of the Guanine nucleotide bases, this single stranded DNA aptamer folds into G-quadraplex structures during binding events with Pb^{2+} ions. Devices presented herein harness this conformational change, which causes an alteration in the electronic configuration in the graphene channel, to transduce binding events.

Chapter 6 – Research Methodology

A description of the techniques and equipment used throughout this contribution is detailed in this chapter. Section 6.1 discusses the method of transferring monolayer graphene from a Cu substrate onto a Si stack. Section 6.2 describes the two phase manufacturing process of fabricating GFETs from monolayer graphene on Si stacks. The various material characterisation techniques are detailed in section 6.3 before the specific methods of conducting electrical characterisation of the finished GFET devices are provided in section 6.4. Finally, the discussion in section 6.5 summarises the preparation and handling of the reagents used throughout this work.

6.1 Graphene Transfer

6.1.1 Polymer Assisted

Graphene on Cu is purchased in square sheets from Graphenea. In order to transfer the graphene onto a substrate of choice the following procedure is followed as outlined in Figure 6.1. The as-received PMMA powder is diluted in chlorobenzene (C_6H_5Cl) to a concentration of 50 mg/mL and mixed for a total of 19 h. Then PMMA is spin coated onto the graphene-metal stack at 3000 rpm for 30 s to ensure uniform deposition. The PMMA is then annealed at 180 ºC for 5 min. The etching process begins when the PMMA-graphene-copper stack is floated on nitric acid (HNO_3) for 3 min. The films are then transferred to DI water for 3 min to remove any residual nitric acid. Next, the stack is floated on ammonium persulfate ($(NH_4)_2S_2O_8$) for 8 h.

Concurrently with the process above the substrate is cleaned with the following process. Firstly, the SiO_2 is sonicated with acetone for 20 min before being immersed in boiling isopropyl alcohol (IPA) (C_3H_8O) for 30 min. Then, the substrate is cleaned with IPA and dried off using a N_2 gun.

After the copper has been etched away, the PMMA-graphene stack is scooped onto the clean substrate and immersed in DIW for 10 min to ensure that the residuals of ammonium persulfate are removed. The PMMA-graphene-SiO_2 substrate is then dried off using a N_2 gun, placed in a vacuum chamber for 5 h and then baked on a hotplate at 180 ºC for 30 min whilst under the UV lamp at 254 nm. The PMMA layer is removed from the surface of the graphene-SiO_2 bilayer by immersion in acetone for 30 min at 60 ºC before two cycles of immersion in IPA and DIW for 3 min.

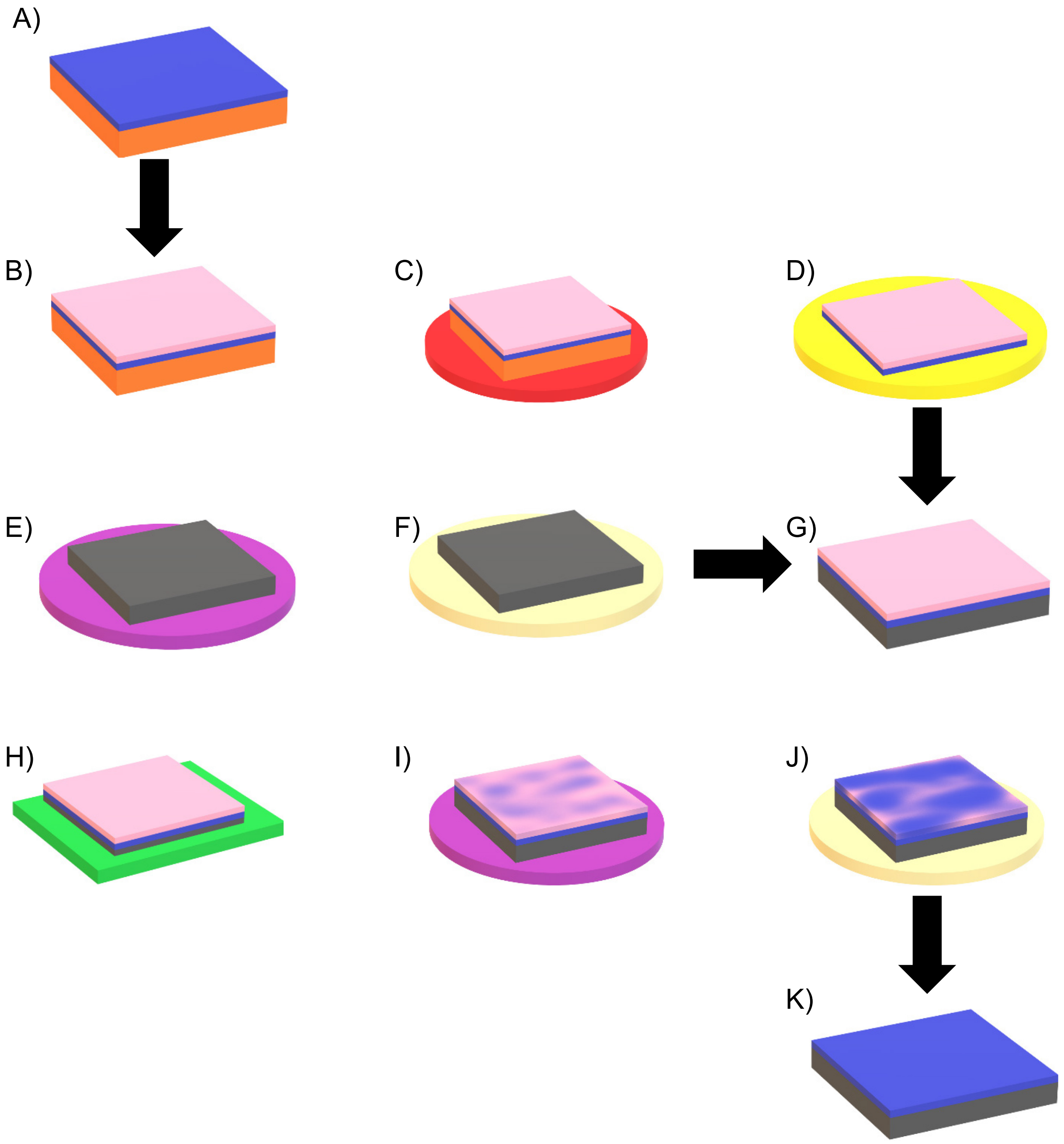

Figure 6.1 The graphene transfer process with salient points illustrated. A) Graphene arrives on the surface of copper, B) PMMA layer is deposited on surface and annealed at 180 ºC, C) Stack is floated on nitric acid for 3 min, D) After rinsing with DIW, stack is floated on ammonium persulfate for 8 h until copper is fully etched, E) Substrate is sonicated in acetone for 120 min, F) Substrate is cleaned in IPA for 30 min, G) PMMA-Graphene stack is scooped onto substrate, H) Stack is heated and exposed to UV radiation, I) Stack is submerged in acetone for 30 min, J) Stack is cycled between IPA and DIW K) The PMMA is removed leaving the graphene-substrate stack

6.2 Graphene Transistor Fabrication Techniques

6.2.1 Graphene Samples

The samples of CVD graphene were purchased from Graphenea. Monolayer CVD graphene from Graphenea is provided deposited on top of 300 nm thermally grown SiO_2 layer serving as the gate dielectric, on top of a P-type doped Si substrate. This arrives as 4" wafers. The first step is to cleave this wafer into smaller substrates of roughly 1.5 cm x 1.5 cm square (referred to as *chips* hereafter) which are of a comparable size to the photomasks used in the photolithography steps.

There are two phases to complete to fabricate GFETs from the monolayer graphene chips. The first is channel shaping, whereby individual rectangular graphene channels of 720 µm by 80 µm are shaped onto each chip in a grid shape. The second phase is the gold (Au) electrode deposition which constructs the Hall Bar configuration for the devices. At the end of the second phase, each of the graphene channels have between 7-8 Au electrodes (dependant on design) allowing for electrical characterisation.

6.2.2 Phase I - Graphene Channel Shaping

6.2.2.1 Spin Coating

The graphene/SiO_2 chips were initially spin-coated with lift-off resist 3B (LOR) (Micro Chem) at 3000 rpm for 30 s. Uniform chemical deposition is conducted by spin coating. During this process, chemicals are drop-casted onto the centre of the wafer to be patterned. The rotation of the substrate ensures that the chemical is spread out in a consistent manner. The thickness of the deposition is controlled by changing the rotation speed [126].

The wafer was then baked in an oven at 175 ºC for 15 min. The next step involved spin-coating S1805 G2 positive photoresist (PR) (Microposit) at 3000 rpm for 30 s before soft-baking on a hotplate at 100 ºC for 1 min. Before the wafer is patterned with a mask it undergoes a pre-exposure bake, otherwise called a soft-bake. The purpose of this step is to solidify the PR by removing the solvents within [126].

6.2.2.2 Photolithography

During the proceeding photolithographic patterning stage, the shield mask used for shaping the graphene channels consists of a grid of rectangular shapes which act to block the chips' exposure to the incident UV light. Optical lithography (photolithography) is the name given to the process of projecting 2D patterns of light onto a substrate in order to build up 3D structures on thin film surfaces [126]. An overview of the entire process is given in Figure 6.2.

This technique relies on printing an image through a mask onto an energy sensitive material, that when developed leaves either an engraving or raised platform in the shape of the image into the material. This is conducted precisely using the OAI Model J500/VIS Mask Aligner (Figure 6.3).

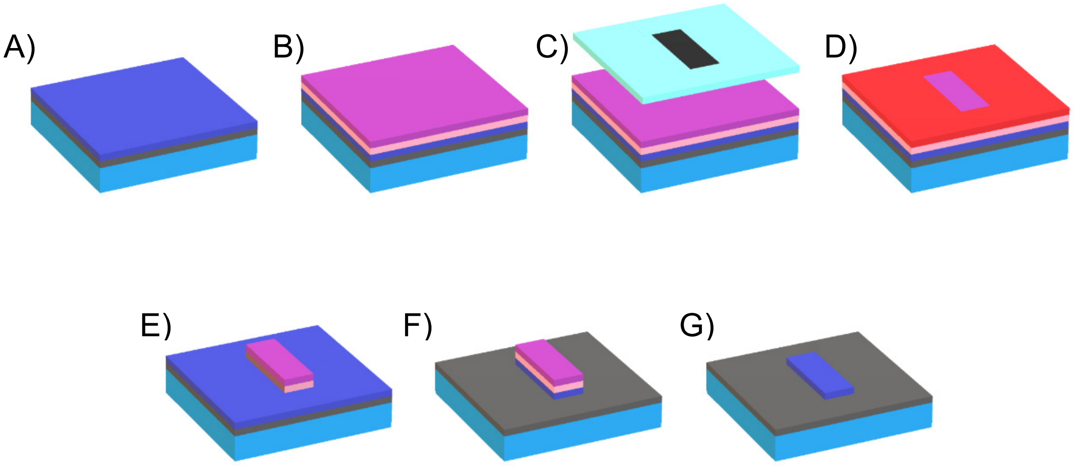

Figure 6.2. Shaping graphene channels overview A) Si (P^{++}), SiO_2, Graphene stack, B) LOR and PR deposited on surface, C) Shield mask used to prevent UV ray transmission, D) Exposed PR and LOR are denatured by exposure of UV, E) Stack is developed which removes denatured PR and LOR, F) Plasma etching removes all graphene that is not protected by a PR and LOR stack, G) PR and LOR stack is removed from graphene channels by use of remover leaving shaped graphene channels.

Subsequent etching or deposition of these layers results in 3D structures forming on the surface [126]. The UV exposure time was set to be 25 s. The PR development stage was achieved by using a solution of 20 ml of 351 Developer (Microposit) and 30 ml of DIW and immersing the chips in this solution for between 10-20 s before rinsing with DIW and drying with a N_2 gun. Exposure to UV light denatures positive PR which is subsequently dissolved during the developer stage, exposing the unwanted graphene-SiO_2 areas of the wafer to the Ar etching completed in the following step.

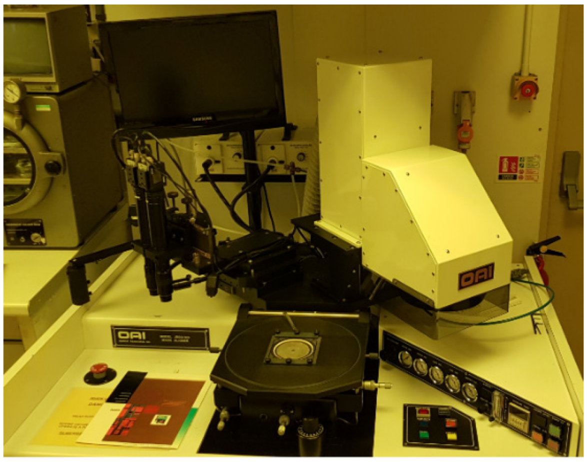

Figure 6.3. OAI Model J500/VIS Mask Aligner

Prior to Ar etching, the wafer was soft-baked on a hotplate at 180 ºC for 8 min under UV exposure of 254 nm wavelength in order to not only harden the remaining PR covering the desired graphene channels but also remove additional chemical residues on the chip surface, following the procedure detailed here [8].

6.2.2.3 Plasma Etching

Plasma etching is conducted within a Sputtering Machine (Nordiko) at a power of 50 W, vacuum level of 10^{-6} torr for a total of 2.5 min. Plasma etching, also referred to as sputter etching relies on the bombardment of Ar ions to remove surface atoms. In this process, which follows the same principles as sputtering and is explained in more details in 6.2.3.3, the sample to be etched is positioned at the cathode which accelerates free electrons throughout the evacuated chamber. When Ar is introduced, Ar^+ ions are formed, by collisions between Ar and the free electrons, these ions will accelerate towards the cathode and consequently bombard and therefore etch the exposed surfaces of the substrate. Plasma etching has the effect of removing all of the exposed graphene from the wafer. Only the protected graphene channels underneath the stack of PR and LOR that were not exposed to UV remain intact [127, 128].

6.2.2.4 Remover

Three heat shrinks between the back of the chips and the substrate holder were used along with the LOR in the first step to ensure that it was possible to remove all residue of PR after the plasma etching. This is performed by immersing the chips in 1165 Remover (Microposit) heated to 60 ºC for 1 h followed by room temperature for 12-14 h. The remover dissolves both the LOR and the unexposed PR which cover the graphene channels. The remover is washed away in DIW and the chips are then dried using an N_2

gun and stored in a vacuum chamber at 25-30 mmHg (33 mbar) for 1 hour [8]. At the end of this phase of the fabrication process the chips consists of a grid of rectangular graphene channels.

6.2.3 Phase II – Electrode Deposition

6.2.3.1 Initial stages

An overview of phase II is given in Figure 6.4. In order to deposit contacts over the graphene channels, the initial stages described in section 6.2.2.1 of spin-coating LOR and PR are repeated.

During this phase, the photolithographic stage deploys a window mask to shape the contacts which is designed to have a periodic grid of contact windows which are in the shape that complement the graphene channels. These windows on the mask will allow UV radiation to denature the photoresist only at these positions, UV radiation at all other points are blocked. When the chips are subsequently developed, the SiO_2 substrate (for contact pads) and parts of the graphene channels (for contact leads) will be exposed allowing Cr and Au to be evaporated and sputtered respectively. The soft-bake that follows the development stage is conducted in the oven at a temperature of 120 ºC for 15 min.

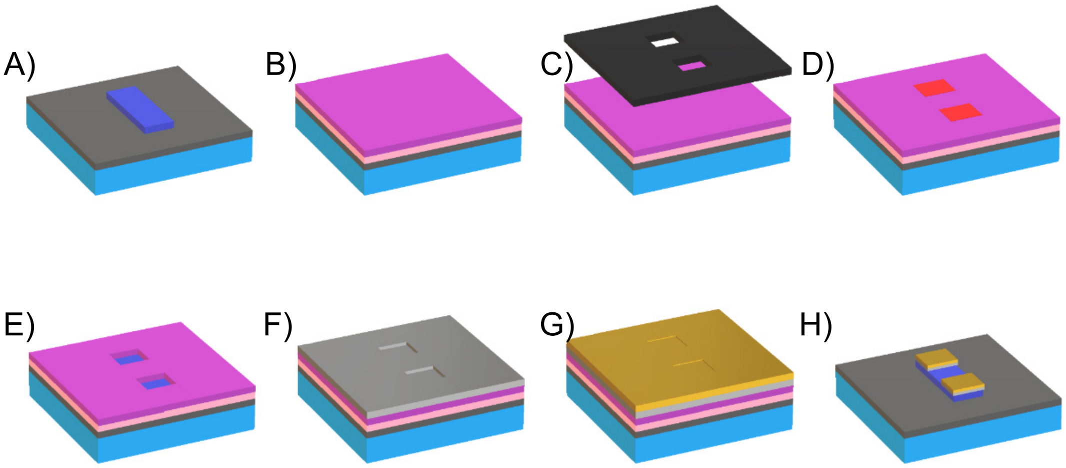

Figure 6.4. Electrode deposition overview A) Si (P^{++}), SiO_2, Graphene stack after channel shaping, B) LOR and PR deposited on surface, C) Window mask used to allow UV ray transmission, D) Exposed PR and LOR are denatured by exposure of UV, E) Stack is developed which removes denatured PR and LOR leaving windows onto graphene surface, F) Cr is evaporated onto the surface, G) Au is sputtered onto the surface, H) PR and LOR coating is removed from surface by use of remover

6.2.3.2 Evaporation

Vacuum deposition is commonly referred to as thermal evaporation and is an example of physical vapour deposition (PVD). An example schematic and system are presented in Figure 6.5. Thermal evaporation takes place in an evacuated chamber in order to reduce contamination from unwanted molecular adsorbents. The substrate is positioned upside-down relative to the evaporation source, so that deposition occurs on the desired surface. The evaporation material, is usually positioned within a tungsten (W), molybdenum (Mo) or tantalum (Ta) boat and undergoes resistive heating to temperatures between 1000-3000 K. The evaporated atoms transit from the boat to the surface of the substrate where they adsorb at a rate dependant on the evaporation source rate, geometry, position relative to the substrate and condensation coefficient of the substrate surface. The deposition rate at a source-substrate distance of 20 cm, with vapour pressure of 10^{-2} Torr can be between 100-1000 nm/min [128].

It is necessary to deposit an adhesive layer prior to sputtering Au because noble metals like Au which are intrinsically unreactive do not adhere well to the SiO_2 substrate causing delamination and subsequent deterioration of device performance [129].

Figure 6.5A has been removed due to Copyright restrictions

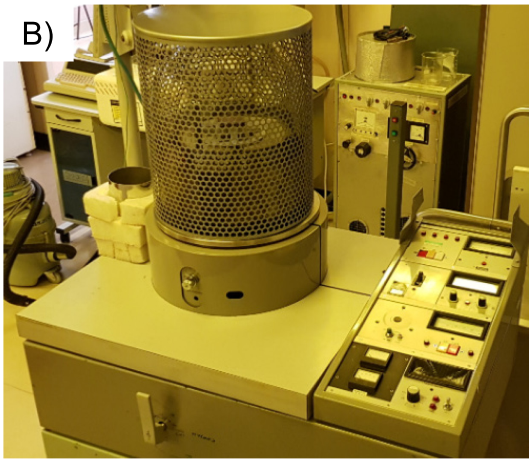

Figure 6.5. A) Thermal Evaporator Schematic [128] B) Edwards Thermal Evaporator System

Therefore, titanium (Ti) and Cr are often used as thin adhesion layers (of the thickness in the order of nm) as they are more chemically active and therefore bind to the substrate. Todeschini found that Cr-Au layers showed enhanced adhesion over Ti-Au layers. The group's measurements linked the high tendency of Cr to form oxides with strong Cr-O bonds created due to the oxygen and water molecules present on the SiO_2 substrate and chamber. In addition, they showed high diffusivity of Cr into the Au overlayer which they speculated was a reason for a higher number of Cr-Au bonds improving adhesion [129].

Thermal evaporation of Cr was performed using a thermal evaporator (Edwards) at a current of 21 mA at a vacuum level of 10^{-6} Torr for a total of 8 s. Following the procedure that Haslam et al used, a layer of ~5 nm was deposited onto the graphene and SiO_2 surfaces [4].

6.2.3.3 Sputtering

Sputtering is another PVD technique used to deposit material onto thin films. An example schematic and system are presented in Figure 6.6. Due to its high throughput and diverse options for material choices, sputtering has been a favoured deposition technique for the semiconductor industry [130]. In this process, energetic ions bombard the atoms on the surface of the target material which are back scattered towards the substrate surface thus covering the exposed areas of the chip [131]. In practice the RF sputtering system consists of two planar electrodes of opposite polarity, with the target material positioned at the cathode and substrate where deposition is wanted positioned at the anode. Free electrons are accelerated from the cathode towards the anode due to the applied electric field between the two. Once the evacuated chamber is flooded with a process gas such as Ar, the free electrons will strip Ar atoms of their electrons forming positively charged Ar^+ ions and a soup of electrons in the plasma. The positively charged Ar^+ ions are then accelerated towards the negative cathode where they sputter the target material which is then collected at the substrate. The species of gas used for the sputtering process (O_2, N_2 and Ar for example) are optimised for specific applications and target materials [131].

Figure 6.6A has been removed due to Copyright restrictions

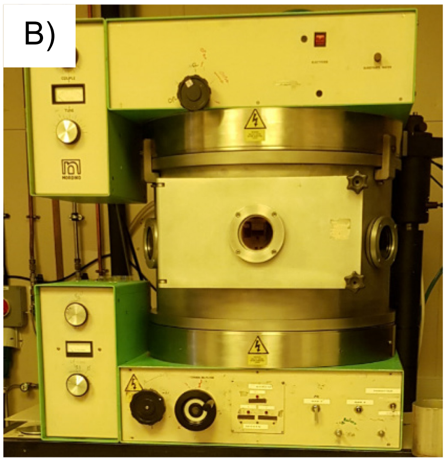

Figure 6.6. A) RF Sputtering Schematic [128], B) Nordiko Limited 6” Sputtering Machine

One drawback of this technique is the high energy particles involved in the process often introduce defects and disorder into the graphene substrate. The consequence of this translates into high contact resistance between the deposited Au and graphene substrate in fabricated devices. Li et al have developed an approach to limit these issues by using a novel shielding technique which has the additional benefit of improving the yield from standard sputtering processes [130]. Li et al used a cylindrical tube with its central axis positioned perpendicular to the PR patterned surface to prevent sputtered Au atoms which travelled off the desired perpendicular trajectory from depositing on the side walls of the LOR and PR as shown in Figure 6.7A-B.

The additional Au deposition to the desired contact patterns that was being caused by these wayward atoms was causing ribbons to be suspended at the contact edges which resulted in varying contact resistance (Figure 6.7C). The aluminium shielding used in the study limited the Au deposition to atoms which were moving along the tube’s axis thus reducing the deposition on the sides of the LOR and PR. The subsequent etching steps resulted in less undercutting of the Au material, thus resulting in sharper patterns for the electrical contacts (Figure 6.7D). A direct result of the sharper patterns was an increase in device yield for each fabrication course for the group as the occurrence of accidental shorting Au bridges across contacts was significantly reduced [130]. An increase in the D peak for the Raman spectra for graphene of the protected graphene layer after these optimised conditions confirms that this method still introduced defects into the lattice [130]. This shielding scheme was used for all chips during this stage of the fabrication process.

Figure 6.7 has been removed due to Copyright restrictions

Figure 6.7. Schematic showing sputtering mechanism A) Before and B) After the use of cylindrical tube to select subset of sputtered Au atoms. Electrode patterns obtained C) Before and D) After sputtering using the cylindrical tube [130].

Sputtering of Au was performed using a Sputtering Machine (Nordiko) at a power of 50 W at a vacuum level of 10^{-6} Torr for a total of 30 min. Following the procedure that Haslam et al used, a layer ~ 30 nm was deposited onto the Cr contacts to form the electrodes [4].

After sputtering was completed, a removal stage as described in 6.2.2.4 was conducted which had the effect of lifting off the LOR and PR areas that were shielded by the window mask during the UV exposure.

6.2.4 Fabricated Transistors

6.2.4.1 Design and Layout

The photomasks used throughout phases I and II are designed to fabricate a total of 25 GFETs for each chip, ordered into five columns A-E of five rows 1-5 (Figure 6.8A and B). It is important to note that up to four chips can be fabricated per phase, limited to the size of the substrate holder for the 6” sputtering machine. The first two columns; A and B consist of two-electrode devices with only source and drain electrodes deposited at the extreme ends of the graphene channel (Figure 6.8C). Column C, consists of asymmetric seven-electrode Hall-bar devices, allowing four independent graphene channels to be measured in the four probe setup with the electrode leads deposited over the full width of the graphene channel (Figure 6.8D). Columns E and D consist of symmetrical eight-electrode Hall-bar devices, which allow the measurement of two independent graphene channels to be measured in the four probe setup. For these devices the leads for each sensing electrode do not fully cross the graphene channel (Figure 6.8E).

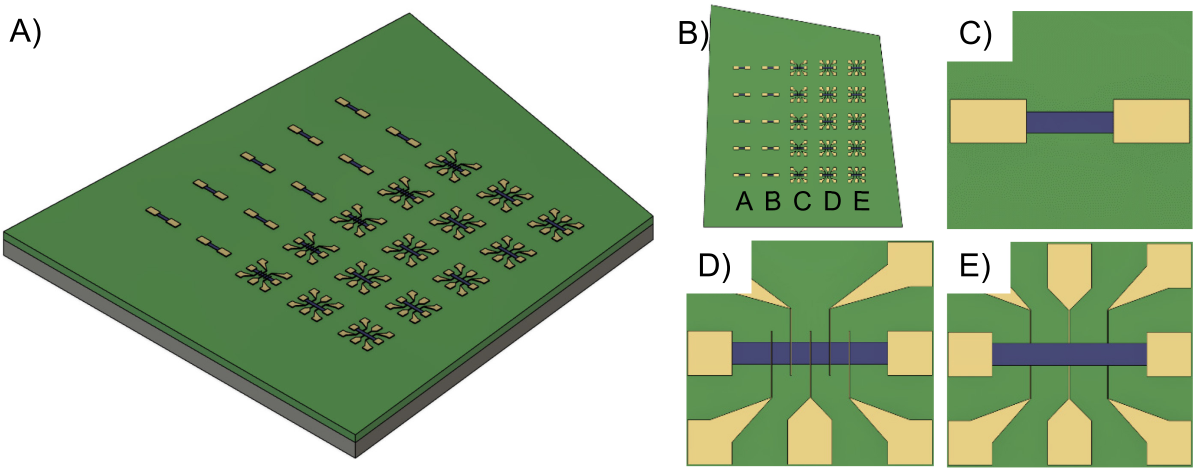

Figure 6.8. A) 3D model of fabricated chip consisting of 25 GFETs, B) Top down view of schematic, C) Two electrode device, D) Asymmetric seven electrode device and E) Symmetric eight electrode

6.3 Material Characterisation Techniques

6.3.1 Optical Microscopy

6.3.1.1 Background

Optical microscopy can be exploited to quantify the thickness of the SiO_2 layer on the surface of a Si substrate. This can be determined by evaluation of the colour alone and is caused by the interference of reflected rays between both the air-SiO_2 and SiO_2-Si interfaces. For a conventional light source, the difference in distance between these two interfaces alters the phase shift between these rays causing colour shifts [132]. It was Roddaro's group who contradicted the accepted view that graphene layers are visible on the SiO_2 layer due to an extension of the optical wavelength in line with aforementioned mechanism. This group suggested that the additional path length caused by these layers would only account for between one or two parts over 1000 for the average wavelength of conventional light which they conjectured would be too small for the human eye to differentiate. By studying the electrodynamics of the mechanism for visibility of graphene, Roddaro concluded that graphene layers instead modulate the transparency of the air-graphene and graphene-SiO_2 interfaces with the optical path length playing a much less significant role [132].

6.3.1.2 Olympus BH-2 Optical Microscope and Olympus BX60M Digital Optical Microscope

Observations made through an optical microscope offer rapid, effective and non-destructive characterisation of the material. The two microscopes used in this work were the Olympus BH-2 Optical Microscope and Olympus BX60M and are depicted in Figure 6.9A and B respectively. In order to visualise clearly using this technique graphene must be transferred onto a suitable material such as SiO_2 at 300 nm or 90 nm. Single and bilayer graphene along with features such as tears, ripples, folds and scratches can be easily distinguished using this technique.

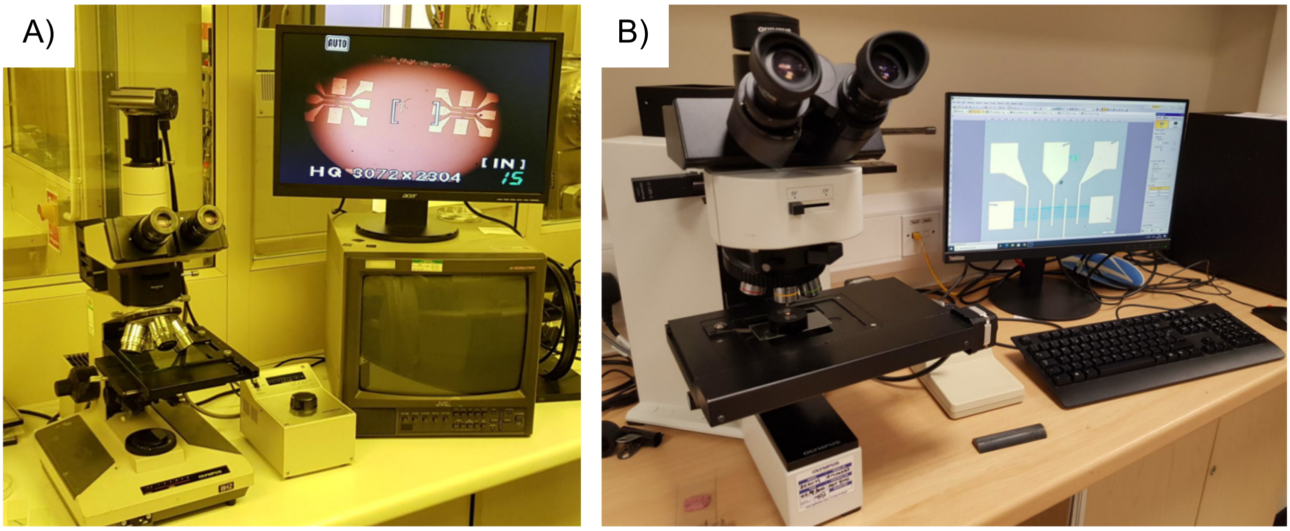

Figure 6.9 A) Olympus BH-2 Optical Microscope. B) Olympus BX60M Digital Optical Microscope with Stream Motion software used to interface with the system.

6.3.2 Raman Spectroscopy

6.3.2.1 Background

Raman spectroscopy is now the standard in providing a definitive, non-destructive and high throughput identification of graphene [133, 134]. It is the dispersion of the π-electrons that give graphene its resonant qualities making this technique so effective at highlighting its electronic properties [133]. Several fundamental characteristics of a material can be determined by using Raman spectroscopy including doping, defects, temperature, strain levels [135] and surface functionalisation [90]. Prior to the wide uptake of this technique atomic force microscopy (AFM) was used. AFM was limited due to its low throughput, and due to the fact that it was only practical to determine single or bi-layer graphene if there were wrinkles and/or folds in the samples [134].

The first stage of acquiring a Raman spectrum is illuminating the sample with laser light. This incident light excites electrons to a virtual energy state, on relaxation, the vast majority of photons are scattered elastically via Rayleigh scattering as the electron returns to its original state. However, a very small percentage of photons are scattered inelastically when the electron relaxes to an energy state lower (higher) than it started, this transfers energy away from (to) the material and is known as Anti-Stokes (Stokes) radiation. Considering a simplified energy band diagram as shown in Figure 6.10, the Rayleigh, Stokes and Anti-Stokes radiation are represented by the green, red and blue photons with the arrows corresponding to their energy transitions. A Raman spectrum plots the intensity against the wavenumber, which is calculated as the difference in the reciprocal values between the wavelengths of incident and scattered radiation and is called the Raman Shift in units of (cm^{-1}) [136, 137]. Since the majority of molecules are found in lower energy states, due to the Maxwell-Boltzmann distribution, the intensity of the Stokes lines are usually greater than the Anti-Stokes lines and are therefore usually used to construct the Raman spectra [138].

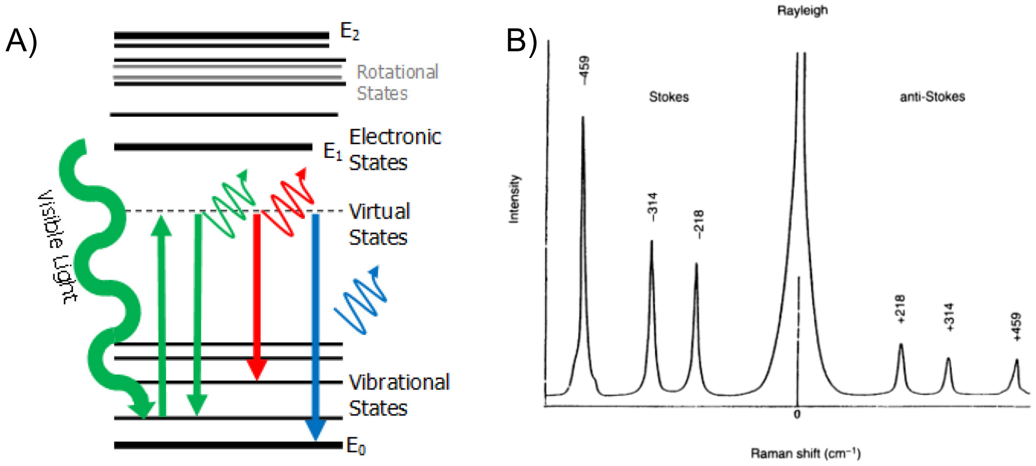

Figure 6.10. A) Schematic representation of Raman emission. Electrons are excited to virtual state and then decay into lower energy vibrational states. Energy transitions for Rayleigh (green), Stokes (red) and Anti-Stokes (blue) radiation are indicated by the coloured photons and arrows. B) Raman spectrum for CCl_4 showing relative intensity of Stokes, Rayleigh and Anti-Stokes radiation [138].

6.3.2.2 Raman Spectrum for Graphene

For graphene/carbon based samples laser light at 532 nm is preferred [139]. There are three main components of graphene's Raman spectrum as shown in Figure 6.11.

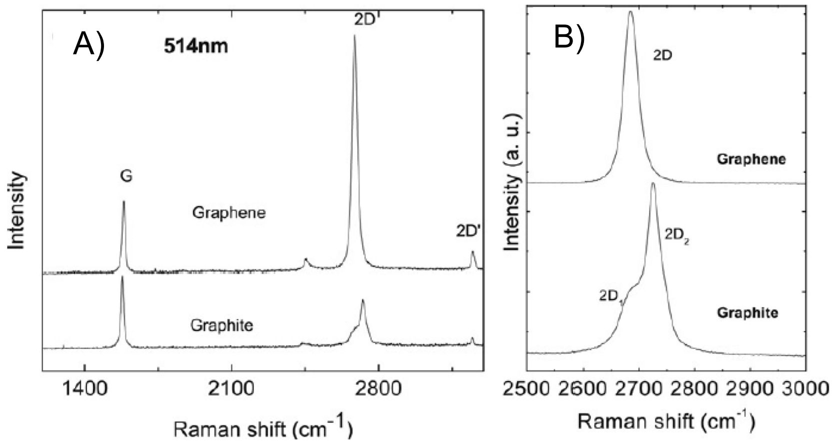

Figure 6.11. Raman spectra for Graphene and Graphite. A) Wide scan spectra. B) Detail focussing around 2D peak [133]

Firstly, the D mode peak, located at a Raman shift of ~1360 cm^{-1} which is caused by the breathing modes of the rings of the sp^2 atoms (Figure 6.12 A) [133]. This feature relies on defects in the graphene lattice and can be caused by sp^3 sites, vacancy sites and grain boundaries [140]. Defect-free graphene does not exhibit a D peak and hence one is not shown in Figure 6.11, however it is well documented that a D peak can be present in Raman spectra where the sample area is located near the graphene edge, which has the effect of acting like defects [140-142]. There is a positive correlation between the relative intensity of the D mode and the disorder displayed in the sample and therefore the intensity of the peak provides a useful metric to compare graphene samples with [135]. It is noted by Kumar's group that the absence of this peak can be down to instrument limitations which are unable to pick up lower density sites for this peak, thus caution must be applied when making claims about defect-free graphene when interpreting Raman spectra [143].

Figure 6.12 has been removed due to Copyright restrictions

Figure 6.12. Phonon vibrations responsible for A) the D and 2D and B) the G band in graphene's Raman spectrum (adapted) [140].

Secondly, the G mode peak is a feature of the Raman spectra of graphene located at a Raman shift of ~1580 cm^{-1} and arises from bond stretching of the rings and chains of all pairs of sp^2 atoms (Figure 6.12B) [133]. The doping level in the sample can be indicated by the position, denoted PP(G) and width (via full width at half maximum (FWHM) measurements), denoted FWHM(G) of this peak. FWHM(G) reaches a maximum and the wavenumber its minimum for electrically neutral graphene. As dopants, in the form of electrons and holes are injected, this line width decreases [135, 142, 144, 145] and the position of the G peak stiffens, that is it increases to higher wavenumbers [133, 135, 142, 144, 145] (Figure 6.13A and B). Contrary to the correlation suggested by Graf et al between the position of the G peak and the number of layers of the graphene sample [146] Casiraghi et al dismissed this claim by highlighting the large variation in these metrics across the sample being too high to confirm this [142].

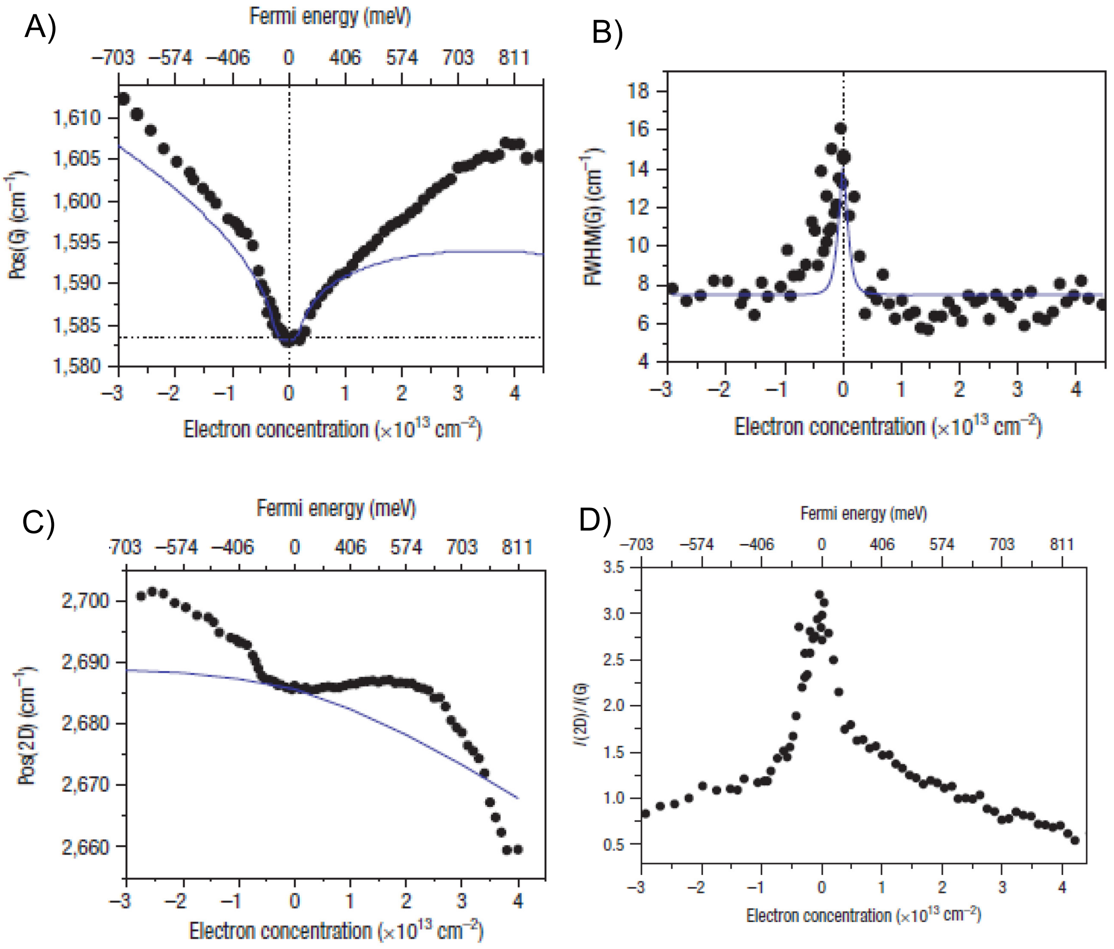

Figure 6.13. Relationship between electron doping level and A) Pos(G), B) FWHM(G), C) Pos(2D) and I(2D)/I(G) ratio (adapted) [145].

Finally the 2D overtone mode, located at a Raman shift of ~2700 cm^{-1} arises from second order of zone-boundary phonons [133, 134]. The position of the peak has been shown to increase (decrease) with hole (electron) doping as depicted in Figure 6.13C [135, 144]. This feature is frequently used to determine the number of graphene layers in the sample, with monolayer graphene showing a (single) narrow peak at a low frequency, which both broadens (larger FWHM) and up-shifts in wavenumber as the number of graphene layers increases [134, 135, 146]. Graf et al also showed this shift but commented additionally on the 2D peak having a similar integrated intensity across graphene samples with different layer numbers [146].

Measuring the relationship between the various features in the Raman spectrum can provide additional metrics to detail the information relating to the graphene sample. The ratio between integrated intensities of the G and 2D modes, denoted by I(G) and I(2D) respectively, was originally conjectured by Graf et al to correlate linearly with the number of graphene layers (up to four layers) [146]. This claim has also been disputed by Casiraghi's group along with Das et al who suggest that the ratio between the 2D and G peak intensities actually describes the dependence on electron concentration and therefore is a suitable metric to describe the doping level in the graphene [142, 145]. By comparing the Raman response of the graphene channel against back and top-gated measurements in a GFET structure (Figure 6.13D), Das et al showed that a large I(2D)/I(G) ratio of ~3.0 corresponded to neutral graphene (with low doping) in contrast to high electron and hole doping which was observed to decrease this ratio to ~0.5 [145]. In a supporting study conducted by Berciaud et al which investigated the properties of free standing graphene, it was shown that the ratio of the intensities for the 2D and G mode was lower in doped regions [135]. Furthermore the I(D)/I(G) ratio can also be used to estimate the level of covalent bonding in the graphene sample. Since I(D) and I(G) relate directly to the number of sp^3 and sp^2 hybridized C atoms [84].

6.3.2.3 Horiba XPLORA Raman System

Zero sample preparation is required for Raman measurements facilitating it as a high-throughput spectroscopy tool. Once the system has been calibrated against a Si reference, the sample is loaded onto the stage, positioned under the objective lens (x10 or x100) using the joystick which interfaces with the piezoelectric stage before being focussed (Figure 6.14A). The light source controls the illumination for optical images. The gate on the central column switches access between laser and illumination light sources when in modes “1” and “2” respectively. The computer interfaces with the CCD of the Raman system using the Labspec 6 software (Figure 6.14B). All Raman measurements were conducted in ambient conditions and with a Laser power of ~4 mW to avoid any heating effects or damage to the samples as per [134].

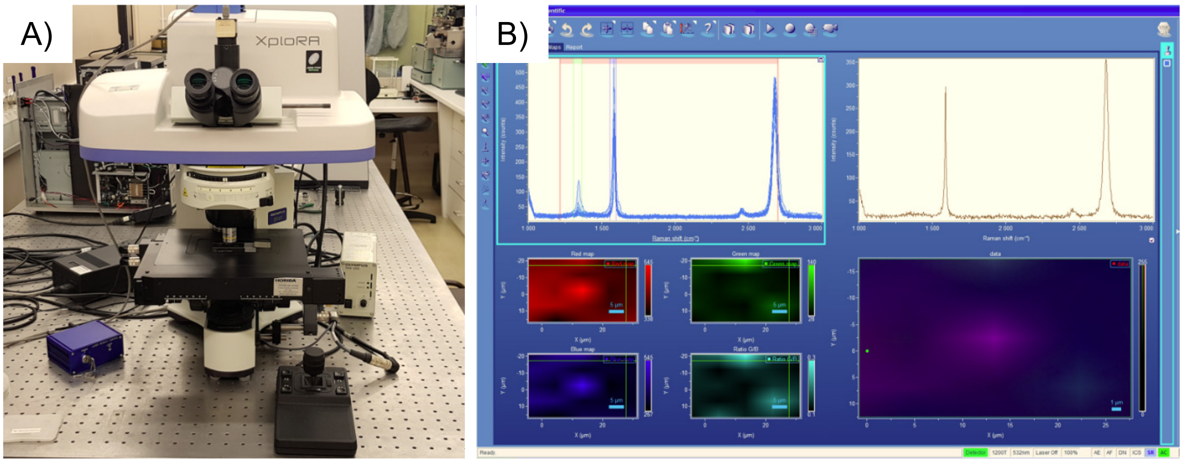

Figure 6.14. A) Horiba XPLORA Raman system, B) Labspec 6 software used to interface with system showing Raman map

6.3.2.4 Raman Mapping

This technique couples chemical and spatial information as the laser scans across the sample surface collecting spectra at discrete spots [136]. Using maps is a convenient way to acquire multiple spectra in a local area which can then be used to determine representative characteristics of the sample. An example of a Raman map is shown in Figure 6.14B.

Raman classification builds on the generic mapping technique and is utilised when there are features within the local area that require further investigation. It allows the user to enter pre-labelled spectra and using classical least squares (CLS) fitting it is able to classify the contributions from these spectra across the map. This presents the user with a clear summary of the distribution of these features. These maps can be used to differentiate between regions of monolayer, multilayer and disordered graphene along with chemical residues and patches that might be present in the sample.

6.3.3 Optical Labelling

6.3.3.1 Background

This technique describes the use of attaching optically responsive labels, tags or probes to samples in order to assist in their visualisation. The optical tags are usually interrogated by the use of a laser at a specific wavelength which induces an optical response in the label which can then be measured, highlighting the specific points where the labels have bound. Several optical labels can be used including fluorescent groups conjugated to antibodies [147], DNA [9], nanoparticles [100] and quantum dots [116].

6.3.3.2 Labelling with Antibodies

The discrete emission of light upon laser excitation is exploited by fluorescent labels to produce highly sensitive responses. In this process, labels absorb photons of light at one wavelength, exciting them into higher energy states; some of this energy is transferred to neighbouring molecules before the system relaxes to its original energy state thus emitting photons of lower energy and correspondingly longer wavelengths. One of the most commonly used fluorescent labels is fluorescein isothiocyanate (FITC) which is frequently conjugated to proteins like antibodies because of the isothiocyanate’s stable reaction with amine groups (Figure 6.15A-B). FITC has an excitation and emission wavelength of 495 nm and 520 nm respectively [97].

In this work, the technique of using optically labelled antibodies is comparable to the ELISA sensing scheme. Some investigations relied on firstly immobilising a primary antibody, with no optical label, onto the surface of graphene. Then, a secondary antibody, which has a fluorescent label covalently bonded to it, is then conjugated to the primary, due to the high affinity between the two (Figure 6.15C).

Figure 6.15A has been removed due to Copyright restrictions

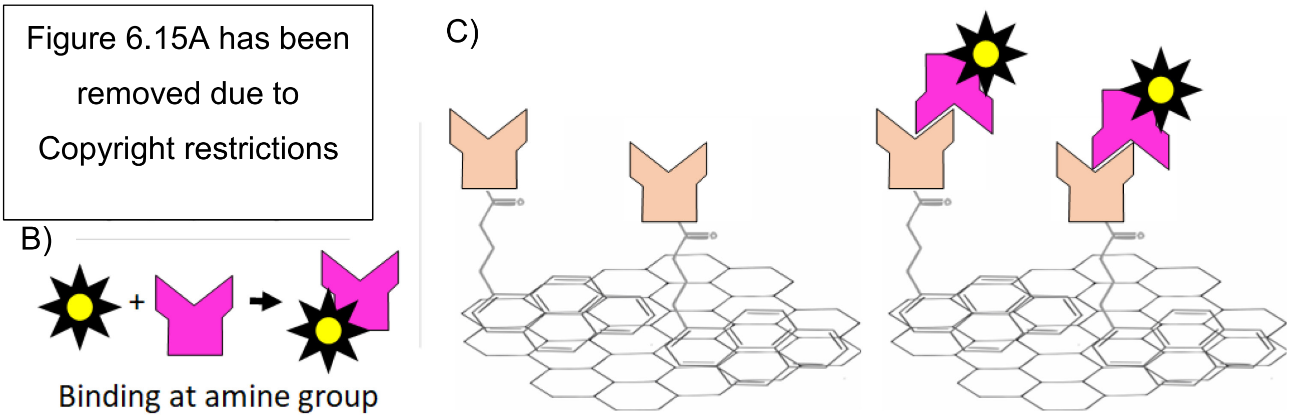

Figure 6.15 A) Molecular structure of FITC. B) Binding between antibody and FITC at amine group site. C) Two-stage antibody labelling process. Left-panel shows primary antibodies bound to the PBASE molecules. Right-panel shows secondary fluorescently labelled antibodies binding to primaries.

6.3.3.3 Labelling with Quantum Dots

Quantum Dots (QDs) are spherical nanoparticles (~10 nm) made up of metal alloys which consist of an internal core and external shell. When exposed to photons of a specific frequency, QDs absorb the energy exciting electrons within the core. Quantum confinement due to the size of the nanoparticle restricts these electrons to within the QD thus ensuring these electrons cannot tunnel out into the surrounding environment via non-radiative processes. When the electron returns to its initial state within the QD, it emits photons of light with a wavelength dependant on the metal alloy and its diameter [97].

6.3.3.4 Nikon Eclipse 80i Epifluorescence Microscope

This apparatus comprises of a microscope with a Nikon DS-Qi1Mc camera attached to it. The camera interfaces with the NIS-Elements Software allowing the light intensity from the label to be measured quantitatively (Figure 6.16). Optical labels can be interrogated by one of four filters for DAPI, FITC, TRITC and Cy5 which have central wavelengths for excitation (emission) at 360 nm (460 nm), 491 nm (516 nm), 544 nm (570 nm) and 651 nm (670 nm) respectively [148]. The stage can be moved freely in the x-y plane allowing qualitative information relating to the position of the labels to be observed which is useful for determining the distribution. All measurements are conducted in ambient conditions.

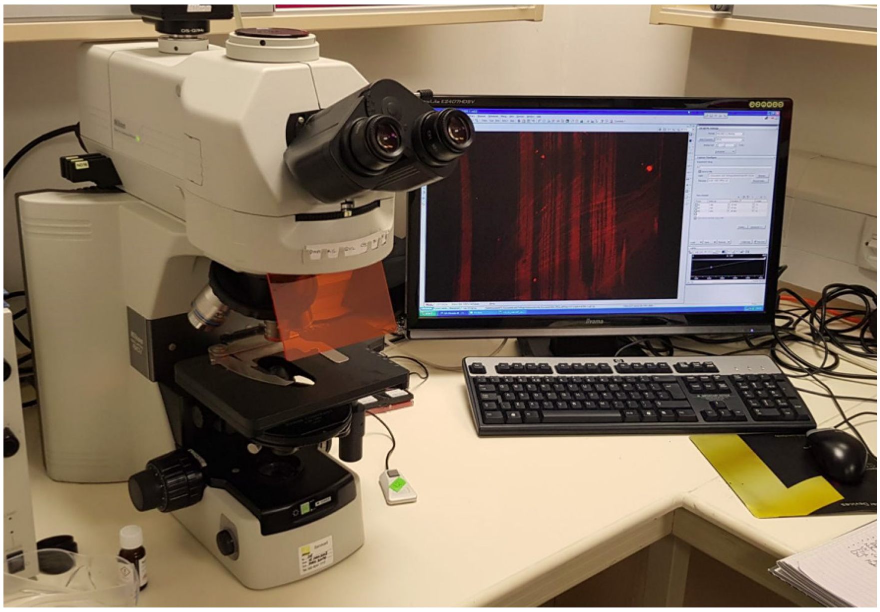

Figure 6.16. Nikon Eclipse 80i Epifluorescence Microscope with NIS Software used to interface with the microscope shown on the monitor

6.3.4 Atomic Force Microscopy (AFM)

6.3.4.1 Background

Nanometre scale, three-dimensional topographical information can be derived from an AFM [149]. This is achieved by measuring the surface height of the material under test using a solid force probe, whereby precise piezoelectric electronics are used to precisely position the tip to the surface of the test material [150]. This probe is usually moved over the surface of the material in a raster to build up a 2D array of height measurements, rendered in colours or tints to the end user [149].

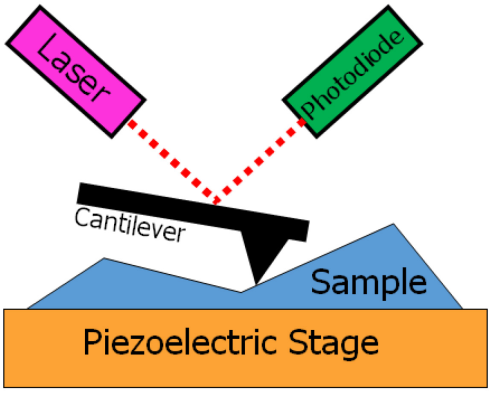

Figure 6.17 Schematic representation of typical AFM measurement

Unlike the previously invented Scanning Tunnelling Microscope (STM) which harnessed tunnelling electrons between the conductive tip and material to measure current, thus inferring topology, an AFM system relies on van der Waals forces between atoms of the tip and surface. Measuring these forces facilitates non-conducting materials to be imaged since these interactions exist between all atoms. However, detecting these forces, which lie within the nano- and pico-Netwon range, demands the use of springs as they allow for very straightforward and sensitive force measurements by relating the spring extension directly to the force via a spring constant. Thus AFM systems rely on the bending of a small cantilever with an atomically sharp tip attached to it. Modern systems use an optical detection system to relay the position of the cantilever by reflecting a laser beam off of the cantilever onto a photodiode [150]. An example schematic of a typical AFM system is given in Figure 6.17.

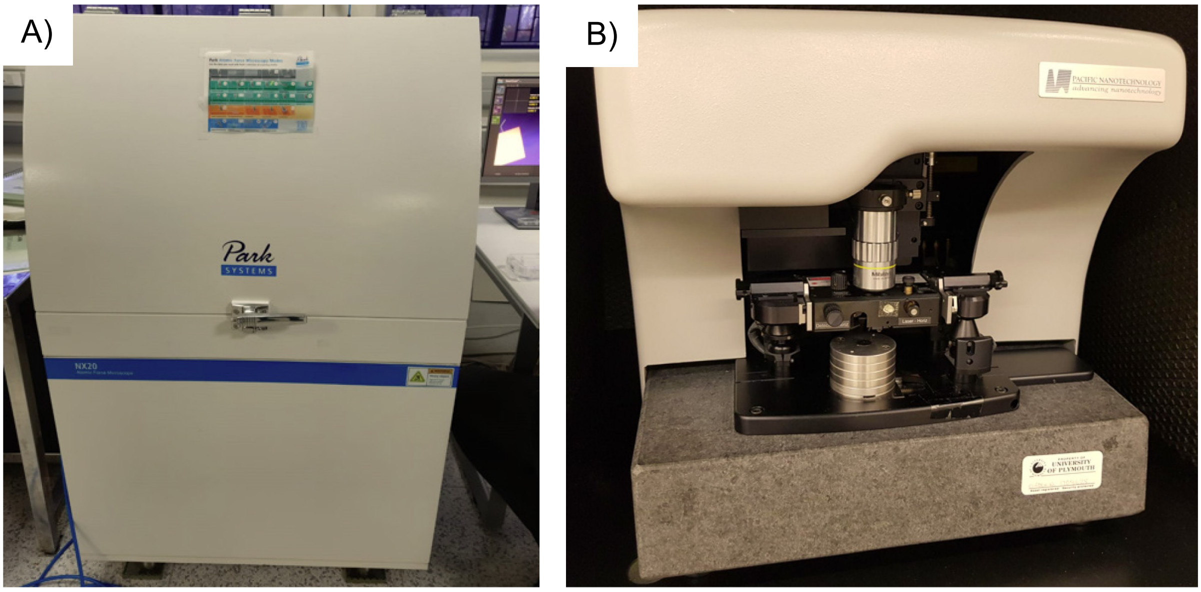

Figure 6.18 A) Park NX20 AFM system B) Close up of another typical AFM system.

6.3.4.2 Park NX20 AFM System and Bristol Nano Dynamics Ltd High Speed (HS)-AFM

AFM measurements were conducted using a Park NX20 (Figure 6.18A) and a Bristol Nano Dynamics Ltd HS-AFM. A more detailed view of a typical AFM system is provided in Figure 6.18B. HS-AFM measurements facilitates rapid data acquisition over large areas minimising drift effects which are common to other AFM [151]. All measurements were conducted in ambient conditions.

6.3.5 X-ray Photoelectron Spectroscopy (XPS)

6.3.5.1 Background

X-ray Photoelectron Spectroscopy (XPS) is a technique used to probe the specific chemical information of materials. The material under test is bombarded with X-rays which cause atoms to eject valence and core electrons (thus creating photoelectrons), in a process called photoionisation. In a process termed the photoelectric effect, if the energy of the incident photon is equal to or greater than the binding energy for the sample, a proportion of these photoelectrons escape from the material and are detected at the instrument's energy analyser (Figure 6.19). Since energy is conserved during these processes equation 6-1 can be used to determine the associated energies [152].

$$\boldsymbol{E_k + E_B^F + \varphi_{sp} = hv} \qquad 6\text{-}1$$

where $\boldsymbol{E_k}$ is the measured kinetic energy of the photoelectron, $\boldsymbol{E_B^F}$ is the electron binding energy with respect to $\boldsymbol{E^F}$ (the Fermi level), $\boldsymbol{\varphi_{sp}}$ is the work function of the spectrometer and $\boldsymbol{hv}$ determines the energy level of the incident X-ray photons; where $\boldsymbol{h}$ is Planck's constant and $\boldsymbol{v}$ is the frequency of the photon. Since $\boldsymbol{E_k}$ is measured by the instrument's energy analyser, $\boldsymbol{hv}$ is determined by the X-ray source (1486.6 eV for Al-Kα) and the equipment's $\boldsymbol{\varphi_{sp}}$ is known equation 6-1 is usually re-written as:

$$\boldsymbol{E_B^F = hv - E_k - \varphi_{sp}} \qquad 6\text{-}2$$

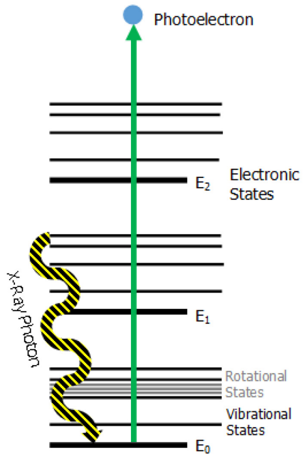

Figure 6.19 Schematic representation of XPS process whereby photoelectron is emitted as high energy incident X-ray gives it sufficient energy to photoionise

The binding energies of the photoelectrons are unique to elements and their chemical state, thus XPS analysis is able to quantify the concentration of these elements within a sample. In addition, this technique can also probe the functional groups associated with elements and therefore determine the proportions of C-O, C=O and O-C=O bonds for carbon for example, since the difference in the electronegativity varies the specific kinetic energy of the emitted photoelectron. Roughly 5% of the total photoelectrons produced, which are present nearer to the surface of the material (10 nm for carbon based materials), are measured by the XPS system making this technique particularly suitable for surface analysis. The detection of nitrogen is exploited by XPS to infer the presence and quantity of proteins for biological characterisation [152].

6.3.5.2 Thermo Scientific NEXSA XPS System

XPS Analysis was performed using a Thermo NEXSA XPS fitted with a monochromated Al kα X-ray source (1486.7 eV), a spherical sector analyser and a 3 multichannel resistive plate with 128 channel delay line detectors (Figure 6.20). All data was recorded at 19.2 W and an X-ray beam size of 200 x 100 µm. High-resolution scans were recorded at a pass energy of 20 eV. All sample data was recorded at a pressure below 10^{-8} Torr and a room temperature of 294 K.

Figure 6.20 has been removed due to Copyright restrictions

Figure 6.20 A) Thermo Scientific Nexsa XPS System B) Thermo Avantage Software package used to interface with the system.

6.3.6 Ultraviolet Visibility Spectrophotometry (UV-Vis)

6.3.6.1 Background

Ultraviolet (UV) spectrophotometry is the standard technique to quantify nucleic acid concentrations in samples. These devices measure the absorbance of UV light at characteristic wavelengths as UV rays pass through the sample (Figure 6.21A). This is conducted at standard path lengths so that concentrations, which are proportional to absorbance, can be determined quantitatively [153].

This technique relies on the phenomenon of peak UV absorption at 260 nm (A_{260}) for both the purine (adenine and guanine) and pyrimidine (cytosine and thymine (and uracil)) rings caused by their conjugated double bonds as depicted in Figure 6.21B. The purity of the sample can be determined in two ways. Firstly, by measuring the ratio of A_{260}/A_{280} since absorption at 280 nm is associated with contamination from proteins, with a ratios above 1.8 indicative of relative purity. Secondly, as strong absorption of chemical contaminants occurs at 230 nm, the ratio of A_{260}/A_{230} can be also be used to determine the sample's relative purity, with measurements above 1.4 required for high purity samples, such as those used in PCR methods. It is worth noting that some commonly used buffer salts such as Tris and Ethylenediamine tetra-acetic acid (EDTA) strongly absorb at 230 nm which can act to increase this ratio. Moreover the presence of free nucleotide bases within the sample interact with the UV light thus elevating both ratios and falsely implying to the user that the DNA sample has successfully formed a continuous chain [153].

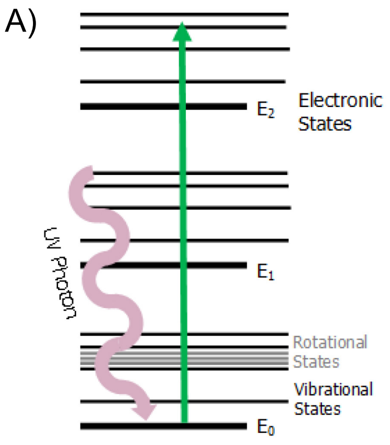

Figure 6.21B has been removed due to Copyright restrictions

Figure 6.21 A) Schematic representation of UV absorption whereby electron is excited to higher electronic states. B) Adenine (top) and Guanine (bottom) structure with double bonds indicated [53].

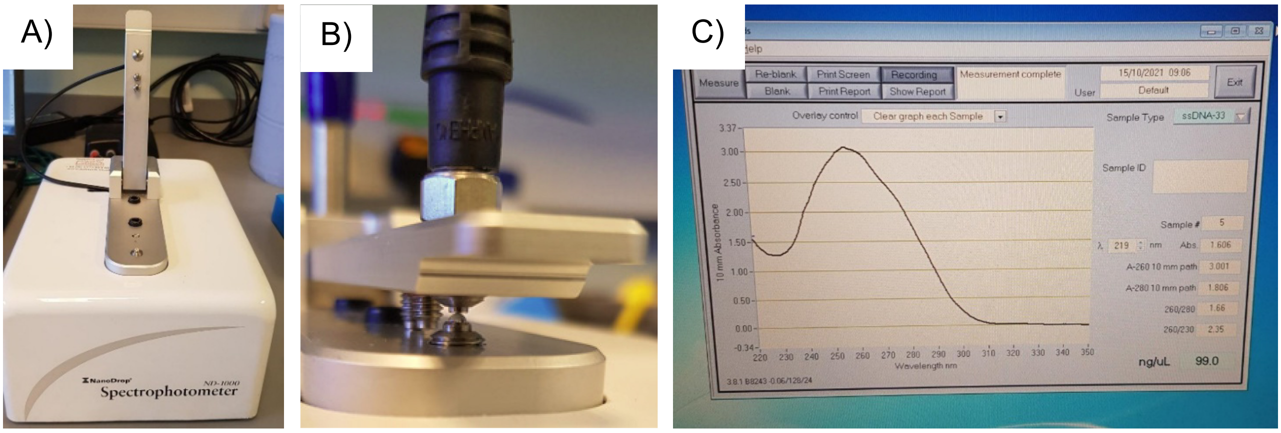

Measurement complete

15/10/2021 09:06

User Default

Overlay control Clear graph each Sample

Sample Type ssDNA-33

Sample # 5

λ 219 nm Abs. 1.606

A-260 10 mm path 3.001

A-280 10 mm path 1.806

260/280 1.66

260/230 2.35

ng/uL 99.0

Figure 6.22 A) Thermo Scientific NanoDrop 1000 B) Side view showing the liquid column between the top and bottom fibre contacts C) Nanodrop 1000 Software used to interface with spectrometer.

6.3.6.2 Thermo Scientific NanoDrop 1000 System

Operation of this equipment is rapid and facile, it begins by placing a 2 µL sample onto the surface of the receiving fibre optic cable (Figure 6.22). The source fibre optic cable is then brought into contact with the sample from above. Next, the equipment controls the distance between the two contacts to precisely 0.2 or 1 mm, before a pulsed xenon flash lamp illuminates the sample. The spectrometer then records the transmitted signal through the light column.

6.3.6.3 Calculating Concentration from Absorbents

Prior to use with the sample of interest, blanking using the buffer of the solution is required in order that the absorbance can be accurately calculated. Once the intensities of both the blank and sample have been recorded, the absorbance is calculated using equation 6-3

$$A = -\log\frac{I_S}{I_B} \qquad 6\text{-}3$$

where A corresponds to the absorbance and I_S and I_B correspond to the recorded intensities of the sample and blank material respectively.

The concentration of the sample can then be calculated by manipulating the Beer-Lambert equation

$$A = \varepsilon \ b \ c \qquad 6\text{-}4$$

$$c = \frac{A}{b \ E} \qquad 6\text{-}5$$

where ε is the extinction coefficient (L mol^{-1}cm^{-1}), which describes the wavelength dependant absorption of light for the material, b is the path length (cm) and c is the concentration of the sample (M) [154].

Calculating the extinction coefficient for DNA can be achieved using the nearest-neighbour model detailed below in Equation 6-6 [155].

$$\varepsilon_{260} = \sum_{i=1}^{N_b-1} \varepsilon_{i,i+1} - \sum_{i=2}^{N_b-1} \varepsilon_i \qquad \text{6-6}$$

where $\varepsilon_{i,i+1}$ is the extinction coefficient from doublets of nucleotides at position i and $i+1$ and, ε_i is the extinction coefficient from the nucleotide at position i. A table which gives the extinction coefficients for single and doublet nucleotide bases can be found at Appendix A1. The second term is required in order that nucleotides counted twice in the first term are removed. More details relating to this model can be found in [155].

6.3.7 Fourier Transform Infrared Spectroscopy (FTIR)

6.3.7.1 Background

Infrared (IR) spectroscopy, which harnesses electromagnetic radiation typically between 4000 and 400 cm^{-1}, can determine the molecular contents and their concentrations in a sample. Molecules absorb light energy of this wavenumber and vibrate generating characteristic spectra with varying degrees of absorbance or transmittance (Figure 6.23A). It follows that individual atoms such as argon and helium and monatomic ions, which are chemically unbound to anything, do not give an infrared response. Water is a commonly used solvent in biosensing and is in fact a molecule that causes an issue for any IR spectroscopy measurements due to its broad peaks around 3500 cm^{-1} and 1600 cm^{-1} that can mask the spectra of any solute within it [156].

Fourier Transform Infrared Spectroscopy (FTIR) is the most common IR technique. One reason for this, is that it offers an improved signal to noise ratio of over 100 times than regular IR spectrometers. This is caused by the greater level of light that is able to hit the detector as in this technique the use of prisms, gratings or slits that act to reduce the light intensity are not used [156].

Every FTIR spectrometer relies on an interferometer, which measures the interference pattern between two light beams. Most FTIR spectrometers are based around the Michelson interferometer design which consists of four arms and is pictured in Figure

6.23B. The top part of this system includes the IR source and the collimating mirror to ensure parallel rays. At the bottom, a mirror with a fixed position is situated. On the right hand side, a mirror which is capable of moving towards and away from the central beamsplitter is positioned. The purpose of the beamsplitter is to allow a proportion of light to transmit through it, towards the fixed mirror, and reflect the remaining light towards the moving mirror. These light rays then recombine at the beamsplitter, due to the superposition of waves, before they are transmitted to the sample and are measured at the detector. Moving the mirror away from and then back to the beamsplitter produces an interferogram which shows the light intensity against the path length for a single scan. The IR spectrum is calculated by Fourier transforming these interferograms which details the intensity and wavenumbers present when light transmits through the sample [156].

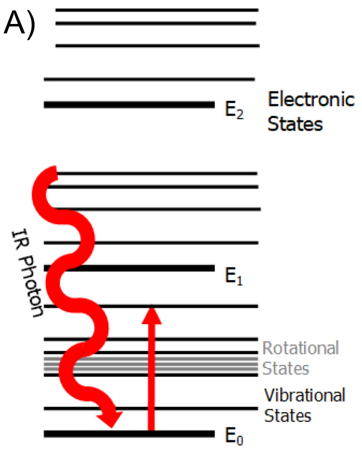

Figure 6.23B has been removed due to Copyright restrictions

Figure 6.23 A) Schematic representation of IR absorption whereby electron is excited to higher vibrational states. B) Michelson interferometer, which forms the basic components of any FTIR spectrometer [156]

6.3.7.2 FTIR System Details

FTIR measurements were conducted using a Bruker Alpha FTIR spectrometer with a detection range of 400-4000 cm^{-1} in ATR mode (Figure 6.24). KBr pellet measurements were conducted using the Bruker Vertex 70 with a detection range of 370-7500 cm^{-1}. All measurements were conducted in ambient conditions.

6.3.7.3 Attenuated Total Reflectance (ATR)

The attenuated total reflectance (ATR) technique relies on trapping the IR radiation within a crystal that is in tight contact with the sample under test. At specific angles dependent on the sample’s refractive index, IR radiation will not leave the crystal and will reflect off the interface indefinitely. At locations of internal reflectance, named hotspots, the incident and reflected beams undergo constructive interference causing an evanescent IR wave to leak from the crystal into the sample, penetrating between <1 μm-10 μm deep.

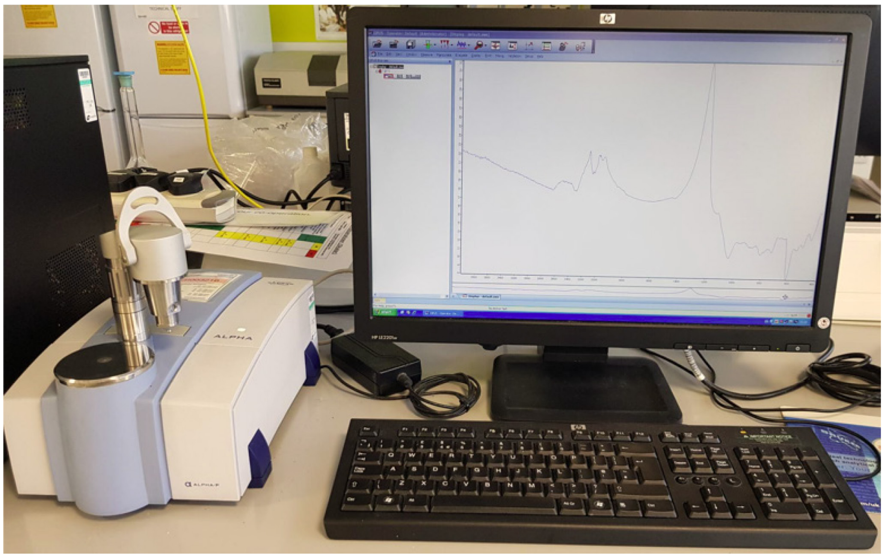

Figure 6.24 A) Bruker Alpha FTIR Spectrometer B) OPUS Software used to interface with spectrometer

As the sample absorbs IR radiation it attenuates the total intensity and characteristic peaks are thus measured at the detector. It offers rapid and simple detection, with the only requirement that solid samples are brought in tight contact with the crystal with the use of clamp. The low penetration depths make it suitable for both surface characterisation and aqueous solutions (due to the reduction of water absorbance), but can limit the sensitivity of smaller analyte concentrations. In addition, the cost of this equipment including that of replacing scratched ATR crystals, which can be diamond, can prove to be prohibitively expensive.

6.3.7.4 Potassium Bromide (KBr) pellets

Measuring the IR spectrum of solids, which can be sufficiently ground, can be achieved by using potassium bromide (KBr) pellets to form solid solutions. During this process the sample is ground to a fine powder with KBr acting as a diluent, with particulate sizes no greater than 2 μm to ensure that scattering of the IR radiation is minimised. This mixture is then pressed under 10 tonnes to create a translucent pellet. This pellet is then placed in a suitable holder before transmission measurements are conducted with the FTIR device. This technique relies on the fact that KBr is not only inert and therefore unreactive with the sample powder but it also it transparent to IR radiation above 400 cm^{-1}. This method can produce low noise, flat baseline and well resolved high quality IR spectra at the cost of increased sample preparation times.

6.4 Electrical Characterisation Techniques

6.4.1 Cascade Microtech (MPS150) Probe Station

This apparatus facilitates four-probe measurements of micro- and nano- devices (Figure 6.25). It consists of four tungsten (W) needles (Cascade Microtech) each located in holders which allow fine adjustments in the x, y and z axes via rotating dials to position the probes onto the device under test (DUT). The positioning of these probes is conducted under a magnification provided by the optical microscope illuminated by an LED ring. The metallic chuck is used to apply electric fields to back-gated devices.

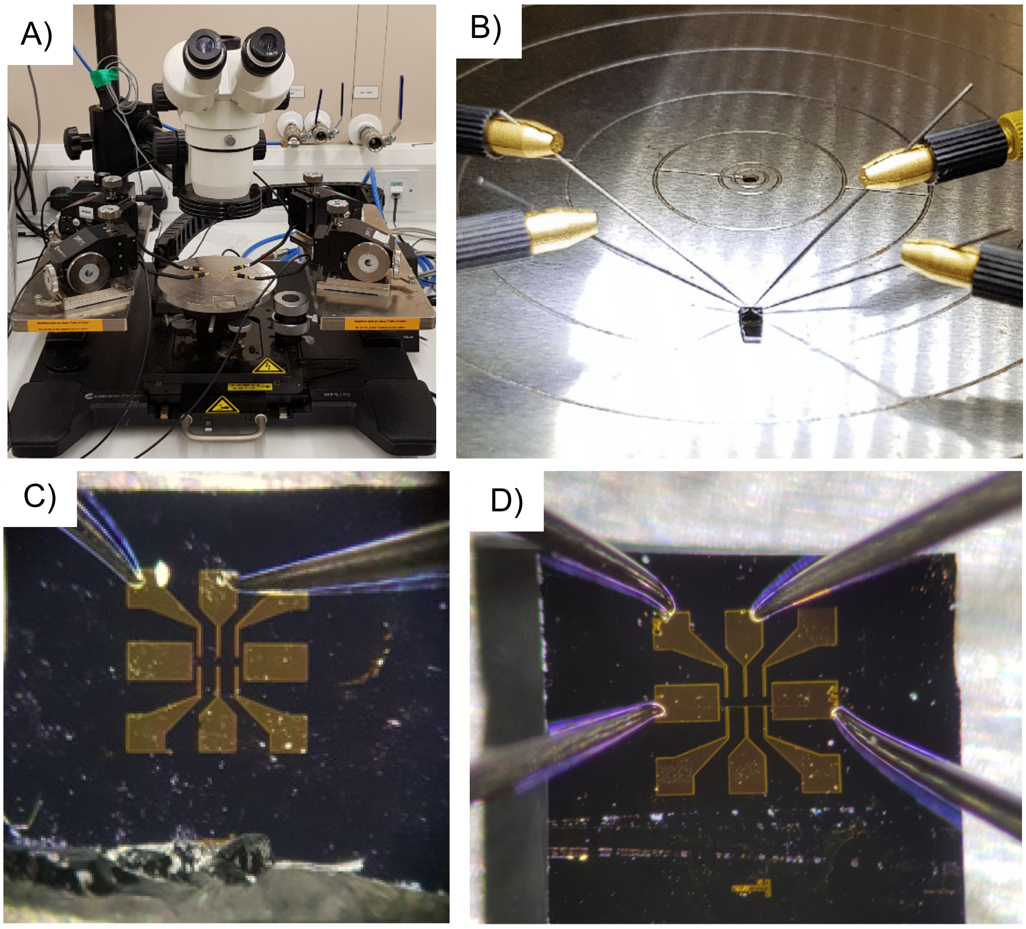

Figure 6.25. A) Cascade Microtech (MPS150) Probe Station, B) Close-up of probe position. View through the binoculars showing the practical probe placement on electrodes of GFETs for C) two-probe and D) four-probe measurements

6.4.2 Two Terminal Probe Measurements

Basic two-probe resistance measurements rely on a current source to induce a current through the DUT. A voltmeter that is connected in parallel measures the potential drop across the DUT which allows the resistance to be calculated using Ohm’s law. A schematic of this measurement set-up is shown in Figure 6.26. Note that an alternative approach relies on a voltage source to induce a potential difference across the circuit, whereby an ammeter connected in series measures the current through the DUT.

This two-probe technique does not eliminate causes of systematic error related to the lead resistances of the cables which attach to the DUT and the contact resistances that occur on the interface between the lead and DUT surfaces. These errors lead to the overestimation of the DUT's resistance value [157].

Figure 6.26 has been removed due to Copyright restrictions

Figure 6.26. Two-probe resistance measurement schematic [157]

6.4.3 Four Terminal Probe Measurements

The four-probe terminal method relies on two independent source and sense circuits as shown in Figure 6.27. For the source circuit, a constant current is passed through the ends of the DUT using two force probes positioned at outer positions. The current through this circuit is measured by an ammeter connected in series. The sense circuit consists of a voltmeter connected in parallel with the DUT using two sense probes positioned at inner positions across the location of interest. The current through the sense circuit is of the order of pico amps and therefore the voltage drop across the sensing leads can be considered as negligible which eliminates the lead resistances as a source of error in these measurements [157].

Figure 6.27 has been removed due to Copyright restrictions

Figure 6.27 Four-probe resistance measurement schematic [157]

6.4.4 Measurement Schematic

The practical setup for applying the four terminal probe measurements to the GFETs used in this contribution is given in Figure 6.28. The conventions for the length and width of the channel under test is also shown here. This schematic shows a sample measurement for a linear voltage sweep whereby the voltage between the source and drain electrodes is swept and the current through the electrodes is measured.

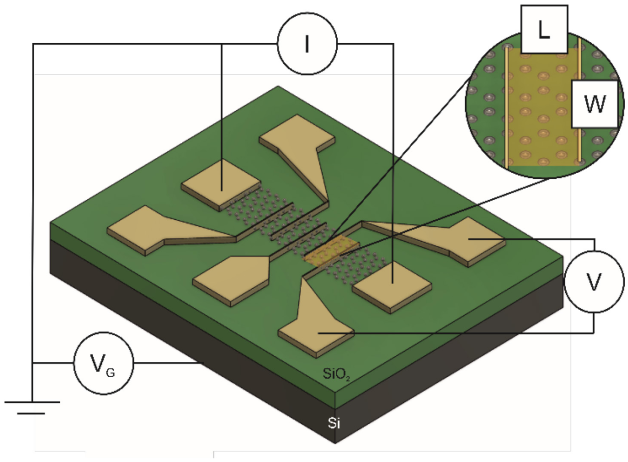

Figure 6.28. Four terminal probe measurement schematic for GFETs

For this measurement, the force probes are placed on the source and drain electrodes and a potential difference (V_{SD}) is applied between them. The sense probes are then placed on inner pads to measure the current (I_{SD}) through the channel highlighted. The back-gate is connected via the chuck and is held at zero for all measurements excluding back-gated sweeps. All electrical measurements were conducted in dry conditions.

6.4.5 Keysight B1500A Semiconductor Device Analyser

6.4.5.1 Measurement setup

GFETs are positioned onto the Cascade Microtech (MPS150) stage with the Si substrate in contact with the metallic chuck. Dependant on the channel to be measured, cables ends (BNC) attached to the probes are connected to the signal measurement units (SMUs) in their appropriate positions located on the back of the Keysight B1500A Semiconductor Device Analyser (SDA) as depicted in Figure 6.29A. The chuck is then connected to the back of the SDA in the same manner. By twisting the dials on the holders, probes are then precisely positioned onto the surface of the appropriate pads, following the four terminal probe measurement scheme described previously. The SDA interfaces with the SMUs via an EasyEXPERT software package shown in Figure 6.29B. In this software package it is possible to design custom measurement procedures. All electrical measurements using this equipment are taken at ambient conditions.

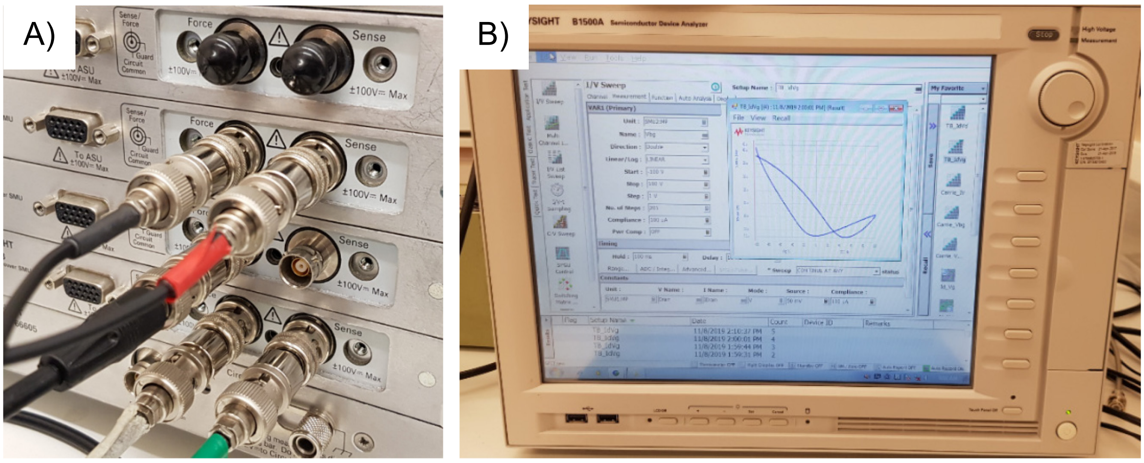

Figure 6.29. Keysight B1500A Semiconductor Device Analyser A) Back; showing SMU Connection ports with Force and Sense circuits clearly labelled B) Front; showing EasyEXPERT software

6.5 Preparation of Reagents

Details of the preparation of substances used throughout the biofunctionalisation process are described below. All chemical reagents used throughout this work were purchased at analytical grade and were unmodified before use.

6.5.1 Reagents

6.5.1.1 De-ionised water

Ultrapure DIW used throughout this work for buffer solutions and rinsing stages was obtained from a Purelab water purification systems with a resistivity value of 18.2 MΩcm.

6.5.1.2 PBS

A 1 x PBS solution, with pH of 7.4 was created by combining 1 PBS tablet (Fisher Scientific) with 200 mL of ultrapure DIW. These two were mixed with a magnetic stirrer to ensure adequate mixing. PBS helps to ensure a constant pH and imitates ionic conditions of physiological solutions which is required to prevent damage to proteins like antibodies.

6.5.1.3 PBASE

PBASE (Sigma Aldrich) arrives from the supplier in powder form. This powder is weighed out and mixed with the appropriate volume of methanol (Sigma Aldrich) or DMF (Sigma Aldrich) before being stirred for several hours using a magnetic stirrer to achieve suitable mixing. The bi-functional molecule PBASE was used in this work to facilitate the non-covalent immobilisation of bioreceptors onto the graphene surface. Concentrations of 2 mM and 10 mM were prepared.

6.5.1.4 DNA

Oligonucleotides (Eurofins Genomics) were synthesised via phosphoramidite chemistry. Tubes of single stranded DNA were ordered at a synthesis scale of 1 µmol with High Performance Liquid Chromatography (HPLC) purification. The synthesis scale describes the initial quantity of material and differs to the synthesis yield which defines the final amount of the oligonucleotide present at the end of the process whereby inefficiencies due to chemical reactions, additional modifications, formations of secondary structures and the purifying processes are taken into account.

Tris-EDTA, pH 8.0, is the recommended buffer for oligonucleotide resuspension by the supplier due to two primary reasons. Firstly, as oligonucleotides are more sensitive than DNA to degradation due to acidic conditions, Tris-EDTA offers a basic environment to prevent damage. Secondly, the inclusion of EDTA inhibits any nuclease activity which act to break down nucleic acids in solution. However, since the oligonucleotides purchased had aptamer modifications on the 5' and 3' end, to assist with the biofunctionalisation via PBASE, it was determined that this buffer would not be suitable since Tris is known to have primary amines and therefore could compete with the amine functionalised aptamer to form stable amide bonds with immobilised PBASE. Instead, a PBS solution was used for these aptamers. The oligonucleotides which were modified with a pyrene group (Metabion) at the 5' end were diluted with DMF (Sigma Aldrich).

The lyophilised oligonucleotides arrive in tubes with a synthesis yield determined by the supplier. These tubes were then centrifuged at room temperature for 1 min at 13,000 g so that any material spread around the tube was relocated to the base. A precise amount of solvent is added to the tubes to make up a stock solution of 100 pmol/μL (equivalent to 100 μM).

Once the solvent was added to the aliquots and the stock solution was combined, the aliquots were firstly centrifuged for 30 s at 3000 g, before being vortexed for 15 s and then centrifuged again. This ensured adequate mixing of the solutions. Aliquots of 20 μM, 10μM, 5μM, 1μM, 100nM, 10nM and 1nM were used in this work and stored in an appropriate freezer (-20/-80 ºC) and thawed before each individual use.

The preparation of the aptamers solutions were conducted with rigorous hygiene procedures in order to reduce the inclusion of nuclease enzymes into the solutions. The chosen filter tips and aliquot tubes (Sigma Aldrich) were all DNase and RNase free. The solutions were handled in a laminar flow cabinet sterilised with UV light and cleaned with CHEM-GENE, DNA-away and RNA Zap, which are surfactants used to destroy enzymes. Additional equipment used to handle the oligonucleotides including gloves, pipettes and tubes were cleaned using the same chemicals. In addition, any lids covering aliquots, the chosen solvent and filter tips were left open for a minimal amount of time to prevent contamination.

6.5.2 Dilution Calculations

The following describes the formulae used to calculate the concentration of the reagents (DNA and Pb^{2+}) used in this work. The pH of these dilutions was not measured. Once the concentration of the stock solution is calculated the process of dilution begins using equation 6-7:

$$\boldsymbol{C_1V_1 = C_2V_2} \qquad \text{6-7}$$

$$\boldsymbol{V_1 = \frac{C_2V_2}{C_1}} \qquad \text{6-8}$$

where C_1 and V_1 are the concentration and volume of the stock solution and C_2 and V_2 correspond to the concentration and volume of the desired dilution.

Once the volume of the stock solution is calculated the volume of buffer solution required to create the desired dilution is calculated using equation 6-9

$$\boldsymbol{V_{Buffer} = V_2 - V_1} \qquad \text{6-9}$$

where V_{Buffer} corresponds to the volume of the buffer solution. In order to produce serial dilutions, this process is repeated treating quantities of the newly diluted material (at a concentration of C_2) as the new “stock” solution.

Chapter 7 – Results

7.1 Electrical Characterisation - Data Processing Software

7.1.1 Motivation and Significance

The fundamental electrical characterisation for GFETs is the I_{SD}-V_G gated sweep as described in more detail in section 6.4.5 and 7.3.2. These gated sweep measurements produce transfer curves which describe the modulation of the charge carriers and thus details the conductive properties of the graphene channel. Therefore the analysis of these curves is essential to understanding the sensing qualities of devices. Additional information related to the graphene surface and interface charges can be obtained by comparing the forward and reverse sweep characteristics as hysteretic behaviour is observed [158].

Large amounts of information can be elucidated from a single I_{SD}-V_G sweep measurement relating to a host of sensing characteristics related to the DUT. Usually, multiple repeats under different environmental conditions, with different functionalisation regimes are conducted resulting in significant amounts of data to process, analyse and visualise.

This large quantity of data produced during the electrical characterisations necessitated the development of a novel, easy-to-use software platform in order to streamline the data processing stages. Therefore the **S**weep **C**omparison **R**esearch **A**pplication for **M**ultiple **B**ack-gated fie**L**d **E**ffect measurements of GFETs (**SCRAMBLE**) package was developed. It provides an easy-to-use graphical user interface (GUI) that allows researchers of all software skill levels to swiftly and accurately monitor key parameters relating to GFETs in large datasets, allowing them to make data driven conclusions relating to their devices. Details relating to SCRAMBLE in this section have been taken from the following publication written by the author [159].

SCRAMBLE automates all aspects of data manipulation, transforming raw data from measurement equipment into useful visualisations, whereby complex parameters (such as Dirac points and mobility values) are calculated and determined at the click of a single button, thus eliminating human error.

SCRAMBLE's source code remains open and adaptable so that users with different characterisation procedures and equipment can easily customise the software to their exact purposes. Since GFET devices are used across a plethora of different research areas including medical diagnostics [4, 69], food adulteration testing [87, 123] and novel electronic component design such as logic gates [78] and logic inverters [160] SCRAMBLE will have a substantial impact across a wide range of exciting fields of study. This software package has the potential to support all researchers working in the field of GFETs by enabling them to rapidly and accurately process datasets.

7.1.2 Software Description

The main components of SCRAMBLE's GUI are shown in Figure 7.1. The front panel is split into the left hand side control panel and the visualisation screen. The control panel contains several inputs and controls that allows the user to import raw .csv files, customise the dimensions and parameters of their devices, select I_{SD}-V_G sweep(s) of choice, average, plot and also export data. The visualisation screen displays the interactive charts once the "Process Data" button is pressed.

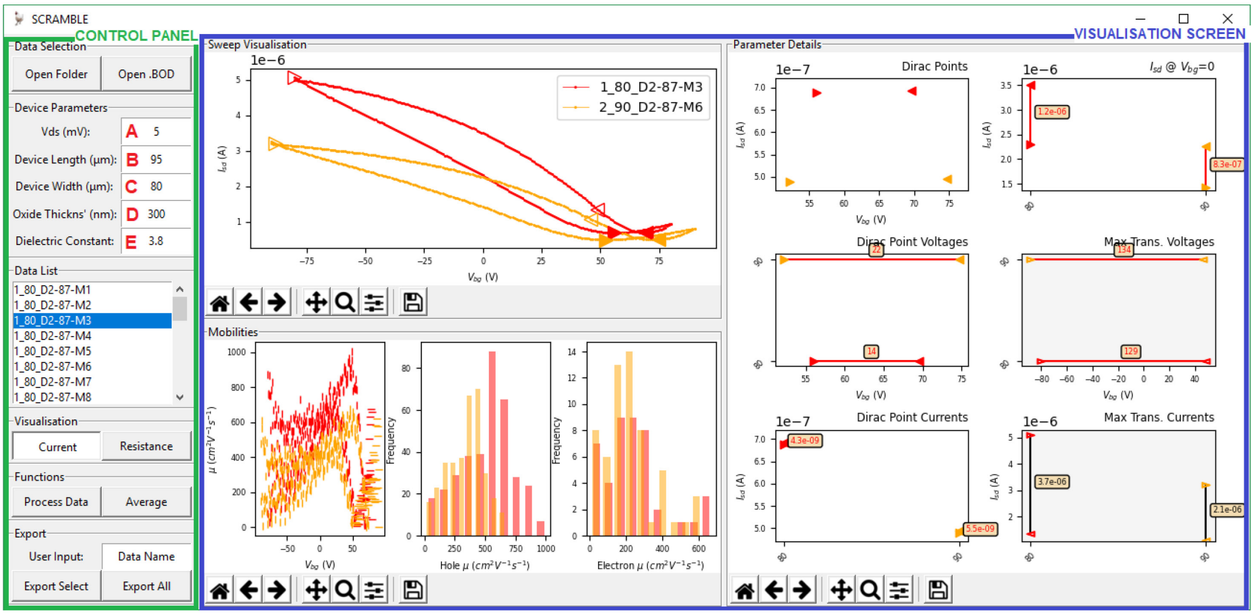

Device Parameters

Vds (mV): A 5

Device Length (µm): B 95

Device Width (µm): C 80

Oxide Thickns' (nm): D 300

Dielectric Constant: E 3.8

Data List

1_80_D2-87-M1
1_80_D2-87-M2
1_80_D2-87-M3
1_80_D2-87-M4
1_80_D2-87-M5
1_80_D2-87-M6
1_80_D2-87-M7
1_80_D2-87-M8

User Input: Data Name

Figure 7.1 SCRAMBLE GUI showing the control panel with input parameters and visualisation screen where data is represented in various charts. A comparison between sweeping V_G between -/+ 80 V (red) and -/+ 90 V (yellow) is shown.

7.1.2.1 Software Architecture

The source code for SCRAMBLE is written in Python, and is split across two modules, "scrambleGUI" and "scrambleFUN" as depicted in Figure 7.2. The "scrambleGUI" module handles all aspects of the GUI including buttons, inputs and charts by implementing code from the tKinter library [161]. The "scrambleFUN" module is where the computation of parameters is performed.

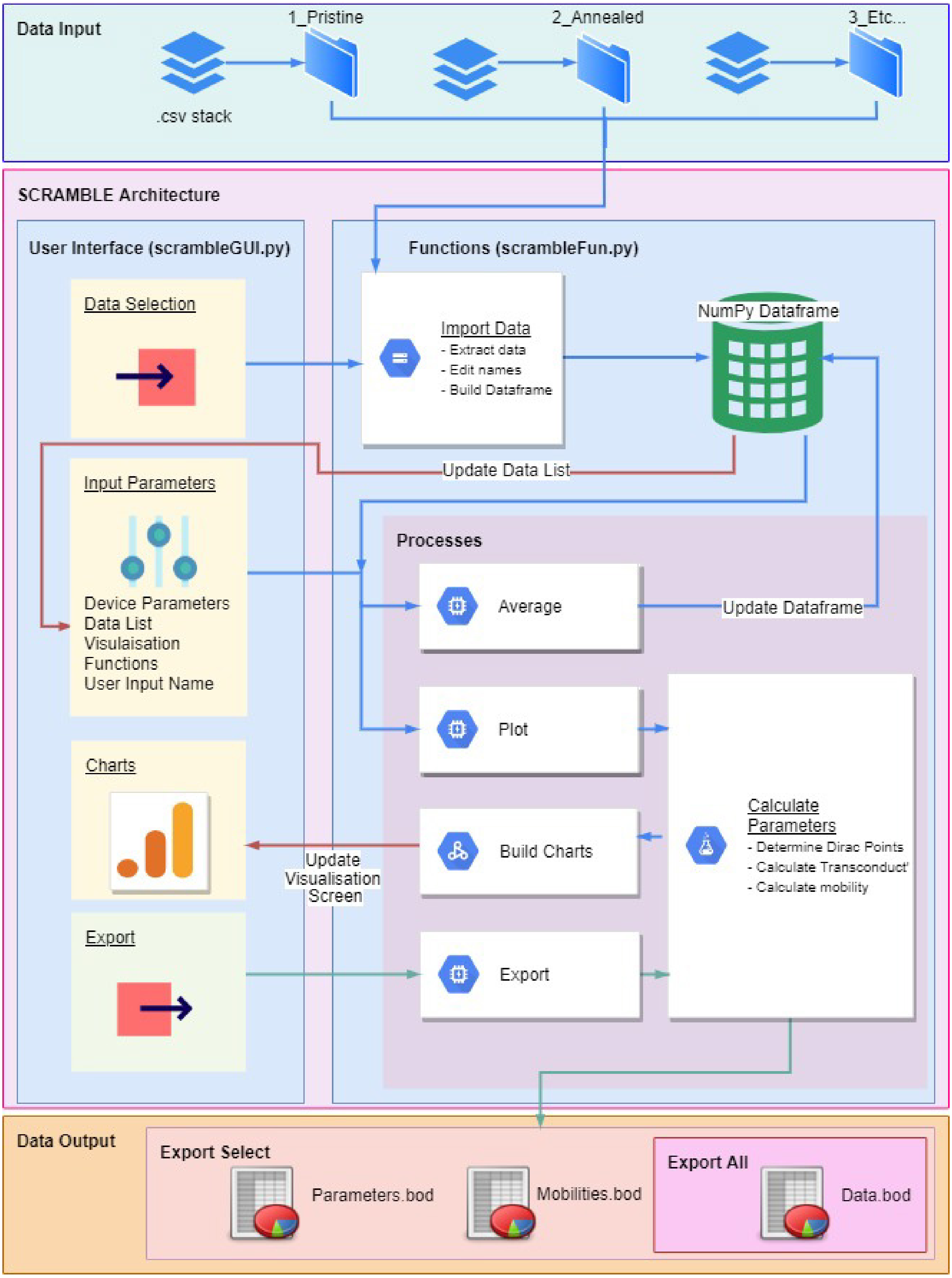

Figure 7.2 SCRAMBLE software architecture overview showing two modular components to the package along with the data input and output locations. Raw data is pulled into the scrambleFUN.py module where it is manipulated based on the input parameters from the control panel handled by the scrambleGUI.py module. A NumPy DataFrame is constructed and updates the “Data List” for the user to choose which measurements they wish to visualise. The processing pathways for averaging, plotting and exporting data are shown with the appropriate arrows. The file types exported by SCRAMBLE are shown under the appropriate button name.

Here, data is imported, manipulated and analysed according to specific functions. Other open source libraries involved in this software package include os, NumPy [162], Pandas [163] and Matplotlb [164].

7.1.2.2 Using SCRAMBLE

The user begins by loading in the raw .csv files from folders of their choice corresponding to the multiple I_{SD}-V_G data acquisitions using the “Open Folder” button within the “Data Selection” frame. An algorithm selects only the two data columns of interest (I_{SD} vs V_G) and ignores the metadata situated in the header rows. The names of the imported files are printed in the list-box within the GUI and the data is held in memory. Note that the “Open. BOD” button should be used on previously exported data to prevent unnecessary computational effort, which reduces re-import times for large datasets.

Next, the user must update the inputs of the “Device Parameters” frame (Figure 7.1) according to the details/dimensions of their GFETs. Here, “A” is the source-drain voltage V_{SD} in mV, “B” is the device length in μm, “C” is the device width in μm (Figure 6.28), “D” is the dielectric thickness t_{ox} in nm and “E” is the dielectric constant ε_r in Fm^{-1}.

The user then decides which of the imported I_{SD}-V_G sweeps they wish to evaluate, by selecting one or more of the labelled names in the “Data List” frame. Next, the user must decide whether they want the data visualised as either current or resistance against V_G. If the user selects the “Resistance” option then both the resistance in ohms (Ω) and the sheet resistance in Ohms/square (Ω/□) will be displayed in the “Sweep Visualisation” frame, on the left hand and right hand y-axis respectively. The sheet resistance of 2D materials is described in more detail in [165]. Note that for the remainder of this section it is assumed that the user has selected the “Current” option.

To begin the core algorithm the user then presses the “Process Data” button, which commences the workflow depicted in Figure 7.2 to determine and calculate the characterisation parameters. For each of the I_{SD}-V_G sweeps selected the following parameters are determined for both the forward and reverse sweeps; current/voltage values of Dirac Points, current value at V_G=0, current/voltage values of maximum transconductance points and the electron and hole mobilities.

For each of these parameters, the forward and reverse values are plotted on the same chart with the difference between them highlighted by a colour coded line which determines whether or not the forward (black) or reverse (red) occurred at a greater value.

Positions corresponding to the Dirac points and maximum transconductance are overlaid onto the “Sweep Visualisation” chart (Figure 7.1).

7.1.2.3 Adaptability

SCRAMBLE’s source code has been left fully adaptable so that the customisation of data import from different Semiconductor Device Analysers (SDAs) and templates along with defining user specific default values for GFET details/dimensions is easily achieved (Listing 1). Further details on the customisation and practical use of SCRAMBLE are given in the online README.md found here:

https://github.com/ElsevierSoftwareX/SOFTX-D-20-00068 .

```
sourceDrainLabel=tk.Label(frame1, text="Vds (mV):",padx=5, pady=5, width=w)
sourceDrainLabel.grid(row=0,column=0,sticky="nesw")
sourceDrainEntry=tk.Entry(frame1, justify="center", width=w)
sourceDrainEntry.grid(row=0, column=1,sticky="nesw")
sourceDrainEntry.insert(0,5)
deviceLengthLabel=tk.Label(frame1, text="Device Length (\u03bcm):",padx=5, pady=5, width=w)
deviceLengthLabel.grid(row=1, column=0,sticky="nesw",columnspan=1)
deviceLengthEntry=tk.Entry(frame1, justify="center", width=w)
deviceLengthEntry.grid(row=1, column=1,sticky="nesw",columnspan=1)
deviceLengthEntry.insert(0,95)
deviceWidthLabel=tk.Label(frame1, text="Device Width (\u03bcm): ",padx=5, pady=5, width=w)
deviceWidthLabel.grid(row=2, column=0,sticky="nesw",columnspan=1)
deviceWidthEntry=tk.Entry(frame1, justify="center", width=w)
deviceWidthEntry.grid(row=2, column=1,sticky="nesw",columnspan=1)
deviceWidthEntry.insert(0,80)
oxideThickLabel=tk.Label(frame1, text="Oxide Thickns' (nm): ",padx=5, pady=5, width=w)
oxideThickLabel.grid(row=3, column=0,sticky="nesw",columnspan=1)
oxideThickEntry=tk.Entry(frame1, justify="center", width=w)
oxideThickEntry.grid(row=3, column=1,sticky="nesw",columnspan=1)
oxideThickEntry.insert(0,300)
oxideDielecLabel=tk.Label(frame1, text="Dielectric Constant: ",padx=5, pady=5, width=w)
oxideDielecLabel.grid(row=4, column=0,sticky="nesw",columnspan=1)
oxideDielecEntry=tk.Entry(frame1, justify="center", width=w)
oxideDielecEntry.grid(row=4, column=1,sticky="nesw",columnspan=1)
oxideDielecEntry.insert(0,3.8)
```

Listing 1. Code snippet from scrambleGUI.py module showing lines of code associated with default values (underlined text) for the control panel which are easily customised by users to correspond with values associated with their own device dimensions and parameters.

7.1.2.4 Software Functionalities

As the I_{SD}-V_G sweeps consist of a forward and reverse direction, the first part of the data manipulation involves splitting the data into these directions. Then, by selecting the minimum current value and its corresponding index for the back-gate voltage, the position of the Dirac points are determined.

The transconductance ($g_m = \partial I_{SD}/\partial V_G$) is computed using the “gradient” function from the “NumPy” Python module [166]. The maximum transconductance values and their corresponding positions in current and voltage space are then determined.

The mobility is described by hole and electron conduction, referring to which charge carrier is the majority contributor to the current through the graphene channel at a particular V_G. At the Dirac point, the voltage of minimum conductance, the Fermi level sits at the intercept between the valence (majority hole) and conduction (majority electron) bands. Conduction in regions below (above) the Dirac point voltage show majority hole (electron) charge carrier contributions. Therefore, once the Dirac points have been identified, they are used to split the raw data into the regions which describe hole and electron conduction.

The field effect mobility is calculated using the direct transconductance method (DTM) described in more detail in 7.3.2.2. The mobility data is plotted in three charts in SCRAMBLE. Firstly, the mobility at each point across the I_{SD}-V_G sweep is plotted with the majority charge carrier at each point determined by the vertical or horizontal bars corresponding to hole and electron charge carriers respectively. Next, histograms detailing the frequency of binned mobility values for the hole and electron charge carriers are given.

SCRAMBLE offers the option to average multiple I_{SD}-V_G sweeps together. This is achieved by firstly selecting the I_{SD}-V_G sweeps from the “Data List” and then pressing the “Average” button. The newly created I_{SD}-V_G sweep is appended to the list with the name formed of the entry in the “User Input” and “AVE” concatenated to the end to signify that it has been processed within SCRAMBLE. This can then be selected for evaluation as previously discussed.

The individual charts shown in Figure 7.1 can be manipulated with their individual navigation toolbars allowing panning, zooming and the configuration of subplots. Pressing the “Save” icon allows the user to export the plots in various formats such as Portable Network Graphics (PNG), Scalable Vector Graphics (SVG) and Raw RGBA bitmap to name a few.

The raw data and calculated parameters for I_{SD}-V_G sweeps can be exported from SCRAMBLE using the “Export Selected” button which performs this on the data highlighted in the “Data List”. This action produces three text files (.bod); one with the raw I_{SD}-V_G data, one with the calculated mobility values and one with the determined parameters. These are labelled accordingly by concatenating the input of “User Input” entry box with “Data”, “Mobilities” and “Parameters” respectively. Note that using the “Export All” button exports only the raw I_{SD}-V_G data for all data within the “Data List”.

7.1.3 Illustrative Example

The influence of applying conventional annealing at a temperature of 215 ºC for 30 mins on a single GFET device is demonstrated in this section to exhibit the main functionalities of SCRAMBLE. In this work, three I_{SD}-V_G sweeps were performed before (A1, A2 and A3) and after (B1, B2 and B3) the annealing process was conducted. The three raw I_{SD}-V_G sweeps before the annealing treatment are shown in Figure 7.3. In this plot, the positions of the forward and reverse (right and left) Dirac points and maximum transconductance points (filled and unfilled) are illustrated by suitable triangles. It is clear from the anomalous step clearly highlighted by SCRAMBLE at I_{SD} at -40 V that the A3 measurement should be excluded from future analysis.

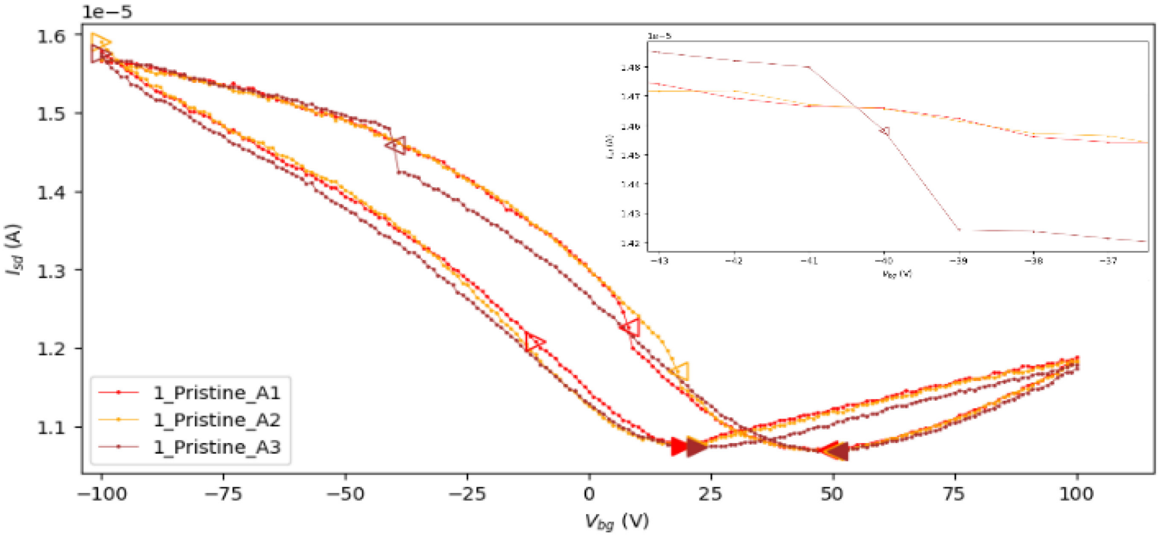

Figure 7.3 Sweep Visualisation Plot for devices A1, A2 and A3, with inset showing an anomalous step in the current between -39 V and -41 V indicated by the left pointing unfilled triangle for A3, corresponding to the maximum transconductance for the reverse sweep.

Averaging and then plotting suitable values for before (A1 and A2) and after (B1, B2 and B3) the annealing process is completed next in order to evaluate the parameter change caused by the annealing process. A summary of some of the salient charts are given in Figure 7.4. Using SCRAMBLE, it is swiftly shown that the annealing process has shifted the Dirac points to higher V_G and I_{SD} values, increased the current value through the GFET at all points and increased the hole (electron) mobilities in the graphene channel by three (two) times (Figure 7.4A). The colour coded lines and text associated with the markers allow for swift conclusions to be made about how this process has influenced the relative positions of the forward and reverse sweeps (Figure 7.4B and C).

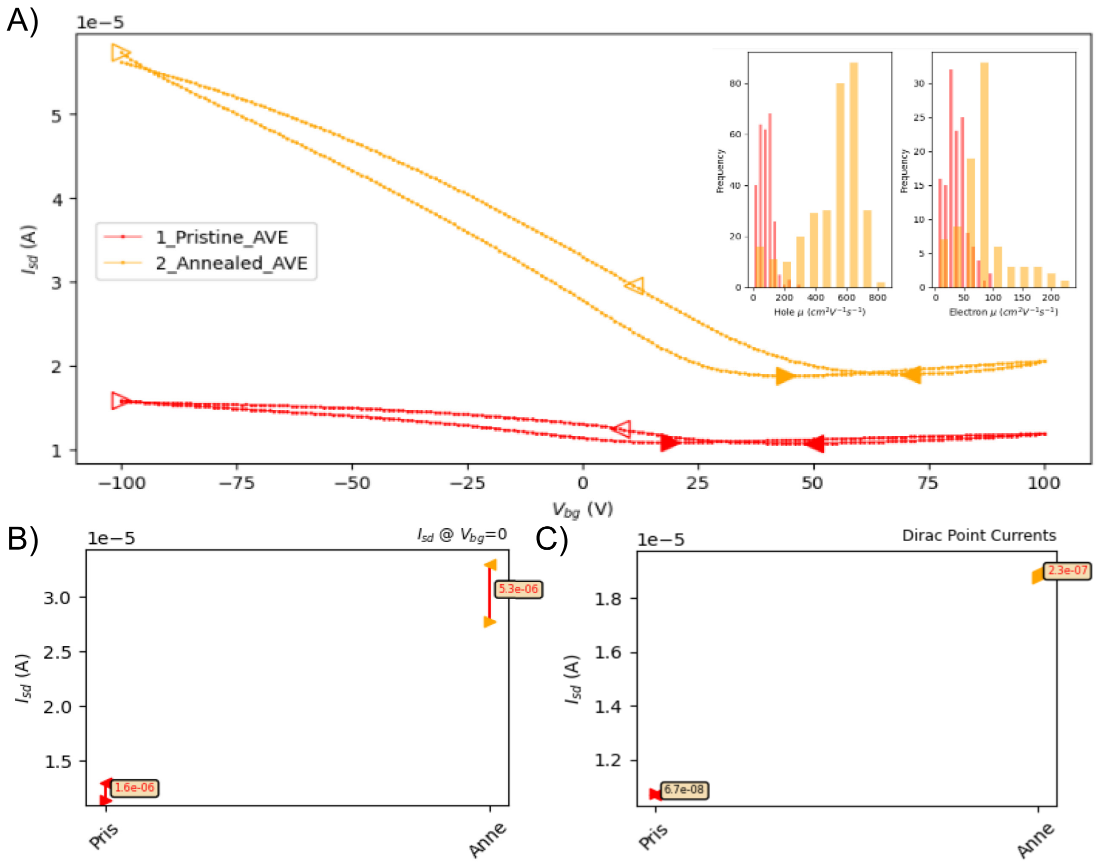

Figure 7.4 A) Visualisation screen showing the sweep characteristics for the pristine and annealed data with inset showing the corresponding mobility values. For the forward and reverse sweeps B) shows the current values at V_G=0 and C) shows the current values for the Dirac points.

For example, the current values for V_{DF} and V_{DR} swap from being higher for V_{DF} at the pristine stage to being higher for V_{DR} at the annealing stage, indicated by the black and red text and bars respectively. A more detailed investigation which considers the impact across multiple devices is provided in 7.5.3.4.

Prior to SCRAMBLE's inception, the end-to-end processing of similar amounts of data would have taken several hours to conduct from collection to visualisation, with several hundred stages to manually complete offering several opportunities for the user to introduce error into the calculations. SCRAMBLE allows users to rapidly compare results maximising time elsewhere and has proved to be an essential tool for sharing critical results such as those shown in Figure 7.4 with others in our group.

7.1.4 Impact

The primary impact of using SCRAMBLE on a daily basis has been the speed at which raw data is converted into informed decisions about next steps in an investigation. Specifically, key artefacts accurately calculated and clearly visualised by SCRAMBLE, that had previously been overlooked, have directed research into new routes of exploration for our group. SCRAMBLE eliminates the delay between acquiring, processing and visualising data as this is all completed in a few automated stages within the package. This means that valuable investigatory time can be applied to further the group's knowledge on how different functionalisation processes impact GFET properties or alternatively into improving experimental design. Data exported from SCRAMBLE is fully compatible with other software processing packages, such as Origin, SigmaPlot and Excel, which eases the transition from raw data to further data analysis. Outputted data from Figure 7.4 is given in Appendix A2.

SCRAMBLE is expected to contribute to any research group working on direct current measurements of GFETs. However, since Python is rapidly growing in popularity across many diverse fields of applications including artificial intelligence, machine learning and big data it is envisaged that the software will be readily refined to suit a plethora of specific applications which involve field effect transistors.

SCRAMBLE has been used in our research group by PhD students for analysis purposes and also as a demonstration tool for Masters students whereby key parameters relating to GFET devices can be clearly visualised and explained. The software also enables students to cover more material during laboratory sessions, due to time saved from processing data, thereby assisting such students in gaining an enhanced understanding of the field. Its use as a training tool in this aspect facilitates the continuous progression of postgraduate students into the group which will secure the future of this research.

7.1.5 Summary

SCRAMBLE is a novel software package which processes raw back-gated field effect sweep measurement data from GFETs into comparable metrics to support researchers to characterise devices in a reproducible manner. It is an easy to use platform, suitable for researchers with limited software skills, which provides key data insights relating to GFETs such as Dirac points and mobility calculations, visualised over several charts and output tables. The combination of SCRAMBLE's simple GUI along with its open and fully customisable source code will make this software package attractive to a large audience of researchers who are developing GFET technologies for a myriad of different applications thus facilitating the discovery of new and exciting avenues for future enquiry. More details can be found at the following source [159].

7.2 Raman Characterisation – Data Processing Software

7.2.1 Motivation and Significance

There are several features of a Raman spectrum that characterise the graphene surface under test including the position, width and intensity ratios between the D, G and 2D peaks (a detailed description of these features is given in 6.3.2.2). It was established early on during this work that the variation in Raman spectra on samples was large (see 7.3.3.1). It would therefore be important to evaluate this level of variation by obtaining large quantities of spectra. Combining the need to evaluate several features per spectra along with a large set of data necessitated the development of a software package to eliminate human error and make reliable conclusions.

RAMAN_VIEWER was thus developed which automates the analysis of raw spectra into useable metrics. Designed to be easy-to-use, this software provides a package of tools that users can harness to streamline their Raman analysis and progress their work forward. Since graphene technologies span a plethora of different research fields it is envisaged that this work will have significant impact to a global research population.

7.2.2 Software Description

The main components of RAMAN_VIEWER's GUI are shown in Figure 7.5. The screen selector tabs above the front panel allow the user to switch between the two functionality views – Parameter and Correlation. The front panel is split into the left hand side control panel and the visualisation screen for all views. The control panel allows the user to import raw .csv files and pre-processed .bod files, select the spectra of choice, fit curves, plot, average, remove baselines and export data. The visualisation screen displays the interactive charts once the plotting buttons are pressed.

7.2.2.1 Using RAMAN_VIEWER - Parameter View

Data can be imported into the RAMAN_VIEWER in one of four ways. The "Open Folder" button will loop over multiple folders to import .txt files each one with multiple spectra acquired during a mapping sequence. Data that has been processed previously in RAMAN_VIEWER and exported can be easily imported using the "Open .BOD File" button saving computational effort. A single .txt file containing one Raman spectrum can be imported using the "Open Simple" button. Using the "Multiple Simple" button imports several .txt files across different folders.

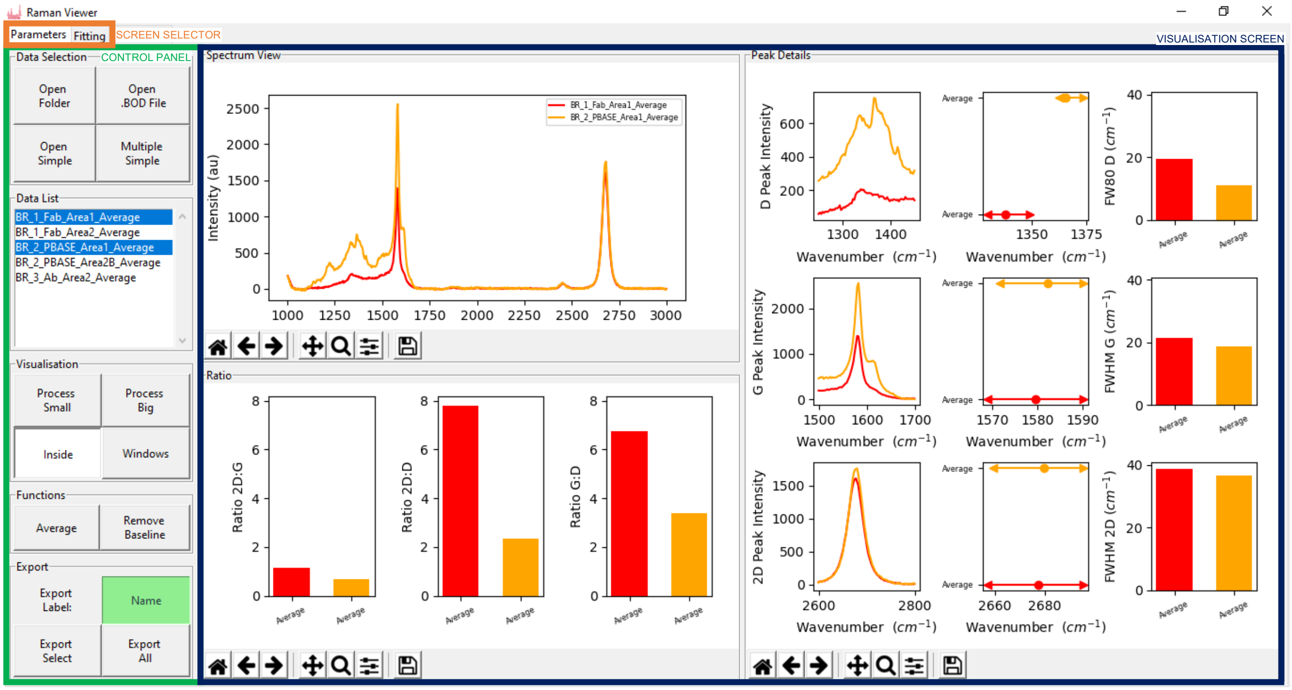

Figure 7.5 RAMAN_VIEWER Parameter View GUI showing the screen selector tabs, control panel with input parameters and visualisation screen where data is represented in various charts. A comparison between Raman spectra for pristine graphene (red) and graphene functionalised with PBASE (yellow) is shown

The user then decides which of the imported spectra they wish to evaluate, by selecting one or more of the labelled names in the “Data List” frame. The user then decides whether they want the charts plotted within the application or in larger individual windows by selecting between “Inside” or “Windows”. Using the “Inside” option is useful for giving an overview of all salient points whereas having the charts plotted in separate windows allows for finer details of each chart to be easily communicated. Next, the user can decide to plot the data in one of two ways. Pressing the “Process Small” button will plot all of the metrics for each spectra in a plain format. This is best suited when comparing smaller quantities of spectra that relate to different functionalisation stages as in Figure 7.5, where two average spectra are compared, one relating to pristine graphene and the other relating to graphene which has been functionalised with PBASE. On the other hand, if the user wishes to display all spectra points for different stages, useful when comparing the variation between spectra for different functionalisation stages, the “Process Big” button should be used. As shown in Figure 7.6, for each of the plotted metrics, an average line is drawn alongside the printed value which helps the user to distinguish anomalies and spectra with significant variation.

7.2.2.2 Software Functionalities – Parameter View

The first stage of the algorithm is to split the spectrum into the three regions of interest surrounding the D, G and 2D peaks.

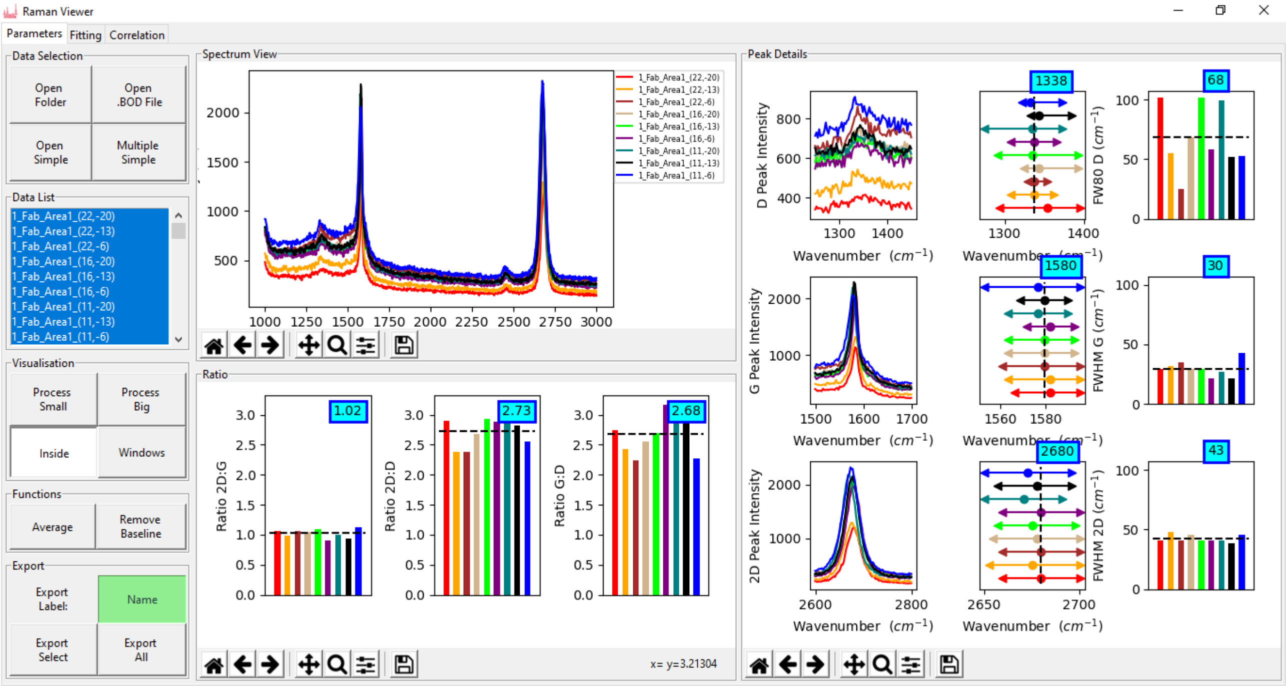

Figure 7.6 Charts plotted when the user presses the “Process Big” option. The broken lines and values presented in blue indicate averages across the displayed metrics

Next, the maximum peak of each region is obtained and then used to determine the wavenumbers representing 50% of the peak intensity (both lower and higher).These values are then used calculate the FWHM. Due to the small intensity of the D peak, wavenumbers representing 90% of the peak are used and therefore full width at 90% of the maximum describes the D peak spread. The peak intensity ratios are computed afterwards. All of these parameters are held in memory and plotted to the charts on the front screen.

RAMAN_VIEWER offers the option to average multiple spectra together. This is achieved by firstly selecting the spectra from the “Data List” and then pressing the “Average” button. The newly created spectra is appended to the list with the text “Average” concatenated to the end to signify that it has been processed within RAMAN_VIEWER. This can then be selected for evaluation as previously discussed.

In order to make comparisons between data sets it was necessary to include the provision of baseline removal in this software. This would eliminate the variation in intensities of each spectrum caused by factors like laser power, laser incidence and ambient temperature. Achieving baseline removal manually using techniques which involved the user selecting the base of peaks is not only labour intensive but also liable to human error and subjective making it unreliable. In a project conducted by Carey et al, six different automated baseline removal techniques on the Raman spectra of minerals were evaluated by measuring the accuracy of classification against mineral samples. The techniques were developed for a wide variety of spectroscopic tools with each one having adjustable parameters, usually selected manually, appropriate for their purpose. This group tested each of the algorithms using the default settings whereby no parameter tuning would be performed. They concluded that the best results were obtained using the Adaptive Iteratively Reweighted Penalised Least Squares (airPLS) method [167, 168].

The airPLS method is an algorithm that is based around Asymmetric Least Squares fitting (ALS). During ALS, Whittaker smoothing is deployed to find a rough estimate of the baseline to be removed before lowering the weight of the points above the baseline and iterating until convergence is reached. The airPLS algorithm builds on ALS by using the sum of the differences between the signal and baseline to iteratively adjust the weights. The reader is signposted to this source [167] for a further description into the algorithm which is outside the scope of this work. Credit for the translation of the algorithm into a useable Python code is given to Liang and Zhimin [169]. The airPLS algorithm is fast, applicable to Raman spectra and crucially independent of user intervention thus improving the consistency of baseline removal across data sets. An example of the airPLS algorithm deployed on a Raman spectrum within RAMAN_VIEWER is shown in Figure 7.7. In this figure, 9 spectra from a map across pristine graphene were averaged together (red line) before the airPLS algorithm was used to remove the baseline (yellow line).

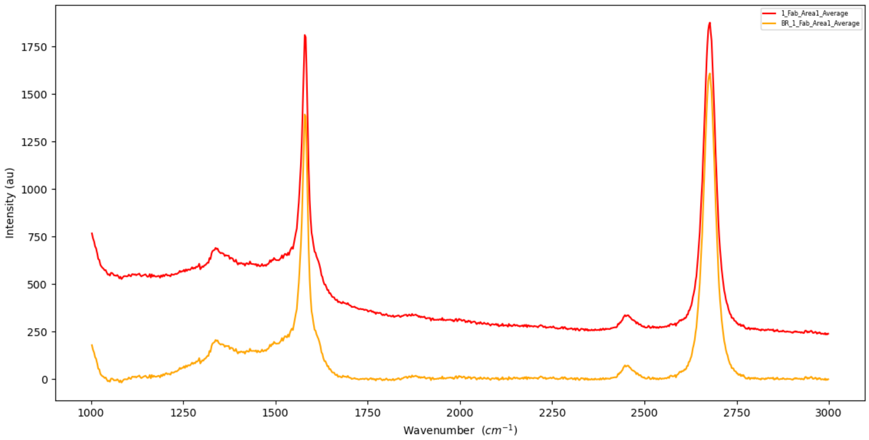

Figure 7.7 Comparison between an averaged spectra of pristine graphene (red) versus one processed with the airPLS algorithm to remove the baseline (yellow).

The individual charts shown in Figure 7.6 can be manipulated with their individual navigation toolbars allowing panning, zooming and the configuration of subplots. Pressing the “Save” icon allows the user to export the plots in various formats such as PNG, SVG and Raw RGBA bitmap to name a few.

The raw data and calculated metrics for spectra can be exported from RAMAN_VIEWER using the “Export Selected” button which performs this on the data highlighted in the “Data List”. This action produces two text files (.bod); one with the raw spectra data and one with the calculated metrics. These are labelled accordingly by concatenating the input of “User Input” entry box with “Export_Selected” and “STATS” for the metrics. Note that using the “Export All” button exports only raw data within the “Data List”. Exported files are given in Appendix A3.

7.2.2.3 Using RAMAN_VIEWER Correlation View

Data must be pre-processed in the Parameter view before it can be analysed in the Correlation view. To do this, the user must select all of the spectra of interest and use the “Export data”, this loops over all selected spectra, determines the metrics of interest and saves them to a file format that is easily read by RAMAN_VIEWER. The user selects one these exported .bod files after pressing the “Open .BOD File” button in the Correlation view. Now the data is listed in terms of the functionalisation stage. Selecting one of the stages will now display all of the individual data points that relates to that stage.

Plotting correlations between data plots can be achieved in two ways. Firstly, the user selects the stages of interest and then chooses which metrics they wish to compare by selecting the two metrics of interest in the selection lists underneath the “Data List”. Then, by pressing the “Process Corr” button, both the correlation matrix and scatter plot is presented as shown in Figure 7.8. The user can see an overview of which metrics correlate by comparing the colours in the matrix, darker red (blues) correspond to stronger positive (negative) correlations.

Alternatively, pressing the “Pre-Defined” buttons will display multiple scatter plots between the metrics as shown in Figure 7.9. These are designed to give the user a quick representation of the relationship between metrics. It is also possible to resolve clustering in these metrics between functionalisation stages which can be clearly seen in the charts on the bottom row of the visualisation screen, which plot the correlation between the peak ratios.

The user also has the option to plot box and whisker charts for the metrics to determine the statistical variation in each functionalisation stage. To do this, the user first selects the functionalisation stage(s) of interest and then presses the “Process Boxes” button. This will produce a 3x3 grid of box and whisker charts relating to data spread for the primary metrics as shown in Figure 7.10. When two functionalisation stages are selected a Welch’s test is conducted to examine the significance of the difference between the two.

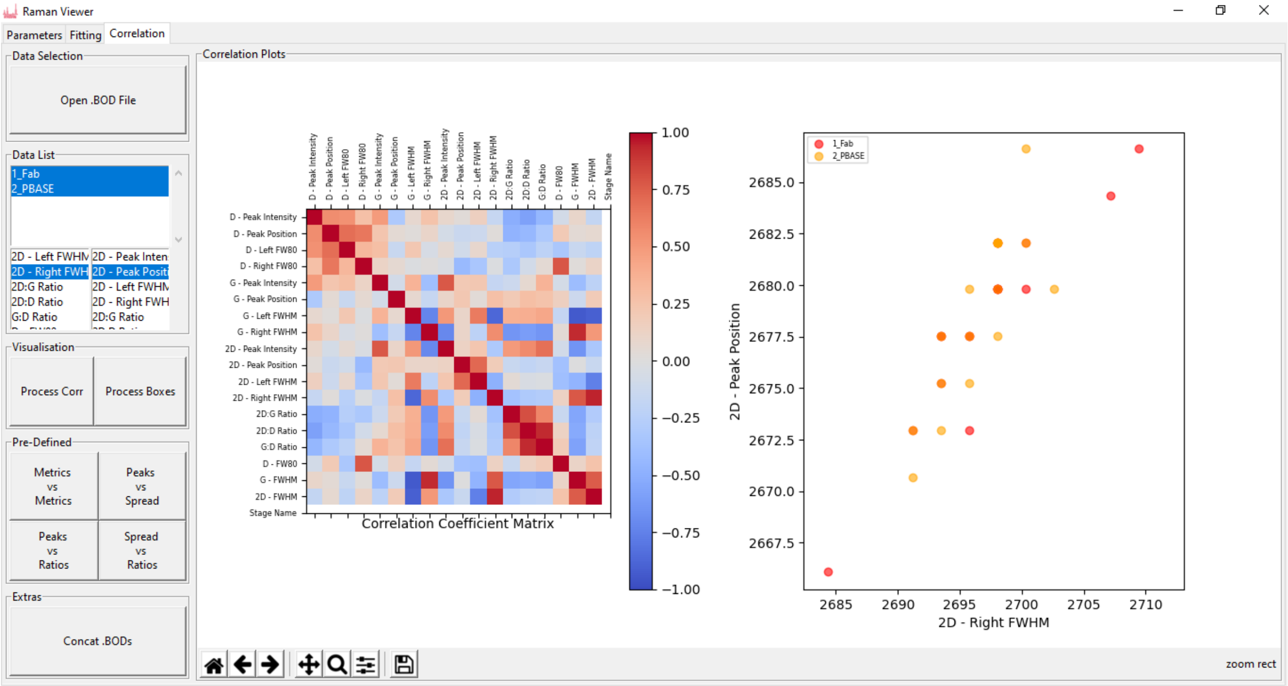

Figure 7.8 RAMAN_VIEWER Correlation View GUI correlation matrix and scatter plot. The matrix displays the correlation across all metrics, darker reds (blues) indicate stronger positive (negative) correlations. The scatter plot shows the individual data points between desired metrics (2D – Right FWHM vs 2D – Peak Position).

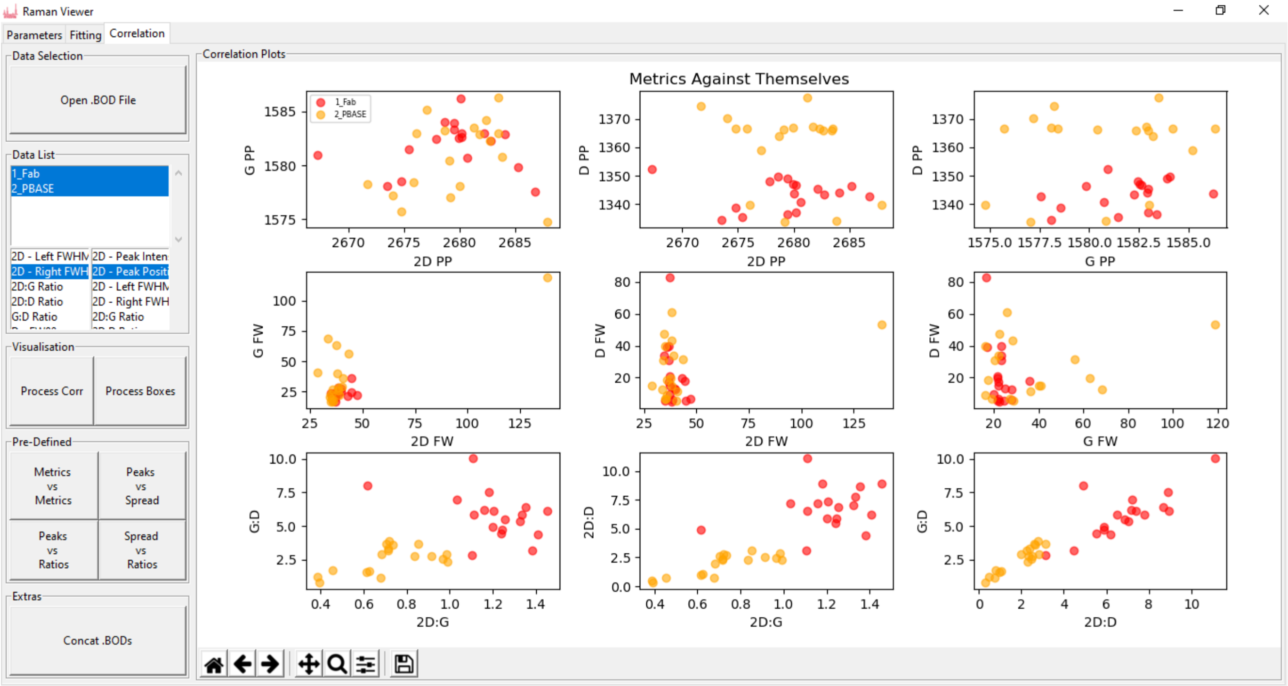

Figure 7.9 RAMAN_VIEWER Correlation View GUI pre-defined scatter plots (Metrics vs Metrics). The charts show the relationships between the metrics with different colours between functionalisation stages showing clear clustering.

When the background of the chart is green there is a statistically significant difference between the two data sets.

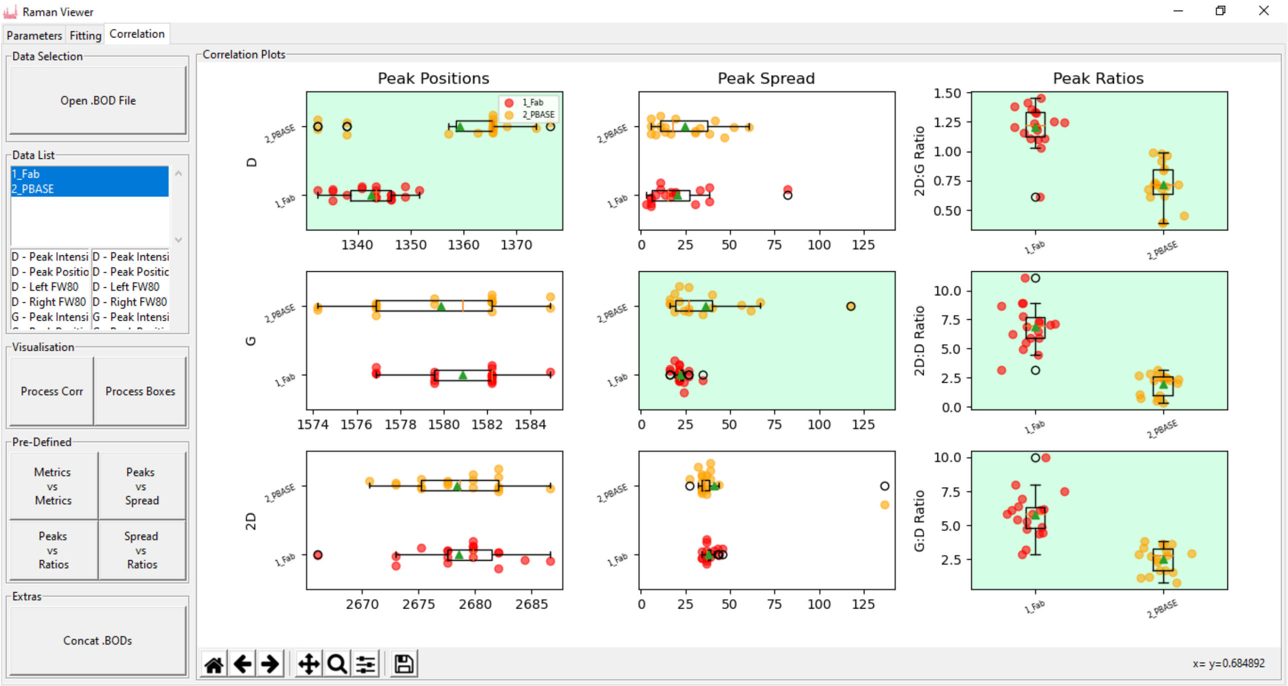

Figure 7.10 RAMAN_VIEWER Correlation View GUI showing box and whisker plots for metrics. Charts which are green highlight to the user that there is a significant difference between the two data sets.

7.2.2.4 Software Functionalities – Correlation View

Statistical testing is an effective way to produce definitive conclusions related to the central tendencies between two populations. The Welch's test (also described as the t-test for unequal variances) is deployed in RAMAN_VIEWER to test the statistical differences between the primary metrics of Raman spectra with a significance set at P=<0.05. Although scarcely used compared to the popular Student's t-test or the Mann-Whitney U test, Ruxton suggests that the Welch test should be used more often due to its suitability when dealing with unequal variances [170]. Unlike the other tests, Welch's test does not assume equal variance between populations, in fact the Student's t-test actually becomes unreliable when the variation is not equal [170]. As the variance is not assessed prior to statistical testing, the Welch's test was selected as the best fit for this application.

The test statistic for the Welch test (t'), along with the degrees of freedom (v) which are both used with the desired P value in the standard t tables to determine significance are calculated using equations 7-1, 7-2 and 7-3:

$$t' = \frac{\mu_1 - \mu_2}{\sqrt{\frac{s_1^2}{n_1} + \frac{s_2^2}{n_2}}} \tag{7-1}$$

$$v = \frac{\left(\frac{1}{n_1} + \frac{u}{n_2}\right)^2}{\frac{1}{n_1^2(n_1 - 1)} + \frac{u^2}{n_2^2(n_2 - 1)}} \tag{7-2}$$

With:

$$u = \frac{s_2^2}{s_1^2} \tag{7-3}$$

where two populations have a mean of μ_1 and μ_2, variance of s_1^2 and s_2^2 and sample sizes n_1 and n_2 respectively.

7.2.3 Illustrative Example

The impact of conjugating PBASE onto graphene is demonstrated here to exhibit the main functionalities of RAMAN_VIEWER. A more detailed discussion on the immobilisation of PBASE onto graphene is provided in section 7.6. Raman spectra across 25 points were captured for fabricated and PBASE treated graphene.

Data validation checks are performed initially, across the collected spectra by looking in detail at each peak to ensure there are no outliers, this is performed using the “Peak Details” screen, which is shown for the fabricated graphene data in Figure 7.11A. Baseline removal is conducted next before averages are calculated and displayed in the “Spectrum View” screen for both functionalisation stages, this screen is shown in Figure 7.11B. This comparison provides the user with a facile technique to highlight the main differences between the spectra. Additional peaks at ~1237 cm^{-1}, ~1370 cm^{-1} and ~1611 cm^{-1} are clearly visualised. Next, the data is imported into the “Correlation View” where summary Box and Whisker plots relating to the Raman metrics are presented, given in Figure 7.11C. These plots show the spread in data for all of the metrics of interest. The user is rapidly able to determine where significant differences occur, indicated by the green backgrounds inferring the result from the Welch’s test.

Significant differences in the peak position and peak spread of the D mode along with the intensity ratios for the 2D:G, 2D:D and G:D are highlighted to the user. This analysis stream, which is completed in a few automated steps, not only removes human error, but rapidly speeds up the process of converting raw Raman data into insightful information relating to the conjugation processes.

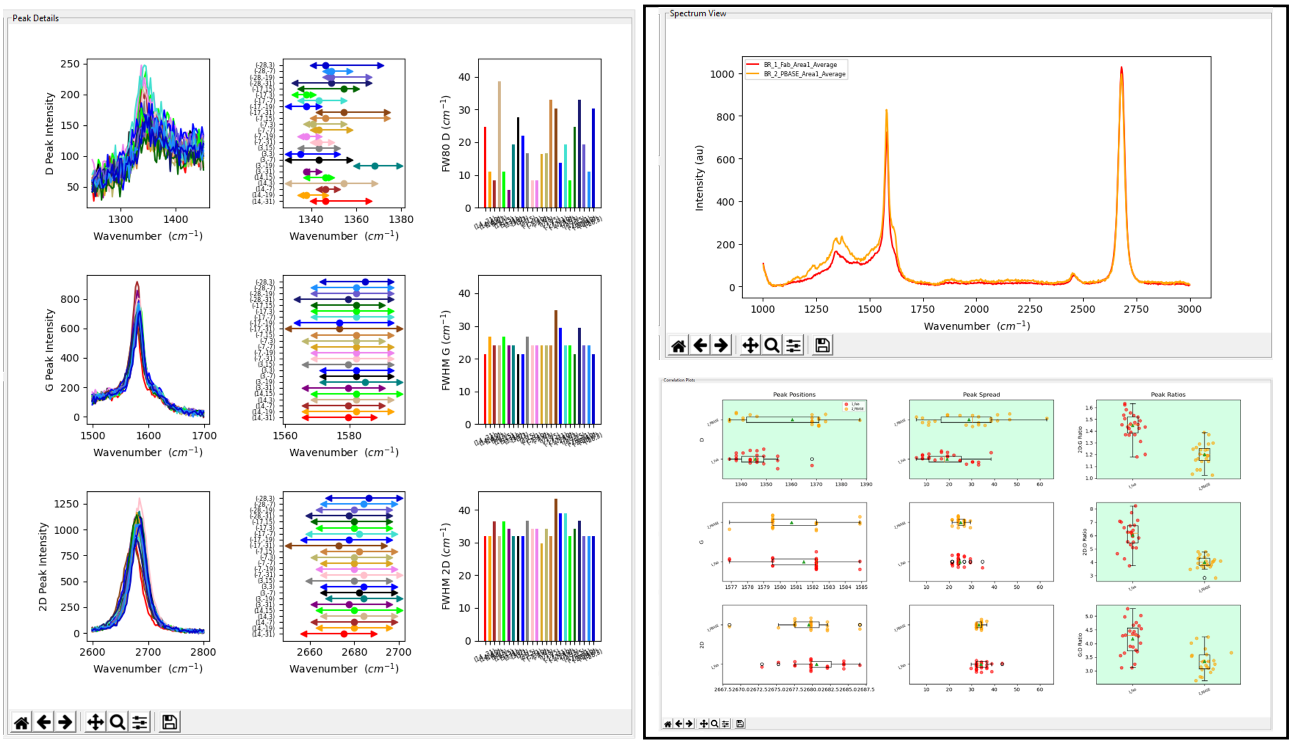

Figure 7.11 RAMAN_VIEWER analysis used to confirm the conjugation of PBASE to graphene channel. A) “Peak Details” screen used to validate data input of raw fabricated graphene spectra. B) “Spectrum View” screen showing average spectra for fabricated and PBASE treated graphene whereby changes in the spectrum, such as additional peaks, are clearly visualised. C) “Correlation View”, showing Box and Whisker plots which show variation across Raman metrics of interest between the functionalisation stages. Differences which are statistically significant are highlighted in green.

7.2.4 Summary

The RAMAN_VIEWER software package processes raw Raman spectral data into insightful visualisations and tables. RAMAN_VIEWER is optimised for assessing metrics associated with all significant peaks across the graphene spectrum (D, G and 2D) automatically deducing comparable metrics such as peak position, FWHM and intensity ratios. The easy-to-use GUI facilitates the rapid processing of Raman data, removing laborious and error-prone procedures for users. Baseline removal, spectral averaging and automatic determination of metrics is included in this package. Correlative analysis can also be completed in RAMAN_VIEWER with useful tools to make comparisons between large data sets easier. In addition, the statistical testing that is embedded in this software allows the user to determine significant differences when making comparisons between collections of individual spectra. This powerful package is envisaged to impact a great number of research fields due to the myriad of exciting applications associated with graphene based research.

7.3 Characterisation Optimisation

This section demonstrates initial results observed through the primary characterisation of the GFET devices using optical, Raman and electrical techniques. For Raman and electrical characterisation, the optimisation of some parameters is illustrated.

7.3.1 Optical Characterisation

Optical characterisation is a high throughput method of assessing the quality of the graphene prior to further investigation. It is a rapid tool for discounting devices with damage which could lead to anomalous results in any biosensor characterisation. Different layers of graphene caused by folding, along with features such as tears, ripples, scrolling, residue and scratches can be easily distinguished using this technique with some examples shown across Figure 7.12. The difficulties in transferring monolayer graphene onto a Si/SiO$_2$ substrate for subsequent GFET fabrication is highlighted in Figure 7.12C-D.

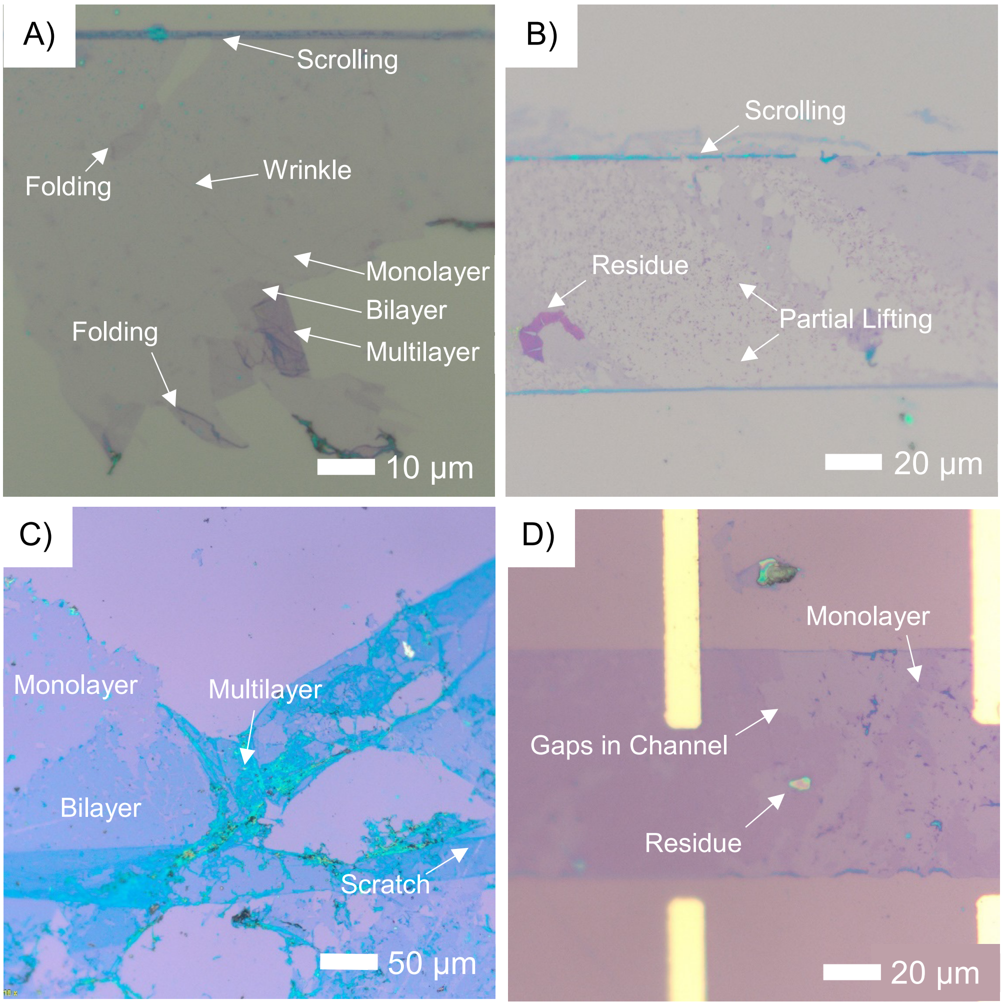

Figure 7.12 (A) & (B) Optical characterisation of graphene channels after fabrication. (C) & (D) Optical characterisation of graphene patch on SiO$_2$ after transfer and then subsequent GFET fabrication.

7.3.2 Electrical Characterisation

7.3.2.1 Linear voltage sweep (I_{SD}-V_{SD})

During a linear voltage sweep, the potential difference between the source and drain electrodes (V_{SD}) is swept from $-V_{SD}^{Max}$ mV up to $+V_{SD}^{Max}$ mV in 101 equal steps. At each voltage step the current through the selected graphene channel is measured. This provides a set of 101 separate current values with which resistance can be calculated from. With zero voltage applied to the back gate, an Ohmic relationship between voltage and current is observed through the current electrodes of the sensor as illustrated in Figure 7.13. It follows that the gradient (inverse) of the line gives the conductance (resistance) of the GFET under test.

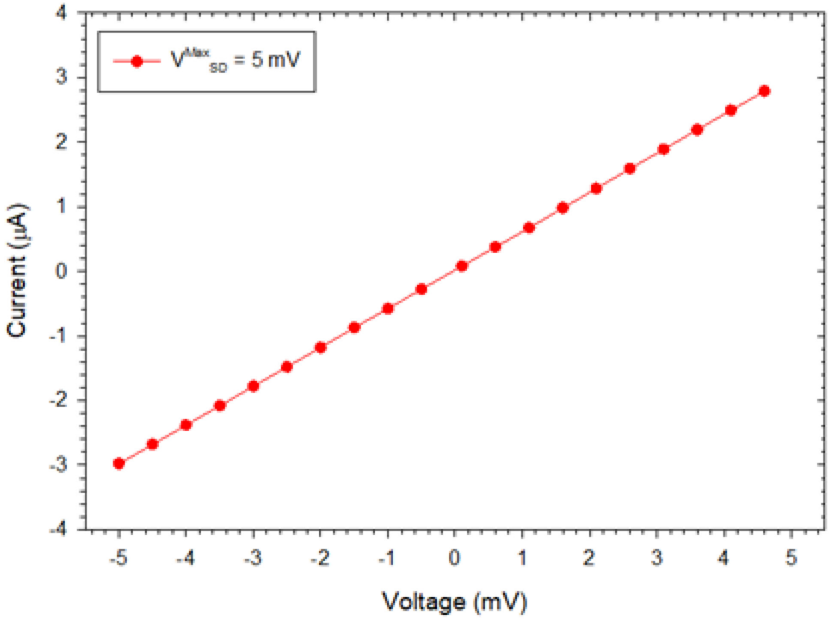

Figure 7.13. Example linear voltage sweep measurement (I_{SD}-V_{SD})

The square (sheet) resistance $R_{\square}$ (R_s) describes the resistance of the measured GFET corrected for its physical geometry and relates to graphene's intrinsic sheet resistivity. As discussed in [165], 2D materials suffer from higher spatial variation in their electrical characteristics which result in a more complicated relationship between devices' resistance and the material's resistivity. Four terminal electrical characterisation performed in this work on Hall bars removes the contact resistance of the probe leads which allows the sheet resistance to be calculated using equation 7-4:

$$R_{\square} = \frac{W}{L}\frac{V_{DS}}{I_{DS}} \qquad 7\text{-}4$$

where $R_\square$ is the square resistance, L, W are the length and width of the device respectively, V_{SD} is the source-drain voltage and I_{SD} is the source-drain current. The reader is signposted to Figure 6.28 which illustrates the convention of length and width when discussing GFET devices. This metric facilitates the comparison between different works in this field.

The impact of sweeping between different V_{SD}^{Max} values is evaluated in Figure 7.14A. As expected for graphene clear Ohmic behaviour, indicated by the single gradient line is displayed across all sweep measurements. On closer examination of this data it is possible to observe outlier measurements clustered around V_{SD} = -1.7 mV and +0.2 mV which manifest themselves above the slope. These values have the effect of increasing the spread of resistance values that are subsequently calculated from the data. Since they occur at similar locations across several devices it is likely this is caused by a systematic error in the measurement equipment and therefore can be removed. Removing these outlier measurements from the calculation, as depicted in Figure 7.14B (2nd box and whisker plots) produces more precise values of the resistance to be obtained. It is clear from Figure 7.14B that the effect of increasing the V_{SD}^{Max} sweep range increases the precision of the resistance, this is due to the improved signal to noise ratio that higher V_{SD} offers.

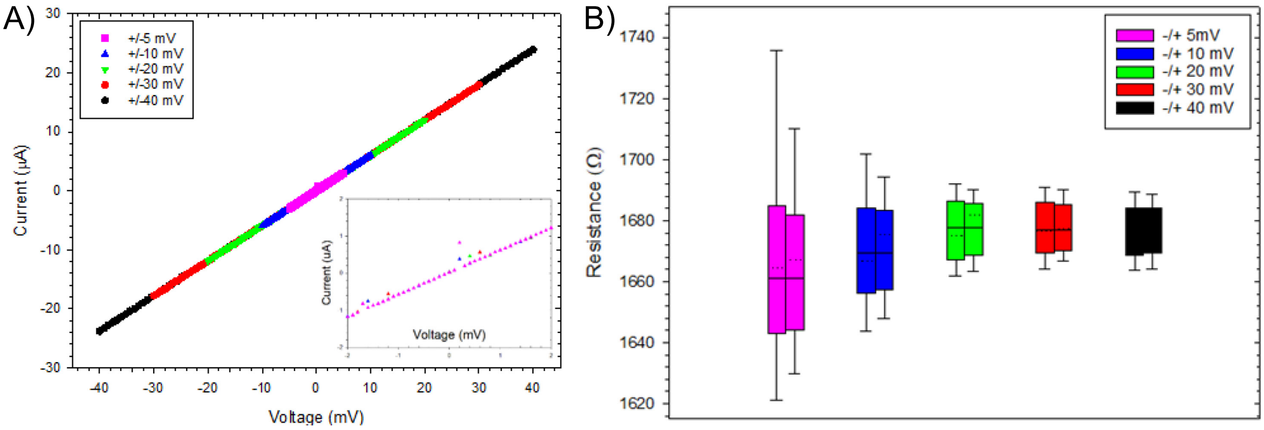

Figure 7.14 A) Overlaid I_{SD}-V_{SD} measurements for different V_{SD}^{Max} values with inset showing outlier measurements caused by equipment artifacts. B) Resistance values before (left) and after (right) outliers removed from data set.

It is possible to alter the I_{SD}-V_{SD} characteristics for the same value of V_{SD} by applying different V_G voltages to the back gate. Since the back-gate modulates the charge carriers in the graphene channel, this alters the mobility within the channel and thus its conductive properties. This is demonstrated in Figure 7.15A, which plots the I_{SD}-V_{SD} measurements of a GFET device with the same V_{SD} (= 5 mV) but with increasing V_G. The conductance in the channel is illustrated by the slope of each line. It is clearly shown in Figure 7.15B that this device does not have symmetrical electrical behaviour about the centre axis as the rate of change in resistance for positive and negative values of V_G is different. These variations in the symmetry of the conductive properties are caused by the fabrication, transfer and handling processes which introduce contaminants and impurities to the graphene channel.

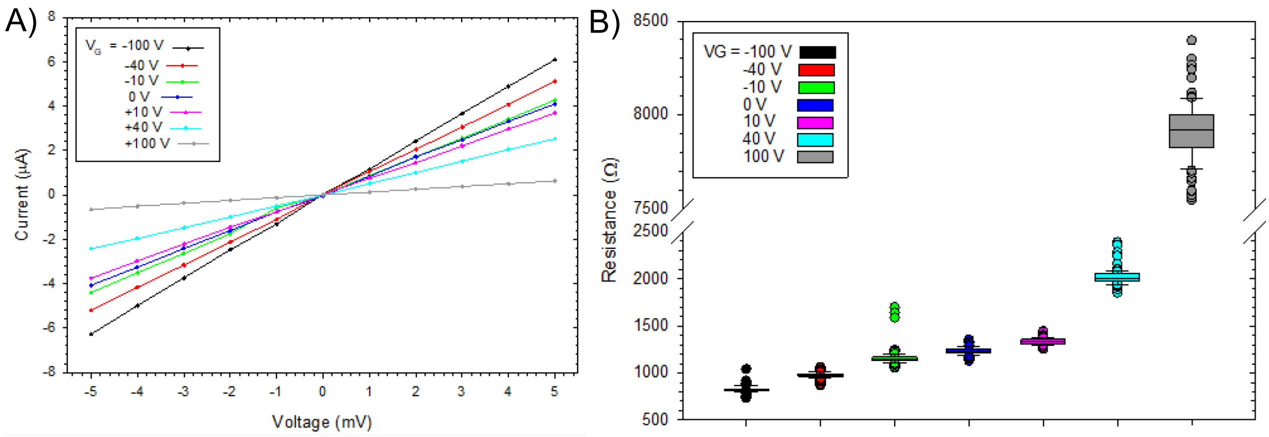

Figure 7.15 A) I_{SD}-V_{SD} measurements with V_{DS}^{Max} = 5 mV and V_G set to different values B) Calculated resistance values for each I_{SD}-V_{SD} sweep.

It is possible to measure several different I_{SD}-V_{SD} sweeps for the same GFET sensor under test as illustrated in Figure 7.16. The variations arise from the minute differences in contact between the probe tips and the Au pads. As the probe tips land and increasing tension builds as they are pushed against the sample stack, their shape changes which impacts their contact to the electrode.

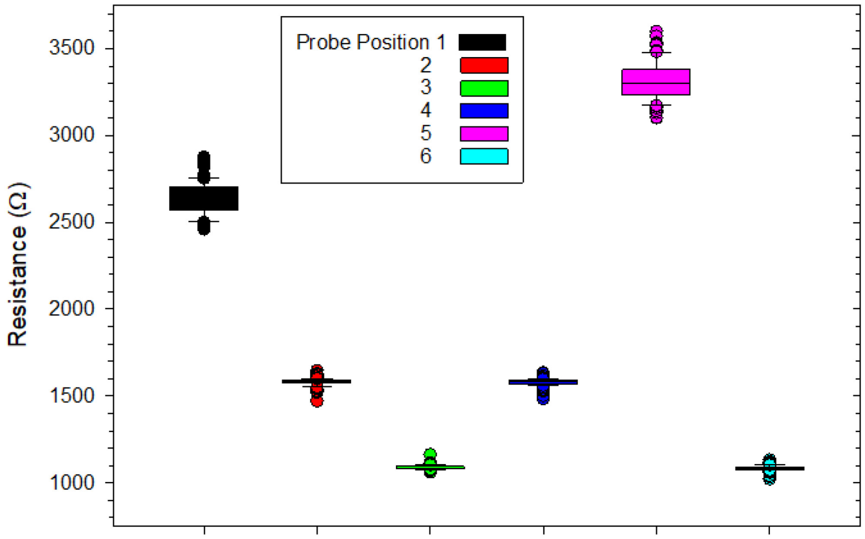

Figure 7.16 Example variability in device resistance which can be observed from different probe positions on the Au electrodes.

Figure 7.16 shows the wide range of calculated resistance possible for a single sensor. Once this effect was observed it was necessary to change the SOP for capturing these measurements in order to combat this. The new SOP developed involves capturing several measurements for each stage with the probes in different positions across their respective pads. Only when there is consistency observed for low resistance measurements (thus improved contact) are the reportable sweeps captured. It is important to note that the device shown in Figure 7.16 is one which shows particularly wide ranging results and is not typical of the majority of devices used in this work.

7.3.2.2 Back-gated voltage sweep (I_{SD}-V_G)

A back-gated voltage sweep relies on sweeping the voltage applied to the gate from $-V_G^{Max}$ up to $+V_G^{Max}$ and then back down to $-V_G^{Max}$ in 401 equal steps. During this measurement V_{SD} is kept constant. The current through the sense circuit is collected at each point on the back-gated sweep and is modulated only due to the effect of the changing applied field at the gate. Hysteretic behaviour is witnessed during these double sweeps leading to two different charge neutral points which correspond to the points of minimum conductivity in the channel, referred to as the Dirac points [158]. The difference in position for the Dirac points is attributed to the interaction between silanol groups (Si-OH) and adsorbed H_2O molecules (from the humid lab environment) which cause charge trapping and transfer which result in dynamic doping of the channel as the V_G is swept in the two directions [171].

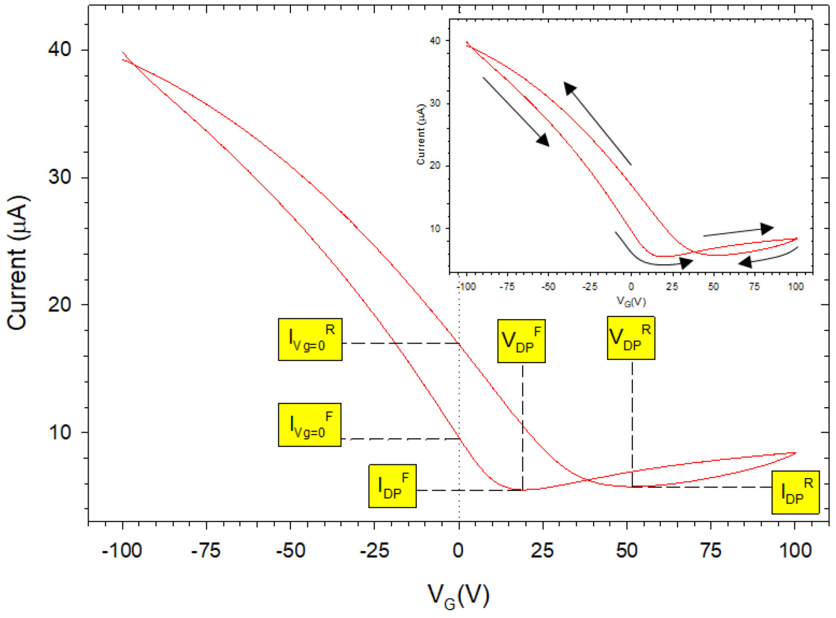

Figure 7.17. Example back-gate sweep measurement (I_{SD}-V_G) with position of prominent metrics indicated. Inset shows the sweep with arrows indicating forward and reverse directions

An example of one such measurement is shown in Figure 7.17. The V_G value of the forward and reverse Dirac points (V_{DP}^F and V_{DP}^R respectively) for device D4 shown are +19 V and +51 V respectively indicating that the graphene channel does not have the symmetrical characteristics described previously (4.3.2) for theoretical graphene conduction. Instead, it is clear from Figure 7.17 that there is a right-shifting in the Dirac points, caused by p-doping effects, creating this asymmetric transfer curve. There are several mechanisms at play which act to introduce p-doping effects into the graphene channel. Weak C-O bonds between graphene and the SiO_2 substrate layer transfer charge to the oxygen group of SiO_2 which act to increase the hole concentration in the channel [171]. In addition, right shifting is also caused by p-doping from additional contaminants on the surface of the graphene, these can be left over from the fabrication/transfer process (LOR/PMMA) or adsorbed to the surface from the ambient laboratory environment (H_2O, O_2 and CO_2 are some examples of adsorbents which can accept electrons from the graphene lattice) [158, 171]. A more detailed discussion into surface adsorbents is provided in section 7.5.

Carrier mobility, which refers to the mobility of both holes and electrons in graphene is a description of how quickly charge carriers move in the material when an electric field is applied [172]. The mobility is described by hole and electron conduction, referring to which charge carrier is the majority contributor to the current through the graphene channel at a particular V_G. At the Dirac point, the voltage of minimum conductance, the Fermi level sits at the intercept between the valence (majority hole) and conduction (majority electron) bands. Conduction in regions below (above) the Dirac point voltage show majority hole (electron) charge carrier contributions.

The field effect mobility is calculated using the direct transconductance method (DTM) described in more detail in [173]. This method relates the mobility of the device (Equation 7-5) with the transconductance (Equation 7-6) and the back-gate capacitance (Equation 7-7). Mobility is calculated at positions of linear conductance from the I_{SD}-V_G transfer curves [73].

$$\mu_{DTM} = g_m \frac{L}{W V_{SD} C_G} \tag{7-5}$$

$$g_m = \frac{\partial I_{SD}}{\partial V_G} \tag{7-6}$$

$$C_G = \frac{\varepsilon_r \varepsilon_0}{t_{ox}} \quad 7\text{-}7$$

where μ_{DTM} is the field effect mobility, g_m is the transconductance, C_G is the back-gate capacitance, L, W are the length and width of the device respectively, V_{SD} is the source-drain voltage, ε_r is the relative permittivity, ε_0 is the permittivity of free space and t_{ox} is the thickness of the insulating layer.

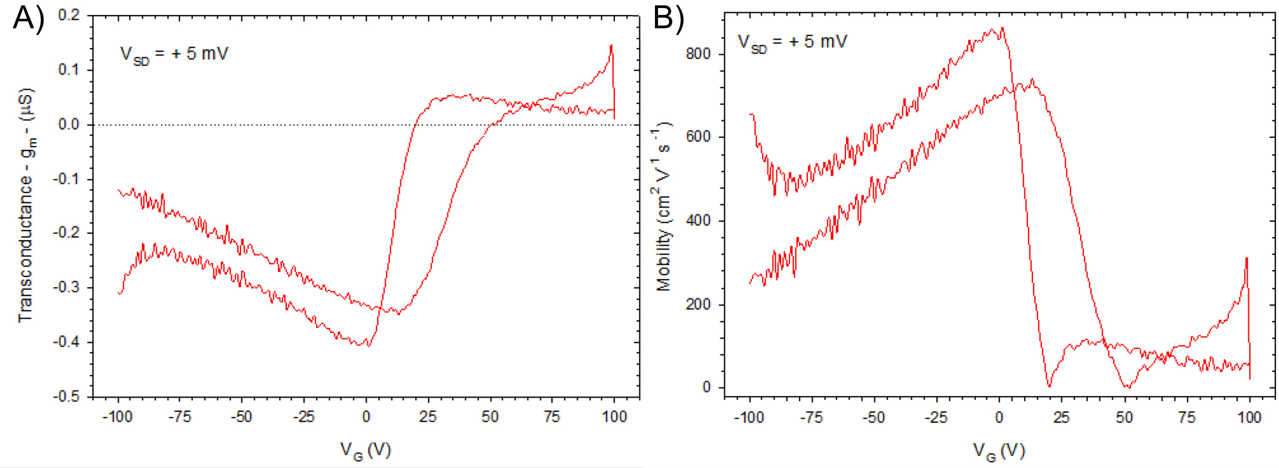

Figure 7.18 A) Calculated transconductance B) mobility using data from Figure 7.17.

The transconductance and mobility is calculated in Figure 7.18A and B respectively. Note that since mobility is directionless, the absolute value of the transconductance is used. Hole and electron mobilities are separated at the values of V_G when the I_{SD}-V_G sweep is at a minimum or at the positions of zero transconductance since they are equivalent. Across Figure 7.18A and B hole (electron) conduction is observed between [-100 V, +24V] and [+50 V,-100 V] ([+25 V, +100 V] and [+100 V, +50 V]).

DTM does not factor in contributions from the contact resistance and therefore always estimates a value lower than the real mobility. This method was chosen as its accuracy has shown to increase for larger channel sizes (>6 µm) which resemble the dimensions of the GFETs used in this work. Reported mobility values in the literature are derived from the peak mobility values calculated using this method [173].

High mobility values are desirable for GFET biosensors due to the increase in sensitivity that follows. Charge carriers in a high mobility material are more affected by alterations in the electric field therefore require less stimuli to impose a change in the conductive properties that are transduced in the GFET device.

Several factors can limit the mobility and therefore sensitivity of GFET devices. The carrier density is impacted by the doping of charge carriers from adsorbed species like water and gas on the surface or between the graphene and oxide layers. It is also influenced by contaminants from the transfer and/or photolithography processes. This impact on carrier density limits the carrier mobility in the GFET device via dominating charged impurity scattering [165].

The transfer curves produced when conducting I_{SD}-V_G sweeps at different V_{SD} values but maintaining V_G between -/+ 100 V are shown in Figure 7.19A. Clearly, the devices are capable of working with a wide range of operating power settings. As shown in Figure 7.19B there is a positive correlation between the V_{SD} value and the maximum transconductance and therefore mobility observed. This indicates that applying a higher V_{SD} value can increase the sensitivity of the biosensor.

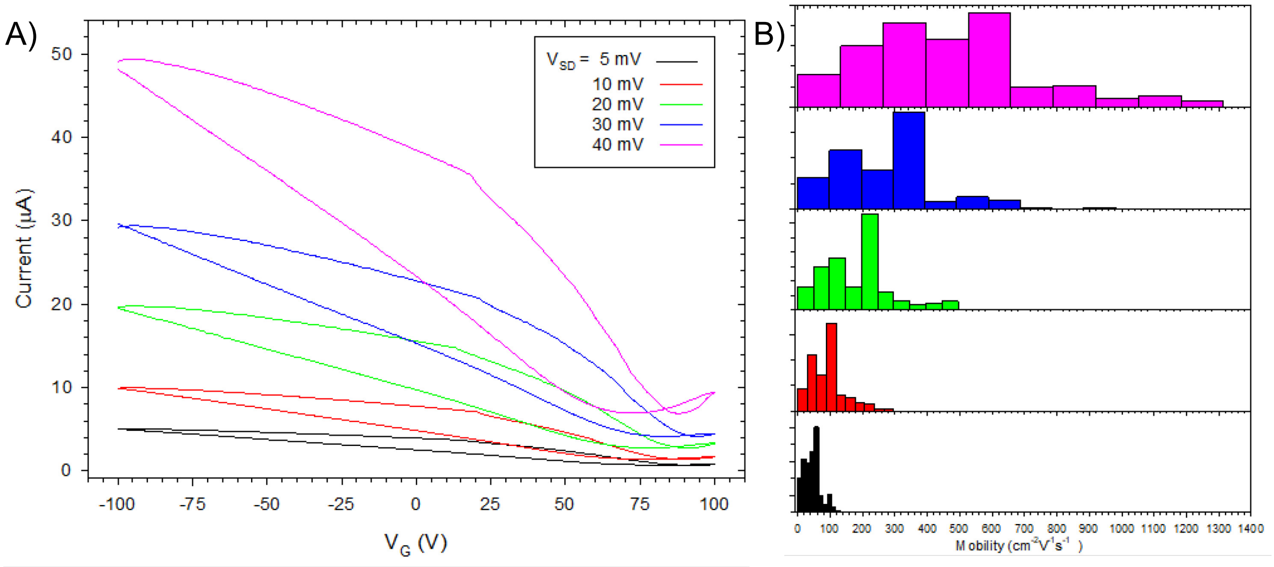

Figure 7.19 A) Example I_{SD}-V_G measurements with different V_{SD} values. B) Calculated mobility values from transfer curves given in A.

The effect of sweeping between different V_G^{Max} values is provided across Figure 7.20. As the sweep range increases both the V_{DP}^F (>) and V_{DP}^R (<) values tend to higher voltages. In addition, the magnitude of hysteresis, quantified by ΔV_{DP} (=V_{DP}^F - V_{DP}^R) increases steadily as illustrated in Figure 7.20B. This is an observation also shared by Wang's group [73]. They conjecture that the physical process behind this relates to the interaction between the V_G and the dangling bonds of the SiO_2 insulating layer. The dangling bonds within the bulk and interface layer act as traps, the charge of which is dependent on the value of V_G. As the V_G changes from its initial starting point these trap sites at the interface between graphene and SiO_2 begin to fill. Holes are trapped initially when the V_G commences at negative values. This results in the graphene feeling a more positive potential than it would with only the V_G applied. At larger - V_G^{Max} values the graphene is exposed to a greater avalanche of charges which become trapped and therefore change the potential that the graphene feels which requires higher positive V_G values in order to reverse the trend. This subsequently increases the voltage between the neutrality points which is transduced as an increase in hysteresis. The reader is advised that the mechanism works in a complimentary fashion for the opposing sweep direction. Alongside the change in V_G^{Max} that these particular sweep measurements were compared against they were also influenced by a difference in sweep rates. Since the same number of points are collected for each sweep, the same hold and delay values of 0.1 s and 0.01 s result in a faster sweep rate for the wider ranges. Since observations by Xu concluded that faster sweep rates were associated with smaller hysteresis [174], it can be inferred from observations here that the interplay between dangling bonds is the dominant contributing mechanism of hysteresis with this device.

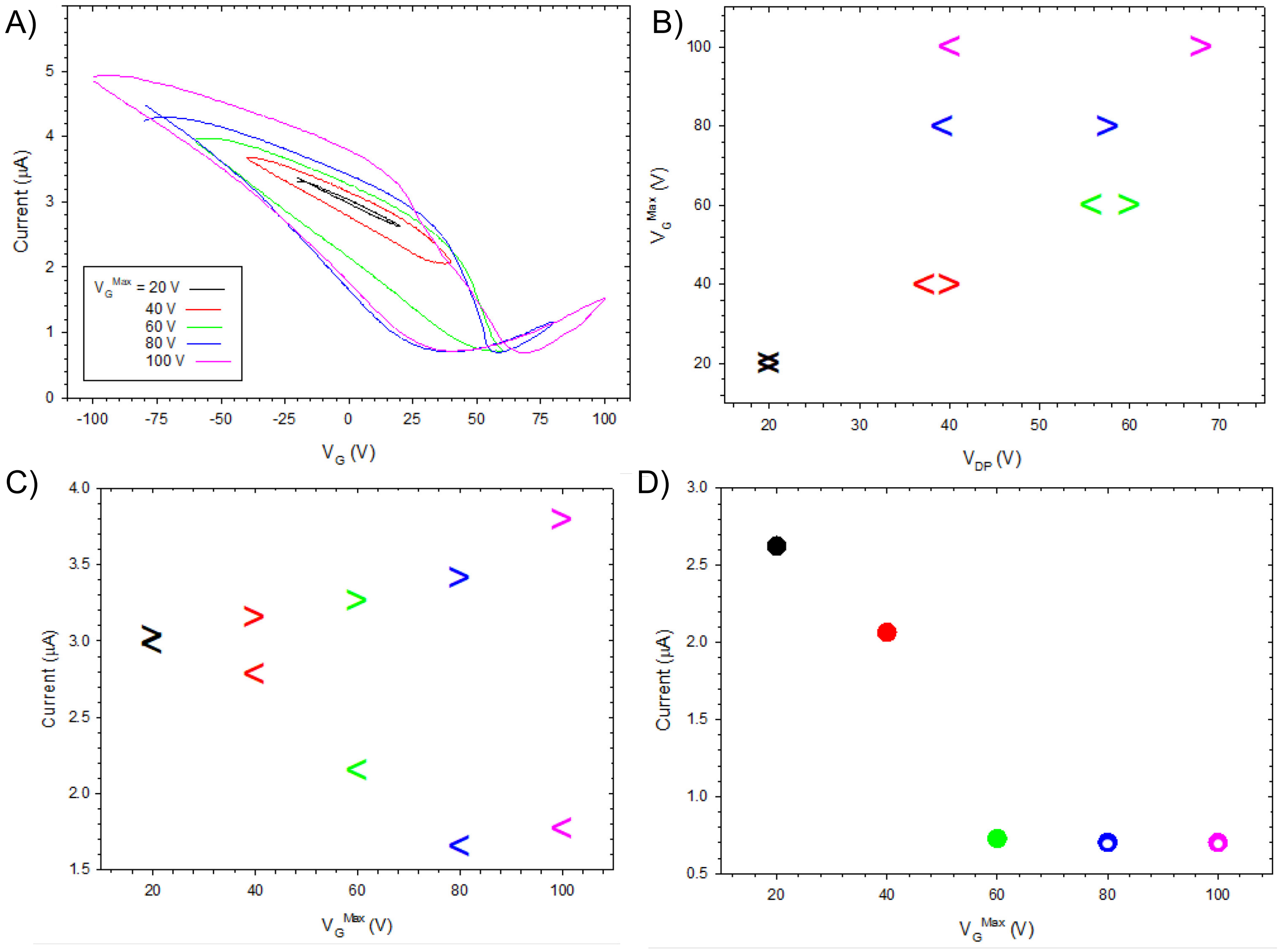

Figure 7.20 Effect of V_G^{Max} on I_{SD}-V_G sweeps. A) Overview of transfer curve. Scatter plots indicating B) V_{DP}^F and V_{DP}^R values against V_G^{Max}. C) $I_{Vg=0}^F$ and $I_{Vg=0}^R$ against V_G^{Max} D) I_{DP}^F and I_{DP}^R values against V_G^{Max}

The current through the device at $V_G = 0$ ($I_{SD}^{Vg=0}$) is plotted in Figure 7.20C and correspond to forward (>) and reverse (<) sweep directions. An increasing (decreasing) trend for this metric is noticed for the forward (reverse) sweep with an increasing V_G^{Max} along with an increasing value of $\Delta I_{SD}^{Vg=0}$ (= $I_{SD}^{F-Vg=0}$ - $I_{SD}^{R-Vg=0}$). It is suggested that the ever-increasing trapping of holes (electrons) caused from higher V_G^{Max} values acts to increase (decrease) $I_{SD}^{Vg=0}$ for the forward (reverse) sweeps because of the additional doping that these charges contribute to the graphene.

The relative position of I_{DP}^F and I_{DP}^R can change depending on V_G^{Max}. This is visualised in Figure 7.20D, which shows filled (unfilled) circles to indicate a higher I_{DP}^F (I_{DP}^R) value. For V_G^{Max} = 40 V and 60 V I_{DP}^F occurs at a higher value than I_{DP}^R. The reverse is true for V_G^{Max} = 80 V and 100 V. Liao's group, who studied hysteresis reversions, observed that when measuring their GFET devices at low temperatures the I_{DP}^F was always higher. They conjectured that charge carriers tended to be de-trapped for the forward sweeps at negative gate voltages [175]. The observations made in Figure 7.20D support this mechanism since I_{DP}^F values were higher for lower values of V_G^{Max} where charge trapping would be smaller. Clearly the impact of temperature has not been factored in here.

7.3.3 Raman Characterisation

7.3.3.1 Raman Parameters

The importance of accurate focussing on the sample, forming an essential step for the SOP, prior to acquiring Raman spectra is demonstrated in Figure 7.21A and B. For these measurements, the sample was brought into focus before a spectra was acquired. Then the sample stage was moved progressively further away and new spectra were acquired at the exact same spot. The intensity across the spectrum with the most accurate focus is the highest and this decreases rapidly with decreasing distance from the focal plane. By considering the spectra normalised against their maximum intensity values, the signal to noise (SNR) ratio can be calculated using the first standard deviation method [176] detailed below in equation 7-8:

$$\boldsymbol{SNR} = \frac{\boldsymbol{S_{peak}} - \boldsymbol{S_{background}}}{\sqrt{\boldsymbol{S_{background}}}} \qquad \text{7-8}$$

The spectra were then normalised and plotted in Figure 7.21B with their calculated SNR values displayed. The difference in the noise is clear when the spectra are normalised.

The D peak (~1318 cm^{-1}) is only discernible when the focus is within 1 µm of the focal plane. The improvement in SNR that appropriate focussing gives between the worst focus (at -10 µm) and the best focus (at 0 µm) is 26 fold. Optimising the SNR is key in order that small peaks which relate to phonon pathways can be identified as these can assist the user in determining whether biofunctionalisation of different molecules to the graphene surface has been successful. It is shown here that appropriate time and effort should be taken to optimise the focus of the sample prior to conducting measurements in order that the SNR of the spectra can be increased.

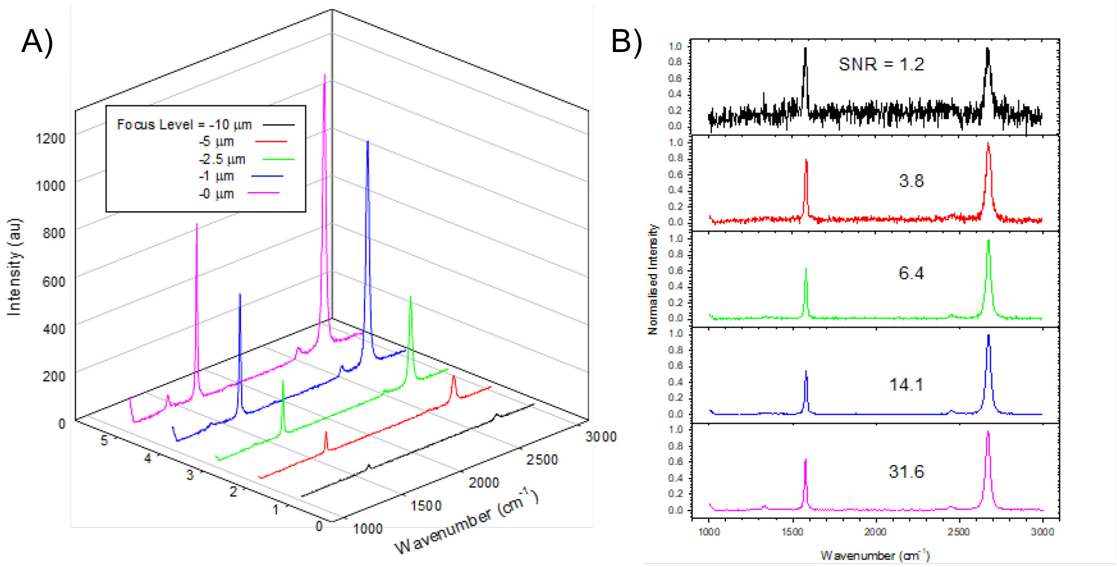

Figure 7.21 A) Raw Raman spectra captured at different levels of focus showing intensity reduction as sample is moved away from the focal plane B) Normalised Raman spectra with calculated SNR

Within the Raman spectrometer the grating is an optical device along the light pathway that receives collimated light and reflects it at wavelength specific angles to the array detector. The gratings are rated by the density of physical grooves (gmm^{-1}) that reflect the light, causing the constructive and destructive interference necessary to reflect it depending on wavelength. This device relates directly to the spectral resolution of the Raman data acquired [177]. High resolution spectra require that this grating is shifted to different positions within the spectrometer during an acquisition. This means that for a single spectra the grating can be shifted multiple times in order that the entire wavenumber range of interest is collected. The additional time that this brings along with the finite time it takes to shift the spectra adds significant delays to the acquisition process, reducing the throughput of this technique. Balance is required between the optimum spectral resolution and acquisition time for this technique. The impact of using gratings at four different groove densities (600 gmm^{-1}, 1200 gmm^{-1}, 1800 gmm^{-1} and 2400 gmm^{-1}) for acquiring a graphene spectrum between 1000 - 3000 cm^{-1} were explored. The spectral resolution for all four groove densities and how they vary across the data points when acquiring data between 1000 – 3000 cm^{-1} is shown in Figure 7.22.

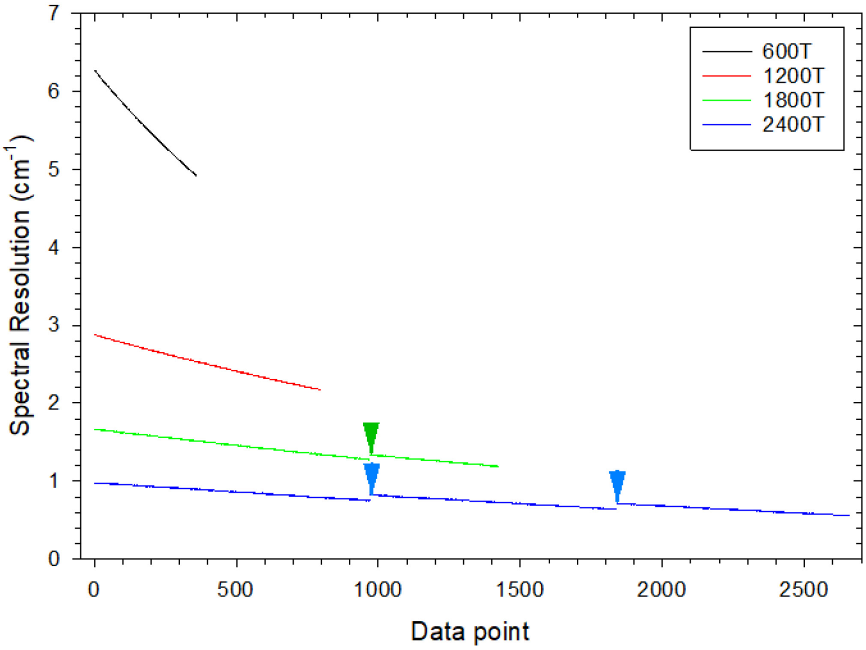

Figure 7.22 Spectral dependence on data point number whilst using 600 gmm^{-1} (black), 1200 gmm^{-1} (red), 1800 gmm^{-1} (green) and 2400 gmm^{-1} (blue) gratings to capture graphene spectra between 1000 -3000 cm^{-1}. Coloured arrows show locations where the spectra is acquired after the grating has shifted.

It was determined that the resolution for 600 gmm^{-1}, 1200 gmm^{-1}, 1800 gmm^{-1} and 2400 gmm^{-1} were between 6.27 – 4.93 cm^{-1} , 2.87 – 2.17 cm^{-1} , 1.67 – 1.19 cm^{-1} and 0.98 – 0.55 cm^{-1} respectively. It is observed that the resolution improves with the number of data points which relates to higher wavenumbers. The reflection angle at the grating is proportional to the wavelength, therefore since higher wavenumbers correspond to smaller wavelengths of light which are reflected less by the grating, the spectral resolution at the array is lower. This mechanism is inferred in Figure 7.22.

For the 600 gmm^{-1} and 1200 gmm^{-1} gratings the entire 1000 - 3000 cm^{-1} spectral range can be captured with the grating in the same position. This is not true for the 1800 gmm^{-1} (2400 gmm^{-1}) gratings which require the grating to move once (twice) during the acquisition, as indicated on Figure 7.22 by the green (blue) arrows which show the first point captured after the grating is shifted. Since the National Physics Laboratory (NPL) recommend a minimum spectral resolution of 3 cm^{-1} for the characterisation of graphene samples [139] it is clear that the grating of 1200 gmm^{-1} provides the optimum balance between resolution and throughput.

During initial Raman characterisation conducted during this contribution a wide spread in data was observed for Raman metrics across the same sample. This phenomenon was then observed across different graphene samples and functionalisation stages.

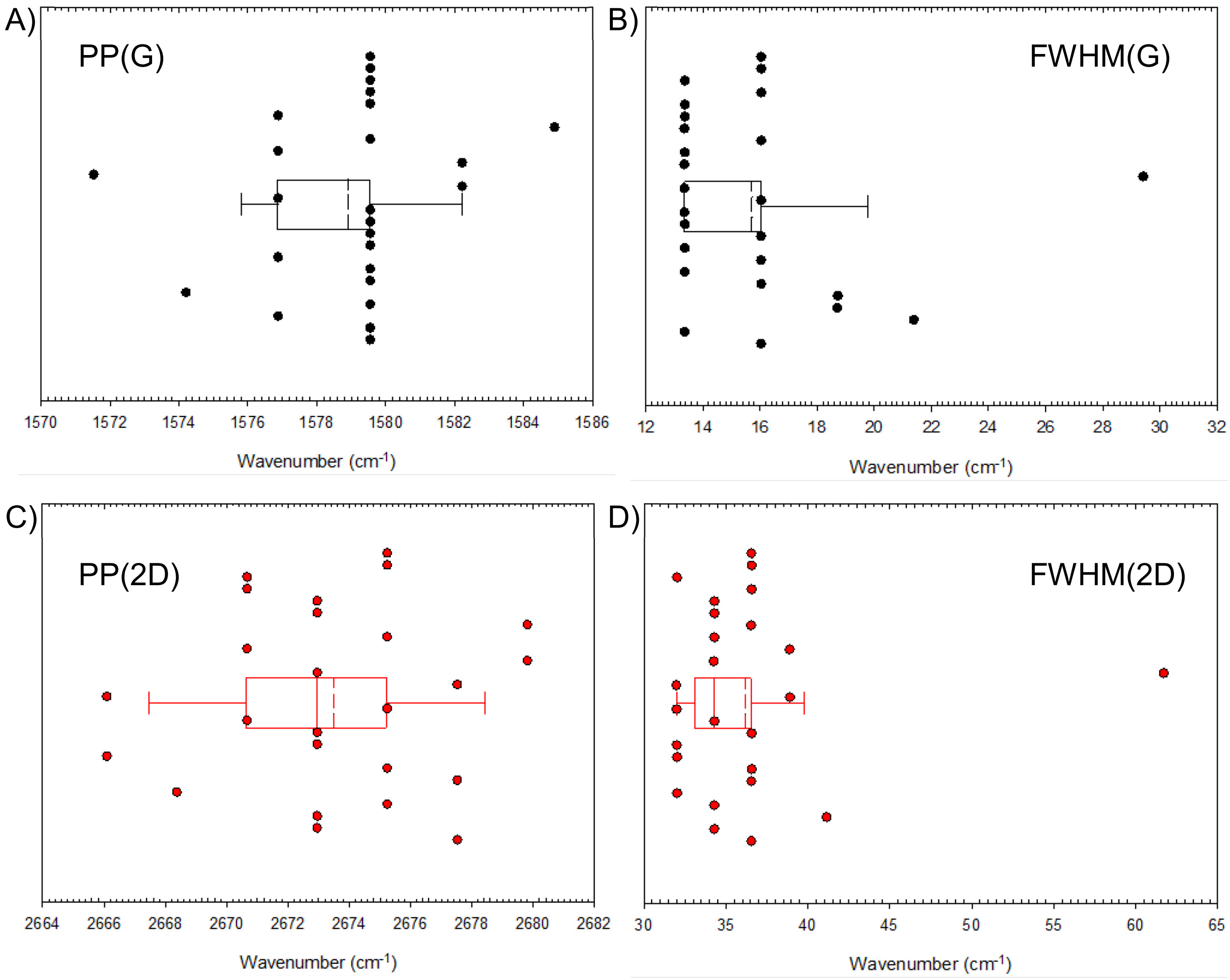

Figure 7.23 Box and whisker plots showing the spread in data for graphene samples for A) PP(G), B) FWHM(G), C) PP(2D) and D) FWHM(2D) for one graphene sample.

This is easily shown during standard mapping whereby 25 individual spectra captured in a 5 x 5 grid across the same sample is captured. Some of the prominent Raman metrics across a pristine graphene sample including G-peak position (PP(G)), FWHM(G), PP(2D) and FWHM(2D) are shown in Figure 7.23A-D respectively. Figure 7.23 details the large variation across the same sample for key Raman metrics. Remnants of PMMA used in the transfer process is attributed to the disparity observed across these metrics [178]. This phenomenon is displayed here to highlight to the reader how important large sample sizes and statistical testing are in making rigorous conclusions based on these measurements (supported by NPL [139]). The reader is cautioned towards studies in the literature that use low sample numbers and/or single spectra to infer conclusions based on these metrics since they can be unrepresentative of the entire sample. It is not uncommon for the literature to omit details related to this variation and it is one objective of this contribution to see a greater discussion on this topic, to improve the validity of future work.

7.3.3.2 Representative Measurements

The influence of the Si/SiO$_2$ substrate on the Raman spectrum can be examined by widening the wavenumber range of interest between 400 – 3000 cm^{-1} as shown in Figure 7.24.

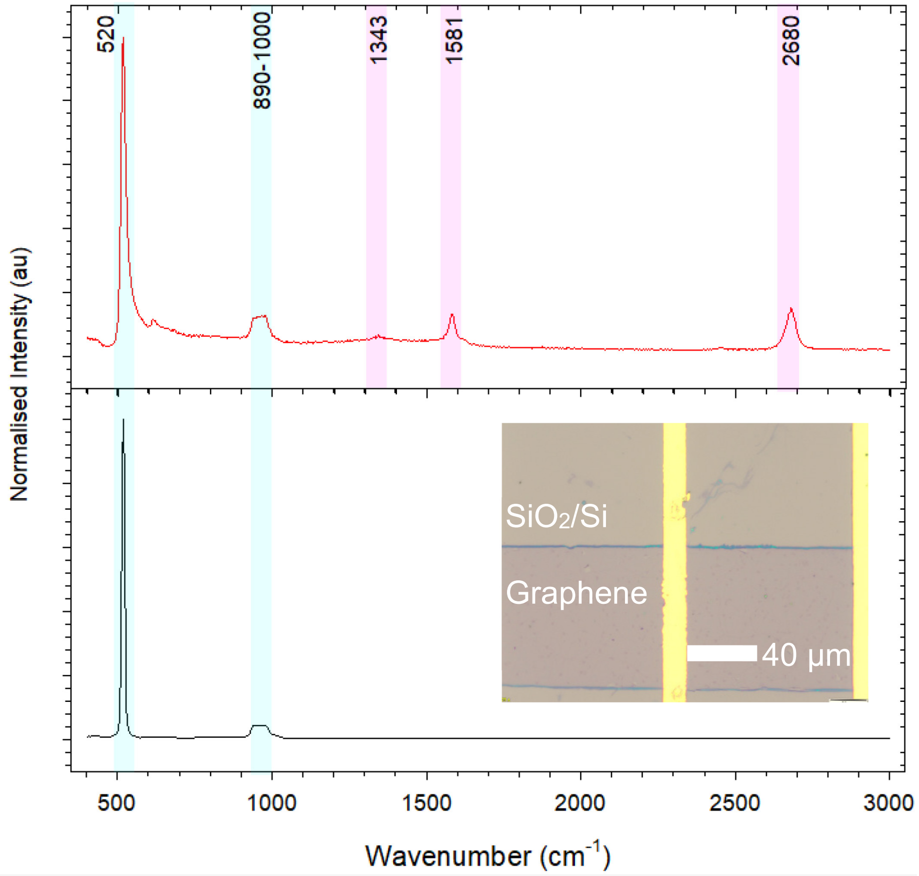

Figure 7.24 Raman spectrum of Si/SiO$_2$ (black line) only and with monolayer graphene deposited over Si/SiO$_2$. The positions of prominent peaks have been highlighted in blue and pink to show features that are caused by the substrate or monolayer graphene respectively. Inset shows typical graphene/SiO$_2$ regions where this data was acquired from.

In this figure, the black spectrum shows the Raman spectrum for Si/SiO$_2$ only whereas the red spectrum represents a typical Raman spectrum for monolayer graphene deposited onto a Si/SiO$_2$ stack. The blue shaded regions indicate features that arise from the Si/SiO$_2$ substrate, namely; the dominant Si 1st order peak at 520 cm^{-1} caused by triple degenerate optical phonons [137] and the broad flat top peak between 890 – 1000 cm^{-1} caused within Si by multi-phonon scattering [179].The trailing edge of this broad peak is visible in most graphene spectra captured between 1000-3000 cm^{-1}. The Si peak at 520 cm^{-1} is used as standard to calibrate the Raman system against, prior to conducting reportable measurements, due to its strong intensity. The position of the D (~1382 cm^{-1}), G (~1574 cm^{-1}) and 2D (~2669 cm^{-1}) peaks which are present only in the red spectrum confirm that this region has had graphene successfully deposited onto the substrate.

7.3.4 Summary

Some of the undesirable features that may be present on graphene were demonstrated initially in this work via optical characterisation. Then, optimisation of the electrical and Raman SOPs were described in order to obtain accurate and repeatable results for this contribution.

The electrical characterisation of GFET biosensors consists of two primary measurements; the I_{SD}-V_{SD} and I_{SD}-V_G sweeps. From the I_{SD}-V_{SD} sweep, the conductance of the channel can be calculated which can be used to determine the square resistance of the graphene, which is a convenient measure to compare against other work in the literature. Typical metrics associated with the I_{SD}-V_G transfer curve were then described along with the derivation of the field effect mobility, yet another metric which is widely used to benchmark devices across the literature. Typical devices used in this work showed non-zero V_{DP} values with hysteretic behaviour indicating p-doping of the graphene along with charge trapping sites caused by the dangling bonds from the insulating layer. The dependency of the sweep characteristics on V_{SD} and V_G^{Max} were then displayed. From the initial characterisations described above, the following SOP for all electrical measurements was developed. This was designed primarily to reduce the variation in probe contact which could influence the results. Firstly, probes needles were positioned on the appropriate pads. An initial I_{SD}-V_{SD} scan would then be acquired and if Ohmic contact was observed, the probe needle positioning was changed before another measurement was captured. Assuming good agreement was observed between these two results, the I_{SD}-V_G transfer curve would then be acquired. Confirming that there is good agreement between the $I_{SD}^{F\text{-}Vg=0}$/ $I_{SD}^{R\text{-}Vg=0}$ and I_{SD} at V_{SD} = +5 mV (via the I_{SD}-V_{SD} sweep) values allows the user to have confidence that the needle positions would not have changed and that the results are an accurate depiction of the sensor under test. Although greater values of V_{SD} were shown to give higher precision resistance values and greater mobility, it was decided that the value for V_{SD} would be set at + 5 mV for biosensing purposes since it reduces the chance of chemical and biological reactions occurring close to the device [180]. In addition, due to the right shifting of the transfer curves it would be necessary to set V_G^{Max} at 100 V for all

I_{SD}-V_G sweeps, to ensure that changes across the key electrical metrics could be tracked for the different functionalisation stages. In order that these devices can be used outside the laboratory setting, further work will need to be done to reduce the p-doping effect these devices exhibit which will facilitate a reduced V_G^{Max} value suitable for low-power field and distributed settings.

The SOP influencing the Raman characterisation was enhanced next. The importance of accurate focussing to maximise the SNR ratio was demonstrated in this work. Although less significant for pristine and fabricated graphene, where the spectra is made up of mainly 3 large peaks, maximising the SNR would allow for additional peaks, introduced from conjugated materials, to be resolved. The appropriate grating for the Raman spectrometer was then selected based on data that demonstrated suitable resolution whilst maintaining a sustainable throughput. The large variation observed across metrics relating to samples of the same specification were demonstrated to the reader to highlight the importance of large data sets and statistical testing to infer significance when making conclusions.

It is the ambition that this work will commence a greater transparency in observations which relate to the variability of devices like those shown here. Quite often the number of repeated measurements for electrical and Raman measurements is not detailed in the literature. This prevents the reader from critically assessing any of the conclusions derived from the results. A greater transparency in this area will act to develop effective SOPs for measuring and handling GFET devices thus improving the confidence of the acquired data subsequently uplifting this exciting research field.

7.4 GFET Fabrication

Unless otherwise stated, reportable results in this work were measured from devices fabricated by following the process described in sections 6.2.2 and 6.2.3 which is hereafter referred to as “Technique A”. This process yielded up to four chips with a maximum of 25 GFET devices on each.

7.4.1 Technique A – Evaporated Cr / Sputtered Au

An image of a typical GFET device and a fabricated chip is given in Figure 7.25. The sensor dimensions highlighted in green in Figure 7.25A are 95 µm by 80 µm for the length and width of the sensor respectively.

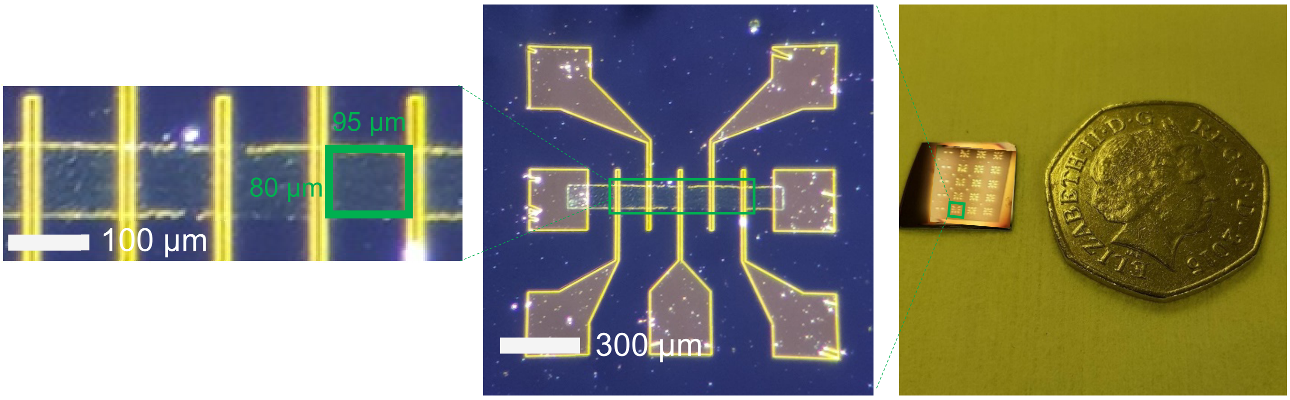

Figure 7.25. Left Panel – Individual sensors between electrodes across GFET device, Centre Panel - Typical 7-electrode Hall-bar GFET device, Right Panel – Fabricated chip at the end of the electrode deposition phase with 50 pence coin for scale.

It is clear from Figure 7.25B that the fabrication has been successful. Firstly, the graphene channel is a distinct rectangle with uniform surface morphology. Secondly, all of the electrode pads and contacts are electrically isolated from each other with well-defined edges. It is worth noting that small scratches visualised on the sides of the electrode pads are the result of initial electrical testing on this particular device. Thirdly, all of the contact pads, including the source and drain pads, make continuous contact with the graphene channel. The successful fabrication of a chip is achieved when the GFET devices are realised with these characteristics. It is estimated that the overall yield of fully functional devices fabricated in this way was 80%. The 20% that were not suitable for further evaluation experienced faults which degraded their quality. This could be due to Au bridges linking electrodes and short circuiting the graphene channels, delamination of the Au bonding leads resulting in poor (or zero) contact to the graphene or gaps in the graphene channel caused by discontinuous CVD growth or unintentional removal during the final remover stage.

Optical investigation of such faults however is not always definitive since some bonding leads can appear connected but are in fact delaminated from the graphene surface. One way that this phenomenon can be screened prior to electrical characterisation is by the use of an AFM as demonstrated by Sikora. This group mapped the surface potential of their GFET device and correlated it with topography maps to find areas of damage. Poorly connected bonding leads showed a clear reduction in the electrostatic potential [181].

7.4.1.1 Raman Characterisation of Fabricated Graphene

The Raman spectra of as-purchased pristine graphene and post fabrication graphene are shown in Figure 7.26. The existence of the D peak in the pristine sample is expected and is attributed to the introduction of defects to the lattice during the CVD process [182]. A detailed description of possible defects is outside the scope of this work but is provided in [183].

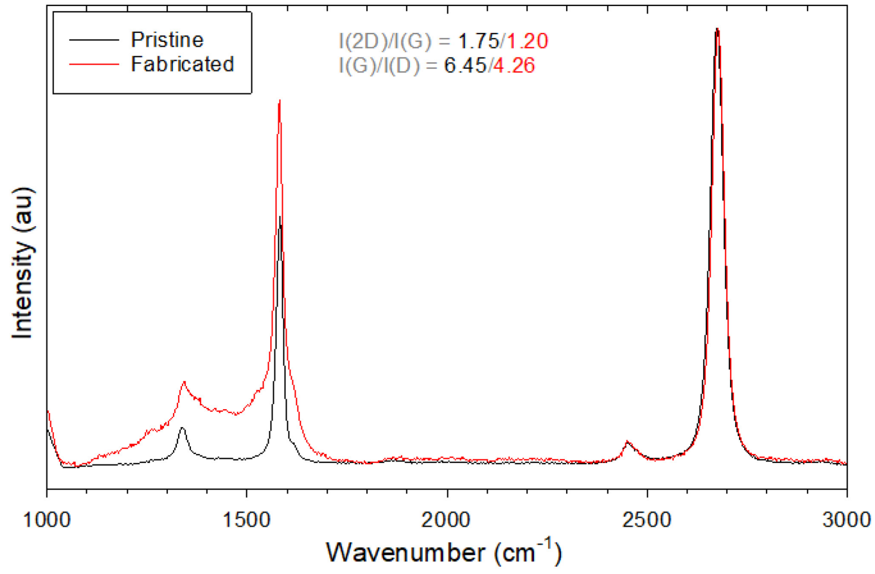

Figure 7.26 Normalised average spectra captured across pristine (black) and fabricated (red) graphene.

Since there is no offset applied to the spectra and they are both normalised against their maximum value, Figure 7.26 shows the significant increase in the D and G peaks caused by the fabrication process. As previously discussed in 6.3.2.2 the ratio between I(2D):I(G) can be used to describe the doping of the graphene channel, with a negative correlation observed between I(2D):I(G) and doping. The reduction of 31% can therefore be attributed to an increase in doping in the graphene channel caused by residues from the fabrication process. In addition, the increase in significance of the D peak, illustrated by the 34%

reduction in I(G):I(D) ratio for the fabricated graphene channel shows that the disorder in the channel is increased [184].

7.4.1.2 Electrical Characterisation of Graphene

The variation in the I_{SD}-V_G sweep characteristics across sensors from fabricated asymmetric and symmetric devices are shown in Figure 7.27B and D. For the asymmetric sensors all transfer curves are very similar which results in similar mobility values (max ~ 1200 cm^{2}V^{-1}s^{-1}) across all sensors. In addition, all of the V_{DP}^F and V_{DP}^R points lie within 4 V and 3 V respectively of each other with a current range of only 0.14 μA. This similarity in transfer curve and Dirac point positions can be explained due to uniform doping from the fabrication process across the device and good connection between the graphene and the Cr/Au leads.

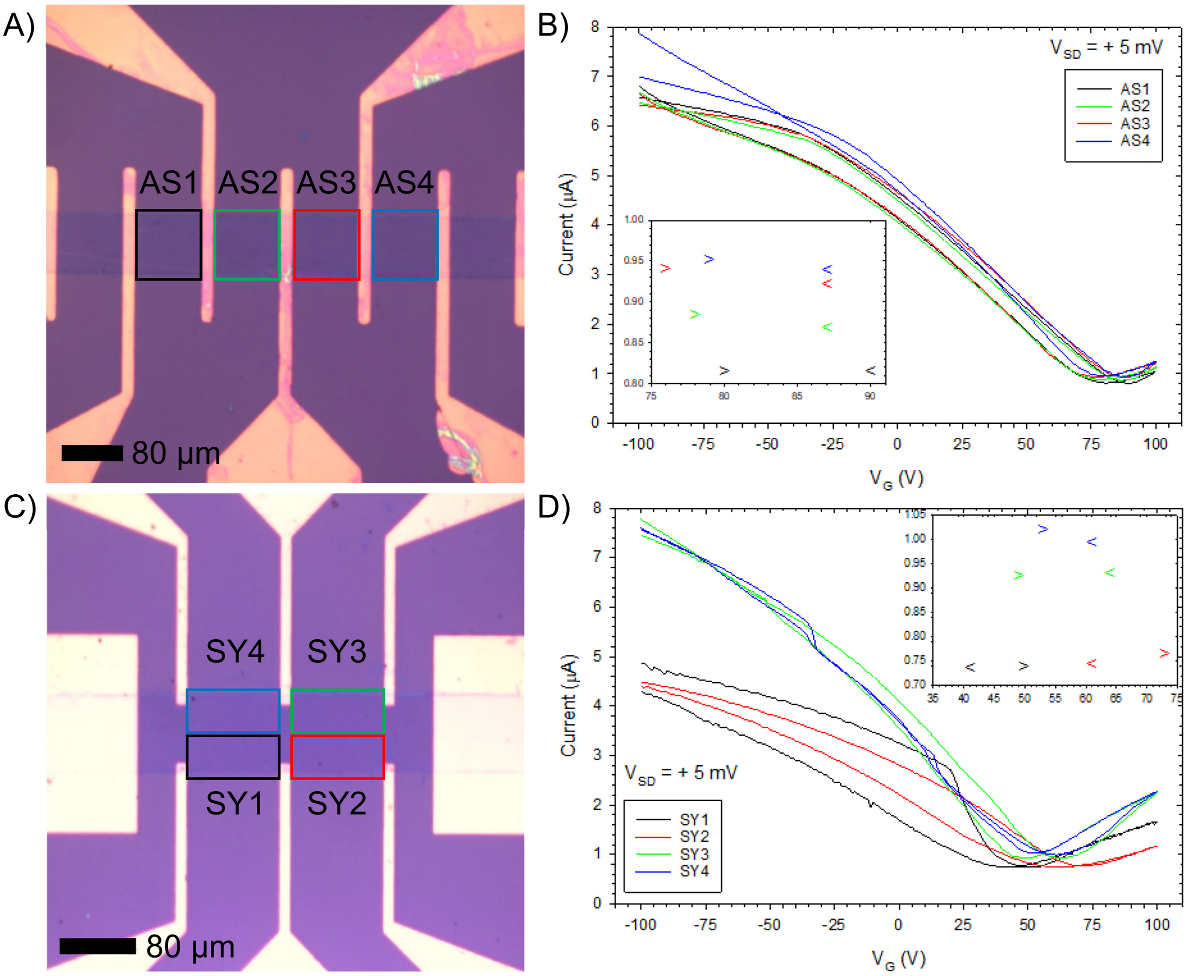

Figure 7.27 Image showing overview of A) asymmetric and C) symmetric devices with transfer curves showing the corresponding electronic characterisation of individual sensors on B) asymmetric and D) symmetric devices.

This is contrasted by the wide variation in the transfer curve characteristics for the symmetric sensors which is depicted in Figure 7.27D. This causes a large variation in the mobilities between the sensors (range ~ 700 $cm^2V^{-1}s^{-1}$) and a greater spread in the range of Dirac point metrics of 24 V and 0.28 μA for voltage and current values respectively. It is believed that the difference in variation observed between the asymmetric and symmetric sensors derives from the design of the contact probes onto the graphene channel. For the asymmetric sensors the contact pad spreads the entire distance (80 μm) across graphene which will improve the opportunity for good contact between the Cr and graphene. Conversely, the symmetric sensors only have ~ 9 μm of electrode to form good contact on the graphene therefore inconsistencies with Cr deposition or the introduction of contaminants is more likely to affect the binding between the two layers. This local variation theory is also supported with the similarity in transfer curve characteristics observed between SY1 and SY2 versus SY3 and SY4. Perhaps, local variations in the fabrication procedure between the bottom (SY1 and SY2) and top (SY3 and SY4) of the channel has impacted the electronic characterisation in these specific regions.

7.4.1.3 AFM Characterisation

AFM measurements were conducted on the graphene channels after fabrication was complete and are shown in Figure 7.28. These measurements were corrected for scratches prior to analysis. The appearance of wrinkles and fabrication residues can be made out on the graphene surface and are highlighted in Figure 7.28A. It is possible that the wrinkles are artefacts of the manufacturing or transfer of this graphene sheet. Polycrystalline formations and a high density of defects are associated with CVD growth.

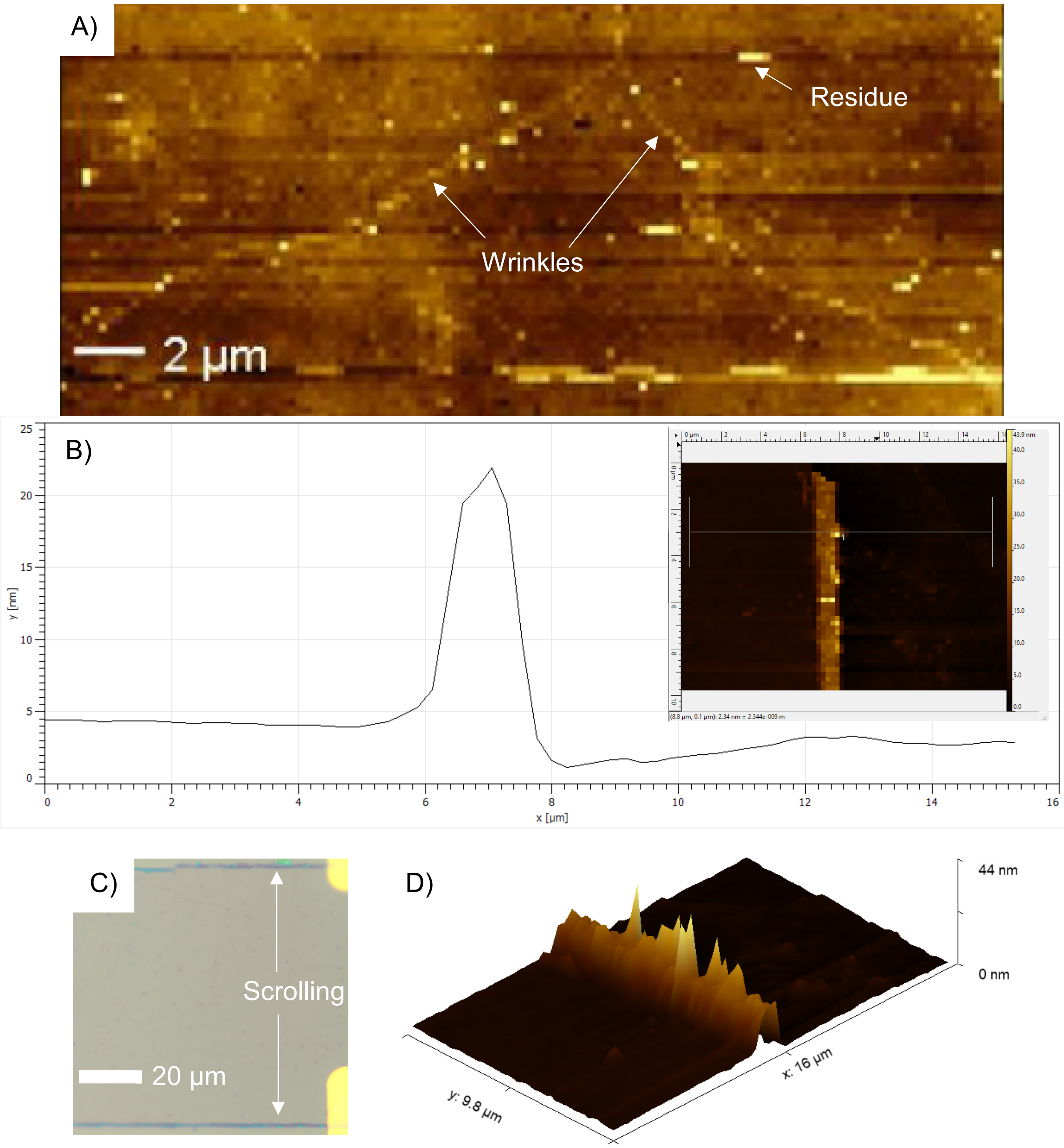

Figure 7.28 A) Surface topology of graphene channel examined by AFM. B) Height profile across graphene and SiO_2 substrate with inset showing the profile line used to extract data. C) Micrograph of graphene channel showing scrolling at the edges D) 3D view of scrolling effect seen at the edge of graphene channel

These wrinkles could be formed as the graphene relaxes the in-plane stress caused by these defects [182]. Additionally, they could be a result of the transfer process, when graphene is placed onto the Si/SiO_2 substrate, whereby it is possible that these wrinkles were formed as water drainage channels [182]. Next, the estimation of the height of graphene was conducted. The average height of the graphene channel and substrate were estimated to be 4.6 nm and 2.8 nm respectively. These values are averages taken across all pixels on each region; with the intention that fluctuations in the surface height, clearly demonstrated in Figure 7.28B, could be removed. The calculated height of this graphene layer is estimated to be 1.8 nm. As part of the manufacturer's characterisation protocol, they claim that AFM measurements < 1.0 nm are taken [185]. It is not understood why these values differ so much. Perhaps the additional height arises from the effective etching of the SiO_2 layer caused by the Ar etching stage. Furthermore, it is possible that the fabrication process causes the graphene sheet to increase its corrugation during interactions with the deposited polymer layers. Since it is accepted that the thickness of graphene is 0.34 nm [182], further work is required to interpret this measurement. Repeating the AFM measurements after etching the graphene with different Ar exposure times or after transferring graphene onto different substrates (such as TEM grids) could help to explain this discrepancy.

The profile line shown in Figure 7.28B illustrates the topography between the graphene and SiO_2 substrate layer. It is formed by the average of 15 pixels at each point to remove surface fluctuations (inset of Figure 7.28B). The phenomenon of graphene scrolling can be inferred by the large peak at the boundary of the two regions in this profile plot. Scrolling is caused by the fabrication process, specifically during the Ar etching stage. Since the phase 1 etching stage does not involve the use of a shield, high energy Ar atoms travelling at angles away from perpendicular to the centre axis can undercut the SiO_2 layer beneath the graphene protected with LOR and PR. Since unsupported graphene becomes unstable, it then self-folds into a scroll-like structure [182]. The effects of scrolling on the graphene channel can be observed in optical images by a darkening effect at the channel edges as shown in Figure 7.28C. The relative height of these scrolling structures with respect to the channel and substrate is illustrated in the 3D topography plot given in Figure 7.28D.

7.4.1.4 XPS Characterisation

XPS measurements were conducted on fabricated graphene and are shown Figure 7.29. The high resolution C 1s scan reveals the presence of the carbon bands and their relative contributions which are clearly visualised at 284.5 eV (C=C), 286.2 eV (C-O/C-N/C-OH) and 286.6 eV (O-C=O). The main contributor to the peak is at 284.5 eV which infers sp^2 hybridisation which is expected for monolayer graphene. The shoulder peak at 286.2 eV is associated with sp^3 binding and therefore infers the presence of defects in the graphene lattice which is supported by Raman measurements (vide supra). The indication of small contributions from hydroxyl and carboxylate groups on the surface can be attributed to the presence of impurities on the graphene surface [186].

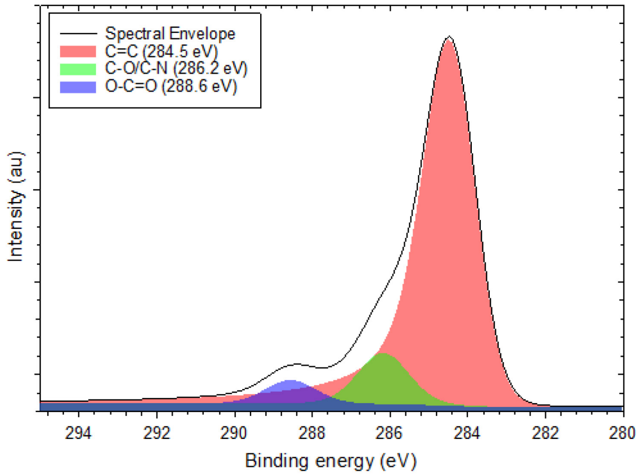

Figure 7.29 High resolution C 1s XPS spectrum of fabricated graphene channel

7.4.1.5 Optical Characterisation

The importance of thorough optical characterisation is described here. Optical images of Device B1 are shown in Figure 7.30A and B. B1 appears as a fully functional device, it is only on closer inspection that it becomes clear that there are patches in the graphene channel, that were most likely caused by the unintentional lift off of the graphene with the LOR during the final removal stage. Since defected graphene will have its electronic properties altered, it is important that devices like these are identified so that are not used for biosensing purposes. Raman characterisation was then deployed in order to classify the areas of B1 with appropriate labels.

Prior to this Raman classification, it was necessary to collect representative spectra of SiO_2, Au, disordered and monolayer graphene which are subsequently depicted in Figure 7.30C and D. A region of highly disordered graphene is represented by the red line in Figure 7.30D. Here, the ratio of I(G):I(D) is roughly 0.98. Raman mapping was conducted over the region highlighted by the orange box in Figure 7.30B. In total, 1600 spectra were acquired over a regular grid of 40 x 40 giving a detailed view of the graphene surface.

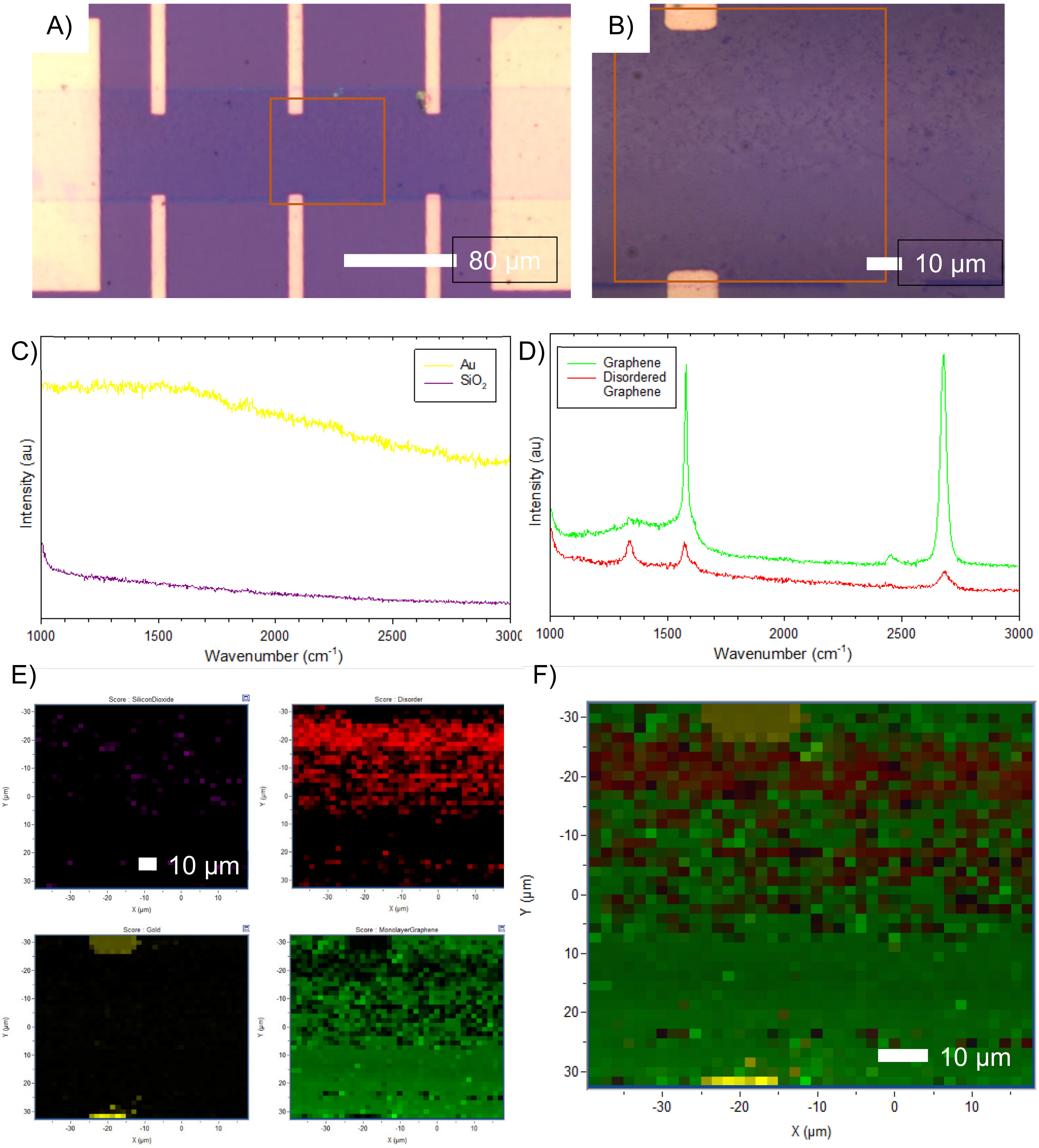

Figure 7.30 A) Micrograph of GFET device with orange box indicating approximate area captured in B) Micrograph with orange box representing approximate area captured in Raman classification. Spectra captured representing typical area of C) SiO_2 and Au D) disordered and monolayer graphene with offset applied for clearer graphical visualisation. E) Maps showing classified pixels for SiO_2 (purple), Au (yellow) disordered graphene (red) and monolayer graphene (green). F) Combined map with pixels overlaid.

Pixel positions associated with SiO_2 (purple), Au (yellow), disordered (red) and monolayer graphene (green) are shown in Figure 7.30E and are overlaid in Figure 7.30F. The gold contacts were included as they provide good reference points to compare the optical and Raman mapped images. Interestingly, there are several pixels which have been classified as Au at ~ 8 µm away from the end of the contact. It appears that the process of washing the GFET after the removal has lifted some flecks of Au onto the graphene channel. Alternatively, these positions correlate with areas where the LOR has not dissolved away. This representation makes it clear that there is an uninterrupted monolayer graphene channel near the bottom of the device providing good conduction through the device. Regions of high disorder, inferred by the red pixels in Figure 7.30E are located close to the areas of broken graphene where the pixels representing SiO_2 are. As noted in Ferrari's work [133] edges of graphene correspond to defects and therefore it is expected to see a correlation in their positions. Although time-consuming (~1 h for this classification map), this technique provides an excellent representation of the constituent parts of the graphene channel and is not only useful as pre-screening tool, to confirm any suspicions observed during initial optical characterisation, but it also provides additional information relating to the local variation in defects across a channel which could inform the development of future fabrication procedures.

In a study led by Ushiba, a similar form of graphene surface classification was conducted using only optical images. Ushiba's group commented on the variation in the transfer curve characteristics that they observed across their fabricated GFET arrays. They designed a neural network which was able to classify individual pixels in an image, assigning them with appropriate labels of graphene, electrode, substrate or contaminants. This process was not only rapid, as it only took 10 s to conduct this classification and determine relative ratios of holes and contaminants to the user, but it was also effective with a success rate of over 80%. By conducting electrical characterisation, this group then correlated the surface graphene coverage with improved conductance [187].

It is conjectured that since some electrical characteristics can be inferred from Raman spectra of graphene that a combination of these techniques in the future could improve the screening of mass produced GFET devices.

7.4.2 Cleaving Devices

Previous measurements of GFET devices had been conducted over the entire chip with all 25 devices simultaneously exposed to environmental factors. This resulted in arduous characterisation periods with extended time delays between the initial and final devices being measured. The large length of time between these measurement periods left the devices exposed to greater environmental influences such as temperature change, absorbents and humidity thus resulting in changes in their properties (see section 7.5).

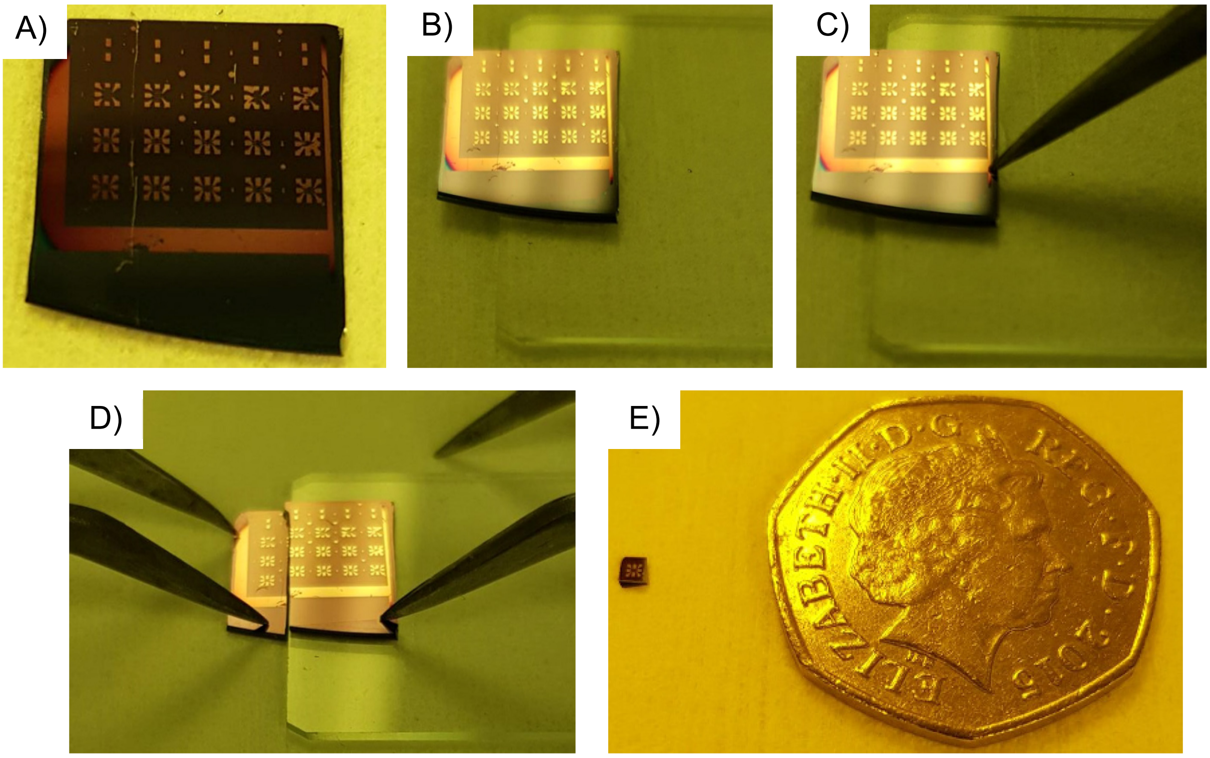

Figure 7.31 Overview of cleaving technique used to separate GFET into individual devices. A) Fabricated chip is scribed in between row/column B) Chip is positioned onto glass slide so that cleaving edge is freestanding over the table surface C) Tweezers are used to hold the non-cleaving side of the chip down, D) Tweezers are used to gently apply pressure to the cleaving side of the chip causing the pieces to separate. E) Individual GFET device after repeated cleaving processes with 50 pence coin for scale

Cleaving the chips into smaller pieces with individual GFETs was desirable so that more control over external influences could be applied thus improving the comparisons between devices.

A novel and rapid technique involving basic cleanroom equipment was developed in this contribution in order to cleave the GFET devices into individual pieces suitable for controlled, reliable characterisation. An overview of the entire process is given in Figure 7.31. Initially, the chip is scribed using a diamond pen, with a small stroke parallel to the graphene channels, in between a row or column. This is performed at the edge of the chip to ensure a minimum amount of residue contaminates any device surface. Then, the chip is placed onto a glass slide, with the edge of the chip to be cleaved off freestanding over the glass slide. Using one set of tweezers to hold the chip in place on the glass slide, another set is required to gently push down on the edge to be cleaved. With small amounts of force this procedure will produce a clean cleave with a row/column of devices cleaved away from the main chip. Both pieces are then air dried using a N_2 gun to remove unwanted surface residue. This entire process is repeated until individual GFET devices are cleaved into their own pieces.

It is important to note that once this technique was developed the standard operating procedure for the photolithography steps was adapted in the following way. During the mask aligner stage (section 6.2.2.2) the pre-cleaved squares of graphene-Si/SiO_2 blanks were aligned so that the edges of these blanks were parallel with the positions of the graphene channels in the mask. It follows that since the wafer's orientation is <100> the graphene channels would run parallel and perpendicular to Si's crystal lattice [188]. Therefore, after fabrication, when cleaving was required, the initial scribing action would be positioned along one of the main crystallographic directions which would ensure that the cleavage line was straight and vitally in-between the individual GFET devices.

7.4.3 Technique B – Sputtered Cr and Au

The impact of sputter coating the Cr adhesive layer was investigated here to study whether this would impact the electronic characteristics of the GFET device. Sputter coating the Cr layer prior to Au deposition offers a significant reduction in the Phase II fabrication processing time since it eliminates the need to evacuate the Thermal Evaporator saving ~ 4 h in pump-out time. In this study, devices followed the Phase I process as per Technique A. Then, instead of evaporating Cr for 8 s at a current of 21 mA at 10^{-6} torr, Cr was sputter coated for 660 s at 200 W at 10^{-6} torr with the shield in position. AFM analysis shown in Figure 7.32A indicates that the total height of the Cr/Au electrode with respect to the substrate is ~ 48 nm for devices fabricated following Technique B. Since the deposition of Au matches that used by Haslam which has previously been estimated to be ~30 nm [4], it is estimated that the deposition of Cr is ~18 nm with an estimated deposition rate of 0.027 nm/s.

An additional fabrication run with the Cr sputter coated was repeated but with the deposition time limited to 60 s (~2 nm). The electrical characterisation for typical GFET devices representing technique A, technique B for 660 s and technique B for 60 s (T1, T2 and T3 respectively) were then compared and are shown in Figure 7.32C and D. An interesting observation is the conductivity maxima seen for devices T2 and T3 illustrated in the inset of Figure 7.32C. T3 also has two sets of Dirac points at positions V_G = -67 V, -43 V, +85 V and +92 V. The Dirac points for T2 would sit in the regions outside the measureable range for this SDA. A double conductance minima is associated with a graphene p-n junction and was also observed by Feng et al in their work on back-gated GFETs [189].

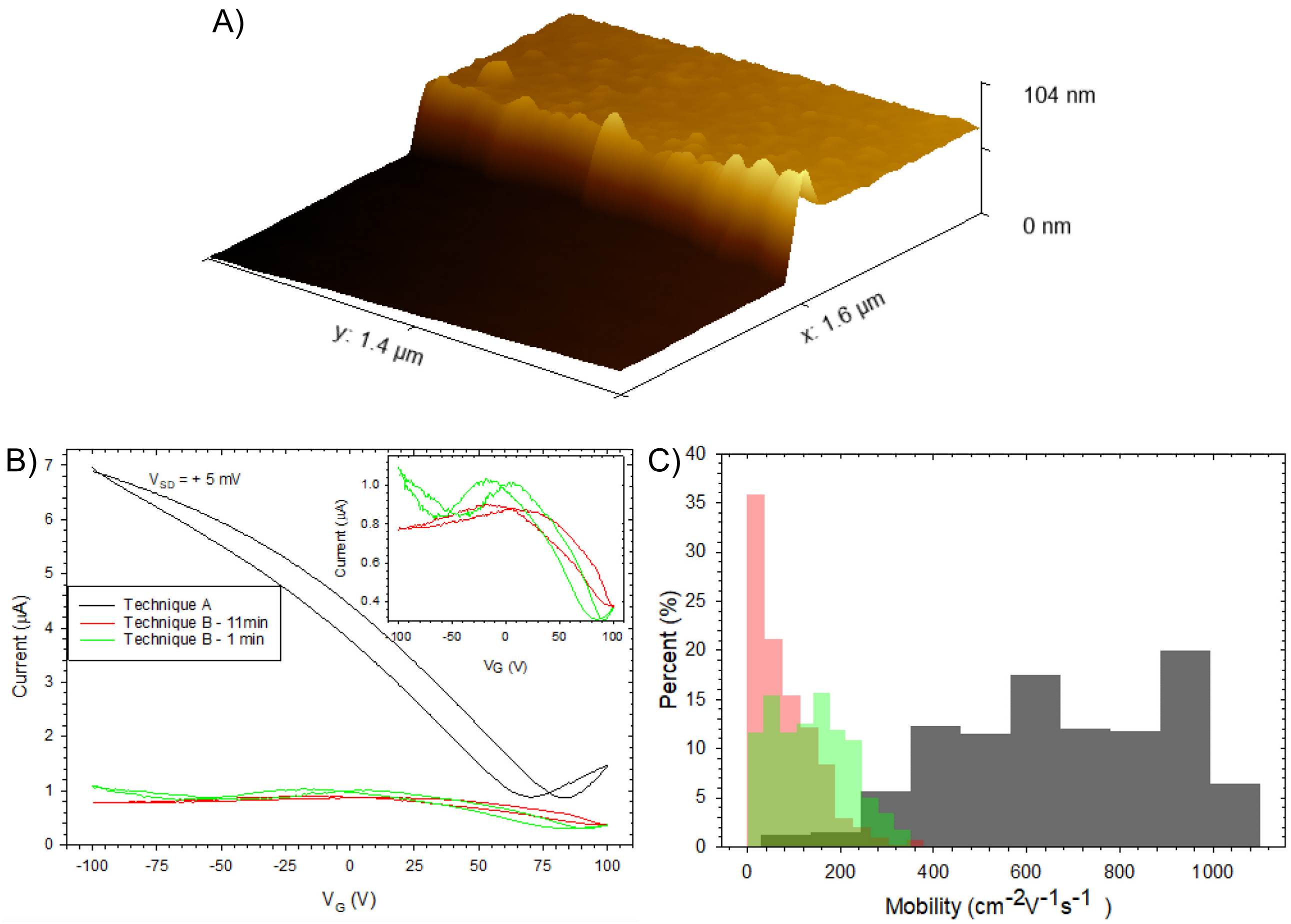

Figure 7.32 A) Surface topology of SiO_2-Cr/Au contact interface examined by AFM. B) Typical I_{SD}-V_G measurements for sensor fabricated via the Technique A (black), Technique B -11 min (red) and Technique B -1 min (green) processes with inset showing the enlarged view from 0.3-1.0 μA. C) Corresponding mobilities calculated across the transfer curve.

Graphene transfers electrons to the metallic contacts, due to the difference in work functions for Cr (4.6 eV), Au (5.1 eV) and graphene (4.5 eV). This makes the region directly under the contacts slightly more p-doped than the rest of the channel [171]. At points of maximum conductance the Fermi level sits in the corresponding bands preferred for the p-type and n-type regions (conduction and valence respectively). Modifying V_G shifts the Fermi level towards the intersection of these bands which leads to conductivity minima. It is suggested that the action of sputter coating, which is well established as causing defects in graphene, due to the large amount of highly energetic particles [190] causes highly disordered graphene patches under the contacts [191]. The following interaction between the highly disordered graphene and the deposited Cr causes complex p-n junctions to form which manifest itself in transfer curves shown in Figure 7.32B. It is also suggested that the disordered graphene in contact with the Cr that can be evidenced by the substantial reduction in the field effect mobility shown in Figure 7.32C and noted in Thodkar’s work [184]. Even with a reduced deposition time of only 60 s, these damaging effects are still present in the electrical characteristics. These observations, combined with the degradation in current and higher noise values across the transfer curve indicate that technique B is not suitable for the fabrication of GFETs for the purpose of biosensors.

7.4.4 Summary

Initial characterisations into fabricated GFET devices were presented in this section. The influence of the fabrication process on graphene was shown to increase both the density of disorder and doping in the lattice elucidated from Raman measurements. Characterising the devices electrically showed that inter-sensor variation on the same GFET device was much wider for the symmetric over the asymmetric devices which is most likely caused by differing contact between the electrodes and the graphene surface. Measurements conducted via AFM showed that the graphene displayed features like wrinkles, scrolling and residue which are consistent with both transfer and fabrication processes. XPS spectra confirmed the sp^2 hybridised lattice along with showing supporting evidence of defects in the lattice and surface impurities. The need for effective characterisation procedures prior to commencing functionalisation was demonstrated by a highly disordered graphene channel, caused by partial lift off of the channel during the final remover stages. This channel, characterised with both optical and Raman measurements, showed patches in the conducting path with several instances of highly disordered graphene present at the edges.

The need for and description of a novel cleaving process to separate GFET devices from a large array was described. This technique uses basic cleanroom equipment and therefore is appropriate for a wide variety of users. It succeeds in facilitating more controlled measurements of individual GFET devices, necessary to limit the effect of external influences (see section 7.5).

An investigation into the effect of sputter coating the adhesive Cr layer was also shown and compared against the traditional thermal evaporation method. This was explored as a possible route to reduce the fabrication time by removing the need for an additional pump out process. Two Cr layers were investigated (~ 18nm and ~2 nm) and both had the impact of severely reducing the conductance and mobility through typical GFET devices. The introduction of high defect levels under the contacts from highly energetic particles were partly responsible for this alteration in the electronic characteristics along with the formation of complex p-n junctions.

7.5 Atmospheric Adsorbents on Graphene

7.5.1 Introduction

The impact of exposing GFET devices to the ambient environment was investigated in order to quantify this effect along with determining suitable strategies to improve the measurement procedure. It is well established that exposing devices to the ambient laboratory impacts the graphene channel [83, 144, 192]. Currently, the majority of studies in the literature which discuss GFET technologies do not discuss the conditions under which the device was handled from storage to initial measurement. It is the ambition of this work to commence the debate and further research into the best practices for storing and handling devices prior to characterisation facilitating the transition of this technology from the laboratory into the industrial settings, necessary to realise this technology into POC devices.

7.5.2 Methodology

This investigation was conducted on fabricated graphene prior to any surface conjugation. Two different electrical measurement runs were conducted to get a broad view of the changes occurring in the GFET devices over time. These were short-, and mid-term runs which corresponded to measurements between 0-5 min and 0-8 hr respectively.

Prior to each run GFET devices had been stored in the vacuum chamber where the internal pressure was evacuated to 25-30 mmHg (~37 mbar) for at least 16 h. The purpose of this stage was to drive out any residuals that may have been on the surface of graphene [83]. The start of each run begins when the vacuum chamber is opened which leaves the samples exposed to the ambient air. For all runs, electrical characterisation in the form of regular I_{SD}-V_G sweep acquisitions were captured at a V_{SD} level of + 5 mV using a four-probe setup. It is important to note that due to equipment limitations, the length of time between opening the vacuum chamber and the initial t=0 measurement was roughly 3.5 min.

A longer-term study, which considered graphene's response over 20 months of ambient environmental exposure was conducted using pristine graphene (prior to any fabrication) and was conducted using Raman characterisation only.

7.5.3 Results

7.5.3.1 Short Term

Initially, electrical characterisation of the impact of atmospheric adsorbents on the conductive properties of the graphene channel were acquired between 0-3 min and 0-7 min periods in the ambient lab environment. During the short-term measurements probe needles were positioned on the electrode pads and remained in the same position whilst the SDA captured regular readings every 15 s. Maintaining the probes in the same position was conducted to remove any variability in contact as shown in 7.3.2.1. This measurement run was conducted on sensors S1 and S2, which were part of two separate GFET devices fabricated from the same graphene sample. S1 and S2 were asymmetric (seven) and symmetric (eight)-electrode Hall-bar devices.

It is clear from Figure 7.33 that there is a noticeable impact on the electrical characteristics of S1 on exposure to atmospheric adsorbents. There is a positive correlation observed between the exposure time and V_{DP}^{F}, V_{DP}^{R}, $I_{Vg=0}^{F}$, $I_{Vg=0}^{R}$ and the $I_{DP}^{Average}$. These metrics all appear to follow a linear relationship. A summary table which calculates the estimated rate of change of these values is provided in Table 7.1. It is noted that a 10% reduction in the field effect mobility was observed for S1 due to the exposure.

It was observed that repeating the above measurements for a longer period of time (7 min) with S2 produced some conflicting results and are shown in Figure 7.34. The exposure of atmospheric adsorbents had the same initial effect on V_{DP}^{F} and V_{DP}^{R} as they increased with exposure time, from 82 V and 73 V to 94 V and 85 V respectively. However, 195 s into data collection it is clear that there is a left shifting in these values, which decrease them to 89 V and 80 V over the course of 120 s. After this, the shift inflects again in the positive direction for the remaining 180 s, where the final values of V_{DP}^{F} and V_{DP}^{R} increase to 94 V and 88 V. Similarly, although the overall change in both $I_{Vg=0}^{F}$, $I_{Vg=0}^{R}$ shows a 7% and 17% increase from exposure, the trend follows a periodic pattern of roughly 2-3 min of decreasing before a swift increase. In direct contradiction to what was shown for S1, S2 shows a negative correlation between the exposure time and the $I_{DP}^{Average}$ values, inferring that the current values for the Dirac points decrease with increasing exposure time. A 3% reduction in the mobility was observed for S2 due to the exposure.

Assuming a linear relationship exists between exposure time and the influence on the electrical metrics Table 7.1 provides a summary of the calculated rates of change observed from these measurements.

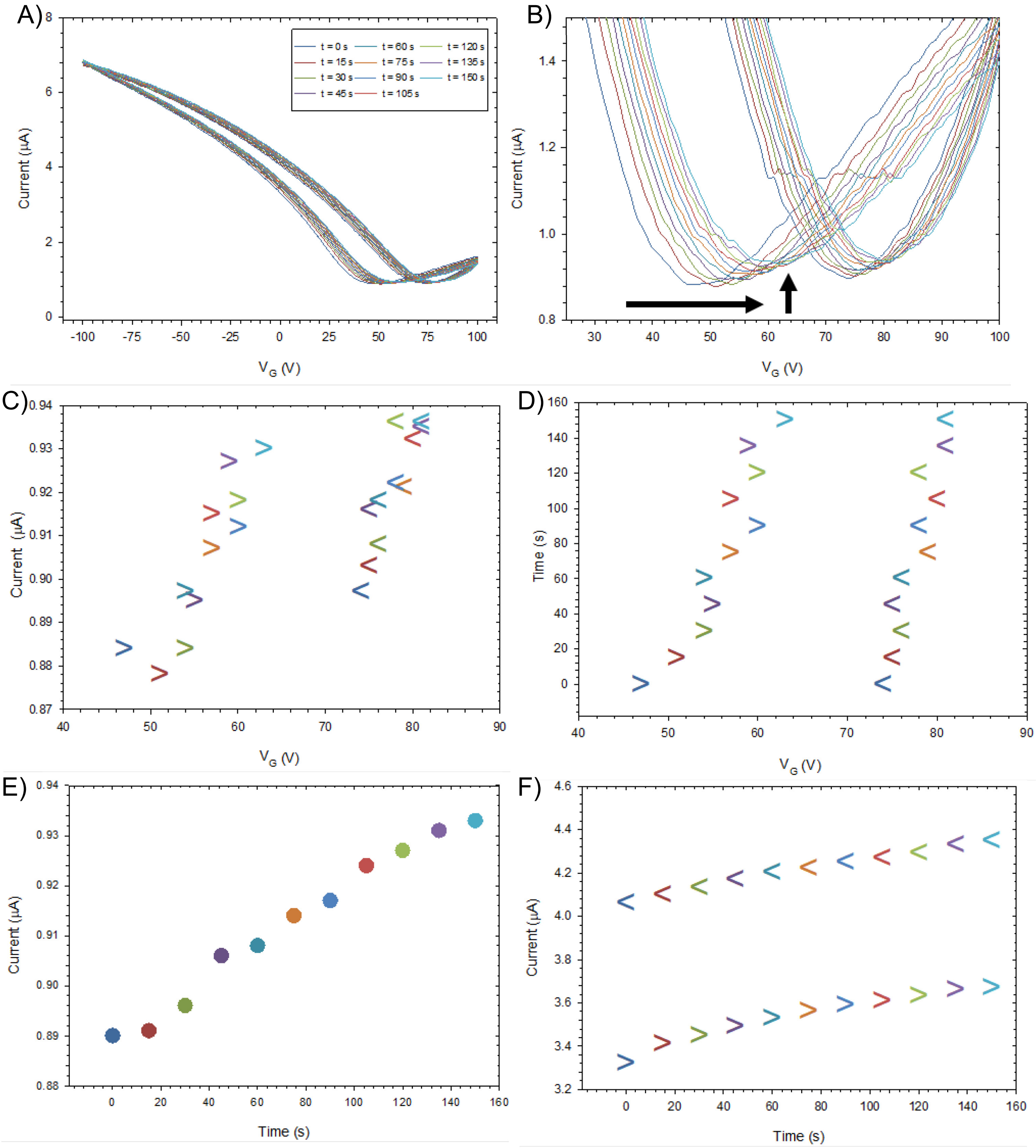

Figure 7.33 Effect of exposure time to atmospheric adsorbents on electrical characterisation of S1 GFET sensor. A) Full range view of back-gate sweep (I_{SD}-V_G) measurements. B) Focussed view of I_{SD}-V_G around Dirac points with arrowts indicating shift with time. Scatter plots indicating C) Positions of Dirac points in I_{SD}-V_G space D) V_{DP}^F and V_{DP}^R values against exposure time E) Average of I_{DP}^F and I_{DP}^R against exposure time F) $I_{Vg=0}^F$ and $I_{Vg=0}^R$ against exposure time.

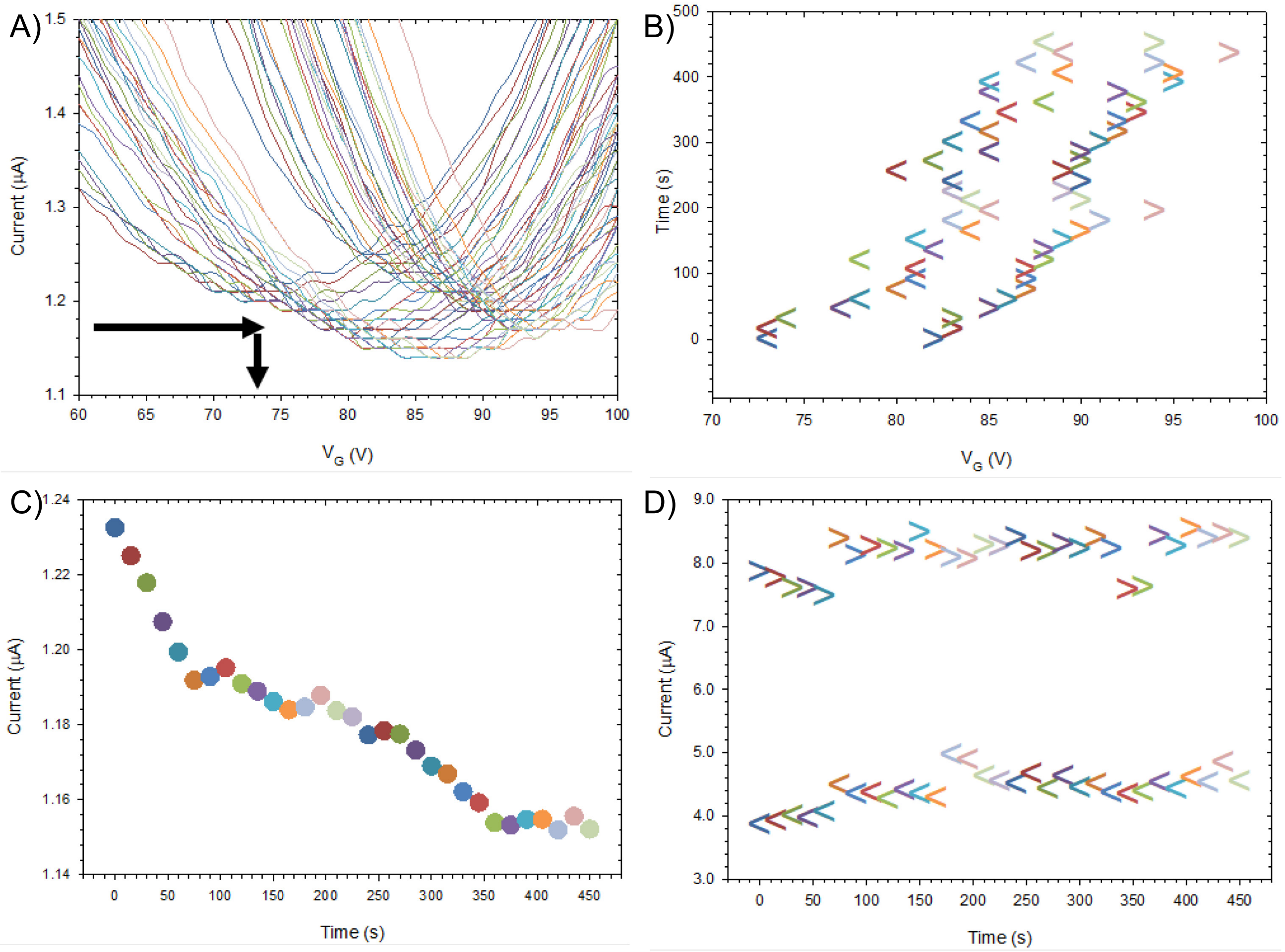

Figure 7.34 Effect of exposure time to atmospheric adsorbents on electrical characterisation of S2 GFET sensor. A) Focussed view of I_{SD}-V_G around Dirac points with arrows indicating shift with time. Scatter plots indicating B) V_{DP}^{F} and V_{DP}^{R} values against exposure time E) Average of I_{DP}^{F} and I_{DP}^{R} against exposure time F) $I_{Vg=0}^{F}$ and $I_{Vg=0}^{R}$ against exposure time.

S1	VALUE AT T=0	VALUE AT T=150	RATE OF CHANGE	S2	VALUE AT T=0	VALUE AT T=450	RATE OF CHANGE
V_{DP}^{F}	47 V	63 V	107 mV/s	V_{DP}^{F}	82 V	94 V	27 mV/s
V_{DP}^{R}	74 V	81 V	47 mV/s	V_{DP}^{R}	73 V	88 V	33 mV/s
$I_{VG=0}^{F}$	3.32 µA	3.67 µA	2.33 nA/s	$I_{VG=0}^{F}$	7.85 µA	8.37 µA	1.16 nA/s
$I_{VG=0}^{R}$	4.06 µA	4.35 µA	1.93 nA/s	$I_{VG=0}^{R}$	3.86 µA	4.53 µA	1.49 nA/s
$I_{DP}^{AVERAGE}$	0.89 µA	0.93 µA	0.27 nA/s	$I_{DP}^{AVERAGE}$	1.23 µA	1.15 µA	-0.18 nA/s

Table 7.1 – Rate of change of electrical metrics caused by atmospheric adsorbents for sensor A) S1 and B) S2.

It is clearly shown that although these calculated rates of change fall into similar orders of magnitude they are different between sensors and therefore it is suggested that a generic

GFET atmospheric adsorbents correction algorithm cannot be obtained. This is further supported by the lack of agreement in the linearity between the two sensors.

An increase in V_{DP}^F, V_{DP}^R witnessed for both S1 and S2 is evidence of p-type doping caused by the adsorbents to the graphene surface. Kunpeng's group also showed evidence of this when they noticed an increase in Dirac point voltages, after 1 month of ambient exposure, which they attributed to the water and oxygen molecules adsorbing to graphene [193]. The inflection in the V_{DP}^F and V_{DP}^R values displayed for S2 can be explained with the following. Since the water and oxygen molecules are only weakly bound to the graphene surface via physisorption or feeble chemisorption interactions [83], it is possible that this negative shift showcases the dynamic removal of adsorbents from the graphene surface. Perhaps, p-type doping adsorbents were removed from the surface during a collisions caused by an impinging molecule of N_2/O_2/H_2O which acted to reduce the p-type doping effect "seen" in the channel, thus causing a reduction in these values. Alternatively electron donors such as NH_3 and CO could be temporarily binding [192]. This would suggest that the doping caused by the atmospheric adsorbents is occurring on timescale of a few seconds and can change with the particular molecules adsorbing to or colliding with the surface.

It has been shown in the literature that the current characteristics can be affected in multiple ways as noted for the S1 and S2 sensors. For example Sojoudi's group showed that after 1 hour of exposure to air, their GFET device showed an increase in $I_{Vg=0}$ and I_{DP} [144] in line with observations from S1. Conversely, during Yang's investigation, increasing exposure to the ambient environment caused a reduction in I_{DP} whilst an increasing value of $I_{Vg=0}$ [83] as replicated in sensor S2. The rippling effect observed in the $I_{Vg=0}^F$, $I_{Vg=0}^R$ metrics for S2 could be further evidence towards dynamic binding of adsorbents. As the timescales of this phenomenon is much lower than the effect previously discussed it is possible that a different species of molecule is responsible since graphene's transport properties have also been shown to be impacted by adsorption/desorption of other molecules found within air such as NH_3, NO_2, CO and NO [192]. It is conjectured that these inconsistencies relate to the complex interactions between scattering from substrate impurities combined with charge screening and transfer from adsorbing species to graphene's surface [83].

7.5.3.2 Mid Term

Next, the impact of the ambient environment was assessed over the course of 7 h for sensors M1 and M2. During these measurements the device was left in a stationary position throughout the day with the probe needles locked in the same position to remove the effect of probe positioning. The I_{SD}-V_G sweeps were conducted every 1 h to uncover if any saturation in electrical metrics was observed. This measurement scheme also had the advantage of eliminating the effect (if any) of temperature increases in the graphene channel from regular bursts of current. Metrics relating to the electrical characteristics of M1 (asymmetric) are given in Figure 7.35. Similar observations were made for sensor M2 (asymmetric) and therefore plots are not repeated for brevity. The reader is advised that the measurement acquired at 3 h has been excluded from Figure 7.35 due to it being anomalous as it showed significant variation across all parameters possibly due to a contaminant binding to the graphene at the moment of data capture.

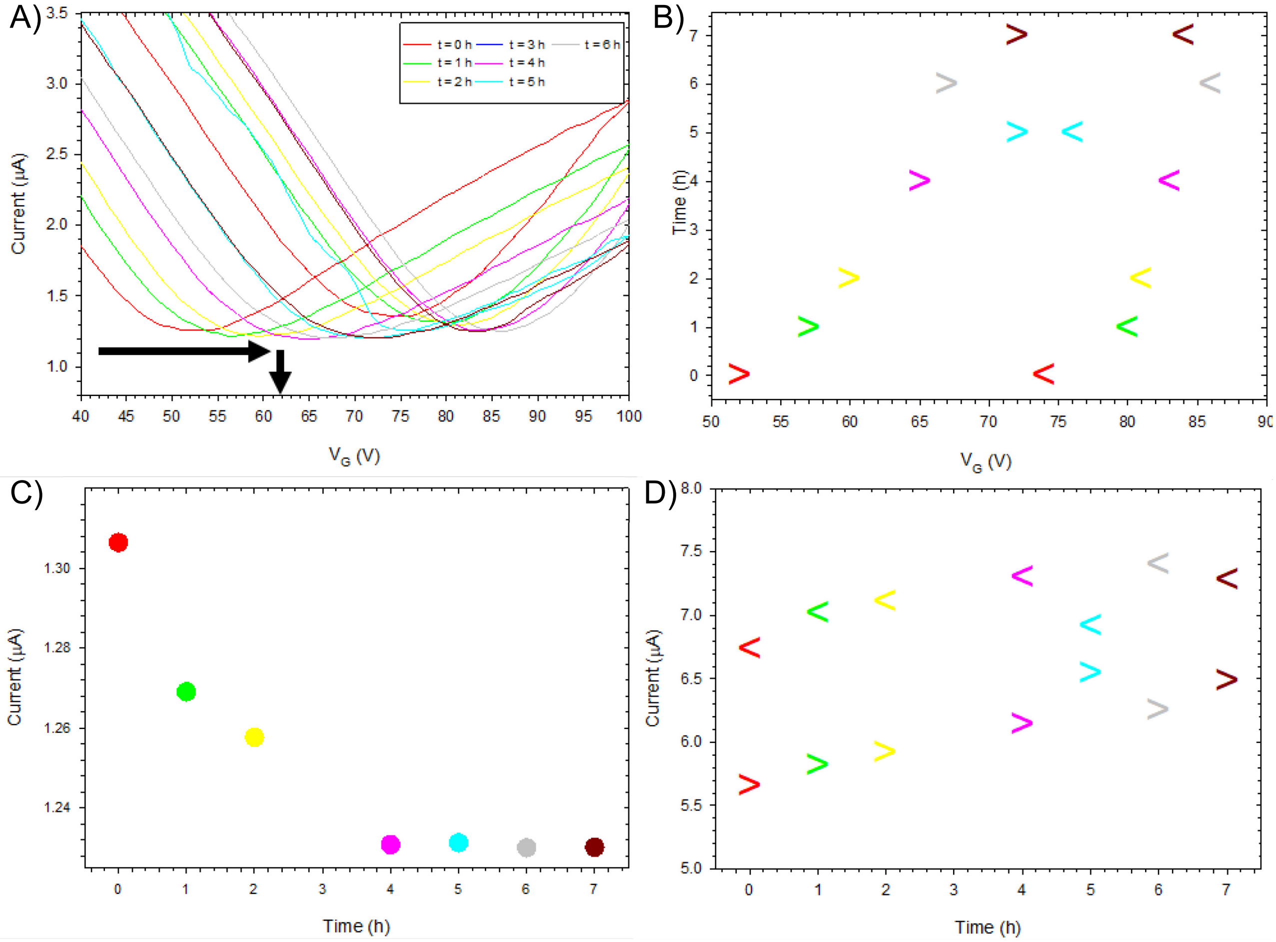

Figure 7.35 Effect of exposure time to atmospheric adsorbents on electrical characterisation of M1 GFET sensor. A) Focussed view of I_{SD}-V_G around Dirac points with arrows indicating shift with time. Scatter plots indicating B) V_{DP}^F and V_{DP}^R values against exposure time E) Average of I_{DP}^F and I_{DP}^R against exposure time F) $I_{Vg=0}^F$ and $I_{Vg=0}^R$ against exposure time.

It is observed that for M1 the values of V_{DP}^F, V_{DP}^R increase by 38% and 14% respectively over the course of the 8 h measurement period although unlike with the short term measurements this change is not linear. It follows that ΔV_{DP} (V_{DP}^R - V_{DP}^F) decreases with exposure time. It is conjectured that the water that is trapped between the graphene surface and the Si/SiO_2 layer evaporates away with time, thus reducing the hysteresis of the device. A 10% reduction in the mobility was observed due to the exposure.

The rate of decrease in $I_{DP}^{Average}$ appears to follow a two stage decay, with substantial reduction in the current observed between 0 h and 4 h (at a rate of -5.25 nA/s) and then saturation for the remaining 3 h. This observation can also be made for the V_{DP} although more obvious for V_{DP}^F (0.63 mV/s). In a similar fashion, the $I_{Vg=0}^F$ and $I_{Vg=0}^R$ metrics can be observed to increase between 0 – 4 h (33.8 nA/s and 39.2 nA/s) and appear to level off after 3 h. In a similar experimental design Yang's group made similar interpretations of their data. They showed that the majority of change seen in their electrical measurements, including right shifting in their Dirac points occurred in the initial 30 min of exposure [83]. They then commented on a saturation effect occurring after 2 h, which indicates that there is a upper limit to the changes observed as a result of atmospheric adsorbents as supported herein [83].

7.5.3.3 Long Term

A longer term investigation into the impacts of atmospheric adsorbents on graphene was conducted by comparing the Raman spectra of graphene samples prior to any fabrication processes. In this study, maps of Raman spectra were acquired on a pristine (pre-fabrication) sample of graphene on delivery from the supplier and one sample previously opened and left in ambient air for 20 months. The reader is advised that the two samples used throughout this comparison were from different batches.

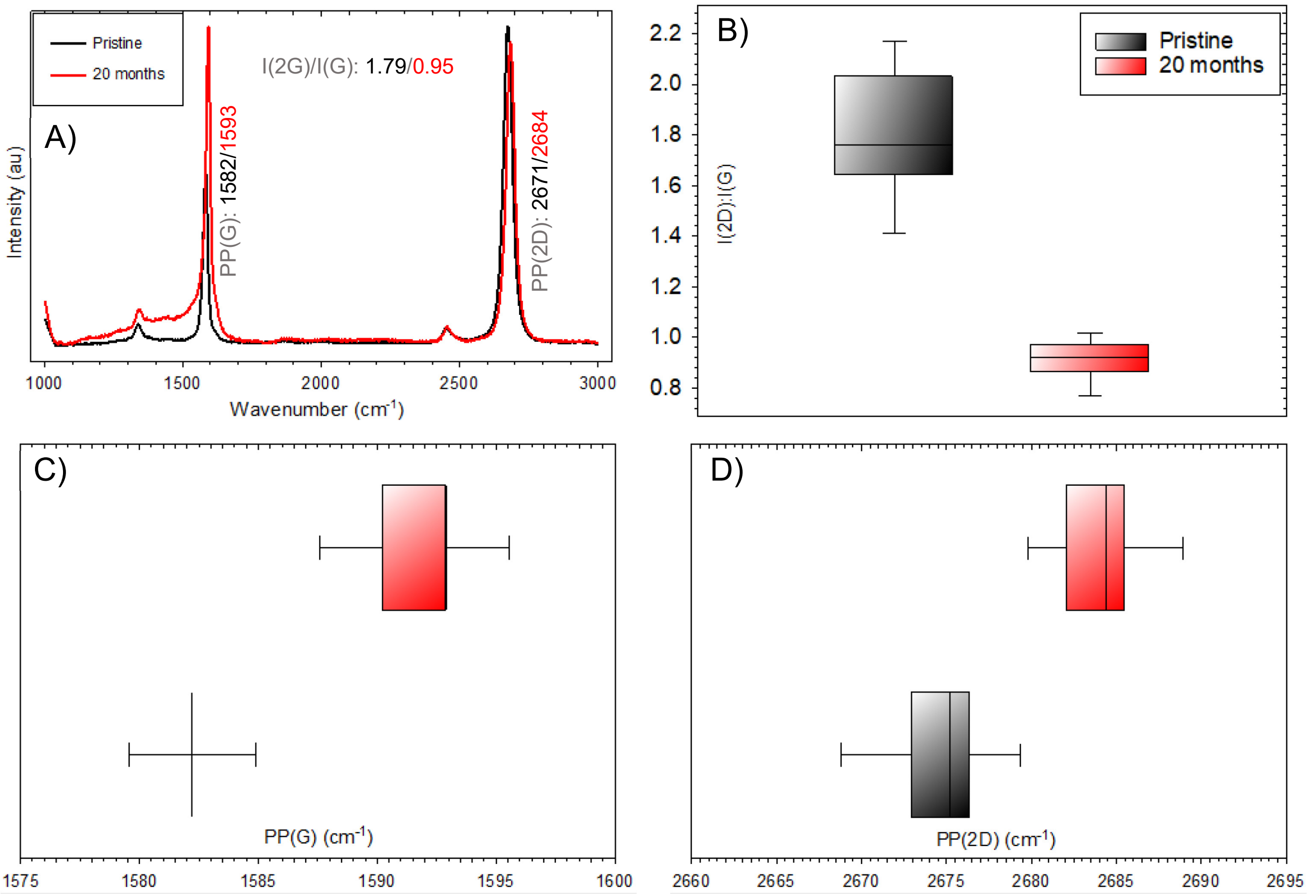

Figure 7.36 A) Normalised averaged spectra captured across pristine (black) and 20 month aged (red) graphene. Box and whisker plots for pristine and 20 month aged graphene showing comparison of B) I(2D):I(G) C) PP(G) and D) PP(2D).

Plotting the normalised average of the spectra for each sample as conducted in Figure 7.36A shows significant differences in the spectra caused by the long-term exposure to the ambient laboratory environment to the graphene. The reduction in the I(2D):I(G) ratio, plotted in Figure 7.36B, infers an increased doping in the channel. Combined with the increase in PP(2D) it is likely that this increase in doping is predominantly caused by environmental p-type dopants [144]. The right shifting in both the PP(G) and PP(2D) of ~9 cm^{-1} and ~13 cm^{-1} respectively are shown in Figure 7.36C and D and are attributed to the adsorption of O_2 and water vapour as supported by Sojoudi's work [144]. In this work, Sojoudi also supports the idea of similar responses to doping caused by electrostatic gating and environmental sources [144].

7.5.3.4 Recovery

The impact of various recovery techniques were investigated next in order to assess if the effects that are documented above could be reversed. The impact of vacuum treating the GFET sensors are shown in Figure 7.37. This treatment involved storing the GFET devices in an evacuated the vacuum chamber, at 25-30 mmHg (~37 mbar) for ~112 h. For this experimental run, the M1 sensor which has already had its response to atmospheric exposure characterised was selected for treatment.

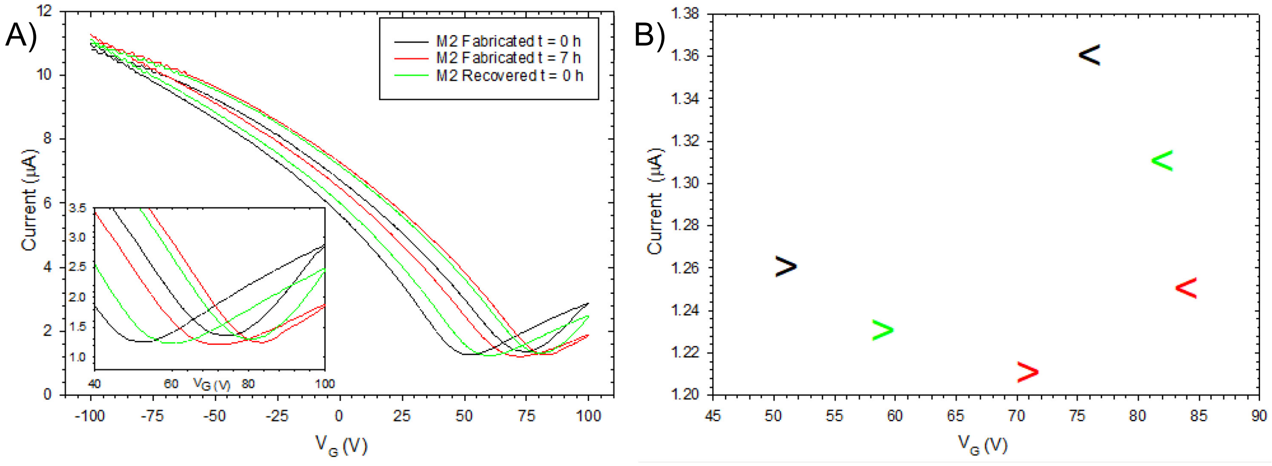

Figure 7.37 Effect of vacuum treatment on electrical characterisation of GFET sensor. A) Full range view of (I_{SD}-V_G) measurements with inset showing focussed view around Dirac points. B) Scatter plot indicating the Dirac points in I_{SD}-V_G space.

DEVICE M1	VALUE AT T=0	VALUE AT T=7	VALUE POST TREATMENT	RECOVERY
V_{DP}^{F}	52 V	72 V	59 V	65%
V_{DP}^{R}	74 V	84 V	82 V	20%
$I_{VG=0}^{F}$	5.65 µA	6.48 µA	6.01 µA	57%
$I_{VG=0}^{R}$	6.73 µA	7.28 µA	7.18 µA	18%
I_{DP}^{F}	1.26 µA	1.21 µA	1.23 µA	40%
I_{DP}^{R}	1.36 µA	1.25 µA	1.31 µA	55%

Table 7.2 – Recovery of electronic metrics by vacuum treatment.

Figure 7.37 and Table 7.2 provide evidence that the low vacuum treatment has been successful in restoring the electronic characteristics of graphene, with similar observations observed by Yang's group [83]. Although not uniform across these metrics, it is clear that vacuum treatment is capable of adsorbent removal most likely due to the low binding energy between the contaminants and the graphene surface. Similar observations were made by Joshi et al who observed that vacuum treatment could not fully return their device characteristics back to pre-exposure levels. They attributed silanol groups, formed from the hydroxylation of the SiO_2 substrate layer during ambient exposure, H-binding to H_2O molecules for the remainder of the contribution which was not recovered. Only vacuum annealing would be able to remove these contaminants. This group also suggested that reducing the density of silanol groups on the surface, by removing the OH terminated ends of the SiO_2, would not only decrease initial p-doping of the graphene channel but also improve device recovery in vacuum treatments [194].

Device recovery was also studied by assessing the influence of thermally annealing devices. Devices H1, H2 and H3 were heated to 200 ºC in a conventional fan over for 1, 2 and 3 h respectively. Post annealing measurements showed a wide variety of inter-sensor responses. The mobility (not pictured) between the pre- and post- annealing measurements showed significant changes across the dataset although whether this increased or decreased depended between sensors. However, contrary to this, one observation that was common to all sensors during post-annealing measurements was that the V_{DP}^F and V_{DP}^R both increased suggesting enhanced p-doping. Since the oven's chamber was not evacuated during these treatments this shift cannot be isolated as being caused by the heating alone. In a similar study led by Ni et al, the impact of heating devices to 500 ºC whilst under a vacuum of 0.5 Pa (0.005 mbar) was investigated. In evacuated conditions and over the course of 400 min, heating (cooling) the devices caused red (blue) shifting in the measured PP(G) and PP(2D) values. Significantly, when they equalised the chamber with the ambient laboratory they observed a very sudden blue shifting indicative of heavy hole doping. They concluded that their vacuum treatment of graphene caused the removal of adsorbents on the surface which meant that during the following exposure to the air, the binding efficiency for H_2O and O_2 was much greater [192]. Perhaps the work of Jang et al, who optimised rapid-thermal-annealing (RTA) to remove n-doping surface residues following device fabrication could be re-purposed for removing p-doping surface adsorbents. These residues act as external scattering sites which act to degrade the transport properties of graphene. In this work, Jang's group optimised RTA treatment of GFETs to 250 ºC for 10 min which they found had the effect of not only returning V_{DP} close to 0 V and increasing the mobility but also minimising the sheet resistance in their devices [195].

7.5.4 Summary

One drawback of graphene's high sensitivity is that it is influenced not only by the desired target analyte but also the environment in which it exists in. It therefore is essential to any practical user of these devices that this impact is understood so that handling techniques can be developed which limit the effect on measurements.

This work provides additional observations as to the role that atmospheric adsorbents have on the graphene's properties. Across the short term studies, devices showed drift in all electrical metrics on exposure to the lab environment. These shifts occurred at different rates depending on the device being measured. It was highlighted in this work that the $I_{DPAverage}$ value drifted in two different directions for different devices, with one device increasing and the other decreasing with exposure. Another observation of interest is that for some metrics the direction of drift changed throughout the exposure time; this was attributed to dynamically adsorbing species in timescales of a few seconds. Similar remarks were deduced for devices which were exposed to the adsorbents for 7 hr. With these longer exposure times however there appeared to be a saturation effect whereby any further exposure after ~ 4 h did not cause significant changes to the metrics. Raman measurements captured over 20 months showed significant changes to the spectra caused by the exposure of atmospheric adsorbents.

These observations were caused by environmental p-type dopants interacting with the graphene channel, mainly O_2 and H_2O. Since the work presented here was completed with graphene from the same supplier fabricated using the same processes and handled in the same way it is made clear just how differently individual devices react with these dopants which shows how sensitive these devices can be to minute differences in their structure. Further work will be required in order to accurately predict the influence these adsorbents have in order that they can be corrected for.

The mobility of all the devices presented in this work decreased throughout their exposure. Doping the graphene lattice with atmospheric adsorbents has the effect of increasing the number of scattering sites which would act to reduce the mobility as per the observations made in this work. Yang's group on the other hand reported the first experimental demonstration of doping improving the mobility of the graphene. They suggested that it is possible for adsorbents to decrease scattering from substrate impurities [83]. Perhaps, similar processes caused the adsorbents to increase the $I_{DPAverage}$ presented in this work.

Two recovery techniques were then studied. Vacuum treating the devices did recover the metrics but they shifted back at different rates. This suggested that the vacuum treatment was able to reduce the effect of some mechanisms more than others, which is most likely down to the spectrum of energy associated with different binding mechanisms between the adsorbents and the graphene. Heating in a conventional oven produced a wide range of results showing no consistency for the recovery of the device, only the consistent enhancement of the V_{DP}^F and V_{DP}^R suggesting greater p-doping effects.

The practical implications of the work presented here relate to the handling of the devices prior to measurements. These observations make it clear that the time these devices are exposed to the ambient lab environment should be controlled and documented in the literature. This will make the evaluation of different works that quote shifts in V_{DP} metrics from functionalisation stages easier to compare. Future work in this area should also investigate the effect of functionalisation stages on this phenomenon. For example, does the addition of a PBASE SAM layer or PBASE + bioreceptor layer act as a passivation film to protect changes to graphene’s properties? If so, could this be an improved way of storing GFET biosensors for longer durations, without the need for evacuated storage. Studies like this will improve the realisation of this technology from rigorously controlled experimental settings to harsh environmental settings where these devices are needed the most.

7.6 PBASE Conjugation

7.6.1 Introduction

The effective immobilisation of the PBASE linker onto the surface of graphene is an essential step in the development of GFET biosensor technology since it facilitates the conjugation of multiple bioreceptors which encourages the use of these devices as generic sensing platforms, suitable for wide variety of applications. The aromatic pyrene group is used to stack on the graphene lattice via π-bonding (Figure 7.38A). After successful conjugation, bioreceptors, which are decorated with amine groups can easily be immobilised at the NHS ester end via nucleophilic substitution (Figure 7.38B). Details of the surface coverage of the PBASE linker following immobilisation are scarcely given in the literature making it difficult for the experimentalist to justify the conjugation factors such as method, substance concentration and time [186].

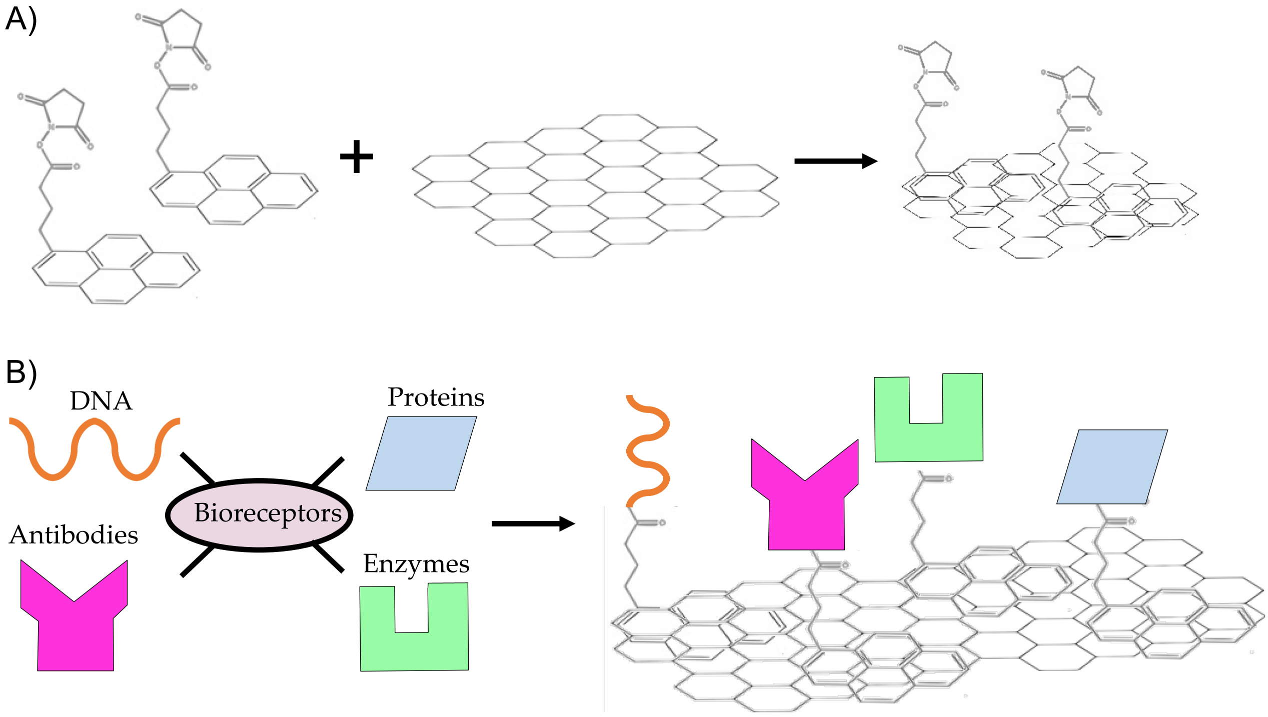

Figure 7.38 A) PBASE is initially conjugated to the graphene channel via π-stacking. B) Aminated bioreceptors are immobilised at the NHS ester end facilitating these devices as generic platforms.

The immobilisation of PBASE onto the GFET channels to form an intermediate layer between the bioreceptors and the graphene was investigated in this section. It was clear early on in this contribution that the SOP would need to be improved after post conjugation Raman measurements were examined. The original SOP consisted of drop-casting PBASE solution at a concentration of 2 mM onto devices, placing them in a humid environment to prevent evaporation and positioning them in a fridge at 2 ºC for 4 h before a rinse cycle with PBS was conducted. This process was conducted as per Haslam's group who used this methodology to functionalise GFETs for selective hCG detection [4]. Raman measurements of graphene channels taken before and after this procedure are shown in Figure 7.39.

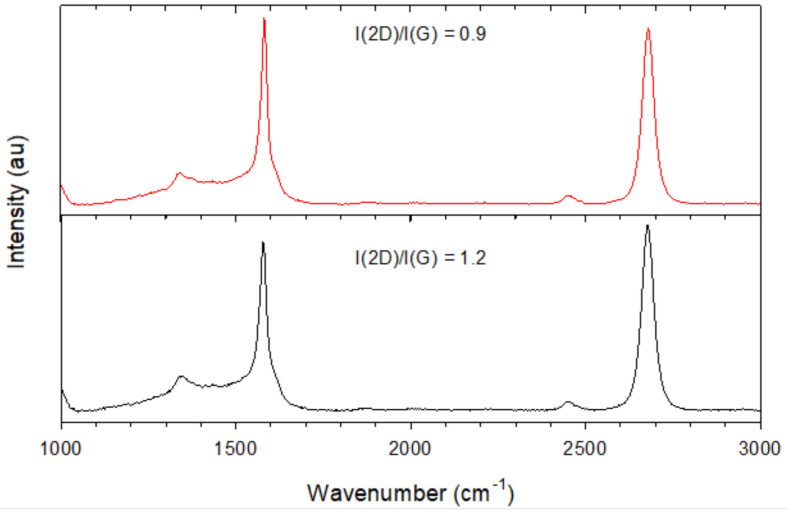

Figure 7.39 Representative spectra for fabricated graphene (black) and PBASE functionalised graphene (red) using the SOP drop-casting method.

As highlighted in Figure 7.39 apart from the difference in I(2D)/I(G) which corresponds with increased doping as should be expected, the Raman spectra between the two states is largely unchanged. The primary reason for this is the surface evaporation rate between large and small surfaces. In Haslam's work the PBASE solution was drop-casted onto a large chip with an array of devices. With a larger surface area, a greater volume of solution could be added which reduces the level of surface evaporation in their work. When the same technique was deployed on individual devices that have been cleaved as in this work, smaller volumes of the solution reduced the amount of time the solvent was present on the surface, which thus prevented it from facilitating the conjugation of PBASE onto the graphene.

7.6.2 Methodology

The process of conjugating the PBASE to the graphene was investigated by studying two different immobilisation techniques. Technique A, "The Droplet Method", which represented the SOP, involved drop-casting 2 μL of the PBASE solution directly on top of the graphene device and storing it in a cool humid environment. Technique B, "The Soak Method" involved fully submersing the graphene devices in the PBASE solution in ambient laboratory temperatures. Devices were then rinsed thoroughly in their respective solvent and DIW, before being gently air dried with N_2. The rinsing stages are necessary to ensure that any unbound PBASE molecules are removed prior to conducting characterisation measurements. As the NHS ester group of the PBASE molecule is insoluble in water it was necessary to replace the rinse cycle of the SOP which used PBS, with one that involved the appropriate solvent. The effect of different solvents (DMF and Methanol), PBASE concentrations (2 mM and 10 mM) and incubation periods (1 h – 16 h) were investigated in this work. This investigation was performed on a variety of two, seven and eight electrode devices.

The primary characterisation technique for this work was conducted using the Raman spectrometer. As discussed in section 6.3.2, graphene has a well-defined spectrum. When a PBASE SAM layer is formed, the phonon interactions in the graphene sheet change which subsequently alters the possible energy transitions possible thus producing modified spectra.

7.6.3 Results

7.6.3.1 Solvent Controls

It was necessary to investigate the effects of the solvents on the graphene surface prior to mixing with PBASE to ensure that any effects caused by them could be observed. In order to do this, Technique B was followed whereby devices were submerged in aliquots filled with DMF or methanol for 16 h before they were rinsed and dried.

No additional features in the spectra were introduced as a result of these treatments. Incubating the graphene channel with both Methanol and DMF caused right shifting in the PP(G) with no change observed for PP(2D). This is unlike the results shown by Wu [178] who observed left shifting in both the PP(G) and PP(2D). This difference is most likely down to variations in the growth/transfer/handling characteristics of the graphene and GFET devices between the two works, which will impact the as fabricated Raman metrics. This contribution also conducted these solvent control tests for 16 h, compared to 4 h for Wu's work, in order to observe the changes present due to an extreme length of incubation time.

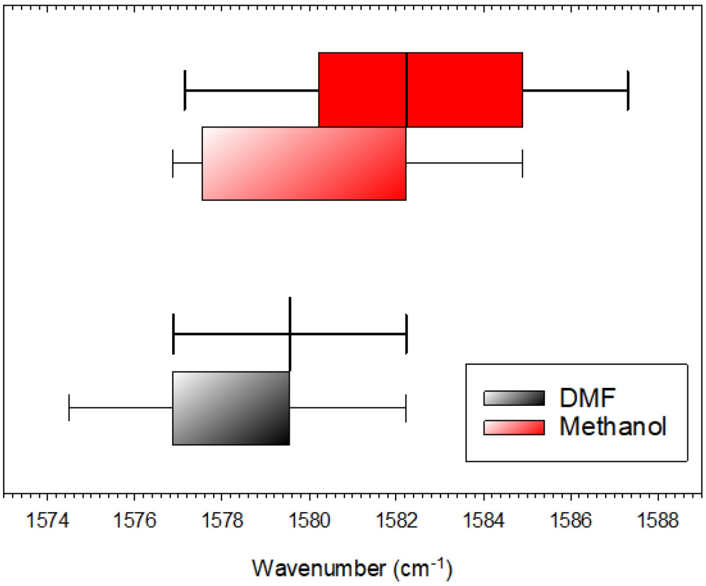

Figure 7.40 Effect on PP(G) of incubating graphene with DMF (black) and Methanol (red). The shaded (block) filled boxes represent the spread in PP(G) prior to (after) the incubation period of 16 h.

A stiffening of PP(G) is associated with an increase in concentration of holes and electrons therefore this observation suggests that there is some direct n-/p- doping caused by charge transfer from these solvents. The decrease in FWHM(G) witnessed only for DMF (not pictured) is also supportive of doping [145].

7.6.3.2 Technique

The impact of conjugating PBASE using Techniques A and B was evaluated next. Both techniques were applied for 4 h with a 2mM concentration of PBASE in DMF/Methanol. The spectra measured after the rinsing stages are depicted in Figure 7.41.

Apart from a reduction in the I(2D)/I(G) ratio exhibited by the methanol/PBASE treated graphene there are no additional features present after following the SOP for conjugation. It is still debated in the literature as to whether the reduction in this ratio can be used to conclude PBASE conjugation via the inference of the formation of bilayer structures on the surface of graphene [196, 197]. On the other hand, following Technique A but replacing DMF as the solvent introduces two features to the Raman spectra that are absent in the fabricated graphene. The first peak is at ~1222 cm^{-1} is most likely caused by the pyrene group which causes a clear peak at ~1240 cm^{-1} [99] and has been observed during PBASE conjugation in Yijun's work [122]. The second feature at ~1373 cm^{-1} is caused by the hybridization of orbitals from the pyrene base of PBASE interacting with those from graphene [96].

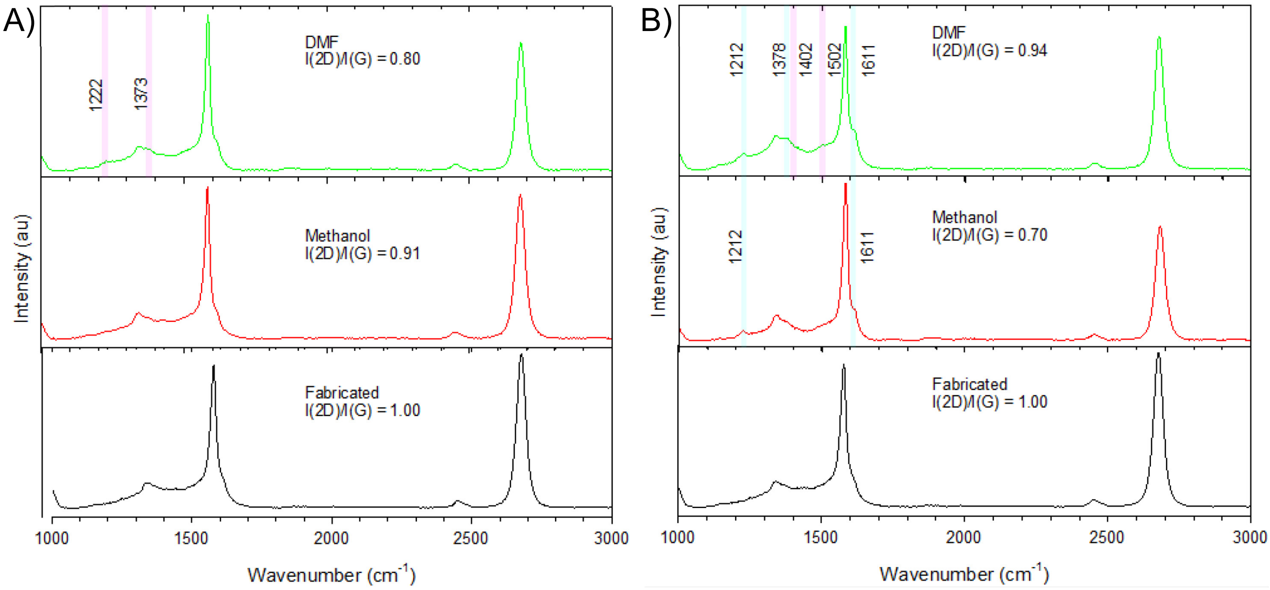

Figure 7.41 Spectra shown for fabricated graphene (black) and graphene treated with Methanol/PBASE (red) and DMF/PBASE (green) after conducting A) Technique A and B) Technique B immobilisation strategies. Features highlighted by the blue shading are shared between Raman spectra of graphene treated with Methanol/PBASE and DMF/PBASE whereas features highlighted in pink shading are only present for graphene treated with DMF/PBASE.

It is clear to see even more additional features in the spectra of Methanol/PBASE and DMF/PBASE treated graphene when they are conjugated using Technique B. It is observed that Technique B acts to introduce the ~1212 cm^{-1} and ~1378 cm^{-1} peaks to graphene's spectrum when treated with Methanol/PBASE. For both DMF/PBASE and Methanol/PBASE treatments, technique B acts to introduce a shoulder peak to the G peak at ~1611 cm^{-1}. This shoulder peak is caused by the pyrene group of the PBASE resonating due to the π-stacking interaction [96]. It provides strong evidence that the PBASE has successfully immobilised onto the graphene channel [178]. Further evidence to support PBASE binding but only resolvable in the graphene treated with DMF/PBASE is the peak at ~1402 cm^{-1}, which is also associated with the presence of pyrene groups [92]. The single peak observed for PP(2D) across all Raman spectra captured in Figure 7.41 indicates that graphene's characteristic electronic properties are unchanged due to the binding of PBASE [88].

It is clear from this investigation that technique B should be used alongside DMF as a solvent for all future PBASE conjugation, since it provides clearer evidence from the spectra that conjugation has been successful with the addition of several tell-tale peaks.

7.6.3.3 Effect of Concentration

An investigation into the influence of PBASE conjugation at 2 mM and 10 mM was then conducted. Technique B was used for both concentrations, for 4 h with DMF used as the solvent. Windows across the Raman spectra highlighting salient peaks are given in Figure 7.42. The pyrene peak at ~1229 cm^{-1} is relatively stronger for 10 mM inferring a stronger density of this molecule. All of the other peaks in the spectra that relate directly to PBASE conjugation (~1369 cm^{-1}, ~1417 cm^{-1}, ~1609 cm^{-1}) also show higher dominance in the graphene treated with PBASE/DMF at 10 mM. It is inferred from these stronger peaks that using the 10 mM has increased the density PBASE conjugation. Interestingly, the relative size of the disorder peak at 1343 cm^{-1} is slightly lower than that for 2 mM suggesting that using a higher concentration does not introduce additional defects into the graphene lattice. Therefore 10 mM in DMF was used for future PBASE treatments.

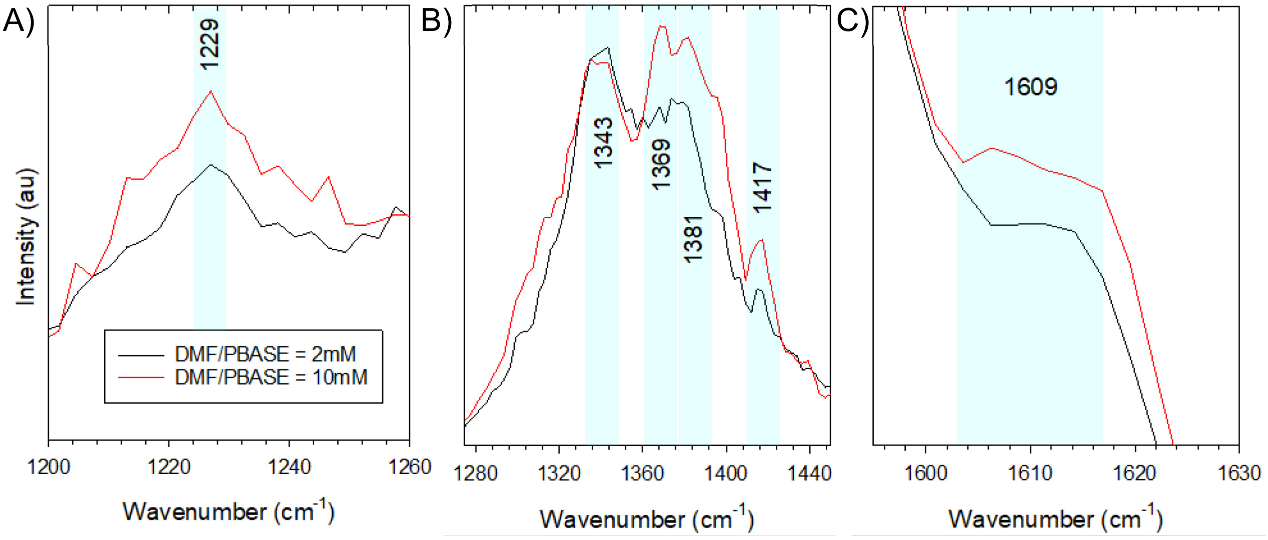

Figure 7.42 Focussed view of Raman spectra for graphene treated with DMF/PBASE 2mM (black) and 10mM (red) showing salient peaks across A) 1200-1260 cm^{-1}, B) 1280-1440 cm^{-1} and C) 1600-1630 cm^{-1}.

7.6.3.4 Effect of Time

The impact of different incubation times is evaluated in Figure 7.43. In this study, technique B was used to conjugate DMF/PBASE at a concentration of 10 mM to the graphene surface for 1 h, 2 h, 4 h and 16 h.

Figure 7.43B shows that the relative intensity of every peak associated with PBASE increases with increasing incubation time which can be used to infer higher density of the PBASE molecule onto the surface of graphene. It can also be observed that the disorder peak increases which suggests that the increasing time causes additional defects to be introduced to the graphene lattice.

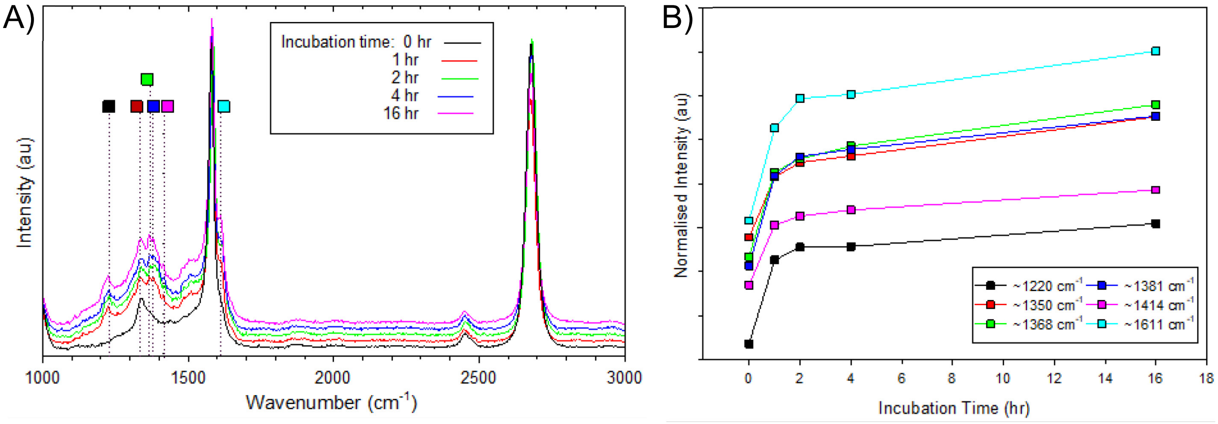

Figure 7.43 A) Normalised Raman spectra captured after incubation for 1 h (black), 2 h (red), 4 h (green) and 16 h (blue), with offset applied for clearer graphical visualisation. The coloured squares show the position of the peaks used to make plot (B). B) Change in relative peak intensities (no offset) for Raman spectra shown in (A).

Since defects offer sites for nonspecific binding it is better to reduce their presence for biosensing technologies [87]. From this data it was determined that the best incubation time to infer adequate PBASE binding without the introduction of unnecessary defects to the graphene surface is 4 h.

7.6.3.5 Optimised Method

Typical electrical measurements that represent fabricated graphene and graphene treated with PBASE are shown in Figure 7.44. The increase in gradient shown in the I_{SD}-V_{SD} measurement infers that the conjugation of PBASE has decreased the resistance through the channel.

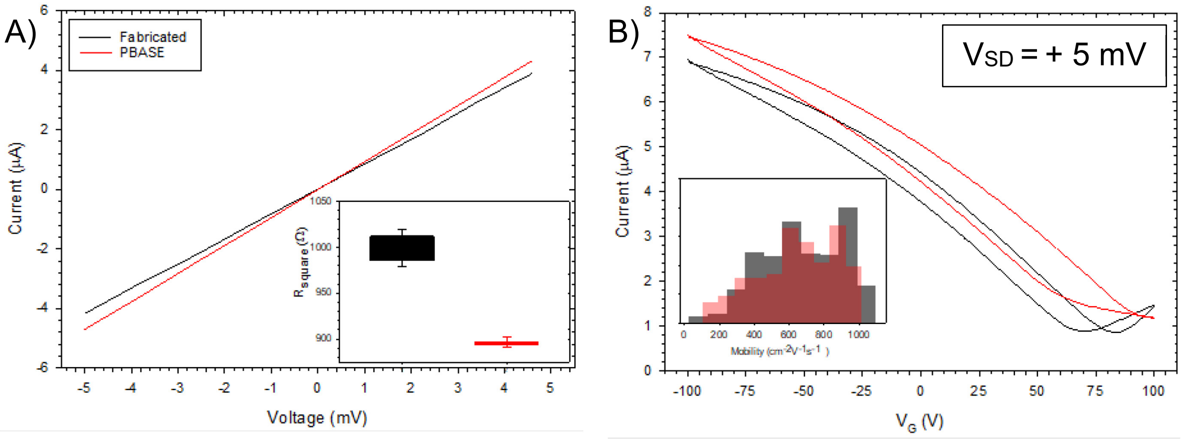

Figure 7.44 Electrical characterisation of GFET device treated with PBASE showing A) I_{SD}-V_{SD} with inset showing the square resistance B) I_{SD}-V_G with inset showing the mobility values across the transfer curve.

The conjugation of PBASE has increased the position of the V_{DF} and V_{DR} to greater than + 100 V, although the rapidly decreasing gradient for the PBASE line suggests that they are positioned somewhere close to it. A right shifting in this position is well documented in the literature [3, 11, 196-198] and infers an increase in the density of hole charge carriers. The existence of an electron acceptor, in the form of PBASE's carbonyl group can be partially credited for this effect [178]. Interestingly, since the gradient of both transfer curves are similar throughout, the doping of the channel has not impacted the mobility of the charge carriers as displayed by the histogram plot in the inset of Figure 7.44B. This is in contradiction to Wu's work who noticed a severe reduction in the carrier mobility when graphene was treated with PBASE/DMF [178]. It can be inferred by the lack of change exhibited in this observation that the non-covalent π-stacking has been successful and has not negatively impacted the graphene's conductive properties [198].

XPS measurements were also conducted to confirm the non-covalent PBASE conjugation to the graphene lattice. A high resolution nitrogen spectra (N1s) at ~ 400.4 eV was recorded for fabricated and PBASE conjugated graphene and is shown in Figure 7.45. The raw data and fitted envelopes, which have been offset to overlay them for easier comparison, are indicated by the "x" symbols and line plots respectively. Since the PBASE molecule contains a single N atom, this peak can be used to determine the presence of it on the surface of graphene. Although a slight increase in the N 1s peak is observed for the PBASE spectrum here, repeated measurements are required to increase the confidence in the data prior to making conclusions as severe delays with samples were likely to have impacted these results. Comparing XPS spectra in this way was used by Liu et al to provide additional evidence of PBASE binding [96].

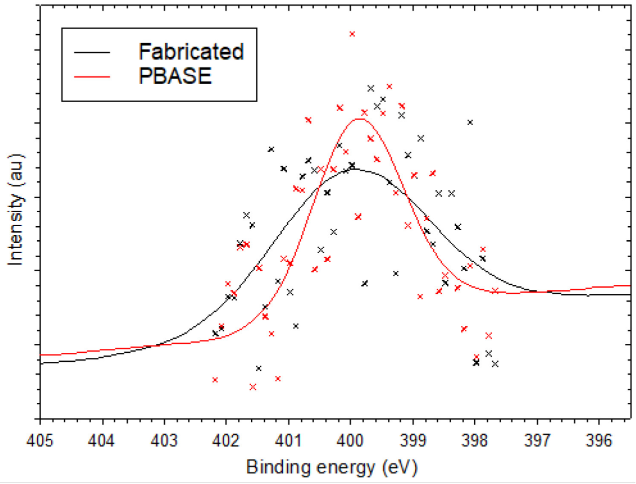

Figure 7.45 High resolution N 1s XPS spectrum of fabricated graphene channel. An offset has been applied to PBASE spectrum to roughly overlay the N 1s peaks for easier comparison.

AFM was another technique used to infer PBASE conjugation. AFM images of a fabricated graphene channel before and after PBASE conjugation were captured and are shown in Figure 7.46. Prior to PBASE treatment the Root Mean Square (RMS) roughness and mean roughness were 0.99 nm and 0.46 nm respectively. For a separate graphene channel treated with PBASE these values increased to 6.20 nm and 3.45 nm after the channel. An increase in surface roughness was also observed by Seo et al to confirm PBASE binding; this group showed a 59% increase in RMS roughness [2]. The estimated increase in RMS in this work of ~526% is most likely an overestimation and could be related to ineffective washing leaving residuals on the surface (illustrated in 3D in Figure 7.46C).

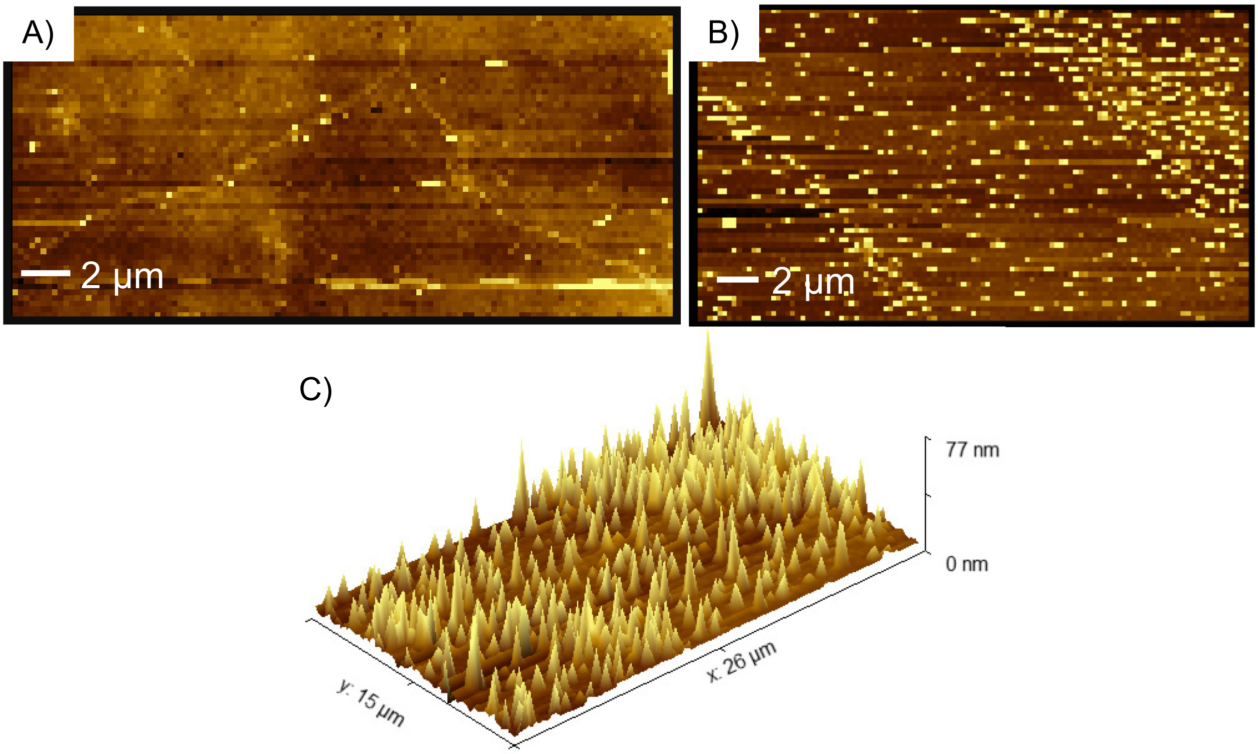

Figure 7.46 AFM image of typical GFET device after A) fabrication B) functionalisation with PBASE C) 3D topological view (B)

PBASE conjugation to graphene was then verified using FTIR measurements by using a sample of graphene on copper foil immobilised in the exact same way. It was necessary to use graphene on copper to take these measurements to exploit copper's high malleability to overcome limitations in sample format for the ATR technique. The FTIR spectra captured for graphene on copper, treated and untreated with PBASE, are shown in the bottom panel of Figure 7.47. Additional peaks are clearly resolved at the wavenumbers of 842 cm^{-1} (C=C bending), 1209 cm^{-1} (C-O stretching) and 1744 cm^{-1} (C=O stretching) for the graphene on copper sample treated with PBASE [199]. The top panel FTIR spectra in Figure 7.47 shows the measurement acquired from the PBASE powder using the KBr pellet technique. The plots have been scaled so that the wavenumbers are aligned. It is observable that the prominent peaks seen in the treated graphene on copper match well with the peaks of the PBASE powder providing strong evidence of successful conjugation.

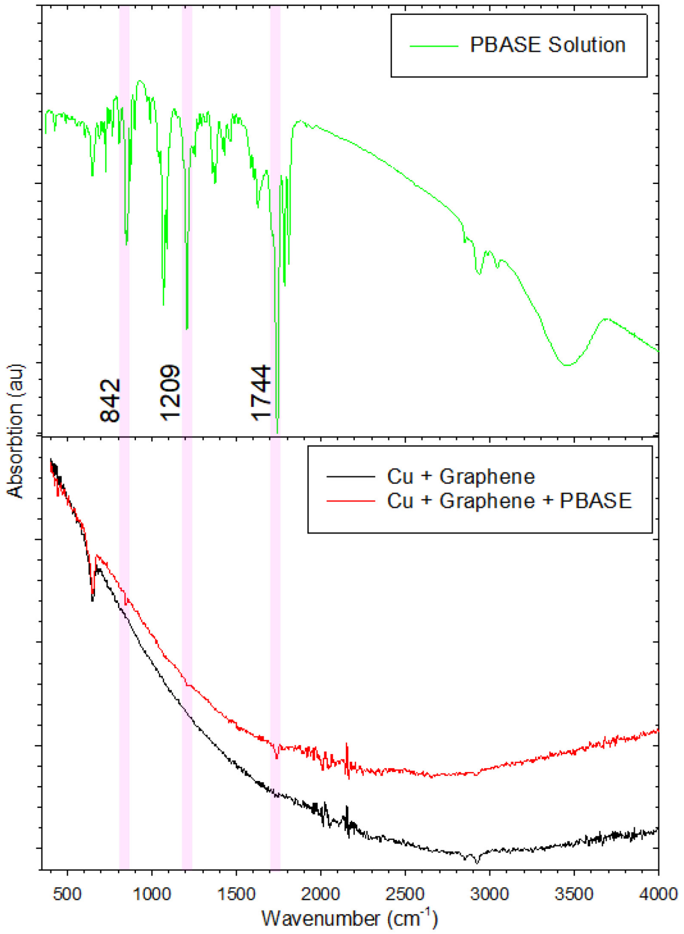

Figure 7.47 Bottom panel) FTIR spectra of graphene on copper (black) and graphene on copper treated with PBASE (red) with offset applied for clearer graphical visualisation. Additional characteristic peaks highlighted by the pink regions. Top panel) FTIR spectra of PBASE powder captured using KBr pellet technique. Peaks that are shared between the PBASE powder and PBASE treated graphene on copper are highlighted in pink.

7.6.3.6 Structural Defects

It was observed that following technique B for the immobilisation of PBASE caused the edges of some graphene sheets to undergo significant structural changes. This occurred with both DMF and Methanol as the solvent, with all concentrations and all immobilisation times. This change has been visualised in Figure 7.48A and B which show the same graphene channel before and after the immobilisation of PBASE.

The effect is seen most significantly at the corners of the channel where the surface area to volume ratio is highest. This change is manifested as a variation in the optical properties for the material which is represented in the optical images as lighter regions closer to the edges of the channel. Raman spectroscopy was used to probe the spectra of these two regions and are shown in Figure 7.48. The darker areas in the images, which correspond to the graphene regions, produce Raman spectra with evidence of standard PBASE conjugation as per details already described in this section.

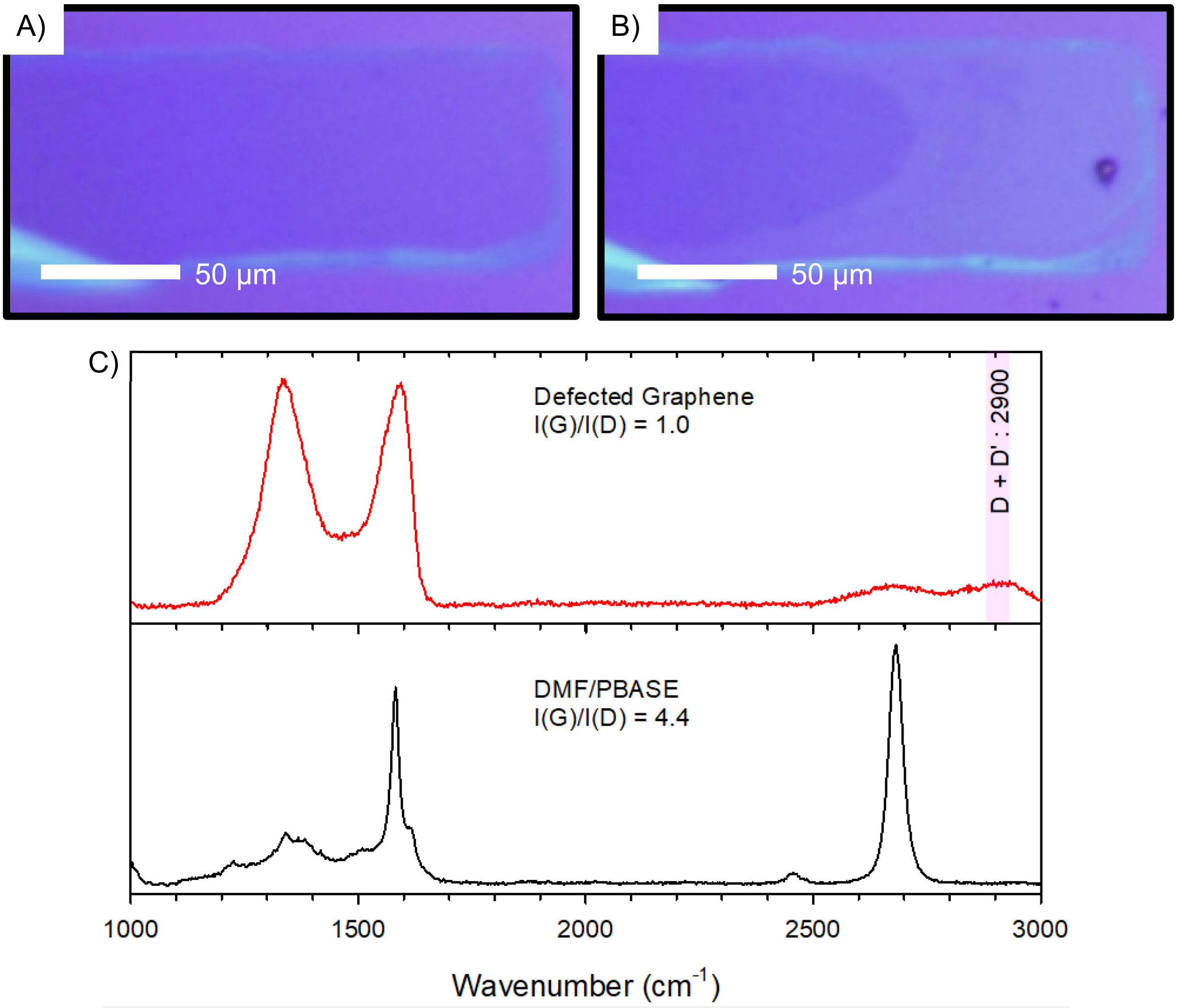

Figure 7.48 Optical image of graphene channel captured A) before immobilisation B) after immobilisation with 10 mM DMF/PBASE treatment with lighter region highlighting areas effected. C) Raman spectra acquired in Bottom Panel) darker regions inferring graphene presence (black), and Top Panel) lighter regions inferring defected graphene (red).

However, when the patches in the lighter regions are examined, the spectrum changes quite dramatically as shown in Figure 7.48C. The significant increase in the D and G peak along with a reduction in the 2D peak are observed. Along with this, an additional peak at ~2900 cm^{-1} can be observed and is denoted as the D+D' peak, which is caused by a combination of phonons around K and Γ with different momenta, which only becomes viable when defects are introduced [200].

Perhaps the exposure causes the introduction of significant levels of disorder modifying the graphene into graphene oxide (GO). The functional groups present on GO require defects, spaces in the lattice and/or sp^3 hybridized carbon atoms to be present producing a non-planar sheet to be formed. The greater proportion of defects in GO, which activates the breathing modes of the aromatic ring is represented in the Raman spectrum as a larger D peak (~1350 cm^{-1}). This disruption to the sp^2 lattice causes the reduction in electrical conductivity for GO [201]. Investigations into Ti- and Cr- coatings on SLG and its impact on Raman spectra conducted by Iqbal support these observations. This group showed similar changes to the Raman spectrum of graphene by thin layer deposition of Ti. When they deposited similar layers of Cr, no such change was observable. They noted that the reason for this difference was that Cr does not introduce as many defects than the Ti [200].

The observations described here were made on graphene functionalised with PBASE after Phase I of the fabrication process. As this phenomena is witnessed on the extreme ends of the channel, where the metallic contact would usually be, it is conjectured that this effect is not described in the literature as metallic electrodes that are usually patterned onto devices act to protect the graphene from this interaction. This phenomena has not been reported in the literature during studies that use similar techniques to immobilise PBASE but is vital to be made aware of since the electrical behaviour of graphene oxide is different to that of graphene. More work is required to understand the mechanism of this structural change. It is conjectured here that DMF’s strong exfoliation and dispersive qualities for graphitic materials could be the cause of this observation [202].

7.6.3.7 Uniformity of PBASE Immobilisation

There is little discussion in the literature that relates to the uniformity of the distribution of PBASE molecules formed in the SAM. This is a useful characteristic to know since it will inform the best strategy for passivation steps necessary to reduce the occurrence of non-specific binding of analytes. A reliable technique for imaging the uniform distribution of PBASE on graphene channels at the macroscale is required and initial investigations are presented here.

Raman mapping was initially used to conduct uniformity studies across graphene channels. This was achieved by high resolution scans consisting of 30 x 30 spectral measurements, separated by ~2 µm distances. An example of such a scan, covering an area of ~55 x 63 µm, conducted with the GFET device in the exact same position prior to and after PBASE treatment is demonstrated in Figure 7.49. It is useful to note that the electrodes, signified by the rectangular blue (I(2D):I(G) ~1.0 –Figure 7.49C) shapes on the left hand side of both figures, were also part of the scan primarily as they are useful structures to accurately position the device for pre- and post- treatment comparisons. These maps display the distribution of the I(2D):I(G) ratio across the GFET device. It can be deduced that for fabricated graphene, there is a high value across the graphene whereas after PBASE treatment, the ratio reduces significantly, inferring widespread doping of the graphene caused by the conjugated molecules. The uniformity could also be inferred in a similar manner by monitoring other metrics such as I(1616). These measurements provide strong evidence for a uniform distribution of PBASE.

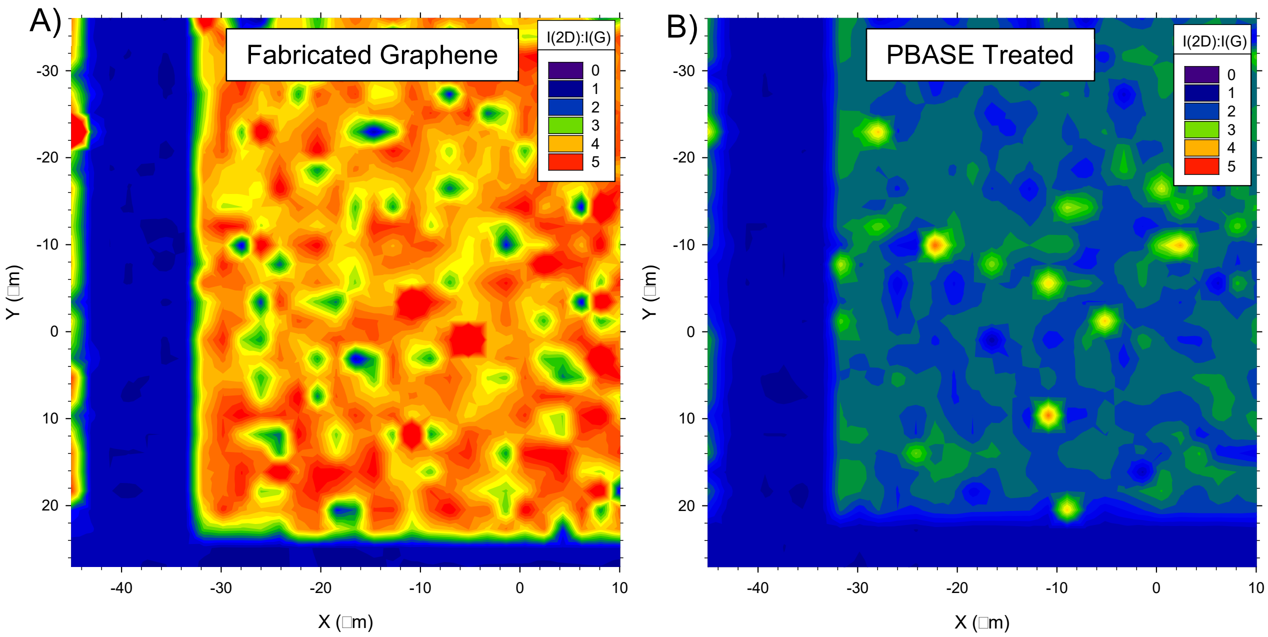

Figure 7.49 Raman mapping showing the I(2D):I(G) ratio across A) Fabricated graphene and B) PBASE treated graphene

This technique (performed in dry conditions) allows the user to determine uniformity of PBASE conjugation across detailed parts of a GFET device. It is also non-destructive which allows further functionalisation to continue afterwards. However, since it is limited to small areas of the graphene channel the large timescales to cover the entirety of the 720 x 80 µm channel used in this work is simply not sensible making this a highly detailed but low throughput technique for this exact purpose.

Fluorescent microscopy was used by Kakatkar et al, as additional confirmation for the immobilisation of DNA onto the surface of graphene. Interestingly this group observed the elongation of DNA strands which they postulated was due to their N_2 gun drying regime (Figure 7.50A) [9]. Similarly, confocal fluorescence microscopy was used by Tehrani et al to verify that their primary antibodies were functionalised onto the epitaxial grown graphene surface only and had not been immobilised onto the SiC substrate (Figure 7.50B) [147]. In another example, the investigation led by Rodrigues de Almeida III deployed antibodies conjugated with FITC bound directly to a PBASE intermediary layer to show that antibodies would only bind to the graphene when PBASE had been previously immobilised [93].

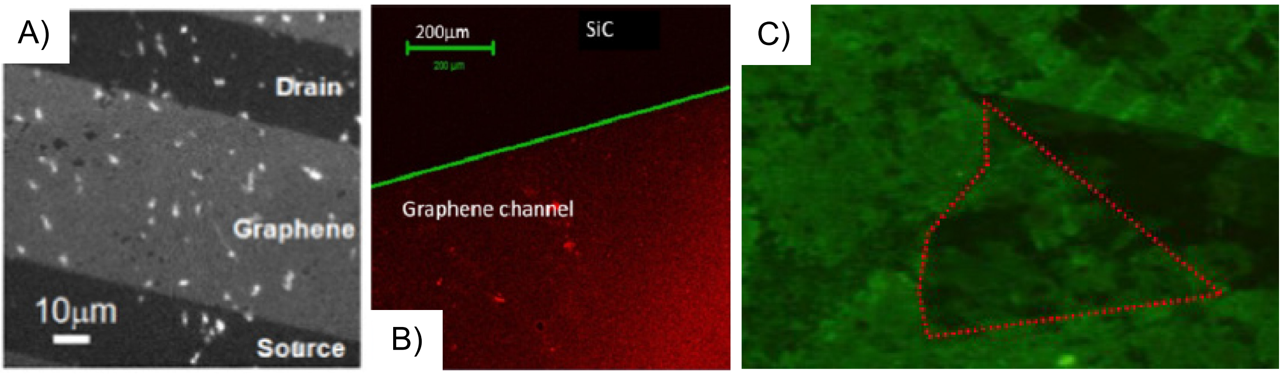

Figure 7.50. A) Fluorescence micrograph of distribution of DNA across GFET [9] B) Confocal fluorescence micrograph of antibodies on graphene substrate [147]. Fluorescent distribution around graphene flake (dotted outline) Adapted from [93]

Optical labelling using fluorescently tagged antibodies (FTAs) as introduced in 6.3.3.2 was developed in this work to attempt to image the entire graphene channel. PBASE conjugation was conducted using the optimum parameters detailed in 7.6.3.5. Details relating to the specific antibodies and fluorescent tags used can be found in Appendix A4. Initial fluorescent microscopy was attempted using direct immobilisation whereby FTAs (Donkey-α-Mouse-488) were bound directly to the PBASE molecules via the NHS ester group. To achieve conjugation, primary antibodies were drop casted on graphene channels and left to incubate at room temperature, in a humid environment to prevent evaporation, for 16 h. Rinsing was then conducted to remove unbound FTAs prior to imaging. When the system was then exposed to the appropriate emission wavelength, the fluorophore group fluoresces signalling the location of the bound FTAs inferring the uniformity of the PBASE SAM. Initial fluorescent microscopy images acquired using this technique are shown in Figure 7.51.

The microscopy images displayed in Figure 7.51 show zero selective fluorescence for the graphene channels indicated by the dark rectangular structures showing minimal fluorescent intensity, clearly standing out against the strongly fluorescing background. This suggested one of two things; Firstly, the PBASE linkers have bound everywhere but the graphene channel. This is not possible since the PBASE linker chemistry does not support PBASE conjugation to the Si/SiO_2 substrate layer. The strongly fluorescing background is most likely caused by inadequate rinsing which leaves unbound FTAs on the surface.

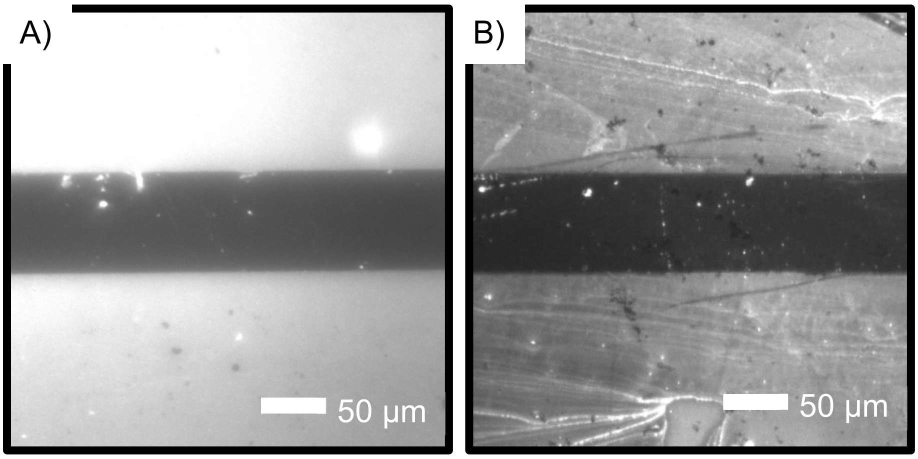

Figure 7.51 Direct immobilisation of FTA to graphene surface for Donkey-α-Mouse-488 with figures A and B presenting repeated experiments. Both images are acquired with an acquisition time of 6s and using FITC filter.

Alternatively, and as supported with Raman spectra which shows clear evidence for the successful conjugation of a uniform PBASE layer, the FTAs bind with a high affinity for the graphene channel but the labels are then fluorescently quenched. Graphene behaves as a fluorescence quencher whereby energy is transferred from fluorescent groups into the graphene lattice. During this process the fluorescent intensity is thus reduced. This mechanism relies on the resonant energy transfer from fluorophores to electron-hole pairs in the lattice [203]. Work by Kasry showed that the fluorescence quenching was distance-dependent further supporting the non-radiative transfer of energy during this process [203]. Fluorescence quenching microscopy (FQM) is a technique developed by Kim et al which exploits this phenomenon to visualise graphene and graphene derivatives in a high-throughput, simple and quick manner [204]. In this study, the group showed fluorescent quenching by graphene and its derivatives across three vastly different dyes (red, green and blue) to show that the quenching effect occurs across a diverse range of fluorophores making these materials general quenchers. Although useful for optical biosensing applications, this particular characteristic of graphene makes it more difficult to assess the distribution of conjugated material on the surface using traditional fluorescence techniques.

In an attempt to increase the distance between the graphene sheet and fluorescent groups to overcome the quenching effect, an additional intermediary layer of unlabelled antibodies were deployed to which FTAs were subsequently bound. This was the second technique developed to infer the uniformity of the PBASE distribution. The secondary FTAs are chosen so that they had a high affinity for the primary antibody and therefore could be bound effectively. Following primary antibody immobilisation (described above), secondary

FTAs were drop casted onto the graphene surface and left to incubate in the same manner for 3-4 hours. After a rinse cycle the fluorescent images were captured and typical measurements are shown in Figure 7.52.

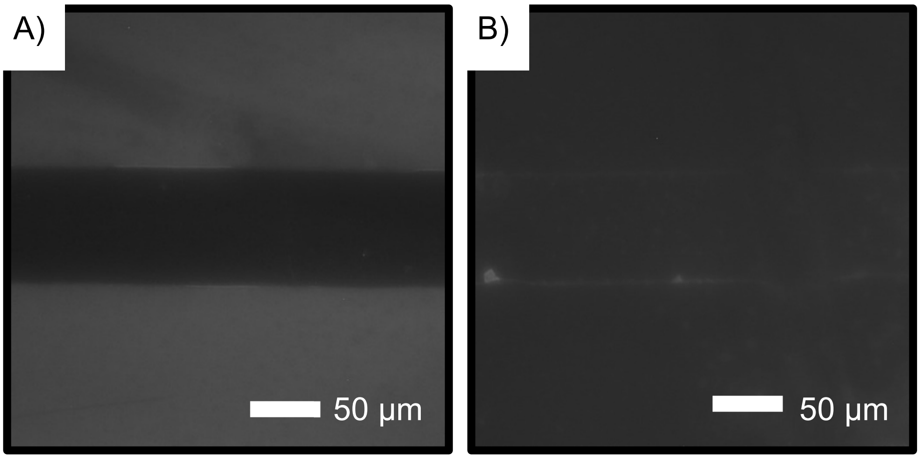

Figure 7.52 Indirect immobilisation of FTA to graphene surface. A) Primary: Mouse-α-NF200, Secondary: Donkey-α-Mouse-FITC. B) Primary: Sheep-α-CGRP, Secondary: Donkey-α-Sheep-FITC. Both images are acquired with an acquisition time of 6s and using FITC filter.

As displayed in Figure 7.52 similar observations were made when the devices were illuminated using both the direct and indirect immobilisation strategies. This suggested that the increase in distance had not been sufficient to overcome the quenching mechanism. A decrease in the background fluorescence is credited with more vigorous rinsing. For a full list of combinations of FTAs used throughout this contribution the reader is signposted to Appendix A4.

More work is required to build on these techniques to successfully image graphene using FTAs. It is unclear what process prevented these measurements from being successful. It is unlikely that the FTAs did not bind to the graphene since effective protocols previously described in [93] were followed. As similar fluorescent groups were used in these techniques, the effect of quenching on different fluorophores can be discounted. It is conjectured that the antibodies used in this work were the limiting factor and were too small to overcome the distance dependant quenching.

7.6.4 Summary

A repeatable method for conjugating the bi-functional PBASE linker was developed in this section. After initial investigations showed that the original SOP was no longer appropriate for post cleaved single GFET devices it was necessary to optimise a new procedure for binding. The organic solvent, technique, concentration and time were all optimised throughout this work. It was determined that fully submersing devices in tubes of PBASE dissolved within DMF, at concentrations of 10 mM for 4 h in the ambient laboratory environment provided the optimum binding results which balanced the need for clear conjugation evidence, minimum disorder introduction whilst maintaining the electrical properties of graphene. Raman, Electrical, AFM, XPS and FTIR characterisation were all used to provide evidence of successful non-covalent binding of the PBASE molecule to the surface of graphene.

A key observation that was identified whilst investigating the effect of PBASE conjugation on graphene only channels was shared in this work. It was highlighted that when graphene channels are exposed to PBASE/DMF and PBASE/methanol solutions there is evidence of an introduction of substantial structural defects starting at the ends of the channels. Since a high level of defects is associated with a reduction in the electrical merits of graphene it is essential to understand the mechanism of this change further. Future work should investigate whether this effect is pacified by metal contact layers and whether the protection (if any) is the same for pre-pattern or post-patterned electrodes. It would also be useful to pattern electrodes on channels which have shown this observation to measure any changes in the electronic configuration.

An investigation into techniques suitable for assessing the distribution of PBASE molecules across graphene was then presented. Using Raman mapping techniques were effective at producing detailed regions, which inferred uniform distribution, however the timescales needed to conduct such measurements across the entirety of the channel would prevent this technique from being widely used. Instead, techniques used to deploy FTAs to infer the distribution of PBASE were presented. Initial results showed that there was no significant fluorescence observable by the FTAs which suggested that the fluorescence was effectively quenched by the graphene channel. To overcome this an additional layer of antibodies (with no optical labelling) were immobilised on the surface prior to conjugating the FTAs however, there were still no evidence of fluorescence. The use of other optical labels such as QDs or nanoparticles should be investigated next to develop a macroscale method of determining distribution. In the meantime, patching together several detailed Raman maps should be completed to confirm that PBASE conjugation results in a widespread uniform SAM layer.

7.7 DNA Conjugation

7.7.1 Introduction

The conjugation of bioreceptors to the graphene surface is fundamental to enabling selective detection of target analytes. In this work TBA was used as a bioreceptor for the specific detection of Pb^{2+} ions. It was immobilised onto the surface of graphene in one of two ways; indirectly and directly. Indirect immobilisation required the use of the PBASE linker to be initially conjugated on the channel. Aptamers which had an amino-modified (C6) 5' end (hereafter TBA) were then cross linked to the NHS ester group via nucleophilic substitution to immobilise them as bioreceptors on the graphene surface (Figure 7.53A). The direct method involved the use of pyrene tagged TBA (hereafter PTBA) which harnesses a pyrene group to bind to the graphene lattice via π-stacking (Figure 7.53B).

Modifying TBA (Figure 7.53A) with an amino (C6) group is competed using a phosphoramidate procedure. This exploits the tendency of 1-Ethyl-3-(3-dimethylamino propyl) carbodiimide hydrochloride (EDC) to react with alkyl phosphate groups to form active complexes called phosphodiesters. The phosphodiester intermediaries are then bound to molecules containing amine binds by phosphoramidate bonds [97]. One way that TBA can be modified with a pyrene modification is by incubating amino-functionalised DNA with the PBASE linker (Figure 7.53B). Although relatively straightforward, the binding efficiency can be as low as 50% which could result in free aptamers/PBASE molecules interfering with the binding of the PTBA bioreceptors to the surface [205].

7.7.2 Methodology

The most effective method of conjugating the DNA and PTDA to the surface of graphene was using a drop-casting method similar to that described in 7.6.2. During this technique 1-2 µL of DNA/PTDA was deposited on the surface of the GFET and incubated at room temperature for 4 h in a humid environment to prevent evaporation. For both circumstances, rinsing with either PBS or DMF and then DIW followed by drying with N_2 was performed to remove any trace of unbound aptamers. This method replicated the graphene face-up approach that most groups use when incubating DNA and PTDA to their devices [7, 116, 123, 124, 206]. These groups usually deploy microfluidic channels or wells to contain the solution over the graphene channel and prevent the evaporation of the solvent. The concentration of 10 µM was used for both immobilisation strategies.

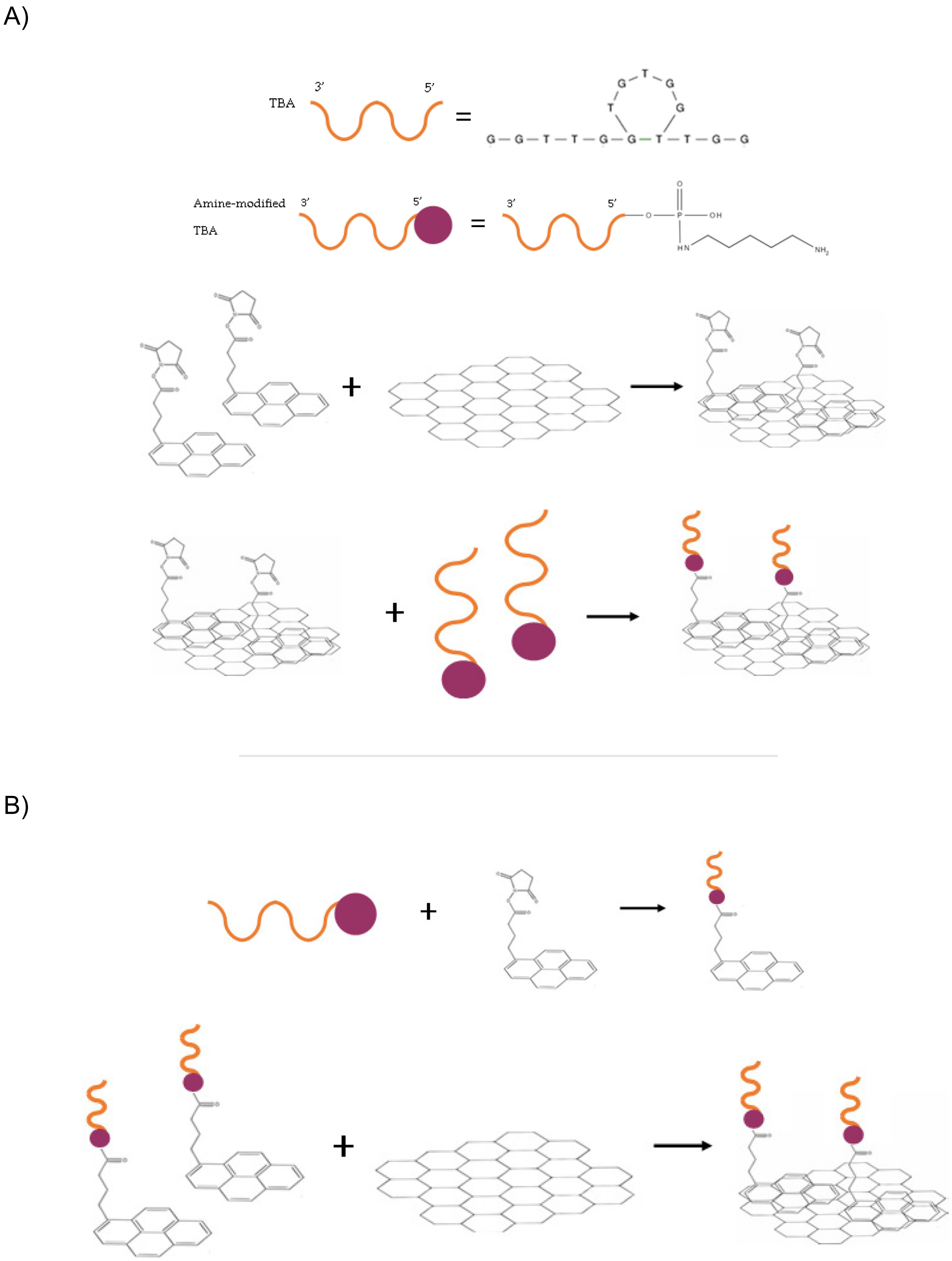

Figure 7.53 A) Overview of Indirect immoobilisation. 1st Panel - Secondary structure of TBA as predicted by Mfold server [117]. 2nd Panel – TBA with amino-modified (C6) 5' end. 3rd Panel – Conjugation of PBASE to graphene surface. 4th Panel - Immobilisation of amino-modified TBA to PBASE B) Overview of direct immobilisation. Top Panel – Showing process of modifying TBA with pyrene-tagged 5' end. Bottom Panel - Pyrene-tagged TBA directly conjugated to graphene surface

For the indirect immobilisation method, PBASE linkers were used to non-covalently immobilise the TBA aptamers to the surface of graphene. GFET devices were soaked in 10 mM PBASE-DMF solution for 4 h at room temperature followed by a thorough washing stage with DMF and DIW before being dried with an N_2 airgun. This was conducted prior to DNA immobilisation. More details on PBASE conjugation is provided in section 7.6.

7.7.3 Results

7.7.3.1 Initial Characterisation

Depending on the synthesis yield detailed by the supplier, the appropriate amount of solvent was initially added to the tube of lyophilized DNA to produce a stock of 100 µM. After solutions of DNA/PTDA were prepared to the desired concentration levels and dispensed into aliquots for single-thaw use, it was necessary to conduct UV-Vis spectrophotometry to confirm the presence of the nucleic acids and determine the level of contamination. UV-Vis measurements of TBA in PBS and PTBA in DMF are shown in Figure 7.54A and B respectively.

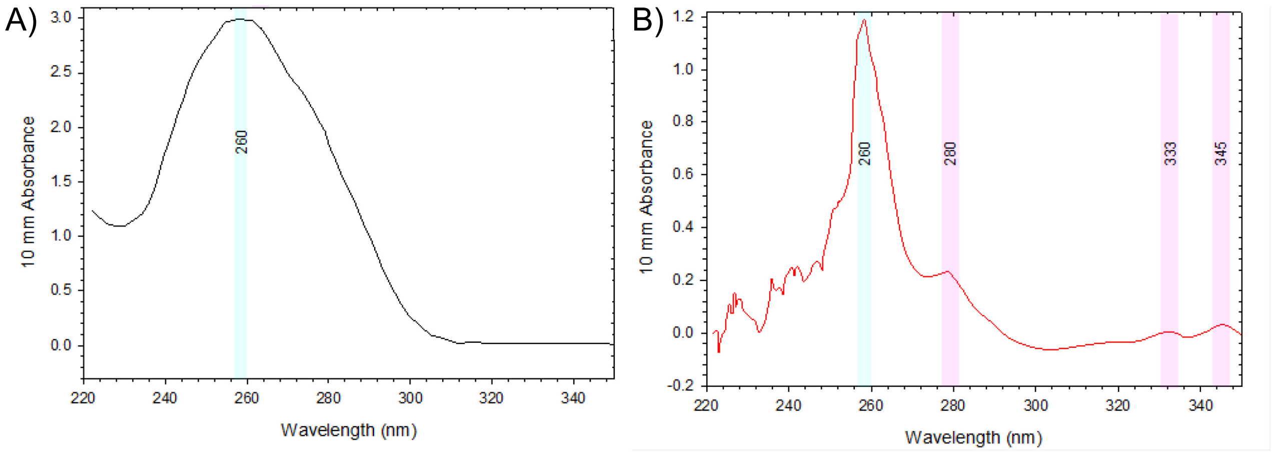

Figure 7.54 UV-Vis spectra of A) 20 µM TBA B) 20 µM PTBA with the characteristic 260 nm peak indicated by the blue shaded region. Pink shaded regions indicate additional peaks introduced as a result of the presence of pyrene groups.

A strong peak in the absorbance at 260 nm for both complexes indicates the presence of DNA. In order to calculate the concentration of the solutions it was first necessary to calculate the extinction coefficient for the TBA sequence. Using the Nearest-neighbour model discussed in 6.3.6.3 with the nucleotide coefficient reference table given in Appendix A1, the following calculation for the extinction coefficient for TBA was conducted:

$$TBA\ Sequence\ = GGTTGGTGTGGTTGG$$

$$\varepsilon_{260}^{n.neighbour} = (GG) + (GT) + (TT) + (TG) + (GG) + (GT) + (TG) + (GT) + (GG) + (GT) + (TG) + (GG)$$

$$\varepsilon_{260}^{n.neighbour} = 4 * (GG) + 3 * (GT) + 1 * (TT) + 3 * (TG)$$

$$\varepsilon_{260}^{n.neighbour} = 4 * (21600) + 3 * (20000) + 1 * (16800) + 3 * (19000)$$

$$\varepsilon_{260}^{n.neighbour} = 276{,}000\ Lmol^{-1}cm^{-1}$$

$$\varepsilon_{260}^{i.bases} = 7 * (G) + 6 * (T)$$

$$\varepsilon_{260}^{i.bases} = 7 * (11500) + 6 * (8700)$$

$$\varepsilon_{260}^{i.bases} = 132{,}700\ Lmol^{-1}cm^{-1}$$

$$\varepsilon_{260}^{TBA} = \varepsilon_{260}^{n.neighbour} - \varepsilon_{260}^{i.bases}$$

$$\varepsilon_{260}^{TBA} = 143{,}300\ Lmol^{-1}cm^{-1}$$

The extinction coefficient at 260 nm is not impacted by the conjugation of the C6-amino group to the 5’ end of the TBA strand as there are no additional carbon double bonds. However, a review of the literature relating to pyrene group modifications of substances shows that there are additional absorbance peaks introduced to the UV-vis spectrum as a result of pyrene group addition [207-210]. Pyrene groups have an absorbance peak at ~260 nm, caused by the carbon double bonds. The additional peaks seen at ~280 nm, ~333 nm and ~345 nm are also attributed to the pyrene group modification [207] and have been observed by Wang in [124] in similar experimental circumstances. Since the calculation of the modified extinction coefficient is beyond the scope of this work, the concentration of the PTBA complex was not verified.

Using the Beer-Lambert law equations, as discussed in 6.3.6.3., the concentration of the TBA solution is completed:

$$c_{DNA} = \frac{2.99}{143{,}300} = 20.9\ \mu M$$

The value of 20.9 μM is an indication of successful dilution steps from the stock DNA. The A_{260}/A_{230} ratio was then examined to determine the level of chemical contamination. For the TBA and PTBA complexes this was calculated to be 2.8 and 18 respectively which infers a low level of contamination, consistent with effective DNA handling techniques.

7.7.3.2 Indirect immobilisation

Raman measurements were conducted on graphene after DNA was immobilised. As shown in Figure 7.55, there are no additional peaks caused by the immobilisation of DNA. This is supported by similar measurements conducted by Nekrasov’s group [7]. The absence of an increase in the D peak highlights that this process does not increase the disorder and density of defects in the channel. This result is expected since the amine group of the DNA binds only to the active succinimidyl ester group of the PBASE molecule and not directly to the graphene channel. Although DNA does have Raman bands around 1584 cm^{-1}, the strong Raman signal from the underlying monolayer graphene between (1350 cm^{-1} and 1650 cm^{-1}) limits the visibility of them [211].

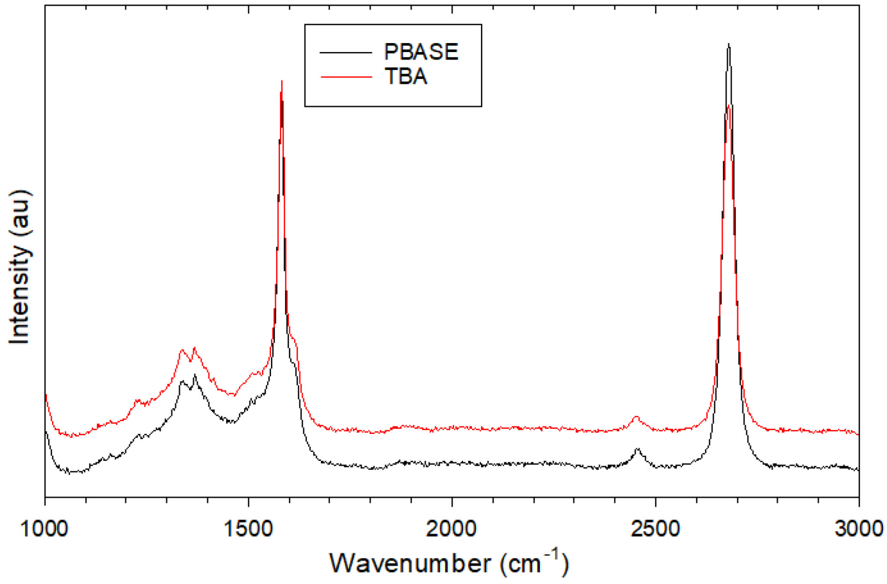

Figure 7.55 Typical Raman spectrum of graphene after PBASE immobilisation (black line) and 10 µM TBA-DNA immobilisation (red line) with offset applied for clearer graphical visualisation.

Conversely, other groups have inferred DNA conjugation by observing additional peaks using Raman spectroscopy. K. Xu et al confirmed the presence of the TBA aptamers used for sensing Pb^{2+}, on the surface of graphene when they witnessed additional peaks between 900-1600 cm^{-1} appear in the spectrum [116]. In addition, the group led by S. Xu showed additional sets of peaks appear, corresponding to nucleic acid Raman modes, which straddle the G peak in their work on exploiting 27 nucleotide base aptamers for ATP detection [206]. S. Xu were able to identify peaks at 1476 cm^{-1}, 1502 cm^{-1} and 1659 cm^{-1} after aptamer immobilisation. Higher resolution Raman measurements with the grating set to 2400 gmm^{-1}, yielding spectral resolutions between 1.67 – 1.19 cm^{-1} were captured (not shown) and did not show peaks introduced at similar wavenumbers.

The Raman measurements can be used to infer the presence of DNA from the change in I(2D):I(G) ratio. Figure 7.56 plots the I(2D):I(G) against the I(2D):I(D) ratios for individual spectra captured at each of the functionalisation stage. As previously discussed in 6.3.2.2 the ratio between I(2D):I(G) can be used to describe the doping of the graphene channel, with a negative correlation observed between I(2D):I(G) and doping. Control measurements were conducted when only PBS was added after successful PBASE conjugation. In direct contradiction to what is shown in Figure 7.56 significant increases in both the I(2D):I(G) and I(2D):I(D) (not pictured) ratios were observed.

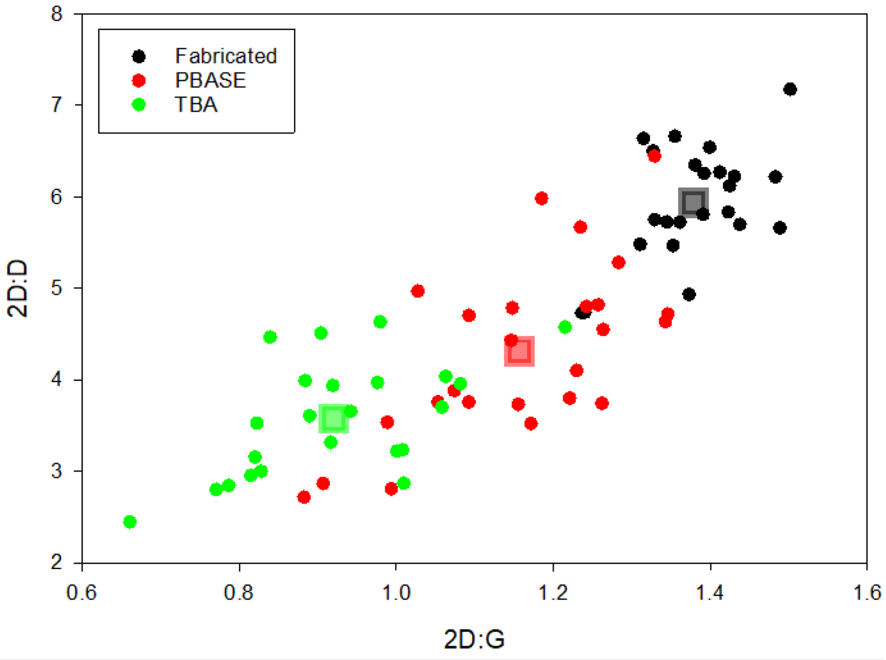

Figure 7.56 Scatter plot showing evolution of I(2D):I(G) and I(2D):I(D) ratios for fabricated (black), PBASE (red) and 10 µM TBA (green) functionalised graphene with average values indicated by square markers.

Firstly, it is observed from Figure 7.56 that there is clear clustering between the functionalisation stages. Since the metrics are bunched together in this manner it shows good repeatability in the data collected at each stage. Next, it is clear that as the functionalisation has progressed the I(2D):I(G) ratio has decreased, firstly from fabricated to PBASE and then from PBASE to DNA. This indicates an increase in the doping of the channel at each step caused by the immobilised structures. Finally the I(2D):I(D) ratio follows the same pattern. The initial reduction in this metric comes from an increase in the D peak caused by the increase in disorder that occurs due to the conjugation of PBASE. The reduction in this ratio during the DNA immobilisation is caused by the reduction in the intensity of the 2D peak which is clearly visible in Figure 7.55.

Electrical measurements were captured before and after DNA was indirectly functionalised to the graphene surface. Figure 7.57 shows the transfer curve characteristics close to the Dirac points for a typical GFET device before and after DNA conjugation. The increase in resistance through the graphene channel, visualised by the reduction in current between the two lines, can be attributed to electron donation from the DNA to the p-typed doped graphene [210]. It follows from this phenomenon that the transfer curve shows a clear left shifting in V_{DP}^{Rev}, from +95 V to +81 V caused by the electron donation from the DNA. This left shifting effect is in agreement with the observations made by Chee et al who used a similar guanine rich aptamer for their work on Pb^{2+} ion detection [123]. The peak mobility values are similar between the two as depicted by the histogram plot in the inset of Figure 7.57 indicating that the graphene lattice remains unchanged and therefore its sensitive electronic structure remains intact after binding, as desired from the non-covalent functionalisation using the PBASE SAM layer. These observations provide evidence to support the binding of DNA to the PBASE SAM layer.

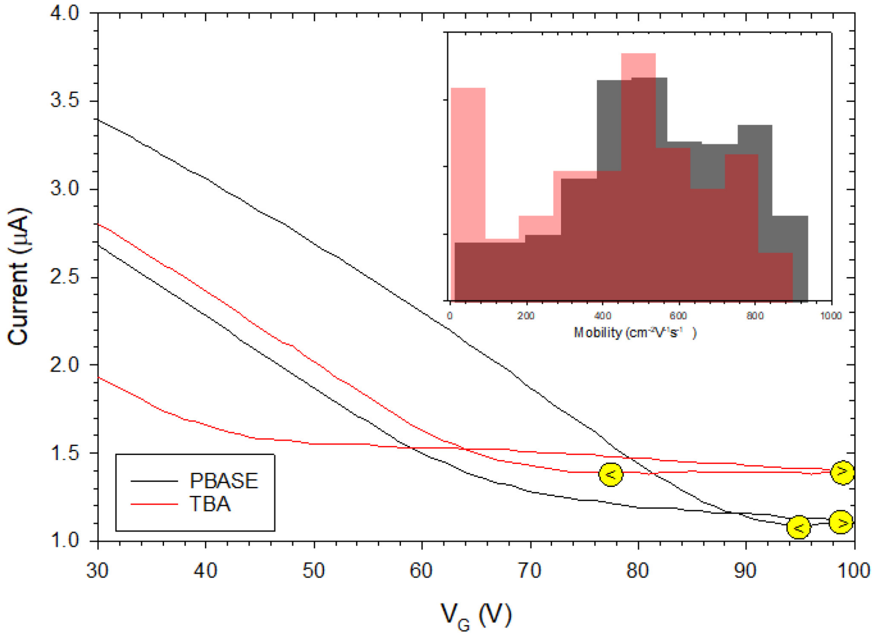

Figure 7.57 Typical electrical characterisation of GFET device treated with 10 µM TBA showing I_{SD}-V_G, with V_D^F and V_D^R indicated by the ">" and "<" symbols respectively, with inset showing the mobility values across the transfer curve.

Interestingly, there is a significant difference between the percentage of points that exhibit the minimum mobility between the two stages. After DNA is immobilised onto the surface there is a clear increase in the percentage of points that are at the minimum mobility value, indicated in the histogram plot by the furthest left hand bar. The majority of these points are observed in the region shown in Figure 7.57 by the flattest gradient and correspond to small changes in the current as the V_G is swept during majority electron conduction. Since the DNA backbone is negatively charged, at high V_G voltages it is conjectured that the electrostatic repulsion from the DNA acts as scattering sites for the electron charge carriers which acts to reduce their mobility. A similar mechanism was speculated by Nakatsuka to explain the change in transconductance seen by their aptamer functionalised FETs during binding events which would modify their aptamers' orientations [212].

AFM measurements were acquired to differentiate the surface topology between fabricated graphene and that of TBA/PBASE functionalised graphene and are shown in Figure 7.58.

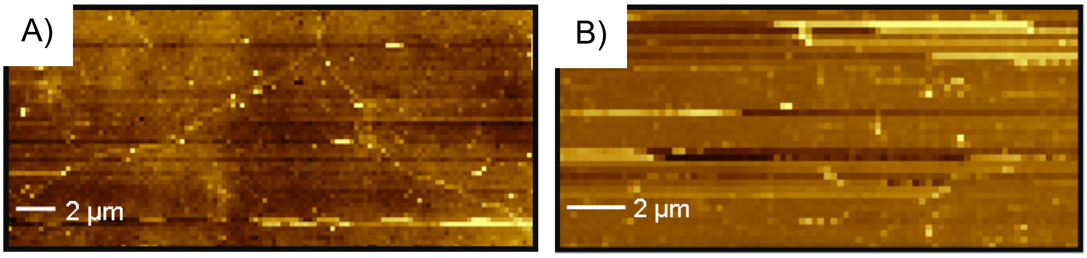

Figure 7.58 Surface topology of graphene channel examined by AFM. A) Fabricated graphene B) TBA/PBASE functionalised graphene.

The successful conjugation between TBA/PBASE binding can be inferred by the 420% and 662% increase in RMS and Mean roughness respectively caused by the TBA/PBASE immobilization.

7.7.3.3 Direct Immobilisation

A comparison of the Raman measurements was conducted after completing the direct immobilisation of PTDA and are shown across Figure 7.59. The existence of the additional ~1616 cm^{-1} shoulder peak was present in some sample positions captured across the 25 point map. This peak, associated with pyrene group resonating with the graphene lattice due to the π-stacking interaction provides evidence of binding. However, the reader is cautioned against relying solely on this metric to confirm successful binding of the PTDA to the graphene. Since this peak is also associated with surface charges and impurities [69], it is possible that it is present in some areas of the graphene sheet prior to PTDA immobilisation. This is illustrated in Figure 7.59A, by the black line which represents a single spot acquisition on fabricated graphene prior to PTDA functionalisation where it is evident that this shoulder peak is present. Analysis relating to the density change in this peak before and after immobilisation is required in order that it can be used as sole indicator for binding. It is unclear whether such analysis was completed in Khan's work [213] who developed a solvent-free PTDA regime for functionalising graphene. They presented three spot positions with this additional peak as evidence of conjugation.

To further strengthen the evidence supporting PTDA functionalisation in this work, further analysis into the Raman spectra are presented (further details are provided in 6.3.2.2) made up from measurements across 25 individual spots. Firstly, enhanced doping of the graphene channel is indicated by the decrease in the I(2D):I(G) ratio shown in Figure

7.59B. Next, left shifting of the PP(2D) specifically infers the doping of graphene by electrons, donated by the conjugated aptamers. Evidence of the formation of a secondary layer from the pyrene groups stacking to the graphene is given by the broadening of the FWHM(2D) peak presented in Figure 7.59C. Control measurements with DMF only, as discussed in 7.6.3.1, showed no significant changes in I(2D):I(G), PP(2D) or FWHM(2D).

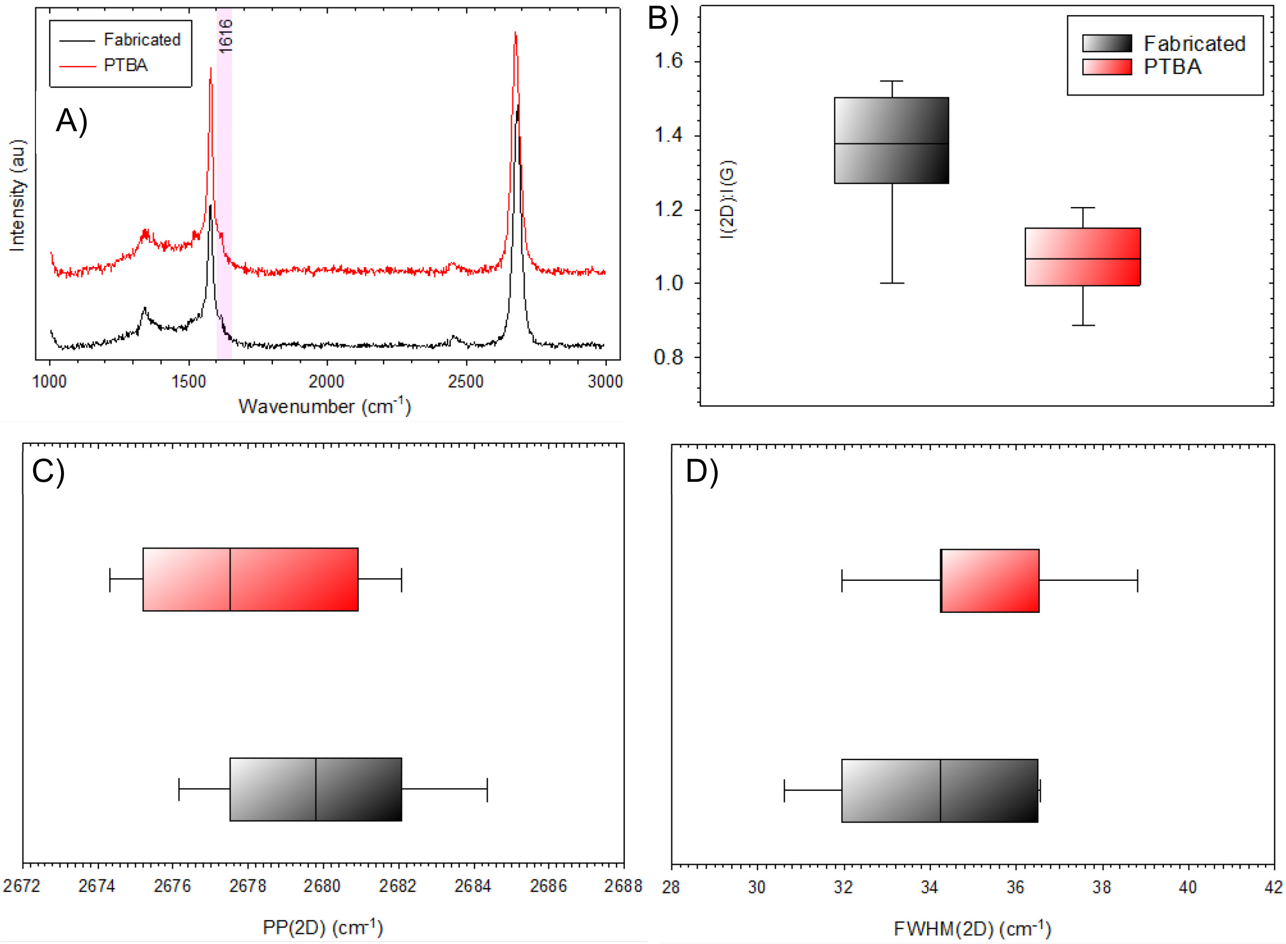

Figure 7.59 A) Single spot Raman spectra captured from fabricated graphene (black) and PTBA functionalised (red) graphene with presence of the ~1615 shoulder peak highlighted with pink region. Box and whisker plots for typical fabricated (black) and PTBA functionalised (red) graphene for A) I(2D):I(G) B) PP(2D) C) FWHM(2D)

Monitoring the transfer curve characteristics is another way that the PTBA immobilisation was confirmed. The transfer curve characteristics of a typical GFET device before and after PTBA immobilisation are shown in Figure 7.60. Similar to the indirect immobilisation of DNA, Figure 7.60A shows that conjugation with PTDA has caused an increase in resistance in the GFET channel. A ~2/3 reduction in the peak mobility is displayed in Figure 7.60C. A reduction in mobility caused by DMF was noted in Wu's work [214] when they investigated GFET responses to the solvent. It is possible, as conjectured in Wu's work that the DMF has the impact of introducing some defects into the graphene lattice.

This could be facilitated by the lower density of binding sites of pyrene in using 10 µM PTDA solution compared to 10 mM for PBASE. However, the lack of increase in D peak in Raman measurements does not support this. Perhaps this observation is caused by untagged aptamers that are present in the PTBA solution binding electrostatically to the lattice, facilitated by graphene's p-doped nature, as noted by Sidorov in [215]. The exact reason is most likely down to the complex interaction between the conflicting mechanisms of electron donation from the DNA backbone and electron withdrawal from the pyrene's carbonyl group along with electrostatic doping effects that are all likely to influence the transfer curve in this way.

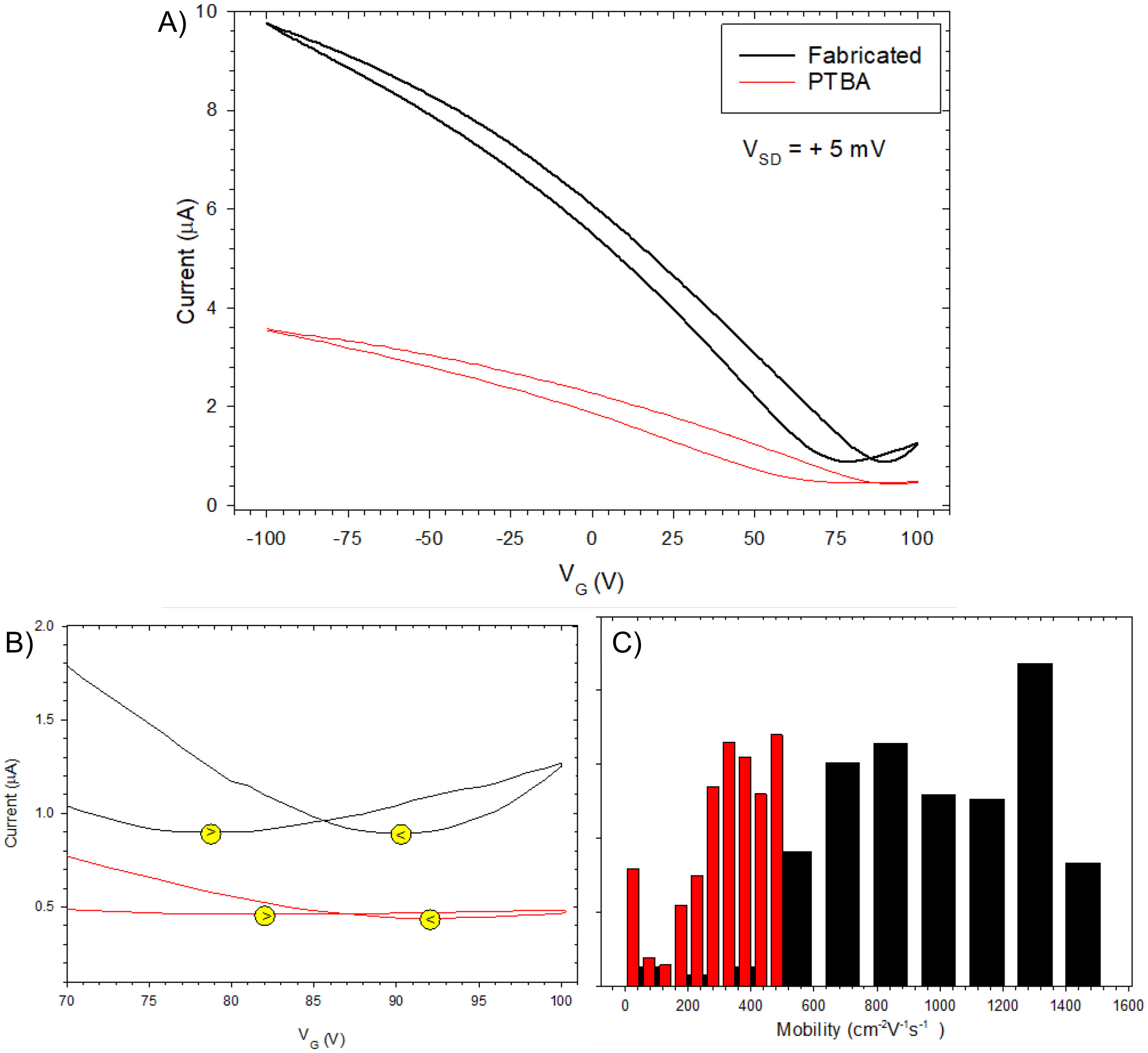

Figure 7.60 A) Transfer curve characteristic of typical GFET device before (black) and after (red) PTBA immobilisation; B) Close up of Dirac points showing shift in position of both V_D^F and V_D^R indicated by the ">" and "<" symbols respectively. C) Histogram plot indicating the reduction in mobility caused by the PTDA.

The large proportion of low mobility values seen for the indirect immobilisation of DNA is replicated in these electrical measurements and is shown in Figure 7.60C. This wider range of low mobility values could be caused by the interaction between the negatively charged DNA backbone and electron charge carriers (vide supra) and supports the conjugation of the PTBAs.

During PTDA immobilisation it is observed that the Dirac points tend to increase to higher V_G values as indicated by Figure 7.60C. A right shifting in these values derives from the carbonyl withdrawing group of the attached pyrene group inducing a p-type doping effect on the graphene lattice or alternatively it could be due to electrostatic gating by the negatively charged aptamer backbone. An increase in the Dirac point was also observed by Xu [116] in their work on conjugating TBA-PTDA to their graphene devices further supporting the successful conjugation of PTDA inferred here in this work.

It is acknowledged to the reader the contradiction that exists between the post PTDA functionalisation observation of FWHM(2D) right shift from the Raman measurements, indicating electron doping and the Dirac point shift to higher values for the electrical measurements, indicating hole doping. Perhaps the dominant mechanism between the electron rich DNA backbone and electron withdrawing group of the carbonyl group from pyrene is different depending on which technique is used to probe the sample. This could occur due to different activation energies between laser illumination and electronic sensing. Alternatively, the difference could be down to local variations in the distribution and secondary structure of the TBA-PTDA complexes across the graphene surface.

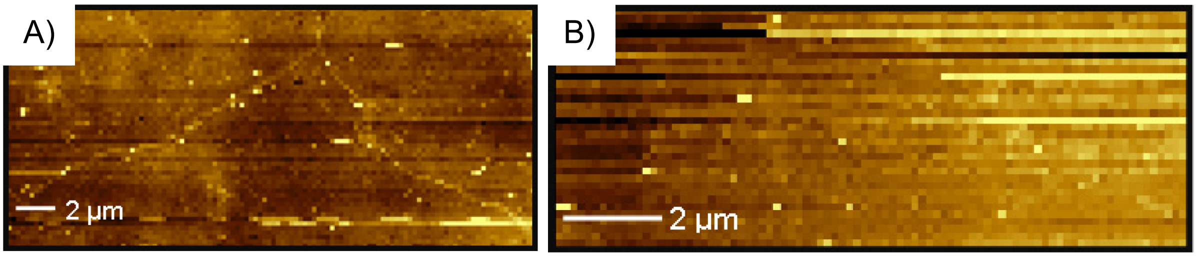

Figure 7.61 Surface topology of graphene channel examined by AFM A) Fabricated graphene B) PTBA functionalized graphene.

AFM measurements were acquired to differentiate the surface topology between fabricated graphene and that of PTBA functionalised graphene and are shown in Figure 7.61. Evidence supporting successful PTBA conjugation is provided by the 227% and 375% increase in RMS and Mean roughness respectively caused by the PTBA oligos. The increase in these values was attributed to the flexibility of the aptamer molecules by Wu in similar observations [101].

7.7.3.4 Uniformity of DNA Immobilisation

It would be advantageous to be able to estimate the distribution of deposited DNA across the entirety of the graphene channel. Since Raman mapping was already discounted (7.6.3.7) as a technique to complete this at the macroscale, a higher throughput method is herein demonstrated. For direct immobilisation using PTBA, Quantum Dots (QDs) were exploited in an attempt to circumvent the issue of fluorescent quenching from FTAs.

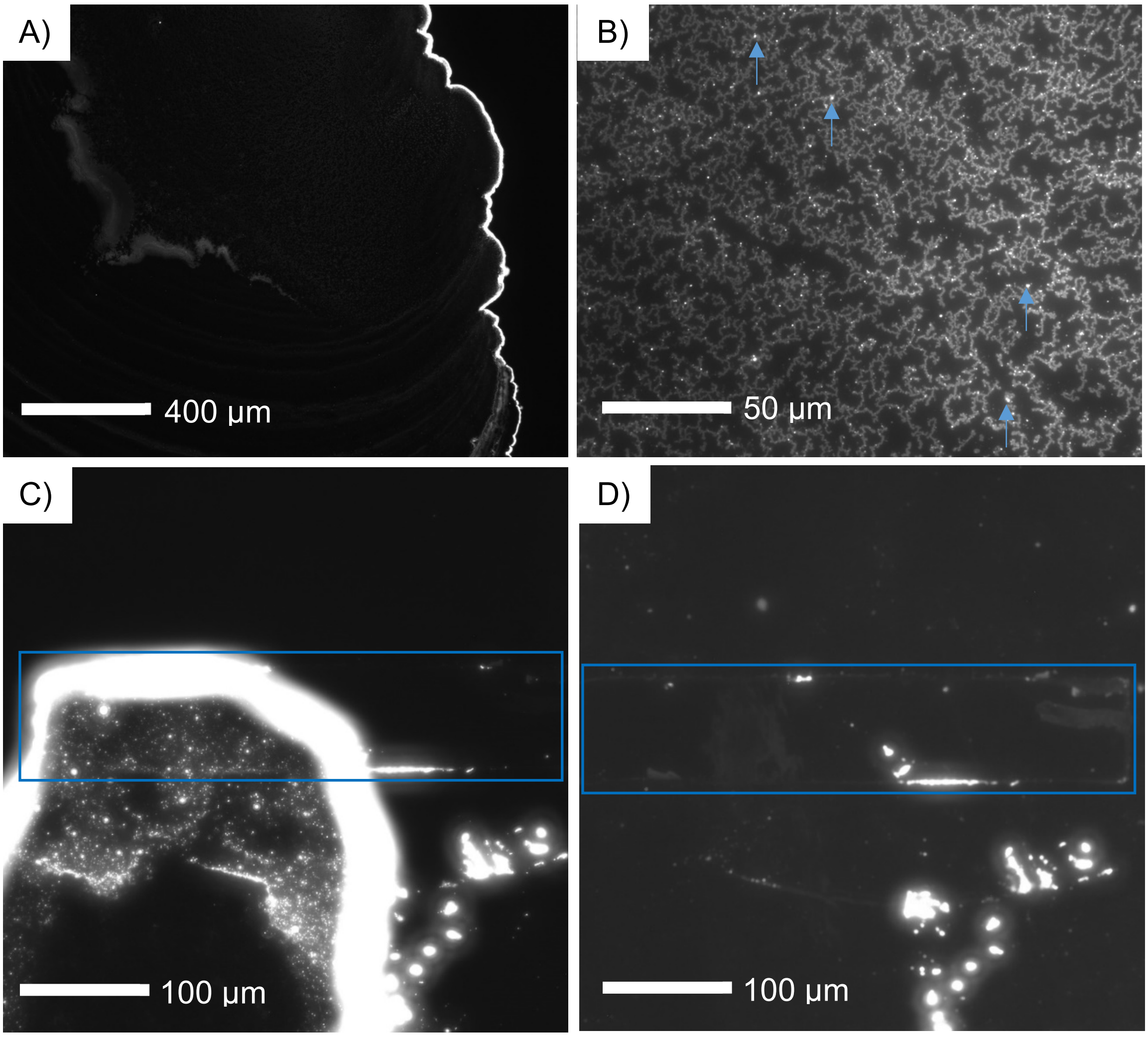

Figure 7.62 CdTe-COOH QDs deposited on glass A) Micrograph showing edge of the dried droplet against the clear glass slide B) Micrograph with arrows pointing to bright spots showing locations where the QDs aggregated together. CdTe-COOH QDs deposited on graphene C) Before and D) After rinsing in DIW. Blue rectangles show graphene channel positions. All images acquired with an acquisition time of 6 s and using the FITC filter.

The preparation of the 5 mg/mL CdTe-carboxylate QD solution is described in the following passage. All glassware used was initially cleaned in a 2% Nitric acid wash. A weight of 10 mg of the QDs was measured out and placed into a sterile vial using a static free spatula. Then, 2 mL of DIW was added to the vial and swirled vigorously in a vortex for 1 min. This bottle is then sonicated at 40 kHz for 1 h until the powder is fully dispersed in the liquid resulting in an orange hue. Initial measurements were captured to determine the QDs' suitability for optical labelling. It was also necessary to establish if the equipment available could be used to image these QDs before continuing to develop this technique further. Firstly, untreated QDs were drop cast onto glass slides and placed in a warm environment to encourage evaporation. After the DIW evaporated away from the glass slide, the QDs show river-like meandering where they have been deposited. It is clear from Figure 7.62A and B that the QDs can be easily visualised using the Nikon Eclipse Epifluorescence Microscope. The bright spots in Figure 7.62B correspond to locations of high QD aggregation.

Next, the QDs were drop casted onto graphene samples and placed in a warm environment to encourage evaporation. These samples contained untreated graphene channels on the surface of the Si/SiO_2 stack. Since these channels were not treated beforehand unselective binding was expected. Initial observations are shown in Figure 7.62C with the blue box highlighting the position of the graphene. It is clear from this image that the QDs were visualised across both the surface of the graphene channel and the SiO_2 substrate layer. This type of deposition is clearly unselective as there is no preference of binding towards the graphene channel. As expected, once the device was rinsed in DIW (Figure 7.62D) this patch of QDs is totally removed. This occurs because the graphene channel does not have the chemical mechanism to bind directly to the carboxylate groups on the surface of the QDs.

The next stage was to develop this technique to show selective binding of the PTBA complexes to the graphene channels. To do this, the process described in [116] was adapted. This process requires that the PTBA complexes have an additional amino C6 modification at the 3' end to facilitate the cross linking reaction with the QDs (Figure 7.63A). It is necessary to activate the carboxyl groups of the QDs so that they can bind to the amino groups at the 3' end of the PTDAs. This is achieved using the EDC mediated reaction shown in Figure 7.63B. Once the carboxylated groups have been activated into an o-Acylisourea active ester the amide bonds can be formed to create a cross linked PTBA-QD complex.

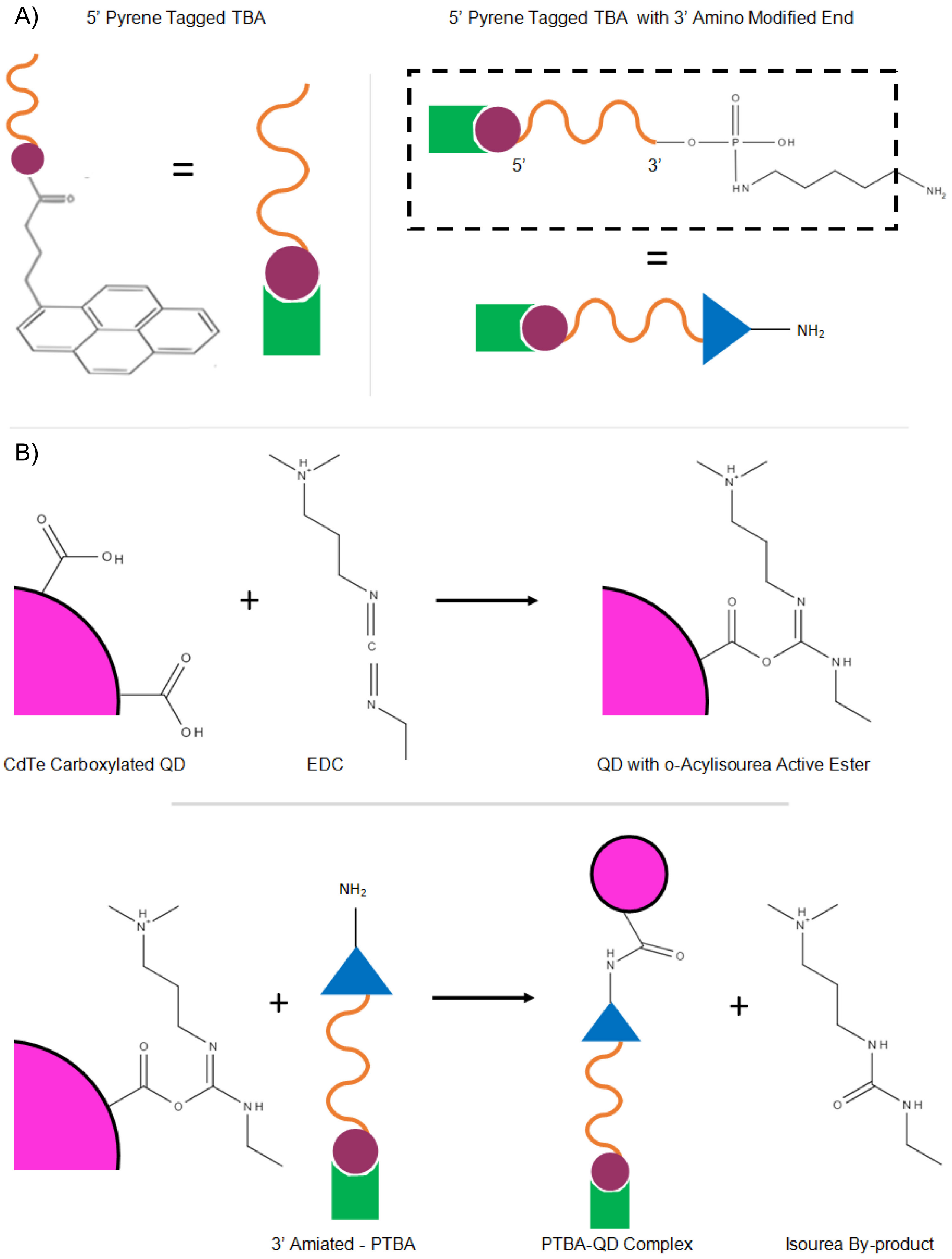

Figure 7.63 PTBA-QD cross linking process. A) Prior to binding with QDs, PTBA (left-panel) have an amine group added to their 3’ end (right-panel). B) Top-panel: Carboxylated QDs are activated using EDC to decorate their surface with an intermediary o-Acylisourea active ester. Bottom-panel: Amide bonds are formed between the QD and the 3’ Aminated PTBA to form the desired PTBA-QD complex. Isourea molecules are produced as a reaction by-product (adapted from [97]).

This process is achieved practically using the following steps. The 5 mg/mL QDs are mixed with EDC and spun at 3000 g, vortexed and spun again for 1 min periods to ensure adequate mixing. Then, unused EDC is removed from the mixture using a 100 K MICROSEP molecular weight cut off (MWCO) device. These devices are centrifugal filters that rely on a membrane to separate molecules based on their molecular weight. The sample reservoir is filled with QD-EDC mixture and spun at 3500 g for 30 min. At the end of the spin, the activated QDs are retained in the sample reservoir and the waste EDC is collected from filtrate reservoir. Next, the amino-modified PTBA are added to the QD solution at a ratio of 1:5 QD:PTBA and spun at 0.01 g for 15 min to encourage adequate mixing for stable cross-linking.

It was essential to establish any background fluorescence from the graphene channels and therefore fabricated channels with no PTBA-QD treatment were imaged first and are shown in Figure 7.64A through C. The difference between images captured in Figure 7.64A-C is the illumination; Figure 7.64A shows the untreated graphene when exposed to FITC excitation of laser light at 491 nm with the ambient laboratory light on as termed in this work as “Laser On, Lab On”; Figure 7.64B and C represent the illumination of the channel for “Laser Off, Lab On” and “Laser On, Lab Off” respectively. It is clear between Figure 7.64A and B that the contribution to the illumination by fluorescence caused by the laser being on is minimal as inferred by the similar intensity of the image between the two states. Further, for the “Laser On, Lab Off” state there is almost no trace of the graphene channel. This confirms that the graphene channels do not have self-fluorescence, therefore any illumination on treated graphene channels in the “Laser On, Lab Off” state must be coming from the presence of the QDs.

The impact of treating the graphene channels with PTBA-QDs was investigated next. Since the QDs were conjugated to the PTBA, binding between the graphene and PTBA-QD complex was achieved via the pyrene group π-stacking to the lattice. Treated PTBA-QDs were drop cast onto graphene channels and immobilised in a humid environment for 24 h prior to rinsing in DMF and DIW to replicate similar conditions to the procedure that was used to immobilise PTBA directly to the graphene. Observations are shown in Figure 7.64D through F.

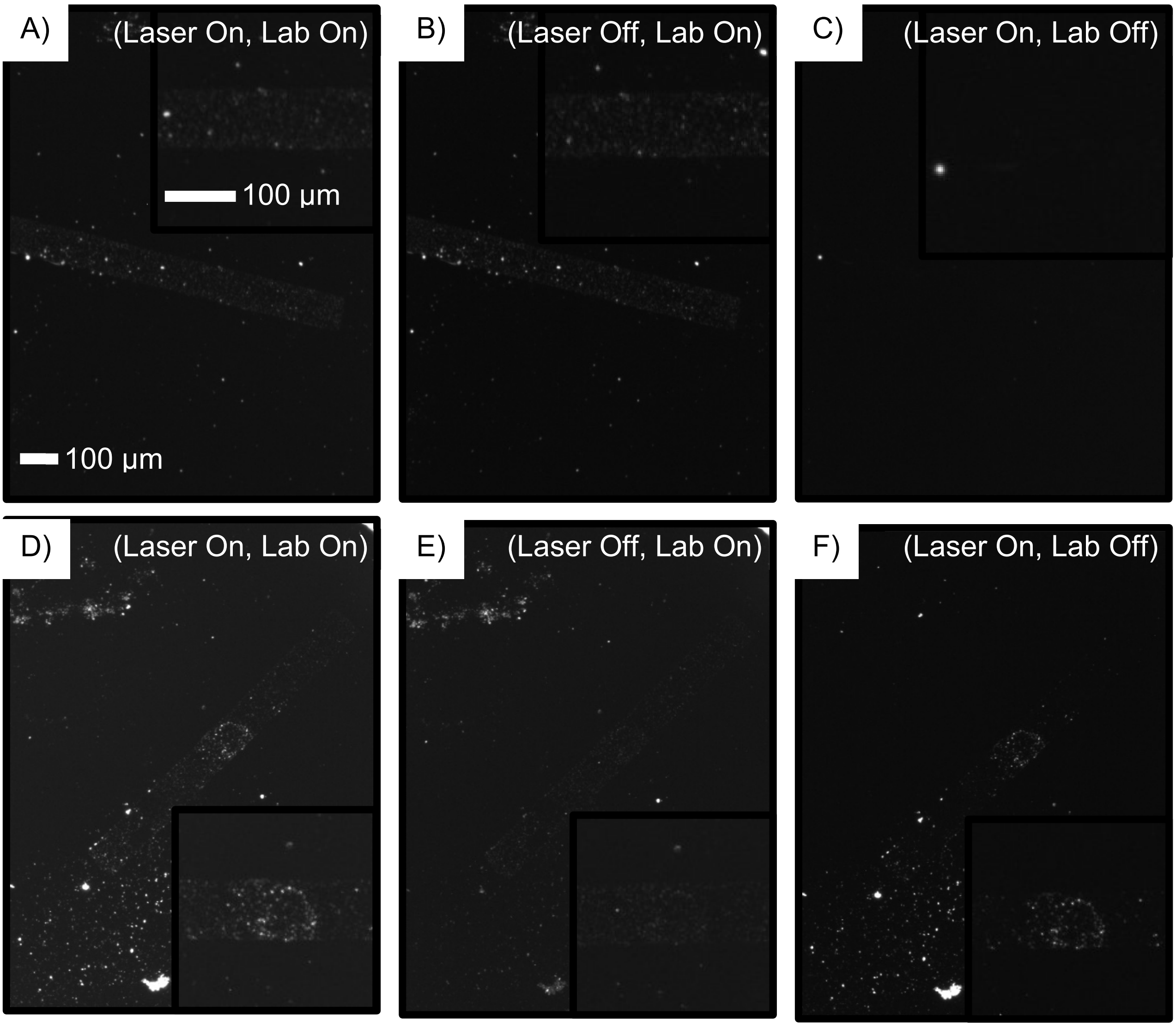

Figure 7.64 Flourescence images of graphene. All insets show close up of channel in that state A) Untreated: Laser On, Lab On B) Untreated: Laser Off, Lab On C) Untreated: Laser On, Lab Off D) Treated with QDs: Laser On, Lab On, E) Treated: Laser off, Lab On, F) Treated: Laser on, Lab off. All images are acquired with an acquisition time of 2s and using FITC filter.

For this scenario it is observed that the difference in intensity between Figure 7.64D and E is much more evident suggesting that the laser light is contributing to an additional luminosity caused by the fluorescence of the QDs. This is further confirmed in Figure 7.64F which shows a clear enhancement in the luminosity caused by the QDs fluorescent mechanism when compared with Figure 7.64C which shows the same state but with no QDs present. The observation that the structure in the top left hand corner of the Figure 7.64D and E is not illuminated in Figure 7.64F provides further evidence that the bright spots are illuminated due to the selective absorption (emission) of specific wavelengths of light to (from) the QD. The rectangular channel is distinctly visualised amongst the dark background in Figure 7.64F confirming successful QD and therefore PTBA conjugation.

Although effective at confirming the binding of the PTBA to graphene more work is required to improve this technique so that it can be used to progress the understanding of the uniform distribution of these complexes across the surface. For example, at this stage it is unclear whether the lack of uniformity in luminosity across the channel is caused by unsuccessful PTBA-QD or PTBA-QD-graphene binding. The rinsing of unbound TBA-QD complexes requires improvement since some complexes, visualised in the bottom left hand corner of Figure 7.64F, remain bound to the substrate SiO_2 layer after a wash cycle in DMF and DIW. Removing these unbound complexes will improve the definition possible in the images. It is also possible that the QDs could impinge the binding of the PTBA to the graphene which could explain regions of lower luminosity in the channel. Finally, the level of QD aggregation, depicted in Figure 7.64C by the regions of high intensity, should be reduced so that there is a narrower intensity range across the images.

7.7.4 Summary

Throughout this section the indirect and direct immobilisation of 10 μM aptamers has been demonstrated. Evidence of successful conjugation has been provided with Raman, Electrical and AFM measurements. Initially aptamers were characterised by UV-Vis measurements which can be used to calculate the concentration of oligonucleotides. There was excellent agreement between the targeted and estimated concentration showing good DNA processing techniques. During conjugation, both techniques showed signs of doping in the graphene channel via Raman measurements. Electrical measurements showed that after conjugation there was an increase in the proportion of low mobility values, especially in the electron charge carrier regime. It was conjectured that at high values of V_G the negatively charged DNA backbones were interacting with these charge carriers in a way that led to a reduction in their mobility.

The indirect immobilisation of aptamers relies on firstly decorating the graphene surface with PBASE onto which amino modified DNA is bound at the NHS ester end. The direct immobilisation of aptamers relies on a one-stage process whereby the PTBA molecules bind to the graphene lattice via π-stacking facilitated by the pyrene tagged group at the 5’ end of the aptamer. This one-stage process not only simplifies the conjugation process but it could also prevent non-specific adsorption and denaturation of the aptamers [124]. However, the additional complexity of tagging aptamers with a pyrene group, or additional cost in sourcing these should be taken into account. Post tagging analysis should be conducted in order to confirm the binding efficiency between pyrene groups and the aptamers. Calculating the tagging yield would allow investigations which study the impact of unbound aptamers and aptamers bound to multiple pyrene groups to be studied with the aim to improve repeatability for this technique [205]. In addition, due to the lower freezing point of organic solvents such as DMF, the need for lower freezing temperatures (-80 ºC) needed to store aliquots long term is another consideration that could prevent the direct immobilisation strategy from further proliferation. That said, it is likely that Farid's group circumvented this issue by freezing aliquots of pyrene-tagged aptamers in PBS at standard temperatures (-18 ºC) before recombining with DMF prior to functionalisation [102].

The uniformity of the distribution of PTBA was then investigated using QDs as an optical label, bound to PTBA at the aminated 3' end. These PTBA-QD complexes were then conjugated to the graphene and visualised. Initial results showed that this was an effective technique for visualising the distribution across the entire channel in a high throughput manner.

7.8 Aptamer Functionalised GFETs for Sensitive Pb^{2+} Detection

7.8.1 Introduction

Herein describes the detection of Pb^{2+} ions using GFET devices. Details relating to the work in this section have been taken from the following publication [216]. Monolayer CVD graphene was patterned into GFET devices using the photolithography method described in section 6.2. Research groups are exploiting aptamers as the next generation of bioreceptors for sensing a wide variety of analytes. The common trend in aptamer immobilisation to graphene is to complete the two stage indirect immobilisation. This require a PBASE layer to be pre-decorated onto the graphene surface to which amino modified DNA is subsequently bound to. An emerging trend is in the use of pyrene modified DNA (PTDA). These complexes simplify the functionalisation steps by removing the need to pre-decorate the graphene surface with PBASE. Instead, the PTDA complexes bind directly to the graphene via π-stacking.

In the work presented here, asymmetric (seven) and symmetric (eight)-electrode Hall-bar GFET devices were functionalised using the indirect and direct strategies for the detection of Pb^{2+} ions in order to produce a direct comparison between the two techniques at a bioreceptor concentration of 10 μM. Details relating to the indirect and direct immobilisation strategies can be found throughout section 7.7. The sensing method of these GFETs relies on measuring the change in conductive properties through the graphene as increasing concentrations of the Pb^{2+} are added.

7.8.2 Methodology

7.8.2.1 Process

GFET devices were firstly conjugated with either TBA or PTBA aptamers. Once this was complete GFETs were exposed to increasing concentrations of Pb^{2+} ions. Specific amounts of Pb^{2+} ions were dissolved in DIW at concentrations of 1 nM, 10 nM and 100 nM. This concentration range was selected due to its proximity to physiological and environmental significant levels since currently the WHO recommend that maximum Pb^{2+} levels in water should be 10 μg/L, equivalent to ~50 nM and claim that even small concentrations of 50 μg/L, equivalent to 242 nM can cause harm (Pb^{2+} molar mass = 207 g/mol) [109, 110].

Multiple GFET devices, each with several individual sensors were measured at every functionalisation step in order to improve the reliability of results. The dimensions of the individual sensors are 80 µm wide by 95 µm long and are pictured in Figure 7.25. Multiple electrical metrics relating to the sensors' response were tracked throughout the course of the sensing stages in order to establish correlative patterns and are discussed in 7.3.2.2.

For Pb^{2+} sensing a ~0.5 µL drop of a specific concentration of Pb^{2+} ions dissolved in DIW was pipetted onto the device and left to incubate in an ambient environment for ~10 min. This time frame was sufficient to achieve solvent evaporation from the sensor surface allowing electrical characterisation to take place in dry conditions. Measurements were captured immediately following evaporation in order to reduce the impact of further atmospheric adsorbents onto the GFET as discussed in section 7.5.

7.8.2.2 Normalisation

In order to improve the reliability of the results several repeated measurements were acquired. Therefore it was necessary to normalise the device responses in order that inter-device variations were eliminated. This was achieved by calculating a ratio of the response against that measured at the previous TBA/PTBA stages. An example of this calculation for $I_{Vg=0}$ is given in Equation 7-9 below.

$$\boldsymbol{R_{Vg=0} = \frac{I_{Vg=0}^{Pb^{2+}}}{I_{Vg=0}^{TBA/PTBA}}} \qquad 7\text{-}9$$

The standard error was calculated in order that error bars could be plotted, which detail the spread in data across the devices. This parameter is calculated using Equation 7-10 below

$$\boldsymbol{SE = \frac{\sigma}{\sqrt{N}}} \qquad 7\text{-}10$$

where σ is the standard deviation across the sample and N is the number of samples.

7.8.3 Results

7.8.3.1 GFET bioreceptor functionalisation

The non-covalent functionalisation of the PBASE SAM layer was confirmed using Raman and electrical characterisation. Typically the electronic configuration of the graphene was undisturbed by this process indicated by the lack of change in the carrier mobility between the two stages. During TBA indirect immobilisation it was observed via additional doping caused by the electron rich DNA backbone that the bioreceptor was present on the sensor surface. In addition, the I_{SD}-V_G electrical sweeps across the GFET devices were also conducted to confirm the successful immobilisation. Right shifting in the electrical data for PTBA immobilisation described an electron withdrawing mechanism dominating in order to confirm its presence. Electrical characterisation in the form of I_{SD}-V_{SD} sweeps were conducted and are presented below to confirm successful bioreceptor immobilisation.

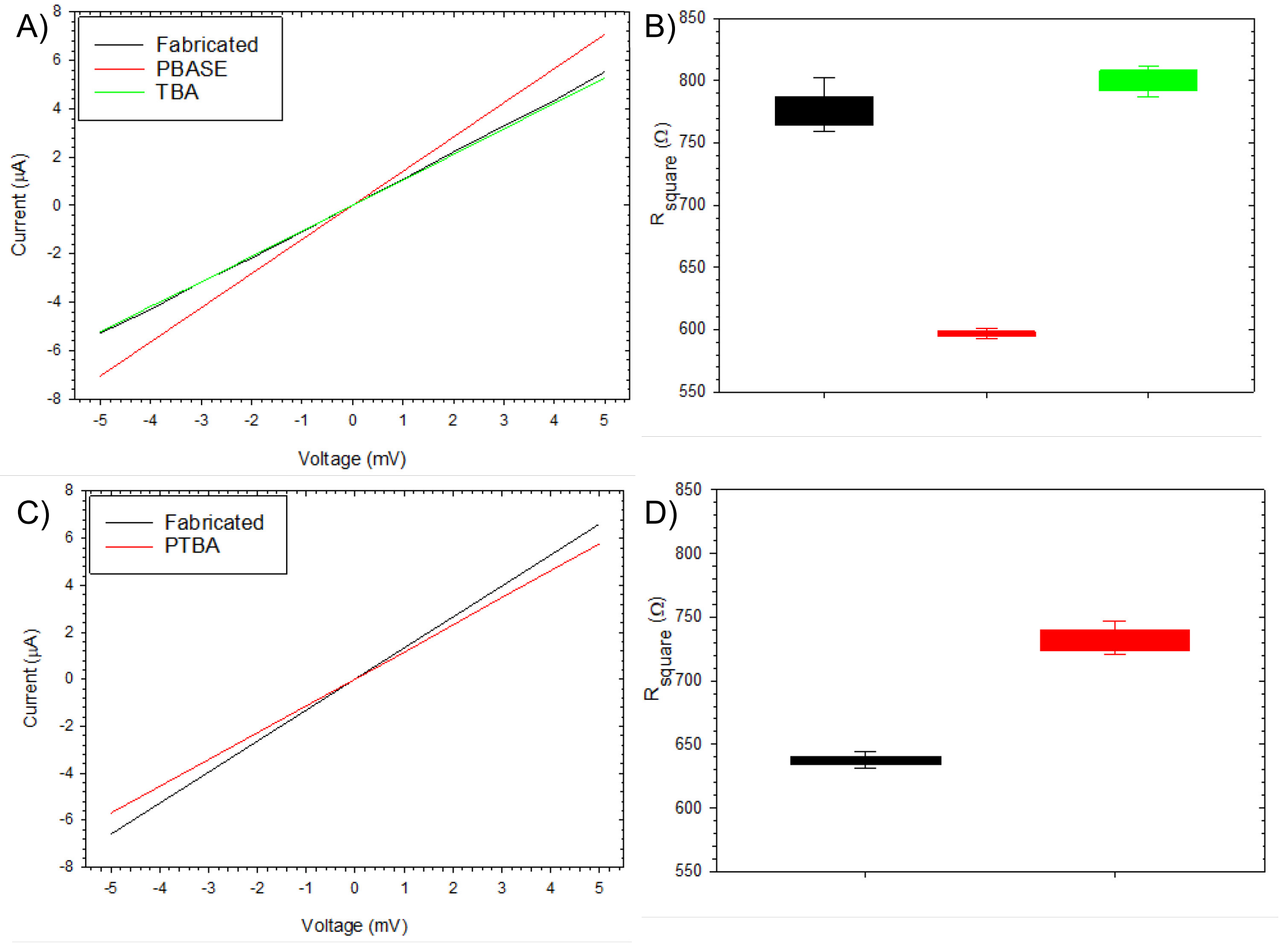

Figure 7.65 Electrical characterisation of typical GFET devices treated with the indirect (A&B) and direct (C&D) immobilisation strategies. For each functionalisation stage, figures A and C show I_{SD}-V_{SD} sweep measurements with figures B and D showing the calculated $R_\square$ values for the channel.

The results shown in Figure 7.65 are representative across all GFET devices for each functionalisation scheme. A typical sensor representing a GFET treated with the indirect immobilisation strategy (10 mM PBASE, followed by 10 µM TBA) is shown in Figure 7.65A and B. The ~24% decrease in $R_\square$ for the sensor confirms the successful conjugation of the PBASE SAM layer as it showcases the electron withdrawing group of the carbonyl group, which acts to increase the density of the majority hole charge carriers in the channel. The subsequent addition of the electron rich DNA backbone from the TBA aptamers is inferred by the ~34% increase in $R_\square$ and is attributed to the electron transfer from the nucleotide bases.

A typical sensor representing a GFET treated with the direct immobilisation strategy (10 μM PTBA) is shown in Figure 7.65C and D. The PTBA conjugation can be inferred by the ~15% increase in $R_\square$ measured for these sensors. This observation is caused by the complex interaction between the conflicting mechanisms of electron donation from the DNA backbone and electron withdrawal from the pyrene’s carbonyl group along with electrostatic doping effects. Further details relating to the successful conjugation of PBASE, TBA and PTBA are provided across sections 7.5.4 and 7.7.

7.8.3.2 Pb^{2+} sensing with TBA

The detection of Pb^{2+} ions was initially conducted using the indirect immobilisation of DNA. This detection method was applied to a total of 12 sensors across 3 GFET devices. Large variation was observed across these different sensors using this technique with no repeatable correlation in metrics against Pb^{2+} concentration.

An example of two very different sensor responses are shown in Figure 7.66A and B and correspond to sensors D1 and D2 respectively. The transfer curves for D1 and D2 differ significantly across all the sensing stages. For D1 there are no Dirac points within the -/+ 100 V range when the Pb^{2+} ions are added. Perhaps the V_{DP}^F and V_{DP}^R exist just outside the + 100 V range as indicated by the decreasing gradient shown for the blue curve of Figure 7.66A but this cannot be confirmed. On the other hand, when the Pb^{2+} ions were added to sensor D2, the Dirac points are clearly visible. Moreover, these Dirac points are observed as left shifting with increasing concentration of Pb^{2+} ions as indicated by the inset of Figure 7.66B.

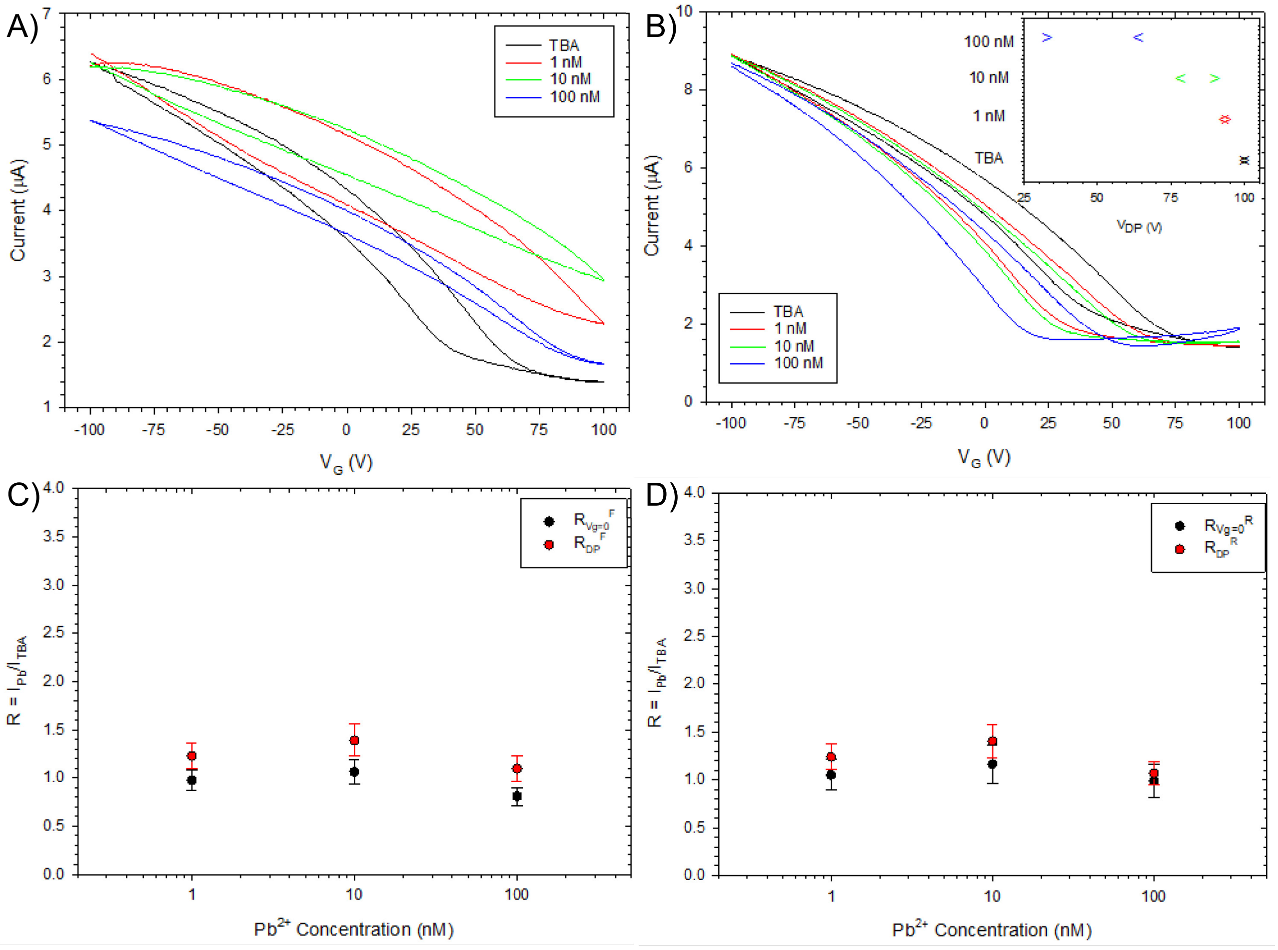

Figure 7.66 Transfer curves of TBA functionalised GFET sensor on exposure to Pb^{2+} ions at increasing concentrations for A) D1 and B) D2 sensors. Normalised values against logarithm of Pb^{2+} concentration showing metrics across Pb^{2+} range of 1 nM to 100 nM for C) $I_{Vg=0}^F$ and I_{DP}^F D) $I_{Vg=0}^R$ and I_{DP}^R.

Decreasing values of V_{DP}^F and V_{DP}^R with increasing Pb^{2+} concentrations can be explained with the following mechanism. As the Pb^{2+} ions bind to the TBA they cause the strands to undergo conformational changes into G-quadruplex structures. The impact of these structures is to bring the nucleotide bases closer to the graphene surface. This simulates an increasing DNA concentration that is observed by the channel which has the result of n-doping the graphene caused by the interaction between the lattice and the electron-rich nucleotide bases as also observed by Chen et al [217]. With ever more G-quadraplex structures forming on the surface in line with an increasing in Pb^{2+} concentration this causes further n-doping and thus enhanced left shifting of the Dirac points. Although this negative shift aligns with the proposed sensing scheme the reader is advised caution in this observation since it only occurred on 25% of the sensors tested. Clearly improved repeatability is required in order that a higher confidence can be made with these results.

The shift in metrics relating to $I_{Vg=0}^{F}$, I_{DP}^{F}, $I_{Vg=0}^{R}$ and I_{DP}^{R} are shown in Figure 7.66C and D. These metrics combine the results of the 12 sensors in order to improve reliability and have been normalised against the TBA stage in order to eliminate variations between sensors. It is observed that there is no correlation in these metrics against Pb^{2+} concentration.

7.8.3.3 Pb^{2+} sensing with PTBA

Unlike for the indirect method, the direct method showed improved repeatability across the sensors. This detection method was applied to a total of 6 sensors across 3 GFET devices.

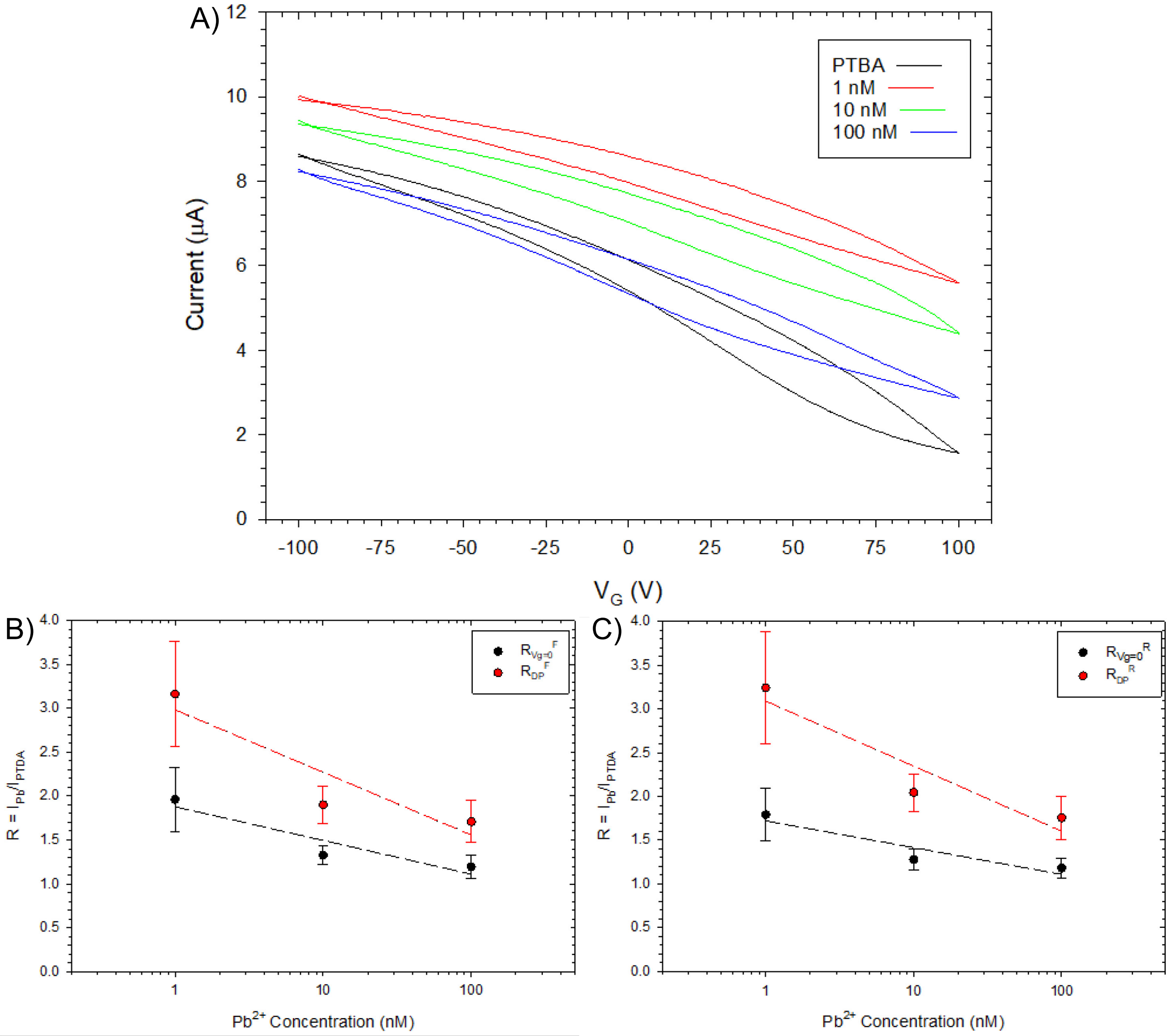

Figure 7.67 A) Typical transfer curves of PTBA functionalised GFET sensors on exposure to Pb^{2+} ions at increasing concentrations. Normalised values against logarithm of Pb^{2+} concentration showing decrease in metrics across Pb^{2+} range of 1 nM to 100 nM for B) $I_{Vg=0}^{F}$ and I_{DP}^{F} C) $I_{Vg=0}^{R}$ and I_{DP}^{R}.

Transfer curves for a typical GFET sensor exposed to increasing Pb^{2+} concentration used in this work are shown in Figure 7.67A. The shift in metrics relating to $I_{Vg=0}^{F}$, I_{DP}^{F}, $I_{Vg=0}^{R}$ and I_{DP}^{R} are shown in Figure 7.67B and C. These metrics combine the results of the 6 sensors in order to improve reliability and have been normalised against the PTBA stage in order to eliminate variations between sensors. It is shown that $I_{Vg=0}^{F}$, I_{DP}^{F}, $I_{Vg=0}^{R}$ and I_{DP}^{R} all decrease with increasing Pb^{2+} concentration. An exponential relationship between these metrics and the concentration of Pb^{2+} is indicated by the straight line best fit plotted in Figure 7.67B and C.

It is shown in Figure 7.67A that the PTBA functionalised sensors exhibit majority p-type charge carrier conduction; the decrease in the metrics relating to current can be ascribed to the impact of doping. Yijun II's group describe the conflicting sensing mechanisms at play here [122]. Firstly, when the nucleotides bind with Pb^{2+} ions they form the G-quadraplex structures which acts to bring more of the negatively charged nucleotides towards the graphene, electrostatically inducing an increase in the hole density and thus p-type doping effect. However, concurrently with this process, positively charged Pb^{2+} ions are brought closer to the surface which will act to neutralise this effect. At low concentrations of Pb^{2+} the initial increase in these metrics from the PTBA stage can be attributed to an increase in hole density. However, the decrease in these current metrics seen for the 10 nM and 100 nM stages suggests that dominant process in this sensing mechanism switches and is likely caused by the greater density of positively charged Pb^{2+} ions on the surface n-doping the graphene channel. Since the positions of the V_{DP}^{F} and V_{DP}^{R} lie outside the detectable range it is not possible to confirm that this effect causes a negative shift in the Dirac points.

The monitoring of I_{SD} against time was conducted next to establish the real-time sensor response to increasing Pb^{2+} concentrations and is shown in Figure 7.68. A reduction in R is attributed to a different graphene sample used. In this sensing scheme the PTBA functionalised GFET sensor was located on the probe station. Probe needles were then placed onto appropriate electrode pads and maintained in the same position throughout. The current through one sensor was recorded when a V_{SD} of + 5mV was applied with increasing Pb^{2+} concentrations and is shown in Figure 7.68. During the initial 140 s it can be seen that the current through the sensor is constant. This provides evidence of some form of surface passivation provided by the PTBA functionalised SAM against atmospheric adsorbents. In order to test the sensor against the Pb^{2+} ions, roughly 0.5 µL of the solution was pipetted directly onto the sensor with the probe needles in position, represented in

Figure 7.68 by the position of the red arrows. The following 190 s, indicated by the orange region shows the sensor response whilst the solution fully encapsulates the GFET device; which shows a steady decrease current in I_{SD}. Next, highlighted in the green regions, the sharp reduction in the I_{SD}, followed by a rapid increase was measured as the DIW begins to evaporate away from the graphene channel and electrode pads. With the DIW fully evaporated, the yellow regions indicate the stable dry case where there are no traces of the DIW and only the Pb^{2+} ions remain on the surface. It is in these regions of stability that electrical measurements as per those captured above in Figure 7.67 would be acquired.

These responses show how rapid these devices are. It only takes 370 s (~ 6 min) before equilibrium is reached following solvent evaporation allowing electrical characterisation. The similarity in the evaporation processes is represented in Figure 7.68 by the equal widths and form of the red and green regions for the I_{SD} trace.

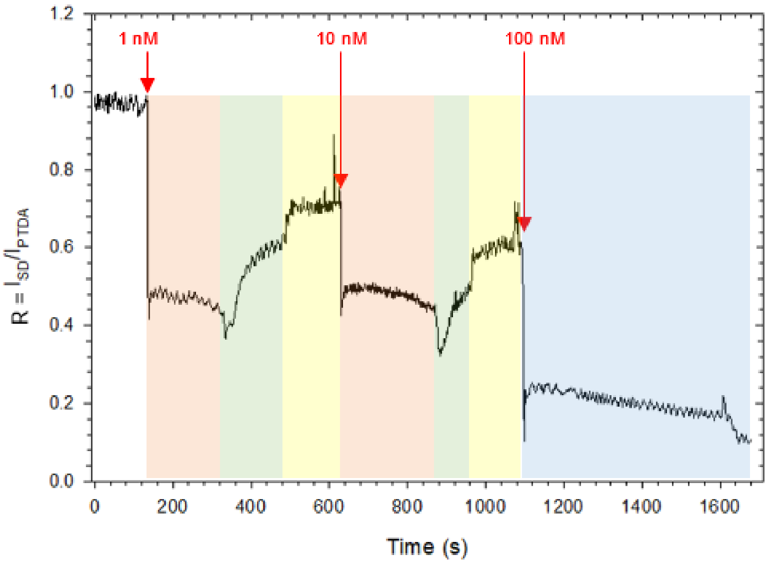

Figure 7.68 Real-time I_{SD} response to Pb^{2+} concentrations in 1 nM to 100 nM range for PTBA functionalised graphene sensor. Different shaded regions indicate the changing kinetics of the evaporating solvent; orange – Pb^{2+} solution fully covers the GFET, green – solution begins to evaporate from channel, yellow – solution fully evaporated from GFET surface, blue – probe needles knocked.

The difficulties in acquiring real-time response measurements on back-gated GFET devices by drop casting small volumes of target analytes directly onto the surface is showcased in Figure 7.68 by the region highlighted in blue. In this region when the pipette was brought close to the needles to place a 0.5 μL drop of 100 nM Pb^{2+} solution onto the sensor surface, one of the probe needles which were locked into position on the electrode pads was knocked. This had the effect of changing the real-time response for this concentration which follows a significantly different current trace to those that proceeded it, most likely due to the change in contact resistance between the probe and electrode pad.

7.8.4 Summary

The two bioreceptor immobilisation strategies were investigated in this section to form a comparison between the two. Evidence for the successful conjugation of both was presented. The rapid sensing principle displayed in these early results also facilitates this technology into future POC devices. For the same concentration of bioreceptor (10 µM) it was observed that sensors functionalised with the direct strategy, using PTBA, showed repeatable correlations between current metrics and the concentration of Pb^{2+} ions between 1 nM and 100 nM. When the indirect strategy was used, there was no significant correlation measured across the data set although individual sensors showed evidence supporting the proposed sensing mechanism. The lack in repeatability show that further work is required with bioreceptor functionalisation in order that the reliability of this sensing method can be improved. A more thorough understanding into the role that the Pb^{2+} ion plays as an electron acceptor could also help to interpret these results further [106]. Adding control measurements to future investigations would improve the rigour of these conclusions. One control study could examine the effect of adding the Pb^{2+} ions to the GFET without any immobilised bioreceptors. An additional control study could examine the effect of adding the buffer solution (with no dissolved Pb^{2+} ions) to the GFET after the bioreceptors were immobilised. Monitoring the GFETs' responses to these controls would provide useful information related to the specificity of the developed biosensor.

The initial results shown in Figure 7.67C and D show the response of the GFET devices (via the direct immobilisation of 10 µM PTBA oligos) to increasing Pb^{2+} ion concentrations in DIW. Although there is some evidence of an enhanced discrimination between these concentration levels, more experiments are required in order that the analytical performance of these devices can be improved. Specifically, it would be advantageous to optimise the signal differences between concentrations whilst decreasing the noise.

It was not possible to confirm targeted Pb^{2+} ion detection using sensors immobilised with 10 µM TBA oligos using the indirect method as the response remains close to 1 across all current metrics for these initial results. One possible explanation for the difference observed between the two techniques is the interplay between the PBASE layer, immobilised at a concentration of 10 mM and the TBA nucleotides, conjugated at a concentration of 10 µM. Perhaps the higher density of PBASE molecules prevents the TBA nucleotides from forming the G-quadraplex structures consistently which could be linked to their stacking orientation at high concentrations [99]. It is recommended that future work should focus on the optimisation of the PBASE and TBA concentration levels. The use of molecular spacers could be one way to optimise the relative distribution between PBASE and TBA which could act to enhance the sensitivity as shown for PSA detection in [100].

Both techniques would benefit from the removal of atmospheric adsorbents prior to functionalisation. It is well documented that graphene's characteristics change on exposure to the ambient environment [83, 144, 192]. Removing such contaminants on graphene's surface would bring the starting V_{DP} closer to the $V_G = 0$ value so that future shifts would remain within the detectable -/+100 V range. This would allow a more comprehensive study of the change in electronic characteristics by tracking the shift in V_{DP}. Possible strategies for achieving this involve vacuum desorption [83, 181, 194], rapid thermal annealing [195] and electrochemical cleaning [218] which have all shown to reduce doping and bring V_{DP} closer to 0 V.

Ongoing improvements to this work will involve testing the sensors' response to interfering agents, such as copper and iron compounds found in drinking water [113]. One way this could be optimised is by exploiting surface passivation techniques such as the use of Ethanolamine. Treating PBASE in this way disables any further cross linking reactions taking place between the NHS group and any possible contaminants.

Re-designing these GFETs with a microfluidic approach is one way that the difficulties of acquiring real-time responses to analytes could be overcome. Microfluidics is an exciting area of biosensing technology that involves systems which manipulate minute volumes of liquids usually in channels with dimensions at the micrometre scale [219]. It is noted in [220] that despite the widespread uptake of this technology, most practical implementations remain simple, consisting of a single channel with an inlet and outlet to flush a sample with a desired analyte. Such a simple design could be integrated with an adapted GFET design to improve this work, benefitting the bioreceptor immobilisation strategies, alongside the accurate and repeatable delivery of the target analyte. However, concurrently with microfluidic integration it will be necessary to investigate the use of solvent-free immobilisation strategies since the organic solvents used to disperse pyrene based molecules are known to dissolve organic compounds, such as thermo plastics and polymers often used in microfluidic infrastructures [205].

Chapter 8 – Conclusion and Future Scope

8.1 Conclusion

The work presented in this thesis facilitates the progression of GFET technologies into the future by highlighting the challenges with working with GFETs whilst casting a spotlight on the exciting avenues for future development. The key challenges identified in this work include; handling enormous datasets, device fabrication, device characterisation, atmospheric adsorbents impacting characterisation and the immobilisation of bioreceptors onto the graphene surface.

By utilising purpose-built software packages, the challenge of converting immense quantities of raw data into informed insights has been improved. Fabrication techniques have been assessed for creating repeatable devices suitable for biosensing purposes. Standard procedures for the characterisation of these devices has been optimised to infer more rigorous conclusions by reducing the variability in the recorded measurements. This has incorporated thorough studies into the impact of atmospheric adsorbents on the devices and ways in which these effects can be reversed. The latest trend of using pyrene tagged DNA aptamers as bioreceptors has been demonstrated in this work, with initial results showing its suitability to replace the traditional approach for immobilisation, offering a saving on sample preparation time.

By developing effective strategies to overcome and limit these challenges, this work has shown that GFETs are suitable candidates for the pursuit of sensitive, biocompatible and easy to functionalise biosensing devices by demonstrating their applicability for the detection of Pb^{2+} ions in water. Intricacies relating to the specific achievements relating to the challenges faced are discussed in detail below.

8.2 Thesis Achievements

The sensitive detection of Pb^{2+} ions using aptamer functionalised GFET devices, fabricated from monolayer CVD graphene has been demonstrated in this work. Achieving this has relied on multiple successes which are discussed below. Two novel data analysis software packages were presented in this contribution. SCRAMBLE is a software package developed to process raw I_{SD}-V_G data. It automatically calculates and visualises key metrics such as Dirac points and charge carrier mobilities that are tracked during GFET biosensing strategies to provide insights into how the functionalisation stages have progressed. RAMAN_VIEWER is an application used to process raw Raman spectral data. It automatically determines key metrics linked with the significant peaks from graphene's spectrum so that changes are easily identified and reported. Baseline removal, averaging and statistical testing of significance are included as useful tools to the user to enhance their analysis of the data. SCRAMBLE and RAMAN_VIEWER have been developed with easy to use GUIs which allows users of all software levels to be confident with their use. Both of these applications contribute to current research through the removal of laborious processing of individual characterisation sets. This eliminates human error and enhances the users' time developing experimental techniques. Since both packages have been designed to be open-source and fully customisable they can be applied to a wide range of graphene based research and therefore it is envisioned that they will contribute to some exciting avenues of discovery in the future.

A key element to effective GFET biosensing is the rigorous testing strategies deployed to characterise them. Work in this thesis focussed on Raman and electrical characterisation techniques. The importance of this element was demonstrated by the variability in measurements that was shown for these methods. Robust SOPs for these techniques were developed which aimed to improve the reliability of the results obtained throughout this contribution. It is hoped that this work will improve the transparency of future research discussing the topic of inconsistencies. These techniques were then applied to newly fabricated devices. The influence of the fabrication and transfer processes on the graphene characteristics was shown. Work presented here shows that simplifying the fabrication process by using only a Sputtering Machine to lay down both the Cr and Au layers should be avoided in favour of a joint Evaporation-Sputtering procedure. Although more time-consuming, the lower energy of the bombarding particles is preferential when reducing damage to the graphene lattice which can subsequently harm graphene's attractive electronic properties required for biosensing strategies.

It has been shown that Hall-bar architectures with electrodes designed to fully bisect the graphene channel should be favoured over ones which partially touch the channel due to the improvement of the contact with the graphene. This choice also simplifies the fabrication process of existing methodologies. A novel cleaving process, using basic laboratory tools, was demonstrated in this work to effectively cleave off individual GFET devices from arrays. This forms a significant part of the testing procedure for GFET devices as it facilitates a greater regulation of experimental controls.

Further analysis as to the effect of atmospheric adsorbents on the GFETs was another achievement of this work. It was shown that both the Raman and electrical characterisation of graphene changed after being exposed to the ambient laboratory environment, mostly attributed to the adsorption of O_2 and H_2O. Predicting and therefore calibrating out this impact was not possible because it was shown that there were differences in the rate and overall direction of drift from these metrics. It was also shown that the drift in some metrics could occur in different directions over the course of the exposure period. This suggests that adsorbent mechanisms were occurring at rapid timescales of a few seconds. Longer periods of observations showed evidence of saturation. Recovery techniques were then introduced, with low-level vacuum treatment causing some recovery of all the electrical characteristics. This research demonstrates the need for greater commentary in the literature as to the handling of devices before and after functionalisation treatments. This is necessary since it is often the magnitude in change of these electrical metrics, that are so often discussed between functionalisation stages, to confirm successful immobilisation.

This thesis presents an optimised method of conjugating the bi-functional PBASE molecule onto the graphene channel. In doing so it provides a layer to which bioreceptors can be immobilised to, facilitating this technology as a generic sensing platform for other groups to benefit from. It improves on the previous SOP for this technique and involves fully submersing the GFET devices in tubes filled with PBASE/DMF for 4 h at a concentration of 10 mM at ambient laboratory temperatures. Evidence which confirms the non-covalent stacking of the PBASE to the graphene lattice via π-bonding is provided by additional peaks introduced into the Raman spectrum caused by interactions between the pyrene group of PBASE and the graphene lattice. Although some disorder was introduced during this process, evidenced by an increase in I(D), electrical measurements confirm that the process does not impact the mobility of the charge carriers in graphene, which acts to maintain its superior electronic properties. XPS, AFM and FTIR measurements were also used to support the successful conjugation using this developed technique. It was demonstrated that there was a uniform distribution of the PBASE layer using detailed Raman mapping. Techniques to confirm this using FTAs, over larger areas were introduced.

Two functionalisation routes for immobilising the specific TBA bioreceptors for Pb^{2+} ions to the surface of graphene were presented in this thesis. The indirect immobilisation route required an initial layer of PBASE to be conjugated to surface before TBA aptamers with an amine modified 5’ end were immobilised to the NHS ester end. The direct immobilisation exploited TBA aptamers that had a pyrene modified 5’ end (PTBA) to bind directly to the graphene surface via π-stacking. Both methods showed evidence of doping and changes to the mobility in the graphene lattice caused by the interaction of the DNA backbone. The uniform distribution of the PTBA bioreceptors across an entire graphene channel (720 x 80 μm) by the use of QDs was also introduced. Although more expensive to purchase, the direct immobilisation approach benefits from a reduced time to functionalise devices making it the favoured technique for the immobilisation of bioreceptors to graphene in the future.

The detection of Pb^{2+} using GFETs was tested for both the indirect and direct aptamer immobilisation strategies. The sensing mechanism relies on the formation of G-quadraplex structures on Pb^{2+} binding which has the impact of changing the electronic properties of graphene. It was shown that the PTBA functionalised sensors showed repeatable sensing characteristics across the 1 nM to 100 nM range. A correlation was demonstrated between the current metrics and the concentration of the Pb^{2+} ions. Combining the ease of functionalisation with the repeatable sensing characteristics, this work shows that the PTBA shows more promising results with regards to the biosensing of Pb^{2+} ions over the two-stage indirect immobilisation approach. Further work is necessary to improve the sensing characteristics for the indirect immobilisation strategy which did not show reliable sensing characteristics in the same range, possibly because of the interplay between the PBASE and aptamer layers preventing the G-quadraplex structures from forming.

The achievements detailed in this thesis are steps forward in the realisation of POC environmental sensors suitable for the sensitive detection of Pb^{2+} ions in water. GFET devices, suitable for scalable production have shown to be sensitive to Pb^{2+} ions after functionalisation with PTBA aptamers, paving the way for inexpensive distributed sensors. Alongside this, the development of novel data processing tools and robust testing/handling strategies combine to enhance this field which will only encourage further work proliferating this lab-based-concept into real-world settings.

Future Aims

The ambition for developing these GFET biosensors is the production of POC devices suitable for monitoring toxic metal ions such as Pb^{2+} in drinking water sources. In order to progress this technology from proof-of-concept into practical settings the following are just some of the avenues recommended for future exploration.

8.3.1 Immobilisation as a Passivation Tool

In order for POC devices to be realised it will be necessary to deploy them in harsh environments away from the laboratory setting where control over the surrounding atmosphere can be difficult. Work presented here has focussed on the changes to the GFET response caused by atmospheric contaminants adsorbing to the surface of graphene directly. Future work should investigate if adsorbents can negatively impact the response of the GFETs after various immobilisation stages. Subsequent work should build on the initial observations made in this thesis that the PBASE SAM layer appears to inhibit the effect of atmospheric adsorbents on the GFET response by forming a passivation layer. Subsequent DNA aptamer binding could also build on this effect. These investigations could inform best practices for extending the storage lifespan of these devices in forward positions away from laboratory settings.

8.3.2 DMF Impact on Exposed Graphene

One of the key observations from this body of work is the impact that immobilising PBASE on graphene can have when it is dissolved within DMF and methanol. Initial results show that structural defects are introduced into graphene channels when they are not covered by electrical contact layers. Since defects to the lattice will change the electronic response of the subsequent GFET device, this change is undesirable [201]. Examining this effect on pre-patterned devices (where one side of the graphene is still exposed) versus post-patterned devices (where both layers are passivated) would be a recommended starting point. It would then be advisable to investigate how the GFET response is different after a channel has had the structure changed in this way; this could be achieved by evaporating and sputtering Cr and Au on a channel that has been affected. Further work in understanding the conditions that make this phenomenon occur such as chemical purity, immobilisation temperature and time would improve immobilisation methodologies so that this effect could be reduced or prevented all together.

8.3.3 Indirect Immobilisation Optimisation

Initial results shown in this thesis show some signs of expected electrical responses from the GFETs when sensing Pb^{2+} ions from the indirect immobilisation approach. However, the fact that they were not consistent across all measurements suggests that the immobilisation procedure requires optimisation. Initial studies should focus on optimising the concentrations of PBASE and DNA aptamers to improve sensitivity and reliability in subsequent Pb^{2+} detection. It is also suggested that incorporating spacers [100] into the PBASE solution could benefit the downstream capture of Pb^{2+} ions by the DNA aptamers since there would be enhanced space for G-quadraplex structures to form.

8.3.4 Selectivity

A biosensing parameter that requires consideration in future investigations is selectivity, which evaluates the sensor response to the target in the presence of other compounds found within the sample solution. Future POC platforms will need to show selectivity of the target analyte within complex mixtures such as drinking water which has several other interfering agents dissolved within it [113].

Once the desired bioreceptors are immobilised, it is critical to prevent non-specific signals from undesired analytes from binding directly to the graphene surface. This is particularly important in complex biological solutions. This can be achieved using a blocking agent or alternatively by deploying molecules which chemically quench the unbound end of PBASE hence preventing further coupling of analytes. BSA is a common blocking agent used to achieve surface passivation and has been demonstrated in [4, 6].

The reactive NHS ester ends of the PBASE molecule can be deactivated with the use of Ethanolamine (C_2H_7NO) [52, 93]. This is a bi-functional molecule which features both a primary amine and primary alcohol as pictured in Figure 8.1. When the Ethanolamine binds to PBASE at its amine end, replacing the NHS group, the surface is pacified due to increase in surface hydroxyl functional groups which prevent the binding of additional aminated substances [221].

Figure 8.1 has been removed due to Copyright restrictions

Figure 8.1 PBASE deactivation using Ethanolamine (adapted) [222]

8.3.5 Lab-on-Chip

One concept to be explored which will facilitate the realisation of these sensors into POC devices is Lab-on-Chip (LOC) technology [223]. This is an exciting field within biosensing and is associated with the concept of one platform handling all aspects of sample transportation, sensing and readout facilitating a sample-in-answer-out detection method similar to that offered by LFIAs [223]. LOC devices are facilitated by microfluidics; this describes the use of miniaturised channels for the separation, mixing, filtration and transportation of analytes across sensing platforms [224]. The implementation of microfluidics has shown to reduce sample volume, increase detection time and reduce the cost of reagents [213]. LOC devices are likely to proliferate this technology since they are more practical for POC sensing in both centralised and low resource settings [225].

The first step towards a LOC platform requires the integration of microfluidics. A simplified microfluidic approach could look similar to the work completed by Kwong et al on their work using a back-gated GFET sensor for the detection of exosomes [69]. This would require increasing the dimensions of the current GFET design to larger scales (of the order mm) in order to support the microfluidic infrastructure. In Kwong’s contribution they integrated a microfluidic channel over a portion of the surface of the graphene, which contained their analytes away from electrodes (Figure 8.2A). They used the microfluidic channels to obtain the electrical characteristics of the graphene when it was filled with their target exosomes and PBS.

Figure 8.2 has been removed due to Copyright restrictions

Figure 8.2 A) Back-gated GFET device with microfluidic integration B) Top-panel: Liquid-gated GFET with microfluidic integration Bottom-panel: Circuit schematic.

Partially exposing the graphene in this way caused an additional conductance minimum to be observed in their I_{SD}-V_G measurements which they attributed to the superposition of two distinct transfer curves caused by the different localised electrical properties [69]. In an alternative strategy, the group led by Khan, developed a liquid-gated GFET with an in-plane gate electrode (Figure 8.2B). They noted that the effect of mass-transfer limitations on the binding process between bioreceptors and analytes, common in static flow measurements, can be limited by harnessing microfluidics [213]. The microfluidic channel was used to immobilise both PBASE and their aptamers onto the graphene channel preventing the concern of solvent evaporation. This group then used their microfluidics with a steady flow rate of 20 µl/min to evaluate the electrical characteristics when different concentrations of analytes were passed through the channel; real-time sensing was demonstrated in this work across the time-dependant measurements [213].

8.3.6 Device Stability

In order for these devices to be realised as POC sensors investigations relating to their stability with time and longer term exposures to the environment will need to be completed.

Assessing the long-term stability would start with investigating the sensing characteristics for Pb^{2+} ions after fabricated devices are left in the ambient environment for several weeks/months. Then, repeated measurements whereby devices are initially functionalised with TBA/PTBA aptamers to see if these functionalised layers act to prevent the degradation caused by adsorbents should be conducted. Initial measurements shown in 7.8.3.3 eluded to some level of passivation. In a parallel study, investigating effective recovery techniques for fabricated graphene will also provide significant steps forward to realise these devices in POC settings. Returning the V_{DP} values closer to 0 V will act to reduce the high voltage requirements necessary for their function, since the need to sweep between -100 V and +100 V will be eliminated. Reducing this sweep range, reduces their power requirement thus improving their suitability as distributed POC devices.

A potential route to enhance the stability of the devices is by using functionalised cross-linked 3D polymeric networks, called hydrogels, which are capable of retaining water, as demonstrated in work by Bay et al [59]. These functionalised hydrogels were precisely positioned over GFET devices using projection microlithography techniques that acted to photopolymerise the PEG linker/bioreceptor complexes. With separately encoded hydrogels, Bay showed that individual GFET sensors immobilised with penicillinase- and acetylcholinesterase enzyme bioreceptors were able to transduce signals relating to their respective (penicillin and acetylcholine chloride (ACh)) target only (Figure 8.3). They also noted that there was no signal interference between the different sensors separated by distances of only 50-100 µm [59].

Figure 8.3 has been removed due to Copyright restrictions

Figure 8.3 A) Schematic showing hydrogel functionalised device consisting of four GFET sensors B) Real-time measurements acquired when microfluidic channel was filled with target analytes [59]

The benefit of using this functionalisation strategy would be three-fold. Firstly, it is conjectured that the functionality of DNA aptamers could be prolonged since the hydrogels were shown in this work to enhance the stability of the enzymes. Secondly, since the graphene sheet would no longer be in direct contact with the ambient environment drift in its electrical metrics such as the decrease in mobility (discussed in section 7.5) could be prevented. Thirdly, it was shown that the surface coverage of these hydrogels supressed non-specific binding on graphene [59]. Building on from this concept, with an adapted sensor design, this innovative use of hydrogels facilitates multiplexed sensing, whereby each hydrogel could be functionalised with aptamers specific to various toxic metal ions [59]. This would immediately broaden the level of information that could be inferred from these platforms, whilst monitoring drinking water sources, since multiple toxic contaminants could be detected simultaneously.

References

1. K. S. Novoselov, A. K. Geim, S. V. Morozov, D. Jiang, Y. Zhang, S. V. Dubonos, I. V. Grigorieva, and A.A. Firsov, *Electric Field Effect in Atomically Thin Carbon Films.* Science, 2004. **306**.
2. Novoselov, K.S., V.I. Fal'ko, L. Colombo, P.R. Gellert, M.G. Schwab, and K. Kim, *A roadmap for graphene.* Nature, 2012. **490**(7419): p. 192-200.
3. Ping, J., R. Vishnubhotla, A. Vrudhula, and A.T.C. Johnson, *Scalable Production of High-Sensitivity, Label-Free DNA Biosensors Based on Back-Gated Graphene Field Effect Transistors.* ACS Nano, 2016. **10**(9): p. 8700-8704.
4. Haslam, C., S. Damiati, T. Whitley, P. Davey, E. Ifeachor, and S.A. Awan, *Label-Free Sensors Based on Graphene Field-Effect Transistors for the Detection of Human Chorionic Gonadotropin Cancer Risk Biomarker.* Diagnostics (Basel), 2018. **8**(1).
5. Yang, Y. and R. Murali, *Binding mechanisms of molecular oxygen and moisture to graphene.* Applied Physics Letters, 2011. **98**(9): p. 093116.
6. Bungon, T., C. Haslam, S. Damiati, B. O'Driscoll, T. Whitley, P. Davey, G. Siligardi, J. Charmet, and S.A. Awan, *Graphene FET Sensors for Alzheimer's Disease Protein Biomarker Clusterin Detection.* Frontiers in Molecular Biosciences, 2021. **8**(188).
7. Nekrasov, N., D. Kireev, A. Emelianov, and I. Bobrinetskiy, *Graphene-Based Sensing Platform for On-Chip Ochratoxin A Detection.* Toxins (Basel), 2019. **11**(10).
8. Suhail, A., K. Islam, B. Li, D. Jenkins, and G. Pan, *Reduction of polymer residue on wet–transferred CVD graphene surface by deep UV exposure.* Applied Physics Letters, 2017. **110**(18): p. 183103.
9. Kakatkar, A., T.S. Abhilash, R.D. Alba, J.M. Parpia, and H.G. Craighead, *Detection of DNA and poly-l-lysine using CVD graphene-channel FET biosensors.* Nanotechnology, 2015. **26**(12): p. 125502.
10. Reddy, D., L.F. Register, G.D. Carpenter, and S.K. Banerjee, *Graphene field-effect transistors.* Journal of Physics D: Applied Physics, 2012. **45**(1).
11. Seo, G., G. Lee, M.J. Kim, S.-H. Baek, M. Choi, K.B. Ku, C.-S. Lee, S. Jun, D. Park, H.G. Kim, S.-J. Kim, J.-O. Lee, B.T. Kim, E.C. Park, and S.I. Kim, *Rapid Detection of COVID-19 Causative Virus (SARS-CoV-2) in Human Nasopharyngeal Swab Specimens Using Field-Effect Transistor-Based Biosensor.* ACS Nano, 2020. **14**(4): p. 5135-5142.
12. Papamatthaiou, S., W. McConnell, V. Kumar, U. Zupancic, E. Lee-Emery, M. Lorenzo, J. Reboud, J. Cooper, P. Estrela, and D. Moschou, *Lab-on-PCB technology for handheld, sample-in-answer-out SARS-CoV-2 diagnostic, 843-844. Paper presented at Miniaturized Systems for Chemistry and Life Sciences (µTAS 2021)* 2021.
13. Andryukov, B.G., *Six decades of lateral flow immunoassay: from determining metabolic markers to diagnosing COVID-19.* AIMS microbiology, 2020. **6**(3): p. 280-304.
14. Wani, A.L., A. Ara, and J.A. Usmani, *Lead toxicity: a review.* Interdisciplinary toxicology, 2015. **8**(2): p. 55-64.
15. Hou, S., L. Yuan, P. Jin, B. Ding, N. Qin, L. Li, X. Liu, Z. Wu, G. Zhao, and Y. Deng, *A clinical study of the effects of lead poisoning on the intelligence and neurobehavioral abilities of children.* Theoretical biology & medical modelling, 2013. **10**: p. 13-13.
16. Iacobucci, G., *Covid-19: US regulator raises "significant concerns" over safety of rapid lateral flow tests.* BMJ, 2021. **373**: p. n1514.
17. Patrick, G., *Instant Notes in Organic Chemistry*. 2004, Abingdon, United States: Taylor & Francis Group.
18. Persano Adorno, D., L. Bellomonte, and N. Pizzolato. *Electronic Properties of Graphene: A Learning Path for Undergraduate Students*. in *Key Competences in Physics Teaching and Learning*. 2017. Cham: Springer International Publishing.
19. Wong, H.S.P. and D. Akinwande, *Carbon Nanotube and Graphene Device Physics*. 2010, Cambridge: Cambridge University Press.
20. Kittel, C., *Introduction to solid state physics*. 7th ed. ed. 1996, New York: New York : Wiley.

21. Castro Neto, A.H., F. Guinea, N.M.R. Peres, K.S. Novoselov, and A.K. Geim, *The electronic properties of graphene.* Reviews of Modern Physics, 2009. **81**(1): p. 109-162.
22. Das Sarma, S., S. Adam, E.H. Hwang, and E. Rossi, *Electronic transport in two-dimensional graphene.* Reviews of Modern Physics, 2011. **83**(2): p. 407-470.
23. Meyer, J.C., A.K. Geim, M.I. Katsnelson, K.S. Novoselov, T.J. Booth, and S. Roth, *The structure of suspended graphene sheets.* Nature, 2007. **446**: p. 60.
24. Lee, E.J., K. Balasubramanian, R.T. Weitz, M. Burghard, and K. Kern, *Contact and edge effects in graphene devices.* Nat Nanotechnol, 2008. **3**(8): p. 486-90.
25. Amin, K.R. and A. Bid, *Effect of ambient on the resistance fluctuations of graphene.* Applied Physics Letters, 2015. **106**(18): p. 183105.
26. Li, B., G. Pan, S. Awan, and N. Avent, *Techniques for Production of Large Area Graphene for Electronic and Sensor Device Applications*. Vol. 1. 2014.
27. *Frontiers of Graphene and Carbon Nanotubes: Devices and Applications*. 1 ed. 2015: Springer, Tokyo. XVIII, 289.
28. Bae, S., H. Kim, Y. Lee, X. Xu, J.S. Park, Y. Zheng, J. Balakrishnan, T. Lei, H.R. Kim, Y.I. Song, Y.J. Kim, K.S. Kim, B. Ozyilmaz, J.H. Ahn, B.H. Hong, and S. Iijima, *Roll-to-roll production of 30-inch graphene films for transparent electrodes.* Nat Nanotechnol, 2010. **5**(8): p. 574-8.
29. Yi, M. and Z. Shen, *A review on mechanical exfoliation for the scalable production of graphene.* Journal of Materials Chemistry A, 2015. **3**(22): p. 11700-11715.
30. Novoselov, K.S., D. Jiang, F. Schedin, T.J. Booth, V.V. Khotkevich, S.V. Morozov, and A.K. Geim, *Two-dimensional atomic crystals.* Proceedings of the National Academy of Sciences of the United States of America, 2005. **102**(30): p. 10451.
31. Torrisi, F., T. Hasan, W. Wu, Z. Sun, A. Lombardo, T.S. Kulmala, G.-W. Hsieh, S. Jung, F. Bonaccorso, P.J. Paul, D. Chu, and A.C. Ferrari, *Inkjet-Printed Graphene Electronics.* ACS Nano, 2012. **6**(4): p. 2992-3006.
32. Leng, T., X. Huang, K. Chang, J. Chen, M.A. Abdalla, and Z. Hu, *Graphene Nanoflakes Printed Flexible Meandered-Line Dipole Antenna on Paper Substrate for Low-Cost RFID and Sensing Applications.* IEEE Antennas and Wireless Propagation Letters, 2016. **15**: p. 1565-1568.
33. Kauling, A.P., A.T. Seefeldt, D.P. Pisoni, R.C. Pradeep, R. Bentini, R.V.B. Oliveira, K.S. Novoselov, and A.H. Castro Neto, *The Worldwide Graphene Flake Production.* Advanced Materials, 2018. **30**(44): p. 1803784.
34. Borin Barin, G., Y. Song, I. de Fátima Gimenez, A.G. Souza Filho, L.S. Barreto, and J. Kong, *Optimized graphene transfer: Influence of polymethylmethacrylate (PMMA) layer concentration and baking time on graphene final performance.* Carbon, 2015. **84**: p. 82-90.
35. Li, X., Y. Zhu, W. Cai, M. Borysiak, B. Han, D. Chen, R.D. Piner, L. Colombo, and R.S. Ruoff, *Transfer of Large-Area Graphene Films for High-Performance Transparent Conductive Electrodes.* Nano Letters, 2009. **9**(12): p. 4359-4363.
36. Suk, J.W., W.H. Lee, J. Lee, H. Chou, R.D. Piner, Y. Hao, D. Akinwande, and R.S. Ruoff, *Enhancement of the Electrical Properties of Graphene Grown by Chemical Vapor Deposition via Controlling the Effects of Polymer Residue.* Nano Letters, 2013. **13**(4): p. 1462-1467.
37. Bhand, S.G., S. Soundararajan, I. Surugiu-Wärnmark, J.S. Milea, E.S. Dey, M. Yakovleva, and B. Danielsson, *Fructose-selective calorimetric biosensor in flow injection analysis.* Analytica Chimica Acta, 2010. **668**(1): p. 13-18.
38. Gan, T., J. Sun, S. Cao, F. Gao, Y. Zhang, and Y. Yang, *One-step electrochemical approach for the preparation of graphene wrapped-phosphotungstic acid hybrid and its application for simultaneous determination of sunset yellow and tartrazine.* Electrochimica Acta, 2012. **74**: p. 151-157.
39. Wang, Y., J. Ping, Z. Ye, J. Wu, and Y. Ying, *Impedimetric immunosensor based on gold nanoparticles modified graphene paper for label-free detection of Escherichia coli O157:H7.* Biosensors and Bioelectronics, 2013. **49**: p. 492-498.
40. Zhang, M., H.T. Zhao, T.J. Xie, X. Yang, A.J. Dong, H. Zhang, J. Wang, and Z.Y. Wang, *Molecularly imprinted polymer on graphene surface for selective and sensitive electrochemical sensing imidacloprid.* Sensors and Actuators B: Chemical, 2017. **252**: p. 991-1002.

41. Justino, C.I.L., A.C. Duarte, and T.A.P. Rocha-Santos, *Recent Progress in Biosensors for Environmental Monitoring: A Review.* Sensors (Basel, Switzerland), 2017. **17**(12): p. 2918.
42. Tu, J., Y. Gan, T. Liang, Q. Hu, Q. Wang, T. Ren, Q. Sun, H. Wan, and P. Wang, *Graphene FET Array Biosensor Based on ssDNA Aptamer for Ultrasensitive Hg2+ Detection in Environmental Pollutants.* Frontiers in Chemistry, 2018. **6**(333).
43. Kim, D.J., H.C. Park, I.Y. Sohn, J.H. Jung, O.J. Yoon, J.S. Park, M.Y. Yoon, and N.E. Lee, *Electrical graphene aptasensor for ultra-sensitive detection of anthrax toxin with amplified signal transduction.* Small, 2013. **9**(19): p. 3352-60.
44. Lei, Y.M., M.M. Xiao, Y.T. Li, L. Xu, H. Zhang, Z.Y. Zhang, and G.J. Zhang, *Detection of heart failure-related biomarker in whole blood with graphene field effect transistor biosensor.* Biosens Bioelectron, 2017. **91**: p. 1-7.
45. Forsyth, R., A. Devadoss, and O.J. Guy, *Graphene Field Effect Transistors for Biomedical Applications: Current Status and Future Prospects.* Diagnostics (Basel), 2017. **7**(3).
46. Bhalla, N., P. Jolly, N. Formisano, and P. Estrela, *Introduction to biosensors.* Essays in Biochemistry, 2016. **60**(1): p. 1-8.
47. Tkáč, J., V. Štefuca, and P. Gemeiner, *Biosensors with Immobilised Microbial Cells Using Amperometric and Thermal Detection Principles*, in *Applications of Cell Immobilisation Biotechnology*, V. Nedović and R. Willaert, Editors. 2005, Springer Netherlands: Dordrecht. p. 549-566.
48. Grieshaber, D., R. MacKenzie, J. Vörös, and E. Reimhult, *Electrochemical Biosensors - Sensor Principles and Architectures.* Sensors (Basel, Switzerland), 2008. **8**(3): p. 1400-1458.
49. Bonanni, A., A.H. Loo, and M. Pumera, *Graphene for impedimetric biosensing.* TrAC Trends in Analytical Chemistry, 2012. **37**: p. 12-21.
50. Donnelly, M., D.C. Mao, J. Park, and G.Y. Xu, *Graphene field-effect transistors: the road to bioelectronics.* Journal of Physics D-Applied Physics, 2018. **51**(49): p. 16.
51. Damborský, P., J. Švitel, and J. Katrlík, *Optical biosensors.* Essays in biochemistry, 2016. **60**(1): p. 91-100.
52. Okamoto, S., Y. Ohno, K. Maehashi, K. Inoue, and K. Matsumoto, *Immunosensors Based on Graphene Field-Effect Transistors Fabricated Using Antigen-Binding Fragment.* Japanese Journal of Applied Physics, 2012. **51**.
53. Ahmed, N., M. Dawson, C. Smith, and E. Wood, *Biology of Disease*. 2006, Cheltenham, UK: CRC Press LLC.
54. Lawrence, E., *Henderson's Dictionary of Biology*. 2011, Harlow, UK: Pearson Education UK.
55. Janeway, C., P. Travers, M. Walport, and M. Shlomchik, J., *Immunobiology: The Immune System in Health and Disease*. 5th edition ed. 2001, New York: Garland Science.
56. Schütze, T., B. Wilhelm, N. Greiner, H. Braun, F. Peter, M. Mörl, V.A. Erdmann, H. Lehrach, Z. Konthur, M. Menger, P.F. Arndt, and J. Glökler, *Probing the SELEX Process with Next-Generation Sequencing.* PLOS ONE, 2011. **6**(12): p. e29604.
57. Komarova, N. and A. Kuznetsov, *Inside the Black Box: What Makes SELEX Better?* Molecules, 2019. **24**(19): p. 3598.
58. Song, K.-M., S. Lee, and C. Ban, *Aptamers and Their Biological Applications.* Sensors, 2012. **12**(1).
59. Bay, H.H., R. Vo, X. Dai, H.H. Hsu, Z. Mo, S. Cao, W. Li, F.G. Omenetto, and X. Jiang, *Hydrogel Gate Graphene Field-Effect Transistors as Multiplexed Biosensors.* Nano Lett, 2019. **19**(4): p. 2620-2626.
60. Cheng, C.-M., A.W. Martinez, J. Gong, C.R. Mace, S.T. Phillips, E. Carrilho, K.A. Mirica, and G.M. Whitesides, *Paper-Based ELISA.* Angewandte Chemie International Edition, 2010. **49**(28): p. 4771-4774.
61. Piliarik, M., M. Bocková, and J. Homola, *Surface plasmon resonance biosensor for parallelized detection of protein biomarkers in diluted blood plasma.* Biosensors and Bioelectronics, 2010. **26**(4): p. 1656-1661.
62. Brownson, D.A.C. and C.E. Banks, *The Handbook of Graphene Electrochemistry*. 2014, London, UK: Springer London, Limited.
63. Mullard, L., *Field-effect transistors*. 1972, London: London, Mullard Ltd.
64. Fiore, J., *Semiconductor Devices: Theory and Application*. 2017: Independently Published.

65. Lee, C.-S., K.S. Kim, and M. Kim, *Ion-Sensitive Field-Effect Transistor for Biological Sensing.* Sensors, 2009. **9**(9).
66. Han, S.H., S.K. Kim, K. Park, S.Y. Yi, H.-J. Park, H.-K. Lyu, M. Kim, and B.H. Chung, *Detection of mutant p53 using field-effect transistor biosensor.* Analytica Chimica Acta, 2010. **665**(1): p. 79-83.
67. Bergveld, P., *Thirty years of ISFETOLOGY: What happened in the past 30 years and what may happen in the next 30 years.* Sensors and Actuators B: Chemical, 2003. **88**(1): p. 1-20.
68. Yan, F., P. Estrela, Y. Mo, P. Migliorato, H. Maeda, S. Inoue, and T. Shimoda, *Polycrystalline silicon ion sensitive field effect transistors.* Applied Physics Letters, 2005. **86**(5).
69. Kwong Hong Tsang, D., T.J. Lieberthal, C. Watts, I.E. Dunlop, S. Ramadan, A.E. Del Rio Hernandez, and N. Klein, *Chemically Functionalised Graphene FET Biosensor for the Label-free Sensing of Exosomes.* Sci Rep, 2019. **9**(1): p. 13946.
70. Xu, S., J. Zhan, B. Man, S. Jiang, W. Yue, S. Gao, C. Guo, H. Liu, Z. Li, J. Wang, and Y. Zhou, *Real-time reliable determination of binding kinetics of DNA hybridization using a multi-channel graphene biosensor.* Nature Communications, 2017. **8**(1): p. 14902.
71. Ohno, Y., K. Maehashi, and K. Matsumoto, *Graphene Biosensor*, in *Frontiers of Graphene and Carbon Nanotubes: Devices and Applications*, K. Matsumoto, Editor. 2015, Springer Japan: Tokyo. p. 91-103.
72. Ohno, Y., K. Maehashi, and K. Matsumoto, *Label-Free Biosensors Based on Aptamer-Modified Graphene Field-Effect Transistors.* Journal of the American Chemical Society, 2010. **132**(51): p. 18012-18013.
73. Wang, H., Y. Wu, C. Cong, J. Shang, and T. Yu, *Hysteresis of Electronic Transport in Graphene Transistors.* ACS Nano, 2010. **4**(12): p. 7221-7228.
74. Ohno, Y., K. Maehashi, K. Inoue, and K. Matsumoto, *Label-Free Aptamer-Based Immunoglobulin Sensors Using Graphene Field-Effect Transistors.* Japanese Journal of Applied Physics, 2011. **50**(7).
75. Kazuhiko, M., M. Kenzo, O. Yasuhide, and I. Koichi, *Recent advances in functional graphene biosensors.* Journal of Physics D: Applied Physics, 2014. **47**(9): p. 094005.
76. Green, N.S. and M.L. Norton, *Interactions of DNA with graphene and sensing applications of graphene field-effect transistor devices: a review.* Anal Chim Acta, 2015. **853**: p. 127-142.
77. Kybert, N.J., G.H. Han, M.B. Lerner, E.N. Dattoli, A. Esfandiar, and A.T. Charlie Johnson, *Scalable arrays of chemical vapor sensors based on DNA-decorated graphene.* Nano Research, 2014. **7**(1): p. 95-103.
78. Sordan, R., F. Traversi, and V. Russo, *Logic gates with a single graphene transistor.* Applied Physics Letters, 2009. **94**(7).
79. Saltzgaber, G., P.M. Wojcik, T. Sharf, M.R. Leyden, J.L. Wardini, C.A. Heist, A.A. Adenuga, V.T. Remcho, and E.D. Minot, *Scalable graphene field-effect sensors for specific protein detection.* Nanotechnology, 2013. **24**(35): p. 355502.
80. Tran, T.-T. and A. Mulchandani, *Carbon nanotubes and graphene nano field-effect transistor-based biosensors.* TrAC Trends in Analytical Chemistry, 2016. **79**: p. 222-232.
81. Béraud, A., M. Sauvage, C.M. Bazán, M. Tie, A. Bencherif, and D. Bouilly, *Graphene field-effect transistors as bioanalytical sensors: design, operation and performance.* Analyst, 2021. **146**(2): p. 403-428.
82. Levesque, P.L., S.S. Sabri, C.M. Aguirre, J. Guillemette, M. Siaj, P. Desjardins, T. Szkopek, and R. Martel, *Probing Charge Transfer at Surfaces Using Graphene Transistors.* Nano Letters, 2011. **11**(1): p. 132-137.
83. Yang, Y., K. Brenner, and R. Murali, *The influence of atmosphere on electrical transport in graphene.* Carbon, 2012. **50**(5): p. 1727-1733.
84. Georgakilas, V., M. Otyepka, A.B. Bourlinos, V. Chandra, N. Kim, K.C. Kemp, P. Hobza, R. Zboril, and K.S. Kim, *Functionalization of Graphene: Covalent and Non-Covalent Approaches, Derivatives and Applications.* Chemical Reviews, 2012. **112**(11): p. 6156-6214.
85. Teixeira, S., G. Burwell, A. Castaing, D. Gonzalez, R.S. Conlan, and O.J. Guy, *Epitaxial graphene immunosensor for human chorionic gonadotropin.* Sensors and Actuators B: Chemical, 2014. **190**: p. 723-729.

86. Suresh, A. and A. Rakshit, *Advanced Oxidation Processes for Wastewater Treatment : Emerging Green Chemical Technology*. 2018, London: Academic Press.
87. Kim, D., H.-J. Kim, S.-B. Shim, S. Jung, N.H. Lee, S.H. Nahm, E.-C. Shin, W.S. Yun, and D.H. Ha, *Electrical conductance change of graphene-based devices upon surface modification for detecting botulinum neurotoxin.* Japanese Journal of Applied Physics, 2017. **56**(6).
88. Kodali, V.K., J. Scrimgeour, S. Kim, J.H. Hankinson, K.M. Carroll, W.A. de Heer, C. Berger, and J.E. Curtis, *Nonperturbative Chemical Modification of Graphene for Protein Micropatterning.* Langmuir, 2011. **27**(3): p. 863-865.
89. Islam, K., A. Suhail, and G. Pan, *A Label-Free and Ultrasensitive Immunosensor for Detection of Human Chorionic Gonadotrophin Based on Graphene FETs.* Biosensors (Basel), 2017. **7**(3).
90. Ramadan, S., R. Lobo, Y. Zhang, L. Xu, O. Shaforost, D. Kwong Hong Tsang, J. Feng, T. Yin, M. Qiao, A. Rajeshirke, L.R. Jiao, P.K. Petrov, I.E. Dunlop, M.-M. Titirici, and N. Klein, *Carbon-Dot-Enhanced Graphene Field-Effect Transistors for Ultrasensitive Detection of Exosomes.* ACS Applied Materials & Interfaces, 2021. **13**(7): p. 7854-7864.
91. Kawata, T., T. Ono, Y. Kanai, Y. Ohno, K. Maehashi, K. Inoue, and K. Matsumoto, *Improved sensitivity of a graphene FET biosensor using porphyrin linkers.* Japanese Journal of Applied Physics, 2018. **57**(6).
92. Fernandes, E., P.D. Cabral, R. Campos, G. Machado, M.F. Cerqueira, C. Sousa, P.P. Freitas, J. Borme, D.Y. Petrovykh, and P. Alpuim, *Functionalization of single-layer graphene for immunoassays.* Applied Surface Science, 2019. **480**: p. 709-716.
93. de Almeida, P.R., 3rd, A.M. Murad, L.P. Silva, E.L. Rech, and E.S. Alves, *Development of a Graphene-Based Biosensor for Detecting Recombinant Cyanovirin-N.* Biosensors (Basel), 2020. **10**(12).
94. Sethi, J., M. Van Bulck, A. Suhail, M. Safarzadeh, A. Perez-Castillo, and G. Pan, *A label-free biosensor based on graphene and reduced graphene oxide dual-layer for electrochemical determination of beta-amyloid biomarkers.* Microchimica Acta, 2020. **187**(5): p. 288.
95. Chen, R.J., Y. Zhang, D. Wang, and H. Dai, *Noncovalent Sidewall Functionalization of Single-Walled Carbon Nanotubes for Protein Immobilization.* Journal of the American Chemical Society, 2001. **123**(16): p. 3838-3839.
96. Liu, Y., L. Yuan, M. Yang, Y. Zheng, L. Li, L. Gao, N. Nerngchamnong, C.T. Nai, C.S.S. Sangeeth, Y.P. Feng, C.A. Nijhuis, and K.P. Loh, *Giant enhancement in vertical conductivity of stacked CVD graphene sheets by self-assembled molecular layers.* Nature Communications, 2014. **5**(1): p. 5461.
97. Hermanson, G.T., *Bioconjugate Techniques*. 2008, Burlington, United States: Elsevier Science & Technology.
98. Martinez, C.R. and B.L. Iverson, *Rethinking the term "pi-stacking".* Chemical Science, 2012. **3**(7).
99. Hinnemo, M., J. Zhao, P. Ahlberg, C. Hägglund, V. Djurberg, R.H. Scheicher, S.-L. Zhang, and Z.-B. Zhang, *On Monolayer Formation of Pyrenebutyric Acid on Graphene.* Langmuir, 2017. **33**(15): p. 3588-3593.
100. Kim, J.P., B.Y. Lee, J. Lee, S. Hong, and S.J. Sim, *Enhancement of sensitivity and specificity by surface modification of carbon nanotubes in diagnosis of prostate cancer based on carbon nanotube field effect transistors.* Biosensors and Bioelectronics, 2009. **24**(11): p. 3372-3378.
101. Wu, G., Z. Dai, X. Tang, Z. Lin, P.K. Lo, M. Meyyappan, and K.W.C. Lai, *Graphene Field-Effect Transistors for the Sensitive and Selective Detection of Escherichia coli Using Pyrene-Tagged DNA Aptamer.* Advanced Healthcare Materials, 2017. **6**(19): p. 1700736.
102. Farid, S., X. Meshik, M. Choi, S. Mukherjee, Y. Lan, D. Parikh, S. Poduri, U. Baterdene, C.-E. Huang, Y.Y. Wang, P. Burke, M. Dutta, and M.A. Stroscio, *Detection of Interferon gamma using graphene and aptamer based FET-like electrochemical biosensor.* Biosensors and Bioelectronics, 2015. **71**: p. 294-299.
103. Raghavan, V.S., B. O'Driscoll, J.M. Bloor, B. Li, P. Katare, J. Sethi, S.S. Gorthi, and D. Jenkins, *Emerging graphene-based sensors for the detection of food adulterants and toxicants – A review.* Food Chemistry, 2021. **355**: p. 129547.

104. Hanna-Attisha, M., J. LaChance, R.C. Sadler, and A. Champney Schnepp, *Elevated Blood Lead Levels in Children Associated With the Flint Drinking Water Crisis: A Spatial Analysis of Risk and Public Health Response.* American journal of public health, 2016. **106**(2): p. 283-290.
105. Zahran, S., S.P. McElmurry, and R.C. Sadler, *Four phases of the Flint Water Crisis: Evidence from blood lead levels in children.* Environmental research, 2017. **157**: p. 160-172.
106. Shtepliuk, I., M.F. Santangelo, M. Vagin, I.G. Ivanov, V. Khranovskyy, T. Iakimov, J. Eriksson, and R. Yakimova, *Understanding Graphene Response to Neutral and Charged Lead Species: Theory and Experiment.* Materials, 2018. **11**(10).
107. WHO, *Guidelines for drinking-water quality: volume 1: recommendations*. 1st ed. 1984, Geneva: World Health Organization.
108. WHO, *Guidelines for drinking-water quality: volume 1: recommendations*. 2nd ed. 1993, Geneva: World Health Organization.
109. WHO, *Guidelines for drinking-water quality: volume 1: recommendations*. 4th ed. 2017, Geneva: World Health Organization.
110. WHO. *Lead poisoning*. 2021 [cited 2021 22/12/2021]; Available from: https://www.who.int/news-room/fact-sheets/detail/lead-poisoning-and-health.
111. Zhou, G., J. Chang, S. Cui, H. Pu, Z. Wen, and J. Chen, *Real-Time, Selective Detection of Pb2+ in Water Using a Reduced Graphene Oxide/Gold Nanoparticle Field-Effect Transistor Device.* ACS Applied Materials & Interfaces, 2014. **6**(21): p. 19235-19241.
112. WHO, *Brief guide to analytical methods for measuring lead in blood.* 2020.
113. Doré, E., D.A. Lytle, L. Wasserstrom, J. Swertfeger, and S. Triantafyllidou, *Field analyzers for lead quantification in drinking water samples.* Critical reviews in environmental science and technology, 2020. **51**(20): p. 2357-2388.
114. Chang, J., G. Zhou, E.R. Christensen, R. Heideman, and J. Chen, *Graphene-based sensors for detection of heavy metals in water: a review.* Analytical and Bioanalytical Chemistry, 2014. **406**(16): p. 3957-3975.
115. Liu, C.-W., C.-C. Huang, and H.-T. Chang, *Highly Selective DNA-Based Sensor for Lead(II) and Mercury(II) Ions.* Analytical Chemistry, 2009. **81**(6): p. 2383-2387.
116. Xu, K., X. Meshik, B.M. Nichols, E. Zakar, M. Dutta, and M.A. Stroscio, *Graphene- and aptamer-based electrochemical biosensor.* Nanotechnology, 2014. **25**(20): p. 8.
117. Zuker, M., *Mfold web server for nucleic acid folding and hybridization prediction.* Nucleic Acids Research, 2003. **31**(13): p. 3406-3415.
118. Rosu, F., V. Gabelica, H. Poncelet, and E. De Pauw, *Tetramolecular G-quadruplex formation pathways studied by electrospray mass spectrometry.* Nucleic acids research, 2010. **38**(15): p. 5217-5225.
119. Liu, W., Y. Fu, B. Zheng, S. Cheng, W. Li, T.-C. Lau, and H. Liang, *Kinetics and Mechanism of Conformational Changes in a G-Quadruplex of Thrombin-Binding Aptamer Induced by Pb2+.* The Journal of Physical Chemistry B, 2011. **115**(44): p. 13051-13056.
120. Lu, Y. and J. Liu, *Functional DNA nanotechnology: emerging applications of DNAzymes and aptamers.* Current Opinion in Biotechnology, 2006. **17**(6): p. 580-588.
121. Liu, J. and Y. Lu, *A Colorimetric Lead Biosensor Using DNAzyme-Directed Assembly of Gold Nanoparticles.* Journal of the American Chemical Society, 2003. **125**(22): p. 6642-6643.
122. Li, Y., C. Wang, Y. Zhu, X. Zhou, Y. Xiang, M. He, and S. Zeng, *Fully integrated graphene electronic biosensor for label-free detection of lead (II) ion based on G-quadruplex structure-switching.* Biosensors and Bioelectronics, 2017. **89**: p. 758-763.
123. Chee, L.H., P. Kumar, C.H. Kang, and Z.A. Burhanudin. *DNA/AuNP-graphene back-gated field effect transistor as a biosensor for lead (II) ion detection*. in *2017 IEEE Regional Symposium on Micro and Nanoelectronics (RSM)*. 2017.
124. Wang, C., X. Cui, Y. Li, H. Li, L. Huang, J. Bi, J. Luo, L.Q. Ma, W. Zhou, Y. Cao, B. Wang, and F. Miao, *A label-free and portable graphene FET aptasensor for children blood lead detection.* Sci Rep, 2016. **6**: p. 21711.
125. Manoharan, A.K., S. Chinnathambi, R. Jayavel, and N. Hanagata, *Simplified detection of the hybridized DNA using a graphene field effect transistor.* Sci Technol Adv Mater, 2017. **18**(1): p. 43-50.

126. Cui, Z., *Micro-nanofabrication: technologies and applications*. 2006: Springer.
127. Wasa, K. and T. Matsushima, *9 - Micro-Fabrication by Sputtering*, in *Handbook of Sputtering Technology (Second Edition)*, K. Wasa, I. Kanno, and H. Kotera, Editors. 2012, William Andrew Publishing: Oxford. p. 597-622.
128. Adachi, H. and K. Wasa, *1 - Thin Films and Nanomaterials*, in *Handbook of Sputtering Technology (Second Edition)*, K. Wasa, I. Kanno, and H. Kotera, Editors. 2012, William Andrew Publishing: Oxford. p. 3-39.
129. Todeschini, M., A. Bastos da Silva Fanta, F. Jensen, J.B. Wagner, and A. Han, *Influence of Ti and Cr Adhesion Layers on Ultrathin Au Films.* ACS Applied Materials & Interfaces, 2017. **9**(42): p. 37374-37385.
130. Li, B., G. Pan, N.Y. Jamil, L.A. Taan, S. Awan, and N. Avent, *Shielding technique for deposition of Au electrical contacts on graphene by sputtering.* Journal of Vacuum Science & Technology A, 2015. **33**(3): p. 030601.
131. Wasa, K., I. Kanno, and H. Kotera, *Handbook of Sputter Deposition Technology: Fundamentals and Applications for Functional Thin Films, Nano-Materials and MEMS*. 2012: Elsevier Science.
132. Roddaro, S., P. Pingue, V. Piazza, V. Pellegrini, and F. Beltram, *The Optical Visibility of Graphene: Interference Colors of Ultrathin Graphite on SiO2.* Nano Letters, 2007. **7**(9): p. 2707-2710.
133. Ferrari, A.C., *Raman spectroscopy of graphene and graphite: Disorder, electron–phonon coupling, doping and nonadiabatic effects.* Solid State Communications, 2007. **143**(1): p. 47-57.
134. Ferrari, A.C., J.C. Meyer, V. Scardaci, C. Casiraghi, M. Lazzeri, F. Mauri, S. Piscanec, D. Jiang, K.S. Novoselov, S. Roth, and A.K. Geim, *Raman spectrum of graphene and graphene layers.* Phys Rev Lett, 2006. **97**(18): p. 187401.
135. Berciaud, S., S. Ryu, L.E. Brus, and T.F. Heinz, *Probing the Intrinsic Properties of Exfoliated Graphene: Raman Spectroscopy of Free-Standing Monolayers.* Nano Letters, 2009. **9**(1): p. 346-352.
136. Coman, C. and L.F. Leopold, *Raman Mapping: Emerging Applications*, in *Raman Spectroscopy and Applications*. 2017.
137. Xu, Z., Z. He, Y. Song, X. Fu, M. Rommel, X. Luo, A. Hartmaier, J. Zhang, and F. Fang, *Topic Review: Application of Raman Spectroscopy Characterization in Micro/Nano-Machining.* Micromachines, 2018. **9**(7).
138. Ferraro, J.R., K. Nakamoto, and C.W. Brown, *Chapter 1 - Basic Theory*, in *Introductory Raman Spectroscopy (Second Edition)*, J.R. Ferraro, K. Nakamoto, and C.W. Brown, Editors. 2003, Academic Press: San Diego. p. 1-94.
139. NPL, *Characterisation of the Structure of Graphene*, in *Good Practice Guides*, N.P. Laboratory, Editor. 2017, NPL.
140. Beams, R., L. Gustavo Cançado, and L. Novotny, *Raman characterization of defects and dopants in graphene.* Journal of Physics: Condensed Matter, 2015. **27**(8): p. 083002.
141. Casiraghi, C., A. Hartschuh, H. Qian, S. Piscanec, C. Georgi, A. Fasoli, K.S. Novoselov, D.M. Basko, and A.C. Ferrari, *Raman Spectroscopy of Graphene Edges.* Nano Letters, 2009. **9**(4): p. 1433-1441.
142. Casiraghi, C., S. Pisana, K.S. Novoselov, A.K. Geim, and A.C. Ferrari, *Raman fingerprint of charged impurities in graphene.* Applied Physics Letters, 2007. **91**(23): p. 233108.
143. Kumar, B., K. Min, M. Bashirzadeh, A.B. Farimani, M.H. Bae, D. Estrada, Y.D. Kim, P. Yasaei, Y.D. Park, E. Pop, N.R. Aluru, and A. Salehi-Khojin, *The Role of External Defects in Chemical Sensing of Graphene Field-Effect Transistors.* Nano Letters, 2013. **13**(5): p. 1962-1968.
144. Sojoudi, H., J. Baltazar, C. Henderson, and S. Graham, *Impact of post-growth thermal annealing and environmental exposure on the unintentional doping of CVD graphene films.* Journal of Vacuum Science & Technology B, 2012. **30**(4): p. 041213.
145. Das, A., S. Pisana, B. Chakraborty, S. Piscanec, S.K. Saha, U.V. Waghmare, K.S. Novoselov, H.R. Krishnamurthy, A.K. Geim, A.C. Ferrari, and A.K. Sood, *Monitoring dopants by Raman scattering in an electrochemically top-gated graphene transistor.* Nat Nanotechnol, 2008. **3**(4): p. 210-5.

146. Graf, D., F. Molitor, K. Ensslin, C. Stampfer, A. Jungen, C. Hierold, and L. Wirtz, *Spatially Resolved Raman Spectroscopy of Single- and Few-Layer Graphene.* Nano Letters, 2007. **7**(2): p. 238-242.
147. Tehrani, Z., G. Burwell, M.A.M. Azmi, A. Castaing, R. Rickman, J. Almarashi, P. Dunstan, A.M. Beigi, S.H. Doak, and O.J. Guy, *Generic epitaxial graphene biosensors for ultrasensitive detection of cancer risk biomarker.* 2D Materials, 2014. **1 025004**(2).
148. AAT_Bioquest. *Fluorescence Spectrum Viewer*. 2019 21/01/2022]; Available from: https://www.aatbio.com/fluorescence-excitation-emission-spectrum-graph-viewer/.
149. Haugstad, G., *Overview of AFM*, in *Atomic Force Microscopy: Understanding Basic Modes and Advanced Applications*. 2012, John Wiley & Sons. p. 1-32.
150. Hoerber, J.K.H., *Atomic Force Microscopy: Applications in the Field of Biology*, in *Surface Analysis and Techniques in Biology*, V.S. Smentkowski, Editor. 2014, Springer International Publishing: Cham. p. 255-287.
151. Cullen, P.L., K.M. Cox, M.K. Bin Subhan, L. Picco, O.D. Payton, D.J. Buckley, T.S. Miller, S.A. Hodge, N.T. Skipper, V. Tileli, and C.A. Howard, *Ionic solutions of two-dimensional materials.* Nature Chemistry, 2017. **9**(3): p. 244-249.
152. McArthur, S.L., G. Mishra, and C.D. Easton, *Applications of XPS in Biology and Biointerface Analysis*, in *Surface Analysis and Techniques in Biology*, V.S. Smentkowski, Editor. 2014, Springer International Publishing: Cham. p. 9-36.
153. Shen, C.-H., *Chapter 7 - Detection and Analysis of Nucleic Acids*, in *Diagnostic Molecular Biology*, C.-H. Shen, Editor. 2019, Academic Press. p. 167-185.
154. Housecroft, C. and E. Constable, *Chemistry*. 2009, Harlow, UK: Pearson Education UK.
155. Tataurov, A.V., Y. You, and R. Owczarzy, *Predicting ultraviolet spectrum of single stranded and double stranded deoxyribonucleic acids.* Biophysical Chemistry, 2008. **133**(1): p. 66-70.
156. Smith, B.C., *Fundamentals of Fourier Transform Infrared Spectroscopy*. 2011, Baton Rouge, United States: Taylor & Francis Group.
157. Ghorbani, M.M. and R. Taherian, *12 - Methods of Measuring Electrical Properties of Material**Hereby from Keithley Co. and Dr. Michael B. Heaney is appreciated due to valuable content used in this chapter*, in *Electrical Conductivity in Polymer-Based Composites*, R. Taherian and A. Kausar, Editors. 2019, William Andrew Publishing. p. 365-394.
158. Yang, J., K. Jia, Y. Su, Y. Chen, and C. Zhao, *Hysteresis analysis of graphene transistor under repeated test and gate voltage stress.* Journal of Semiconductors, 2014. **35**(9): p. 094003.
159. O'Driscoll, B., *SCRAMBLE: Sweep Comparison Research Application for Multiple Back-Gated FieLd Effect measurements of graphene field effect transistors.* SoftwareX, 2021. **15**: p. 100757.
160. Kim, E., N. Jain, Y. Xu, and B. Yu, *Logic Inverter Implemented with CVD-Assembled Graphene FET on Hexagonal Boron Nitride.* IEEE Transactions on Nanotechnology, 2012. **11**(3): p. 619-623.
161. Lundh, F., *An introduction to tkinter.* URL: www. pythonware. com/library/tkinter/introduction/index. htm, 1999.
162. Harris, C.R., K.J. Millman, S.J. van der Walt, R. Gommers, P. Virtanen, D. Cournapeau, E. Wieser, J. Taylor, S. Berg, N.J. Smith, R. Kern, M. Picus, S. Hoyer, M.H. van Kerkwijk, M. Brett, A. Haldane, J.F. del Río, M. Wiebe, P. Peterson, P. Gérard-Marchant, K. Sheppard, T. Reddy, W. Weckesser, H. Abbasi, C. Gohlke, and T.E. Oliphant, *Array programming with NumPy.* Nature, 2020. **585**(7825): p. 357-362.
163. McKinney, W. *Data Structures for Statistical Computing in Python*. in *Python in Science Conference (SCIPY)*. 2010.
164. Hunter, J.D., *Matplotlib: A 2D Graphics Environment.* Computing in Science & Engineering, 2007. **9**(3): p. 90-95.
165. Bøggild, P., D.M.A. Mackenzie, P.R. Whelan, D.H. Petersen, J.D. Buron, A. Zurutuza, J. Gallop, L. Hao, and P.U. Jepsen, *Mapping the electrical properties of large-area graphene.* 2D Materials, 2017. **4**(4): p. 042003.
166. Oliphant, T.E., *A guide to NumPy*. Vol. 1. 2006: Trelgol Publishing USA.

167. Carey, C. *Baseline Removal in Raman Spectroscopy: Optimization Techniques*. in *46th Lunar and Planetary Science Conference*. 2015. Texas.
168. Zhang, Z.-M., S. Chen, and Y.-Z. Liang, *Baseline correction using adaptive iteratively reweighted penalized least squares.* Analyst, 2010. **135**(5): p. 1138-1146.
169. Zhimin, Y.L.a.Z. *Translation of airPLS source code from R to Python* 2014 16/11/2021]; Available from: https://github.com/zmzhang/airPLS/blob/master/airPLS.py.
170. Ruxton, G.D., *The unequal variance t-test is an underused alternative to Student's t-test and the Mann–Whitney U test.* Behavioral Ecology, 2006. **17**(4): p. 688-690.
171. Bartolomeo, A.D., F. Giubileo, S. Santandrea, F. Romeo, R. Citro, T. Schroeder, and G. Lupina, *Charge transfer and partial pinning at the contacts as the origin of a double dip in the transfer characteristics of graphene-based field-effect transistors.* Nanotechnology, 2011. **22**(27): p. 275702.
172. Liang, X., *Chapter 19 - Transition from Tubes to Sheets—A Comparison of the Properties and Applications of Carbon Nanotubes and Graphene*, in *Nanotube Superfiber Materials*, M.J. Schulz, V.N. Shanov, and Z. Yin, Editors. 2014, William Andrew Publishing: Boston. p. 519-568.
173. Zhong, H., Z. Zhang, H. Xu, C. Qiu, and L.-M. Peng, *Comparison of mobility extraction methods based on field-effect measurements for graphene.* AIP Advances, 2015. **5**(5).
174. Xu, H., Y. Chen, J. Zhang, and H. Zhang, *Investigating the Mechanism of Hysteresis Effect in Graphene Electrical Field Device Fabricated on SiO2 Substrates using Raman Spectroscopy.* Small, 2012. **8**(18): p. 2833-2840.
175. Liao, Z.M., B.H. Han, Y.B. Zhou, and D.P. Yu, *Hysteresis reversion in graphene field-effect transistors.* J Chem Phys, 2010. **133**(4): p. 044703.
176. HORIBA. *How to Calculate Signal to Noise Ratio*. 08/12/2021]; Determining Signal to Noise Ratio of a Spectrofluorometer: Methods and formulas to ensure accurate sensitivity comparisons]. Available from: https://www.horiba.com/en_en/technology/spectroscopy/fluorescence-spectroscopy/how-to-calculate-signal-to-noise-ratio/.
177. Adar, F. *Considerations of Grating Selection in Optimizing a Raman Spectrograph Molecular Spectroscopy*. 2013.
178. Wu, G., X. Tang, M. Meyyappan, and K.W.C. Lai, *Doping effects of surface functionalization on graphene with aromatic molecule and organic solvents.* Applied Surface Science, 2017. **425**: p. 713-721.
179. Borowicz, P., M. Latek, W. Rzodkiewicz, A. Łaszcz, A. Czerwinski, and J. Ratajczak, *Deep-ultraviolet Raman investigation of silicon oxide: thin film on silicon substrate versus bulk material.* Advances in Natural Sciences: Nanoscience and Nanotechnology, 2012. **3**(4): p. 045003.
180. Vieira, N.C., J. Borme, G. Machado, Jr., F. Cerqueira, P.P. Freitas, V. Zucolotto, N.M. Peres, and P. Alpuim, *Graphene field-effect transistor array with integrated electrolytic gates scaled to 200 mm.* J Phys Condens Matter, 2016. **28**(8): p. 085302.
181. Sikora, A., M. Woszczyna, M. Friedemann, F.J. Ahlers, and M. Kalbac, *AFM diagnostics of graphene-based quantum Hall devices.* Micron, 2012. **43**(2): p. 479-486.
182. Deng, S. and V. Berry, *Wrinkled, rippled and crumpled graphene: an overview of formation mechanism, electronic properties, and applications.* Materials Today, 2016. **19**(4): p. 197-212.
183. Tian, W., W. Li, W. Yu, and X. Liu, *A Review on Lattice Defects in Graphene: Types, Generation, Effects and Regulation.* Micromachines, 2017. **8**(5).
184. Thodkar, K., M. El Abbassi, F. Lüönd, F. Overney, C. Schönenberger, B. Jeanneret, and M. Calame, *Comparative study of single and multi domain CVD graphene using large-area Raman mapping and electrical transport characterization.* physica status solidi (RRL) - Rapid Research Letters, 2016. **10**(11): p. 807-811.
185. Graphenea. *Monolayer Graphene on 300 nm SiO_2/Si*. 12/01/2022]; Available from: https://eu.graphenea.com/collections/buy-graphene-films/products/monolayer-graphene-on-sio2-si-4-wafer.
186. Zhen, X.V., E.G. Swanson, J.T. Nelson, Y. Zhang, Q. Su, S.J. Koester, and P. Bühlmann, *Noncovalent Monolayer Modification of Graphene Using Pyrene and Cyclodextrin Receptors for Chemical Sensing.* ACS Applied Nano Materials, 2018. **1**(6): p. 2718-2726.

187. Ushiba, S., N. Miyakawa, N. Ito, A. Shinagawa, T. Nakano, T. Okino, H.K. Sato, Y. Oka, M. Nishio, T. Ono, Y. Kanai, S. Innami, S. Tani, M. Kimuara, and K. Matstumoto, *Deep-learning-based semantic image segmentation of graphene field-effect transistors.* Applied Physics Express, 2021. **14**(3): p. 036504.
188. Tilley, R.J.D., *Understanding Solids: The Science of Materials*. 2005: Wiley.
189. Feng, T., D. Xie, J. Xu, H. Zhao, G. Li, T. Ren, and H. Zhu, *Back-gate graphene field-effect transistors with double conductance minima.* Carbon, 2014. **79**: p. 363-368.
190. Pliatsikas, N., O. Karabinaki, M. Zarshenas, G.A. Almyras, I. Shtepliuk, R. Yakimova, J. Arvanitidis, D. Christofilos, and K. Sarakinos, *Energetic bombardment and defect generation during magnetron-sputter-deposition of metal layers on graphene.* Applied Surface Science, 2021. **566**: p. 150661.
191. Qiu, X.P., Y.J. Shin, J. Niu, N. Kulothungasagaran, G. Kalon, C. Qiu, T. Yu, and H. Yang, *Disorder-free sputtering method on graphene.* AIP Advances, 2012. **2**(3): p. 032121.
192. Ni, Z.H., H.M. Wang, Z.Q. Luo, Y.Y. Wang, T. Yu, Y.H. Wu, and Z.X. Shen, *The effect of vacuum annealing on graphene.* Journal of Raman Spectroscopy, 2009. **41**(5): p. 479-483.
193. Kunpeng, J., Y. Jie, Yajuan Su, N. Pengfei, Z. Jian, L. Qingqing, and Z. Huilong, *Stability analysis of a back-gate graphene transistor in air environment.* Journal of Semiconductors, 2013. **34**(8).
194. Joshi, P., H.E. Romero, A.T. Neal, V.K. Toutam, and S.A. Tadigadapa, *Intrinsic doping and gate hysteresis in graphene field effect devices fabricated on SiO2 substrates.* J Phys Condens Matter, 2010. **22**(33): p. 334214.
195. Jang, C.W., J.H. Kim, J.M. Kim, D.H. Shin, S. Kim, and S.-H. Choi, *Rapid-thermal-annealing surface treatment for restoring the intrinsic properties of graphene field-effect transistors.* Nanotechnology, 2013. **24**(40): p. 405301.
196. Wang, S., M.Z. Hossain, K. Shinozuka, N. Shimizu, S. Kitada, T. Suzuki, R. Ichige, A. Kuwana, and H. Kobayashi, *Graphene field-effect transistor biosensor for detection of biotin with ultrahigh sensitivity and specificity.* Biosensors and Bioelectronics, 2020. **165**: p. 112363.
197. Zhou, L., H. Mao, C. Wu, L. Tang, Z. Wu, H. Sun, H. Zhang, H. Zhou, C. Jia, Q. Jin, X. Chen, and J. Zhao, *Label-free graphene biosensor targeting cancer molecules based on non-covalent modification.* Biosensors and Bioelectronics, 2017. **87**: p. 701-707.
198. Ono, T., T. Oe, Y. Kanai, T. Ikuta, Y. Ohno, K. Maehashi, K. Inoue, Y. Watanabe, S.-i. Nakakita, Y. Suzuki, T. Kawahara, and K. Matsumoto, *Glycan-functionalized graphene-FETs toward selective detection of human-infectious avian influenza virus.* Japanese Journal of Applied Physics, 2017. **56**(3).
199. Chemistry-Library. *Infrared Spectroscopy Absorption Table*. 2020 2020/11/3/ 13/12/2021]; Available from: https://chem.libretexts.org/@go/page/22645.
200. Iqbal, M.W., A.K. Singh, M.Z. Iqbal, and J. Eom, *Raman fingerprint of doping due to metal adsorbates on graphene.* Journal of Physics: Condensed Matter, 2012. **24**(33): p. 335301.
201. Liu, B., S. Salgado, V. Maheshwari, and J. Liu, *DNA adsorbed on graphene and graphene oxide: Fundamental interactions, desorption and applications.* Current Opinion in Colloid & Interface Science, 2016. **26**: p. 41-49.
202. Gürünlü, B., Ç. Taşdelen-Yücedağ, and M. Bayramoğlu, *Graphene Synthesis by Ultrasound Energy-Assisted Exfoliation of Graphite in Various Solvents.* Crystals, 2020. **10**(11).
203. Kasry, A., A.A. Ardakani, G.S. Tulevski, B. Menges, M. Copel, and L. Vyklicky, *Highly Efficient Fluorescence Quenching with Graphene.* The Journal of Physical Chemistry C, 2012. **116**(4): p. 2858-2862.
204. Kim, J., L.J. Cote, F. Kim, and J. Huang, *Visualizing Graphene Based Sheets by Fluorescence Quenching Microscopy.* Journal of the American Chemical Society, 2010. **132**(1): p. 260-267.
205. Khan, N.I. and E. Song, *Detection of an IL-6 Biomarker Using a GFET Platform Developed with a Facile Organic Solvent-Free Aptamer Immobilization Approach.* Sensors, 2021. **21**(4) 1335.
206. Xu, S., C. Zhang, S. Jiang, G. Hu, X. Li, Y. Zou, H. Liu, J. Li, Z. Li, X. Wang, M. Li, and J. Wang, *Graphene foam field-effect transistor for ultra-sensitive label-free detection of ATP.* Sensors and Actuators B: Chemical, 2019. **284**: p. 125-133.

207. Gao, Y., M. Shi, R. Zhou, C. Xue, M. Wang, and H. Chen, *Solvent-dependent fluorescence property of multi-walled carbon nanotubes noncovalently functionalized by pyrene-derivatized polymer.* Nanotechnology, 2009. **20**(13): p. 135705.
208. Jones, G., V. Vullev, E.H. Braswell, and D. Zhu, *Multistep Photoinduced Electron Transfer in a de Novo Helix Bundle: Multimer Self-Assembly of Peptide Chains Including a Chromophore Special Pair1.* Journal of the American Chemical Society, 2000. **122**(2): p. 388-389.
209. Barry, N.P.E. and B. Therrien, *Chapter 13 - Pyrene: The Guest of Honor*, in *Organic Nanoreactors*, S. Sadjadi, Editor. 2016, Academic Press: Boston. p. 421-461.
210. Wang, H., Y. Liu, and G. Liu, *Reusable resistive aptasensor for Pb(II) based on the Pb(II)-induced despiralization of a DNA duplex and formation of a G-quadruplex.* Microchimica Acta, 2018. **185**(2): p. 142.
211. Mikoliunaite, L., R.D. Rodriguez, E. Sheremet, V. Kolchuzhin, J. Mehner, A. Ramanavicius, and D.R.T. Zahn, *The substrate matters in the Raman spectroscopy analysis of cells.* Scientific Reports, 2015. **5**(1): p. 13150.
212. Nakatsuka, N., K.-A. Yang, M. Abendroth John, M. Cheung Kevin, X. Xu, H. Yang, C. Zhao, B. Zhu, S. Rim You, Y. Yang, S. Weiss Paul, N. Stojanović Milan, and M. Andrews Anne, *Aptamer–field-effect transistors overcome Debye length limitations for small-molecule sensing.* Science, 2018. **362**(6412): p. 319-324.
213. Khan, N.I., M. Mousazadehkasin, S. Ghosh, J.G. Tsavalas, and E. Song, *An integrated microfluidic platform for selective and real-time detection of thrombin biomarkers using a graphene FET.* Analyst, 2020. **145**(13): p. 4494-4503.
214. Wu, G., X. Tang, M. Meyyappan, and K.W.C. Lai. *Chemical functionalization of graphene with aromatic molecule*. in *2015 IEEE 15th International Conference on Nanotechnology (IEEE-NANO)*. 2015.
215. Sidorov, A.N. and T.M. Orlando, *Monolayer Graphene Platform for the Study of DNA Damage by Low-Energy Electron Irradiation.* The Journal of Physical Chemistry Letters, 2013. **4**(14): p. 2328-2333.
216. O'Driscoll, B., V. Raghavan, T. Bungon, P. Davey, T. Whitley, S. Awan, and S. Gorthi, *Aptamer functionalisation of back-gated gra-phene field effect transistors for Pb2+ sensing.* Eng. Proc, 2021. **3**.
217. Chen, T.-Y., P.T.K. Loan, C.-L. Hsu, Y.-H. Lee, J. Tse-Wei Wang, K.-H. Wei, C.-T. Lin, and L.-J. Li, *Label-free detection of DNA hybridization using transistors based on CVD grown graphene.* Biosensors and Bioelectronics, 2013. **41**: p. 103-109.
218. Fu, W., L. Feng, G. Panaitov, D. Kireev, D. Mayer, A. Offenhauser, and H. Krause, *Biosensing near the neutrality point of Graphene.* Science Advances, 2017. **3**: p. 7.
219. Farré, M., L. Kantiani, and D. Barceló, *Chapter 7 - Microfluidic Devices: Biosensors*, in *Chemical Analysis of Food: Techniques and Applications*, Y. Picó, Editor. 2012, Academic Press: Boston. p. 177-217.
220. Lafleur, J.P., A. Jönsson, S. Senkbeil, and J.P. Kutter, *Recent advances in lab-on-a-chip for biosensing applications.* Biosensors and Bioelectronics, 2016. **76**: p. 213-233.
221. Almeida, L.C., T. Frade, R.D. Correia, Y. Niu, G. Jin, J.P. Correia, and A.S. Viana, *Electrosynthesis of polydopamine-ethanolamine films for the development of immunosensing interfaces.* Scientific Reports, 2021. **11**(1): p. 2237.
222. Fischer, M.J.E., *Amine Coupling Through EDC/NHS: A Practical Approach*, in *Surface Plasmon Resonance: Methods and Protocols*, N.J. Mol and M.J.E. Fischer, Editors. 2010, Humana Press: Totowa, NJ. p. 55-73.
223. Jolly, P., J. Rainbow, A. Regoutz, P. Estrela, and D. Moschou, *A PNA-based Lab-on-PCB diagnostic platform for rapid and high sensitivity DNA quantification.* Biosensors and Bioelectronics, 2019. **123**: p. 244-250.
224. Zupančič, U., J. Rainbow, C. Flynn, J. Aidoo-Brown, P. Estrela, and D. Moschou, *Strategies for Multiplexed Electrochemical Sensor Development*, in *Modern Techniques in Biosensors: Detection Methods and Commercial Aspects*, G. Dutta, A. Biswas, and A. Chakrabarti, Editors. 2021, Springer Singapore: Singapore. p. 63-93.
225. Dutta, G., J. Rainbow, U. Zupancic, S. Papamatthaiou, P. Estrela, and D. Moschou, *Microfluidic Devices for Label-Free DNA Detection.* Chemosensors, 2018. **6**(4), 43.

Appendix

A1. Oligonucleotide Extinction Coefficients

The reference table for the extinction coefficients of oligonucletodies used for the nearest-neighbour model is given below [155].

Base	Extinction Coefficient ($Lmol^{-1}cm^{-1}$)	Base	Extinction Coefficient ($Lmol^{-1}cm^{-1}$)
A	15400	CG	18000
C	7400	CT	15200
G	11500	GA	25200
T	8700	GC	17600
AA	27400	GG	21600
AC	21200	GT	20000
AG	25000	TA	23400
AT	22800	TC	16200
CA	21200	TG	19000
CC	14600	TT	16800

Table A1.1 – Extinction coefficient of oligonucleotides [155].

A2. SCRAMBLE Exported Files

Exported files from SCRAMBLE are shown below:

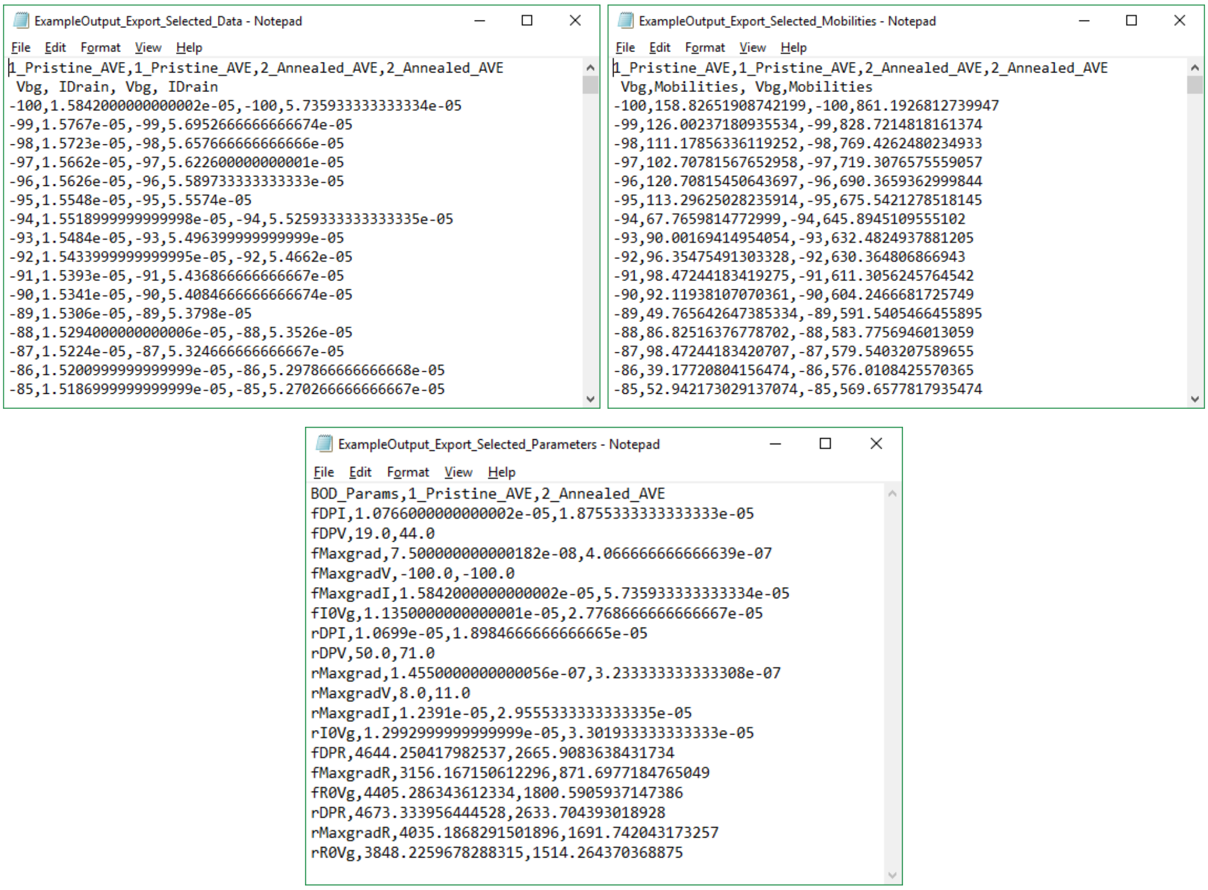

```
1_Pristine_AVE,1_Pristine_AVE,2_Annealed_AVE,2_Annealed_AVE
 Vbg, IDrain, Vbg, IDrain
-100,1.5842000000000002e-05,-100,5.735933333333334e-05
-99,1.5767e-05,-99,5.6952666666666674e-05
-98,1.5723e-05,-98,5.657666666666666e-05
-97,1.5662e-05,-97,5.622600000000001e-05
-96,1.5626e-05,-96,5.589733333333333e-05
-95,1.5548e-05,-95,5.5574e-05
-94,1.5518999999999998e-05,-94,5.525933333333335e-05
-93,1.5484e-05,-93,5.496399999999999e-05
-92,1.5433999999999995e-05,-92,5.4662e-05
-91,1.5393e-05,-91,5.436866666666667e-05
-90,1.5341e-05,-90,5.4084666666666674e-05
-89,1.5306e-05,-89,5.3798e-05
-88,1.5294000000000006e-05,-88,5.3526e-05
-87,1.5224e-05,-87,5.324666666666667e-05
-86,1.5200999999999999e-05,-86,5.297866666666668e-05
-85,1.5186999999999999e-05,-85,5.270266666666667e-05
```

```
1_Pristine_AVE,1_Pristine_AVE,2_Annealed_AVE,2_Annealed_AVE
 Vbg,Mobilities, Vbg,Mobilities
-100,158.82651908742199,-100,861.1926812739947
-99,126.00237180935534,-99,828.7214818161374
-98,111.17856336119252,-98,769.4262480234933
-97,102.70781567652958,-97,719.3076575559057
-96,120.70815450643697,-96,690.3659362999844
-95,113.29625028235914,-95,675.5421278518145
-94,67.7659814772999,-94,645.8945109555102
-93,90.00169414954054,-93,632.4824937881205
-92,96.35475491303328,-92,630.364806866943
-91,98.47244183419275,-91,611.3056245764542
-90,92.11938107070361,-90,604.2466681725749
-89,49.765642647385334,-89,591.5405466455895
-88,86.82516376778702,-88,583.7756946013059
-87,98.47244183420707,-87,579.5403207589655
-86,39.17720804156474,-86,576.0108425570365
-85,52.942173029137074,-85,569.6577817935474
```

```
BOD_Params,1_Pristine_AVE,2_Annealed_AVE
fDPI,1.0766000000000002e-05,1.8755333333333333e-05
fDPV,19.0,44.0
fMaxgrad,7.500000000000182e-08,4.066666666666639e-07
fMaxgradV,-100.0,-100.0
fMaxgradI,1.5842000000000002e-05,5.735933333333334e-05
fI0Vg,1.1350000000000001e-05,2.7768666666666667e-05
rDPI,1.0699e-05,1.8984666666666665e-05
rDPV,50.0,71.0
rMaxgrad,1.4550000000000056e-07,3.233333333333308e-07
rMaxgradV,8.0,11.0
rMaxgradI,1.2391e-05,2.9555333333333335e-05
rI0Vg,1.2992999999999999e-05,3.3019333333333333e-05
fDPR,4644.250417982537,2665.9083638431734
fMaxgradR,3156.167150612296,871.6977184765049
fR0Vg,4405.286343612334,1800.5905937147386
rDPR,4673.333956444528,2633.704393018928
rMaxgradR,4035.1868291501896,1691.742043173257
rR0Vg,3848.2259678288315,1514.264370368875
```

Figure A2.1 – Saved ".bod" files exported from SCRAMBLE A) Data - Raw data from input ".csv" is processed into columns of V_G and I_{SD} with all metadata removed, B) Mobilities – The mobility at every V_G value is calculated, C) Parameters – The determined parameters for Dirac points, maximum transconductance and current at V_G = 0 are given.

Names of Parameters given in the Parameter.bod file:

Exported Name	Explanation
fDPI	Current value for forward Dirac point
fDPV	Voltage value for forward Dirac point
fMaxgrad	Maximum gradient (conductance) value for the forward sweep
fMaxgradV	Voltage value for the maximum gradient for forward sweep
fMaxgradI	Current value for the maximum gradient for forward sweep
fI0Vg	Current value at V_G=0 for the forward sweep
rDPI	Current value for reverse Dirac point
rDPV	Voltage value for reverse Dirac point
rMaxgrad	Maximum gradient (conductance) value for the reverse sweep
rMaxgradV	Voltage value for the maximum gradient for reverse sweep
rMaxgradI	Current value for the maximum gradient for reverse sweep
rI0Vg	Current value at V_G=0 for the reverse sweep
fDPR	Resistance value for forward Dirac point
fMaxgradR	Resistance value for the maximum gradient for forward sweep
fR0Vg	Resistance value at V_G=0 for the forward sweep
rDPR	Resistance value for reverse Dirac point
rMaxgradR	Resistance value for the maximum gradient for reverse sweep
rR0Vg	Resistance value at V_G=0 for the reverse sweep

Table A2.1 – Explanations of the exported names in the “Parameters.bod” file

A3. RAMAN_VIEWER Exported Files

Exported files from RAMAN_VIEWER are shown below:

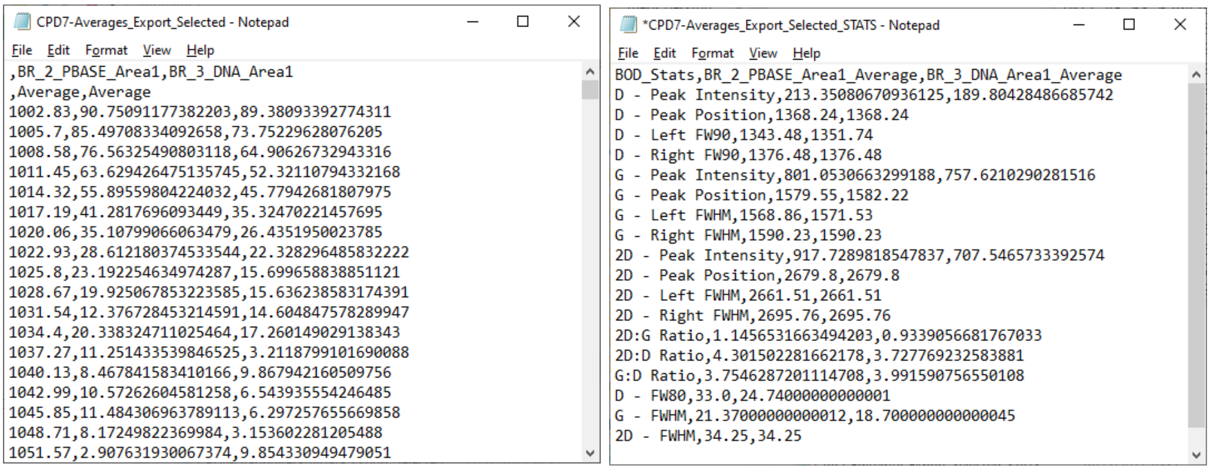

```
,BR_2_PBASE_Area1,BR_3_DNA_Area1
,Average,Average
1002.83,90.75091177382203,89.38093392774311
1005.7,85.49708334092658,73.75229628076205
1008.58,76.56325490803118,64.90626732943316
1011.45,63.629426475135745,52.32110794332168
1014.32,55.89559804224032,45.77942681807975
1017.19,41.2817696093449,35.32470221457695
1020.06,35.10799066063479,26.4351950023785
1022.93,28.612180374533544,22.328296485832222
1025.8,23.192254634974287,15.699658838851121
1028.67,19.925067853223585,15.636238583174391
1031.54,12.376728453214591,14.604847578289947
1034.4,20.338324711025464,17.260149029138343
1037.27,11.251433539846525,3.2118799101690088
1040.13,8.467841583410166,9.867942160509756
1042.99,10.57262604581258,6.543935554246485
1045.85,11.484306963789113,6.297257655669858
1048.71,8.17249822369984,3.153602281205488
1051.57,2.907631930067374,9.854330949479051
```

```
BOD_Stats,BR_2_PBASE_Area1_Average,BR_3_DNA_Area1_Average
D - Peak Intensity,213.35080670936125,189.80428486685742
D - Peak Position,1368.24,1368.24
D - Left FW90,1343.48,1351.74
D - Right FW90,1376.48,1376.48
G - Peak Intensity,801.0530663299188,757.6210290281516
G - Peak Position,1579.55,1582.22
G - Left FWHM,1568.86,1571.53
G - Right FWHM,1590.23,1590.23
2D - Peak Intensity,917.7289818547837,707.5465733392574
2D - Peak Position,2679.8,2679.8
2D - Left FWHM,2661.51,2661.51
2D - Right FWHM,2695.76,2695.76
2D:G Ratio,1.1456531663494203,0.9339056681767033
2D:D Ratio,4.301502281662178,3.727769232583881
G:D Ratio,3.7546287201114708,3.991590756550108
D - FW80,33.0,24.740000000000001
G - FWHM,21.370000000000012,18.700000000000045
2D - FWHM,34.25,34.25
```

Figure A3.1 – Saved ".bod" files exported from RAMAN_VIEWER A) Spectral data which gives the wavenumber against intensity for averaged spectra. B) Calculated Metrics – Metrics that are calculated each of the exported spectra are given.

Names of Parameters given in the STATS.bod file:

Exported Name	Explanation
D - Peak Intensity	Intensity of the D peak, I(D)
D - Peak Position	Peak position of 2D peak, PP(D)
D - Left FW90	Rising edge of PP(D) for 90% of I(D)
D - Right FW90	Falling edge of PP(D) for 90% of I(D)
G - Peak Intensity	Intensity of the G peak, I(G)
G - Peak Position	Peak position of G peak, PP(G)
G - Left FWHM	Rising edge of PP(G) for 50% of I(G)
G - Right FWHM	Falling edge of PP(G) for 50% of I(G)
2D - Peak Intensity	Intensity of the 2D peak, I(2D)
2D - Peak Position	Peak position of 2D peak, PP(2D)
2D - Left FWHM	Rising edge of PP(2D) for 50% of I(2D)
2D - Right FWHM	Falling edge of PP(2D) for 50% of I(2D)
2D:G Ratio	Intensity ratio I(2D)/I(G)
2D:D Ratio	Intensity ratio I(2D)/I(D)
G:D	Intensity ratio I(G)/I(D)
D – FW90	Full width at 90% intensity of I(D)
G - FWHM	Full width at half maximum of G peak, FWHM(G)
2D - FWHM	Full width at half maximum of 2D peak, FWHM(2D)

Table A3.1 – Explanations of the exported names in the "STATS.bod" file

A4. Fluorescently Labelled Antibodies

Details are provided on the antibodies and fluorophore groups used in developing fluorescent technique determine. All antibodies were diluted in PBS to a concentration of 10 µg/mL.

Florophore Name	Excitation Wavelength (nm)	Emission Wavelength (nm)
AT-555	555	568
AF-488	499	520
Cy5	651	670
FITC	491	516

Table A4.1 – Fluorophore group details, sourced from [148].

Host	Anti-	Fluorophore Group
Donkey	Sheep	Cy5
Donkey	Mouse	AT-555
Donkey	Mouse	FITC
Donkey	Sheep	FITC
Donkey	Goat	AF-488
Donkey	Goat	AT-555
Donkey	Goat	FITC

Table A4.2 – Primary antibodies used for direct immobilisation of FTAs

Primary Host	Primary Anti-	Secondary Host	Secondary Anti-	Fluor. Group
Rabbit	Human	Donkey	Rabbit	AT-555
Rabbit	Human	Donkey	Rabbit	AF-488
Mouse	NF 200	Donkey	Mouse	FITC
Mouse	Rat TLR4	Donkey	Mouse	FITC
Goat	Rat TNFα	Donkey	Goat	FITC
Rabbit	Rat β Tubulin	Donkey	Rabbit	AF-488

Table A4.3 – Primary/Secondary antibodies used for indirect immobilisation of FTAs